Microscopic Study of Granular Material Behaviours under General Stress Paths

By

Dunshun Yang

B.Eng, M.Sc

Thesis submitted to the University of Nottingham

for the degree of Doctor of Philosophy

November 2013

Abstract

The granular material behaviour is determined by the local contact behaviour between particles and the spatial arrangement of particles. Investigation of particle-scale mechanism provides fundamental insights into global granular material behaviour. A multi-scale investigation has been carried out to study granular material behaviour under general stress paths using discrete element method (DEM). The commercial software Particle Flow Code in Three Dimensions (PFC3D) is employed for numerical simulations and the linear contact model is used to describe local contact behaviour. General loading paths were achieved by implementing a boundary control programme with independent control of both the magnitudes of three principal stresses and their principal directions.

The intermediate principal stress ratio $b = (s_2 - s_3)/(s_1 - s_3)$, where s_1, s_2, s_3 are the major, intermediate and minor principal stresses, and material anisotropy both had significant effect on granular material strength. The true triaxial simulation results indicated that the peak stress ratio was mainly contributed by the micro-scale contact force anisotropy. A smaller stress ratio was observed at greater a b value due to smaller degree of contact force anisotropy. Fabric anisotropy was another contributor to the material stress state. A lower peak stress ratio was obtained at a larger tilting major principal stress direction a from the vertical deposition direction since smaller fabric anisotropy degree developed at larger a. However, the material initial anisotropy had negligible effect on the critical stress ratio owing to the same contact force anisotropy and fabric anisotropy achieved.

In true triaxial simulations, the intermediate strain increment rate ratio $b_{d\varepsilon}$ was generally larger than the stress ratio b since the particle-scale tangential force ratio b_t was observed to be smaller than b value. The non-coaxial deformation observed in monotonic loading with various loading direction a can be explained due to the non-coincidence between the principal fabric direction and the principal stress direction. And the degree of non-coaxiality decreased against shearing as the principal fabric direction approached loading direction gradually.

The granular material response to rotational shear showed significant volumetric contraction and deformation non-coaxiality. The material internal structure rotated continuously along the principal stress rotation. The principal fabric direction did not exactly follow the rotation of principal stress direction. The fabric reorganisation mechanism accompanied by irrecoverable plastic deformation, leading to non-coaxial deformation behaviour.

During rotational shear, the ultimate void ratio was determined by the stress ratio and b value but independent of initial void ratios. Under otherwise identical conditions, the greater internal structure anisotropy was observed at the higher stress ratio and at a greater b value, resulting in smaller ultimate void ratio (larger volumetric contraction). The general degree of deformation non-coaxiality decreased with increasing stress ratio and b value for rotational shear. The difference between the major principal stress direction and the major principal fabric direction was smaller at higher stress ratio and greater b value.

It was interesting to note that the sample could fail during rotational shear, resulting in significant deviatoric strain developed in the first few cycles. The sample failed at a stress ratio $h = 0.9$, which was lower than the peak stress ratio $h_p = 1.08$ obtained in monotonic loading but higher than the critical stress ratio $h_c = 0.82$. This indicated importance of considering stress rotation in geotechnical design and the material strength should be chosen based on the critical stress ratio rather than the peak value.

The multi-scale investigation of granular material explains the strength characteristics from the micromechanical point of view. Observations on the fabric evolution have been made under various loading conditions. This may be useful information for the development of an advanced constitutive model.

Acknowledgement

First and foremost, I am deeply grateful to Prof. Hai-sui Yu, my supervisor, for his valuable advice, encouragement and financial support throughout the project. It is him who leads me into the geotechnical community. His professional attitude and example will be the driving force of my future geotechnical career.

I would like to express special thanks to my co-supervisor, Dr. Xia Li, for her patient guidance in the four years research life. Without her valuable suggestions and encouragement, the project would be difficult. What I can learn from her includes not only the professional knowledge but also the attitude to the research. Her rigorous scholarship and high standard self-motivation will influence me in whatever future position I am.

Appreciation also goes to my colleagues, particularly Dr. Jun Ai, Mr. Nian Hu, in Nottingham Centre for Geomechanics (NCG). The discussions with you prove to be useful. The time spent in NCG was funny and memorable. I wish you all the best in the future.

Finally, I would like to express my sincere gratitude to my parents and my brother for their unconditional support and love.

Table of contents

List of Figures

List of tables

Chapter 1 Introduction

1.1 Research Background

In geotechnical engineering problems, e.g., earthquakes, traffic loading, sea waves and river embankment, soil goes through complicated loading paths, where the magnitudes of three principal stresses often vary and their directions rotate. Sand behaviour is loading path dependent. The loading paths involved in soil testing are generally classified as proportional loading path and non-proportional loading path. The proportional loading path is defined as that the deviatoric stress components are kept in a constant ratio to each other during loading and the soil element does not rotate in reference to the frame of principal stresses. Loading path does not fit the above definition refers to non-proportional loading path. Experimental study showed significant effect of the intermediate principal stress on soil behaviours under true triaxial shearing (Ko and Scott, 1967, Sutherland and Mesdary, 1969, Lade and Duncan, 1973, Ochiai and Lade, 1983). Rotational shear generates significant plastic deformation with continuous rotation of the principal stress directions even though the magnitudes of stress invariants are fixed (Miura et al., 1986, Sayao, 1989, Tong et al., 2010, Yang, 2013). Significant pore pressure build-up was observed in undrained rotational shear, even tested on dense sand (Nakata et al., 1998, Yang and Li, 2007). And the flow deformation was generally non-coaxial, which is termed as

the principal strain increment direction does not follow the principal stress direction (Gutierrez et al., 1991). Consideration of loading path dependence is important in geotechnical engineering design and construction since loading paths commonly encountered in engineering practice are non-proportional.

Granular material is generally anisotropic. The sand response is sensitive to loading direction since most soils are inherently anisotropic. A lower strength was reported when the major principal stress direction inclined further from the vertical deposition direction (Arthur and Menzies, 1972, Oda, 1972, Miura et al., 1986). And significant non-coaxial behaviour between the major principal stress direction and the major principal strain increment direction has also been observed (Miura et al., 1986, Symes et al., 1988, Cai et al., 2013).

Though soil has been studied extensively in laboratory tests, constitutive models describing the observed behaviour, e.g., anisotropic behaviour and non-coaxial deformation remain challenging. Lacking of fundamental understanding in the observed complex behaviour is identified as the bottleneck for the development of advanced constitutive models for better capturing the stress-strain responses under both proportional and non-proportional loading paths. The current project sets out to explore the fundamentals of granular material behaviour through multi-scale investigation for the potential development of the constitutive models.

The global behaviour of granular materials is determined by the local contact behaviour between particles and the spatial arrangement of particles. Study of particle-scale mechanism provides fundamental insights into global granular material

behaviour. Moreover, it guides the direction of more applicable constitutive modelling of granular material.

Extensive experimental study has been reported on micromechanics of granular material (Oda, 1972a, Calvetti et al., 1997, Majmudar and Behringer, 2005, Ando et al., 2012, Fonseca et al., 2013). The experimental micromechanics examine the real soil behaviour and it provides the referenced database for verifying numerical study. Limitations of laboratory experiments include difficulty in preparing identical samples; difficulty in obtaining information on particle interactions and extremely time consuming for data post-processing.

In parallel, the discrete element method (DEM) has been employed of increasing usage to conduct multi-scale investigation on granular material behaviour (Rothenburg and Bathurst, 1989, Thornton, 2000, Li and Yu, 2009, Fu and Dafalias;, 2011). Although DEM models granular material with idealised particle shape and of limited particle numbers, the typical stress-strain behaviours have been found as qualitative reproduction of observed sand responses. The advantage of the DEM simulation is that it can easily provide the instant microscopic information of particles, e.g., contact force vector and contact normal vector, at any stage of shearing in a non-destructive way, which is convenient for multi-scale investigations.

In this research, DEM is employed to provide multi-scale information for a multi-scale investigation on three-dimensional granular material behaviour subjected to various loading paths. DEM simulations on general three-dimensional stress conditions with independent control of three principal stresses and principal stress

directions will be conducted and reported. The commercial software, Particle Flow Code in Three Dimensions Version 3.1 (PFC3D) (Itasca, 1999), is used to carry out numerical simulations, which is user friendly and has been widely applied for multi-scale study by researchers (Li and Yu, 2009, Yimsiri and Soga, 2010, Guo and Zhao, 2013). The anisotropy of granular material is an important aspect of granular material behaviour. The micromechanical analysis will be followed focusing on material anisotropy, including the evolution of contact forces and contact normal fabric. The information on the contact force and contact normal fabric will be interpreted in terms of their correlation to the strength-deformation characteristics of granular materials.

1.2 Aim and objectives

The primary aim is to investigate the granular material response to general stress paths, both proportional and non-proportional, with independent control of three principal stresses in terms of both their magnitudes and principal directions using DEM. The macroscopic stress-strain behaviour will be presented and qualitatively compared with the sand responses observed in laboratory. The micro-scale contact force and fabric evolution will be extracted and interpreted focusing on their correlations to the observed global behaviours.

To achieve the aim, the following objectives will be accomplished:

Objective 1: To develop a virtual experiment model for numerical simulations under various loading paths within the commercial software PFC3D (Itasca, 1999) and qualitative verification with existing experimental data.

Objective 2: To investigate the influence of intermediate principal stress by conducting true triaxial simulations on the initially isotropic samples. The micro-scale information of contact force and contact normal fabric will be analyzed to interpret the effect of intermediate principal stress on strength characteristics.

Objective 3: To study the influence of material anisotropy by conducting true triaxial tests on the initially anisotropic samples and by investigating the loading direction dependent strength-deformation behaviour under three-dimensional simulations with tilting principal stress directions. The strength anisotropy and non-coaxial behaviour will be explained by examining the microstructural contact force tensors and contact normal fabric tensor.

Objective 4: To study the granular material behaviour under rotational shear with fixed magnitudes of stress invariants while continuous rotation of the major principal stress direction. The microscopic fabric evolution will be presented for better understanding of material deformation behaviour.

Objective 5: To discuss the effect of particle shape on granular material response by comparing simulation results on samples with spherical particles and samples with non-spherical particles of two identical overlapping balls under monotonic shear and rotational shear. The micro-scale contact force anisotropy and fabric anisotropy will

be evaluated to explain the particle shape effect on strength characteristics. And the effect of particle shape on fabric evolution will be discussed.

1.3 Thesis structure

The thesis is divided into 9 chapters. The content of each chapter is briefly summarised as follows:

Chapter 1 gives a brief background introduction and states the aim and objectives of this research.

Chapter 2 reviews previous study of granular material behaviour. The state dependent dilatancy and granular material anisotropy are introduced in Section 2.1. Section 2.2 presents the experimental study of sand behaviours under general three-dimensional stress paths. And the recent multi-scale study on granular material using DEM is provided in Section 2.3. The final section introduces the macro-micro relations, to set up the connections between particle-scale observations and continuum-scale material responses.

Chapter 3 introduces the discrete element method. The advantages and disadvantages of DEM are briefly introduced in Section 3.1. As the commercial software PFC3D is used, Section 3.2 gives the principles of PFC3D. In Section 3.3, the geometrical properties of individual particle for numerical simulation are specified and a parametric study is conducted to determine the sufficient sample size to serve as a representative volume. The mechanical parameters for the local contact

model are specified from the parametric study as shown in Section 3.4. Finally, a brief summary is given in Section 3.5.

Chapter 4 elaborates on the virtual experiment set-up using PFC3D. It includes the generation of the polyhedral shaped boundary. The numerical implementations of general loading paths, stress-controlled or strain-controlled, are introduced. The accuracy of boundary controls and test control in maintaining the quasi-static material behaviour are examined. The realisation of particular loading paths will be exemplified. Typical simulation results are presented for validating the applicability of the numerical experiment model. This is also the objective 1 of the proposed research.

Chapter 5 investigates the influence of intermediate principal stress by loading initially isotropic samples with spherical particles under true triaxial test, to achieve objective 2 through multi-scale investigations. The influence of initial void ratios on material response will also be covered.

Chapter 6 study the influence of material anisotropy by presenting the simulation results of the anisotropic sample with spherical particles under various tilting angle of the major principal stress direction relative to the vertical direction. The anisotropic samples can be initially anisotropic due to the deposition process and the pre-loaded sample. The results are analysed to fulfil the objective 3.

Chapter 7 presents the simulation results of samples consisting of non-spherical particles. The effects of material anisotropy and loading direction on material behaviour are demonstrated to be supplement to the objective 3. And the

results are compared to those from sample with spherical particles to discuss the influence of particle shape as in objective 5.

Chapter 8 shows the rotational shear results of the sample with non-spherical particles to achieve the objective 4. And the influence of initial void ratios on rotational shear behaviour is also presented.

Chapter 9 summarises the major conclusions from the research and recommendations for future study.

Chapter 2 Literature review

The granular material behaviour has been widely investigated during the past a few decades and it is still an interesting subject to researchers. This is probably due to the complexity of granular material behaviour. Section 2.1 introduces the state-dependent dilatancy behaviour and the anisotropy of granular material. As the granular material behaviour is loading path dependent and sensitive to loading direction owing to initial anisotropy, the granular sand responses to general three-dimensional stress paths are reviewed in Section 2.2. The macroscopic granular material behaviour is governed by the local contact behaviour due to its discrete nature. Hence, the micromechanical investigation provides insights into particle-scale mechanism. The recent multi-scale investigation of granular material behaviour using DEM is reviewed in Section 2.3. To apply the micro-scale observations in continuum-scale, the two scales are linked by the macro-micro relations as shown in Section 2.4. Finally, a brief summary of the literature is given in Section 2.5.

2.1 Mechanical behaviour of granular material

2.1.1 State dependent dilatancy

Dilatancy is defined as the volume change of granular substance when subjected to shearing, mathematically referred to the ratio of the plastic volume increment to the plastic deviatoric strain increment. Rowe (1962) formulated a stress-dilatancy relationship by assuming minimum energy dissipation, suggesting the rate of dilatancy be only a function of stress ratio. Rowe's stress-dilatancy formulation works satisfactorily for cohesive soils. However, experimental results have indicated that the rate of dilatancy for granular material is not only affected by stress ratio but also other material state variables, e.g., relative density. It is well-known that dense sand tends to dilate and loose sand contracts even sheared at the same stress ratio. Therefore, treating dilatancy only a function of stress ratio cannot model granular material response over a wide range of densities.

The density is used to characterise sand dense or loose by determining how close sand density to its maximum or minimum density. If sand density is closer to its minimum density, it is termed as dense, reversely defined as loose. However, the contraction or dilation of sand not only depends on density, i.e., dense sand performed contraction, similar to loose sand behaviour, when sheared at extremely high confining pressure (Bolton, 1986). Been and Jefferies (1985) proposed a state parameter y to decide sand dilation or contraction by the difference between the current state void ratio e and the critical state void ratio e_c under the same mean effective stress, $y = e - e_c$, where the critical state is defined as granular material

deformed at constant mean effective stress and deviatoric stress, sample volume unchanged while continuous increase of deviatoric strain. Sand with negative state parameter y would dilate to the critical state and sand with positive state parameter would contract to the critical state.

Besides Been's state parameter, there are many other indices proposed to quantify the dilatancy of granular materials under the framework of the critical state theory, e.g., the combination of e and e_c stated as state index I_s for characterising sand dilatancy behaviour during shearing (Ishihara, 1993) and a state pressure index I_p defined as the ratio of the current state mean effective pressure over the critical state mean effective pressure (Wang et al., 2002). In spite of different state parameter definitions, they all choose the critical state as a reference state and a single parameter is proposed to reflect influences of both effective confining pressure and density on dilatancy behaviour.

It was observed both experimentally and numerically that granular material behaved more dilative in triaxial compression test with the major principal stress perpendicular to the bedding plane than in triaxial compression test with the major principal stress within the bedding plane (Oda, 1972a, Arthur and Menzies, 1972, Li and Yu, 2009, Yimsiri and Soga, 2011). In addition, experimental findings showed that sand experienced significant volume contraction under pure rotation of principal stress direction with constant magnitudes of stress invariants (Tong et al., 2010, Yang, 2013). It indicates that other internal state variables, e.g., sand anisotropy, also affect dilatancy besides stress ratio and state parameter. Accordingly, a general state-dependent dilatancy function was expressed as (Li and Dafalias, 2000) :

$$d = d\left(h, e, Q, C\right) \tag{2.1}$$

where d is the dilatancy rate, Q and C denote internal state variables other than void ratio e and intrinsic material constants, respectively.

In summary, the dilatancy behaviour of granular material could be modelled over a wide range of densities and stress levels by incorporating state parameter in reference to the critical state. However, effects of other factors, e.g., material anisotropy, on the dilatancy behaviour of granular material have not been fully understood and considered in constitutive modelling.

2.1.2 Anisotropy of granular materials

The anisotropy of granular material has been extensively investigated in the past a few decades. It is considered to be an important parameter affecting soil behaviour. In considering soil anisotropy, it was first distinguished as inherent anisotropy and induced anisotropy (Casagrande and Carrillo, 1944). The inherent anisotropy is produced during the geological sedimentation process and the induced anisotropy is formed by nonelastic deformation due to anisotropic external loading.

2.1.2.1 Inherent anisotropy

Arthur and Menzies (1972) developed a cubic triaxial cell for three-dimensional true triaxial test to study the material inherent anisotropy. The samples were prepared by pouring sand into a tilting mould with various angles to the vertical deposition direction in order to conduct true triaxial test under various principal stress directions. It was found that the material performed anisotropic strength and

pre-failure stress-strain behaviour at different loading directions. This clearly indicated that the prepared sample was inherently anisotropic.

Yamada and Ishihara (1979) examined the anisotropic deformation characteristics of loose sand specimen prepared by depositing the sand under water, under drained three-dimensional stress conditions. The major conclusion was that the influence of inherent anisotropy on deformation behaviour was large at the small shear stress level and disappeared at the failure shear stress level. Later, they (1981) tested the same material of loose specimen in undrained conditions. Similar behaviour was observed as that in drained tests. It was summarised that the inherently anisotropic specimen showed higher strength sheared vertically than sheared horizontally during triaxial compression.

Haruyama (1981) clarified the material inherent anisotropy in deposited sample consisting of spherical particles by the isotropic compression test. The specimen showed a lower compressibility in the direction of deposition than in the direction perpendicular to the deposition direction.

Kumruzzaman and Yin (2010) investigated the anisotropic behaviour of decomposed granite in a series of undrained tests with fixed principal stress direction using hollow cylinder apparatus. The results showed obvious undrained strength anisotropy due to material inherent anisotropy.

The above experimental results clearly indicate that a sand specimen is inherently anisotropic. The inherent anisotropy is reflected as the loading direction dependent stress-strain behaviour. The effect of inherent anisotropy is significant at

small strain level while it disappears at large deformation as a result of the inherent anisotropy destroyed at large deformation, which is related to the stress induced anisotropy (Oda et al., 1985b, Sadrekarimi and Olson, 2011).

2.1.2.2 Induced anisotropy

When subjected to shearing, the anisotropy of soil evolves continuously. Oda et al. (1985a) investigated stress induced anisotropy to find the contact normal vectors tend to concentrate in the principal stress direction. It indicates the material anisotropy changes in response to the applied anisotropic loading. The induced anisotropy could have significant effects on response of granular soils.

Arthur et al. (1977) carried out series of tests on dense sand to examine effects of induced anisotropy on sand behaviour. The samples were initially monotonically loaded to a high pre-failure stress ratio, followed by unloading to isotropic stress state. Then, they were monotonically sheared again at various principal stress directions. The results indicated that the stress induced anisotropy had great influence on magnitudes of strain increment while negligible effect on dilation angle and the non-coaxiality between principal directions of stress and strain increment was small.

Gajo and Wood (1999) studied the effects of both drained and undrained pre-loading history on the undrained behaviour of loose Hostun sand samples under triaxial tests. The results showed that the pre-loading history had considerably effects on the evolution of yielding surface and elastic anisotropy.

These results clearly show that the previous loading history changes the material anisotropy significantly. The induced anisotropy could have a great effect on soil behaviour. Various loading paths induce different material anisotropy. The induced anisotropy dominates material stress-strain behaviour. For example, soil performs a lower strength during triaxial compression than triaxial extension, due to different material anisotropy induced.

2.1.2.3 Fabric anisotropy of granular material

The anisotropy of granular material is mainly due to the anisotropic internal fabric. Brewer (1964) first referred fabric to the spatial arrangement of solid particles and the associated voids. It was pointed out that fabric should include at least three concepts: (1) orientation distributions of elongated particles; (2) contact normal distributions between interacting particles; (3) void distributions (Oda and Iwashita, 1999).

In laboratory study, it is difficult to characterise the contact normal distribution of sand. Alternatively, the sand fabric may be described by the preferred orientation of non-spherical particle long axis. Oda (1972a) prepared both natural and reconstituted sand samples reinforced by injecting resin binder and then cut samples into vertical and horizontal thin sections to study the statistical distributions of sand particle orientations. The results showed that orientations of grains were not randomly distributed in space but with preferred alignments of long axis in the horizontal bedding plane. Consistent statistical study of particle orientation fabric has also been reported by Yang et al. (2008). Even for spherical particles deposited

under gravity, they tended to stand in a stable position relative to forces acting upon them, which produced anisotropic packing structure with more contact normal oriented in the deposition direction. The anisotropic packing structure of granular assembly with spherical particles was confirmed by experimental isotropic compression tests to find a lower compressibility in the direction of deposition than in the radial direction (Haruyama, 1981, Lade and Abelev, 2005).

2.2 Three dimensional soil behaviours

In engineering practice, the stress state of soils is general, with three principal stresses being not always equal to each other ($s_1 \geq s_2 \geq s_3$) and the varying principal stress directions. The relative magnitude of intermediate principal stress is described by a non-dimensional parameter $b = (s_2 - s_3)/(s_1 - s_3)$ ($0 \leq b \leq 1$). The influence of intermediate principal stress on soil behaviour has been widely investigated by true triaxial test in 1970s. However, the material inherent anisotropy was not considered at that time. Since 1980s, the influence of material anisotropy on three-dimensional soil responses has been investigated with tilting principal stress directions using hollow cylinder apparatus. In addition, the soil response to non-proportional loading path, i.e., pure principal stress rotation, has also been studied by hollow cylinder test. The complex soil behaviours are briefly reviewed in this section.

2.2.1 Effect of intermediate principal stress on soil behaviour

In the early 1960s, the triaxial compression test and plane strain test were commonly used to investigate sand behaviour. It was reviewed by Oda et al. (1978)

that the characteristics of shear strength and dilatancy behaviour observed in plane strain test of sand were concluded as follows:

1. Dense sand tested under low confining pressure gave a greater friction angle up to $10\% \sim 20\%$ in plane strain test than that in triaxial compression test.
2. Sand at similar densities, strain to failure was smaller in plane strain test than in triaxial compression test.
3. Sand performed more dilative in triaxial compression than in plane strain test.

The differences of strength and dilatancy behaviour observed in plane strain test (e.g., $b = 0.3 \sim 0.5$) and triaxial compression ($b = 0$) clearly indicated that the intermediate principal stress did have great effects on sand stress-strain behaviour. Since the importance of influence of b value on sand behaviour was realised, a few cubical triaxial test apparatuses were developed to conduct true triaxial test with independent control of magnitudes of three principal stresses.

Lade and Duncan (1973) designed a cubical triaxial tester to investigate the influence of b value on stress-strain behaviour of Monterey sand. The results showed that, with increasing b value, both dense and loose sand became more dilative while strain to failure decreased. The peak friction angle increased significantly to the maximum value with increasing b value and then decreased slightly with further increasing b to 1.

Reades and Green (1976) carried out independent stress control tests on Ham River sand samples over a wide range of densities using cubical triaxial cell. Their results presented that the axial strain to failure decreased as b increased from 0 to 0.5

and then increased with further increasing b values. The peak friction angle increased rapidly from triaxial compression ($b = 0$) to $b = 0.15$ and remained constant between $b = 0.15$ and $b = 0.4$, followed by gradually increase in friction angle for $b > 0.4$. However, in the discussion session of this paper, Ergun (1977) doubted about the increasing friction angle for b value greater than 0.4. It was argued that the high shearing resistance observed in the tests at $b > 0.4$ was due to the possibility of boundary interference. Ergun further indicated the platen interference by performing tests on loose Ham River sand samples using flexible lateral platens to show that friction angle did not increase but decreased when $b > 0.4$ under otherwise identical conditions to Reades and Green's tests. However, Ergun failed to provide results over full range of b values varied from 0 to 1.

Arthur et al. (1977a) showed that the angle of shearing resistance increased to maximum value at $b = 0.5$ and then decreased almost 5^{o} at $b = 1$ for Leighton Buzzard sand with flexible lateral platen control. It confirmed Ergun's results with decreasing friction angle at large b values.

Many other researchers have reported true triaxial test data while the results did not conclude to a common failure criterion for all types of sand (Ko and Scott, 1967, Matsuoka and Nakai, 1974, Yamada and Ishihara, 1979). Though controversy still exists in this topic, the representative relationship between friction angle f and b value can be generally sorted into three groups, as shown in Fig. 2.1. The results differing from groups is probably due to other factors affecting the measured strength under three-dimensional stress conditions, such as effect of shear band occurrence in hardening regime related to work in Fig. 2.1(b), effect of slenderness

ratio between height and diameter of cylinder specimen, experimental equipment reliability et al. (Lam and Tatsuoka, 1988, Wang and Lade, 2001, Lade, 2006).

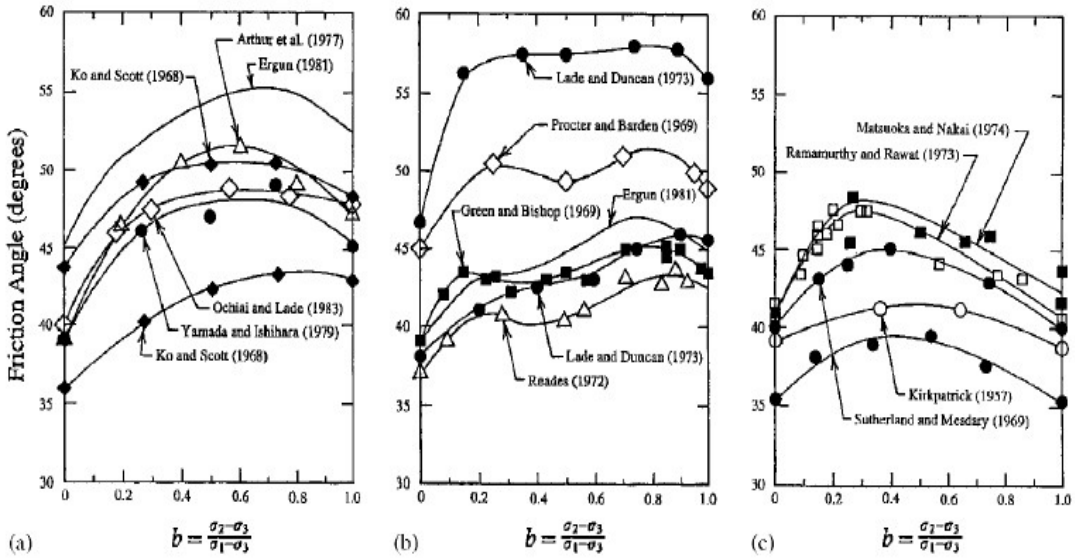

Fig. 2.1 $f - b$ relationships from true triaxial tests on sand (after Lade, 2006)

All those results show significant effect of the intermediate principal stress on strength characteristics of sand. The experimental findings are useful for formulating a three-dimensional isotropic failure criterion for constitutive modelling of soil behaviour in general three-dimensional stress conditions. However, the effect of inherent anisotropy, which is considered as an important parameter affecting soil behaviour, is not considered in those groups of work.

2.2.2 Effect of cross-anisotropy on soil behaviour

The terminology cross-anisotropy referring to the gravitational deposited sand possess an inherently transversely isotropic microstructure, exhibiting

transversely isotropic behaviour in the horizontal bedding plane or cross-anisotropic behaviour in the vertical deposition plane.

Yamada and Ishihara (1979) studied the anisotropic sand behaviour under three-dimensional radial stress paths on dense and loose sand specimens, with lode angle q varying from 0º to 180º in the octahedral plane as shown in Fig. 2.2. The stress-strain behaviour was affected by the inherent cross-anisotropy only at small shear stress levels while the specimen inherently anisotropic characteristics disappeared after failure. The peak stress ratio of the dense sample showed little difference in three sectors. The stress ratio of the loose sample, up to the same shear strain in three sectors, decreased with increasing lode angle before failure, indicating anisotropic yielding behaviour. Similar observations were also reported on spherical particles assembly with initial cross-anisotropy during radial shear stress paths, which concluded that the three-dimensional yielding criterion of anisotropic material could not be discussed by test results only from Sector I (Haruyama, 1981).

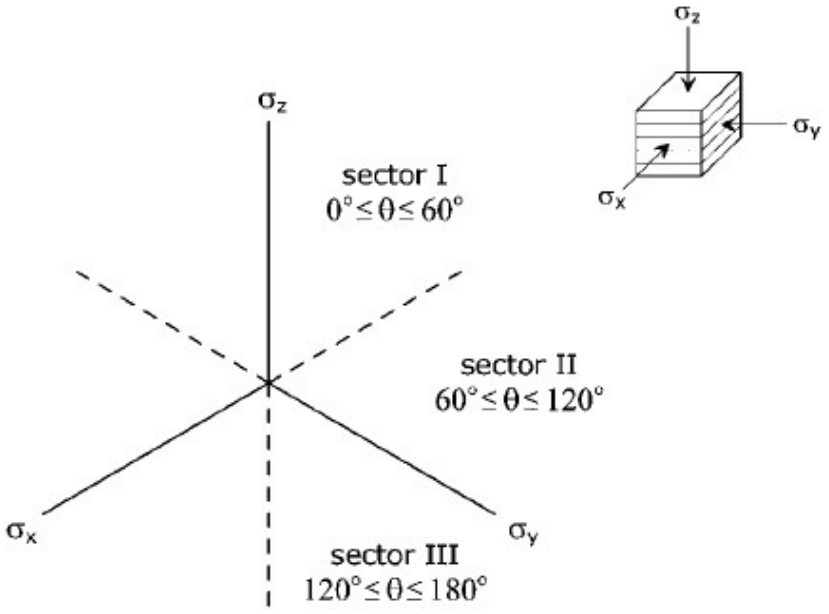

Fig. 2.2 Configuration of sample cross-anisotropy

Ochiai and Lade (1983) investigated the effect of cross-anisotropy on stress-strain behaviour of dense Cambria sand with relatively long and flat sand grains by cubical true triaxial test. The loading was applied with the major principal stress direction fixed to align three directions of material axes, respectively. It was found that effects of initial cross-anisotropy on stress-strain behaviour were mainly observed before failure and the friction angle did not show much difference by rotating the principal stress direction from the vertical direction (Sector I) to the horizontal direction (Sector II and Sector III) at the same b value.

Abelev and Lade (2003a, 2003b) carried out series of true triaxial tests on dense Santa Monica beach sand. The stress-strain behaviour showed clear effect of inherent cross-anisotropy on friction angle, approximately 5º difference between Sector I and Sector III at the same b value; and the greatest dilation angle was observed in Sector I at the same b value.

Those results clearly show the combined effect of intermediate principal stress and material cross-anisotropy on sand behaviour. Hence, it is difficult to distinguish the effect of b value and material anisotropy on sand behaviour in a laboratory test, due to the difficulty in preparing an initially isotropic sample. The three-dimensional failure envelop is cross-anisotropic in the deviatoric stress plane. This observation is useful for formulating cross-anisotropic yielding criteria in constitutive modelling accounting for inherent anisotropy effect.

The cross-anisotropic behaviour also implies the loading direction dependent sand response since all the reviewed true triaxial tests were conducted with the major

principal stress either perpendicular to the bedding plane or within the bedding plane. Hence, to have a better understanding of the three-dimensional anisotropic soil behaviour, a complete variation of principal stress direction from the vertical to horizontal direction is preferred.

2.2.3 Effect of loading direction on anisotropic soil behaviour

The loading direction is defined by an angle a, which is the major principal stress direction relative to the vertical deposition direction, as shown in Fig. 2.3.

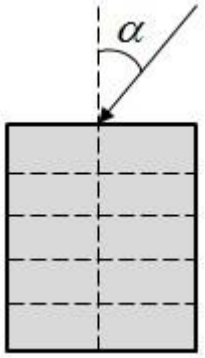

Fig. 2.3 Illustration of loading direction a

The effect of a on the stress-strain behaviour was mainly observed at small strain level. A greater shear strain to the pre-failure stage was observed at larger inclination angle a, as shown in Fig. 2.4 (Arthur and Menzies, 1972; Miura et al., 1986). Oda (1972) reported that sand deformation behaviour at pre-failure stage was significantly influenced by the inherent fabric anisotropy when sheared at various loading directions, with secant modulus decreased with increasing angle a. Significant effect of loading direction on dilatancy behaviour was also observed on anisotropic sand. When sheared at different loading directions, sand became more

contractive at a greater inclination angle a (Oda et al., 1978; Symes et al., 1984; Yoshimine et al. 1998; Sivathayalan & Vaid, 2002).

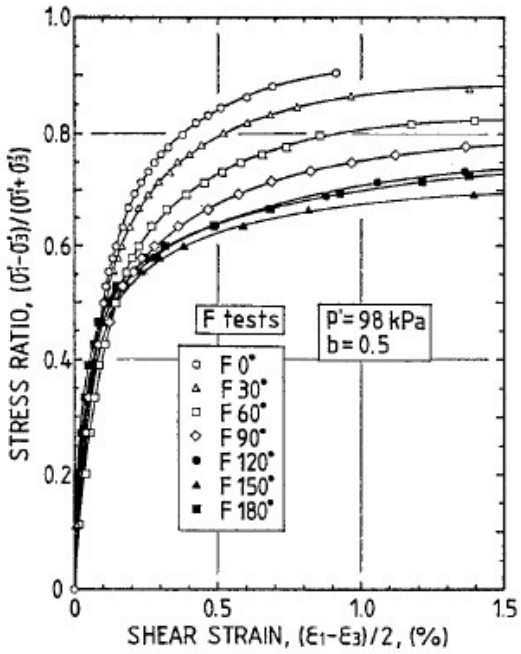

Fig. 2.4 Stress-strain behaviour at different loading directions (after Miura et al., 1986)

The strength of anisotropic material was loading direction dependent. By preparing specimens in a tilting mould (Arthur and Menzies, 1972, Oda, 1972a), their drained triaxial compression tests indicated that the strength decreased with increasing angle a, with the lowest strength observed when the direction of major principal stress parallel to the bedding plane. However, Oda et al. (1978) studied strength anisotropy by the same sample preparation method under plane strain test. The results showed that strength initially decreased with increasing angle a and then increased with the lowest strength observed at $a = 66^{\circ}$. Consistent results were also obtained by Guo (2008) with samples prepared in a tilting mould in direct shear tests on both angular and spherical sand particles.

Saada and Townsend (1981) pointed out that inclined specimens tested in triaxial cell generated large stress non-uniformity near end platens due to non-coincidence of the deposition direction and the specimen symmetry axis. They recommended the better way to study anisotropy effect was to incline the principal stress direction rather than the specimen axes.

Symes et al. (1984, 1988) studied the undrained and drained anisotropic behaviour of medium-loose saturated sand under various principal stress directions using hollow cylinder apparatus. The anisotropic strength decreased with increasing angle a . However, the tests were only performed at $a = 0^{o}$, $a = 24.5^{o}$ and $a = 45^{o}$.

Miura et al. (1986) investigated the drained anisotropic strength behaviour of dense sand sheared under different principal stress directions using hollow cylinder torsional shear device. The anisotropic strength declined at greater tilting angle and then increased slightly, with the lowest strength achieved at $a \approx 60^{o}$, in which the inclination direction of shear band was nearly parallel to the bedding plane. Fig. 2.5(a) showed similar results from different tests and the test details were give in Table 2.1.

The other group of work summarised in Fig. 2.5(b) (more details in Table 2.1) showed that sand strength decreased continuously with increasing inclination angle a using hollow cylinder torsional shear test apparatus in both undrained conditions (Yoshimine et al., 1998, Sivathayalan and Vaid, 2002) and drained conditions (Lam and Tatsuoka, 1988, Kumruzzaman and Yin, 2010).

Controversy arises on the minimum strength obtained at what a value. Miura et al. (1986) argued that minimum strength observed at a around $60^{\circ} \sim 75^{\circ}$ was due to the shear plane parallel to the bedding plane, where the material exhibited the lowest shear resistance. Oda (1972) and Arthur and Menzies (1972) explained the minimum strength achieved at $a = 90^{\circ}$ was a result of particle preferred orientation distribution in the horizontal bedding plane, where particles sliding mechanism occurred easily. Consequently, more evidence on this topic is helpful for a better understanding of strength anisotropy.

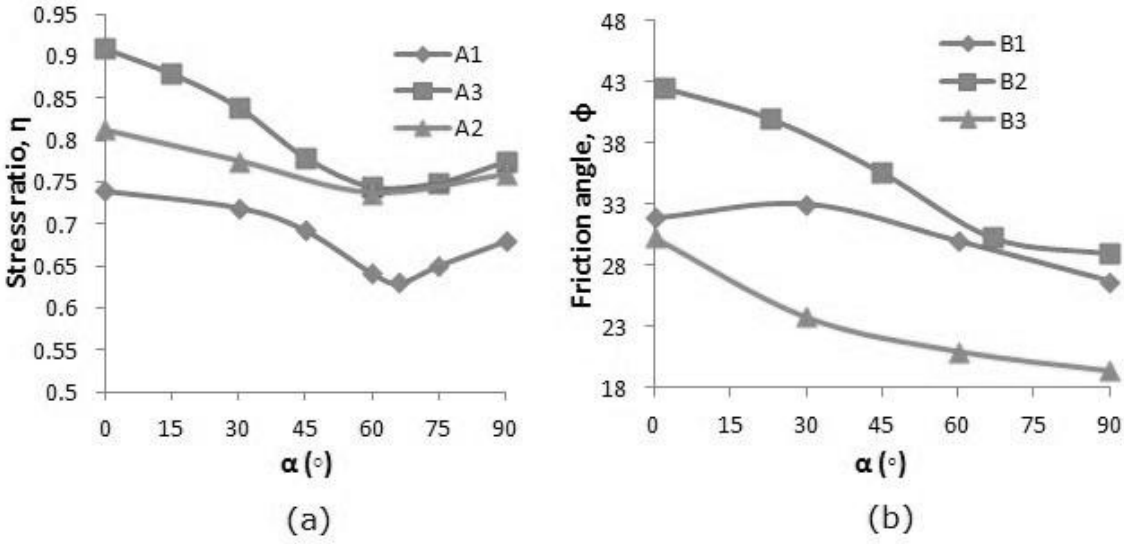

Fig. 2.5 Variation of strength anisotropy with loading direction

Table 2.1 Tests detail of results reported in Fig. 2.5

	Test device	Material	Relative density (%)	Stress (kPa)	Drainage	Authors
A1	PS	Toyoura sand	89	σ_3=392	Drained	Oda et al., 1978
A2	DS	Ottawa sand	86	p=100	Drained	Guo, 2008
A3	HCT	Toyoura sand	82	p=98 b=0.5	Drained	Miura et al., 1986
B1	TC	Toyoura sand	75	σ_3=98 b=0	Drained	Oda, 1972
B2	HCT	Decomposed grantie	Unspecified	p=400 b=0.5	Undrained	Kumruzzaman and Yin, 2010
B3		Fraser river sand	21	p=200 b=0.4	Undrained	Sivathayalan and Vaid, 2002

Notes: PS−Plane strain, DS−Direct shear, HCT−Hollow Cylinder Test, TC−Triaxial compression

The non-coaxial behaviour of granular material was first reported by experimental simple shear deformation (Roscoe et al., 1967). It was observed that the direction of principal strain increment rate did not follow the change of principal stress direction. The principal stress direction rotated gradually to approach the strain increment direction at large shear strain.

The non-coaxiality between the principal stress direction and the principal strain increment direction has been reported in laboratory monotonic shearing using hollow cylinder test apparatus (Symes et al., 1988, Cai et al., 2013, Eugene J. Van Dyck, 2012). It can be seen from Fig. 2.6, where the solid arrow refers to the strain

increment vector and the solid line indicates the stress vector in the deviatoric plane, that non-coaxial behaviour was generally observed with the larger angle a_{de} of strain increment vector than the angle a of stress vector, except asymmetric loading conditions with $a = 0^{o}$ and $a = 90^{o}$. And the degree of non-coaxiality decreased with increasing deviator stress.

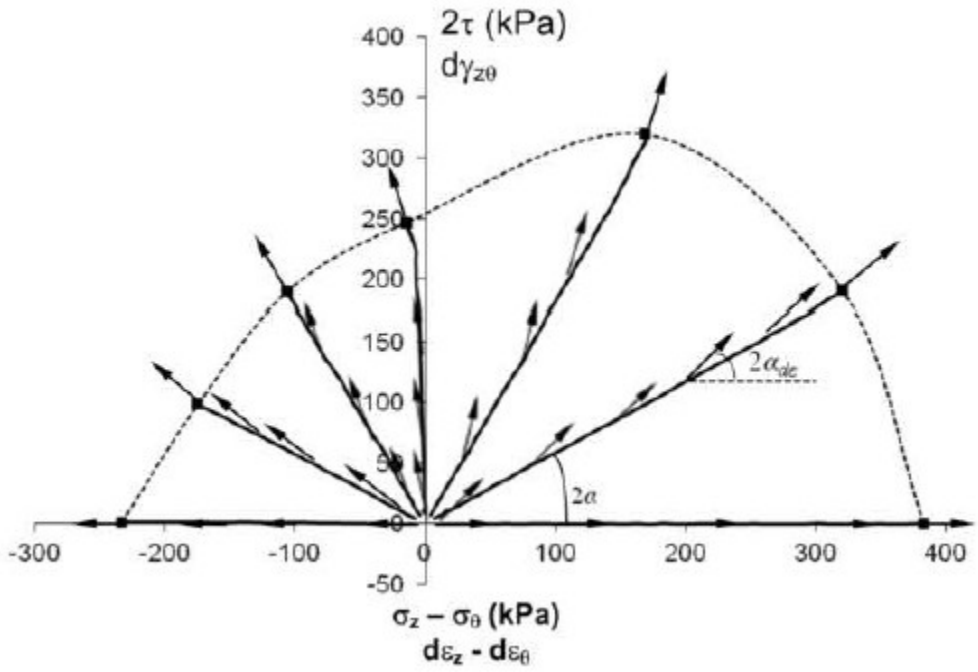

Fig. 2.6 Non-coaxial deformation (after Cai et al., 2013)

2.2.4 Sand response to rotational shear

The granular material behaviour has been widely reported under proportional loading paths. During non-proportional loading path, i.e., rotational shear, significant plastic deformation would be observed, though the magnitudes of stress invariants are unchanged and only the major principal stress direction rotates continuously.

Significant volumetric contraction was observed during the drained rotational shear, even tested on dense material (Miura et al., 1986, Sayao, 1989, Tong et al., 2010, Yang, 2013). During undrained rotational shear, the volume change was reflected as significant pore pressure build up (Nakata et al., 1998, Yang and Li, 2007). The rotational shear deformation was influenced by many other factors, e.g., the mean normal stress, b value, stress ratio and initial void ratio. It was observed that the higher the influential factor value, the severer the volume contraction (Sayao, 1989, Tong et al., 2010, Yang, 2013).

The non-coaxial flow deformation characteristic has been widely reported during rotational shear (Miura et al., 1986, Guitierrez et al., 1991). It was illustrated in Fig. 2.7 that the principal strain increment direction generally did not coincide with the principal stress increment direction, which is tangential to the failure surface. In addition, the total strain increment direction showed little difference to the plastic strain increment direction, indicating the contribution of elastic strain increment to total strain increment being small. The degree of non-coaxiality was smaller at rotational shear with a greater stress ratio (Yang, 2013). The influence of b value on degree of non-coaxiality was found to be small (Tong et al., 2010).

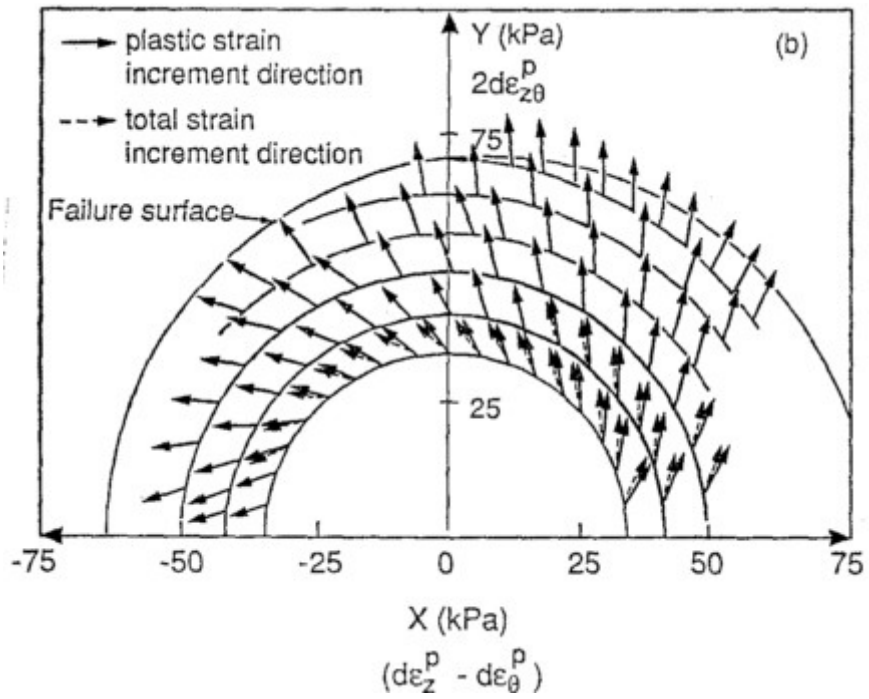

Fig. 2.7 Non-coaxial deformation in rotational shear (after Gutierrez et al., 1991)

2.3 Multi-scale investigation on granular material behaviour

As reviewed in the previous sections, the three-dimensional soil behaviour has been widely reported in laboratory tests. The observed complex behaviour, e.g., anisotropic behaviour and non-coaxial deformation, brings challenges in the existing constitutive modelling. To develop advanced constitutive models, fundamental understanding of the observed complex behaviour is required. The granular material behaviour is dominant by the local contact behaviour and the spatial arrangement of particles. The study of granular material micromechanics provides fundamental insights into the observed global behaviour.

The experimental micromechanics (photoelsticity, stereophotogrammetry, x-rays, computed tomography) are used for investigating micromechanics of granular material, benefiting from the modern technology development (Drescher and Jong, 1972, Oda, 1972a, Majmudar and Behringer, 2005, Croll et al., 2013, Fonseca et al., 2013). It examines the real granular material behaviour and the observed micromechanics provide the referenced confidence for numerical simulation. However, limitations of laboratory experiments are: difficulty in preparing the identical and isotropic samples; difficulty in observing the microscopic response of particle rearrangement and extremely time confusing for data post-processing. In parallel, the numerical DEM simulation can easily provide the instant microscopic information of particles at any stage of shearing in a non-destructive way, which is a useful tool to investigate the properties of granular material from particle scale. The DEM study of granular material behaviour in mimic laboratory tests have been implemented by many researchers in both two-dimensional and three-dimensional simulations (Rothenburg and Bathurst, 1989, Chen et al., 1990, Bardet, 1994, Thornton, 2000, Cui and O'Sullivan, 2006). Although the DEM models granular assembly with idealised particle shape and limited sample size, those results have shown that the numerical simulation can qualitatively reproduce the general stress-strain behaviour of granular material as observed in laboratory sand testing.

Thornton (2000)Thornton (2000)Thornton (2000)Thornton (2000)Thornton (2000)Thornton (2000) carried out numerical simulations of isotropic spherical particles system in general three-dimensional stress conditions with constant intermediate principal stress parameter b. It was found that DEM simulation produced similar stress-strain behaviour to those observed in experimental true

triaxial tests. Microscopically, the induced structural anisotropy of internal variables, e.g., fabric anisotropy, contact force anisotropy, were reported due to the deviatoric loading. The strength difference of dense and loose sample was due to a higher degree of contact normal anisotropy developed in the dense sample. He also pointed out that the developed deviatoric stress capacity was mainly due to the contribution of developed anisotropic normal contact force while the contribution of tangential contact force anisotropy was quite small.

The influence of loading direction on initially anisotropic granular material behaviour has been studied by preparing samples at different tilting angles of material symmetry axis relative to the loading direction (Mahmood and Iwashita, 2010). The two-dimensional DEM biaxial tests results showed that the anisotropic strength decreased with increasing angle a and the evolution of fabric anisotropy were quite different at different loading directions. The same sample preparation method was used to prepared the initially anisotropic samples for direct shear tests (Fu and Dafalias, 2011). The 2D direct shear results were presented in Fig. 2.8, with minimum strength and maximum strength observed at $a = 60^{\circ}$ and $a = 115^{\circ}$. For unknown reasons, the material response was quite different with loading direction within the region $a \in \left(0^{\circ},90^{\circ}\right)$ and $a \in \left(90^{\circ},180^{\circ}\right)$. Since the initially anisotropic sample has a cross-anisotropic fabric structure, the material behaviour was expected to be symmetric with the bedding plane, i.e., similar behaviour when loaded at $a = 60^{\circ}$ and $a = 120^{\circ}$. No experimental direct shear results have been produced with inclination angle a from 90° to 180° to confirm this observation yet. In addition, the various loading direction was realised by inclination of material

symmetry axis rather than inclination of principal stress direction, which was not recommended by Saada and Townsend (1981).

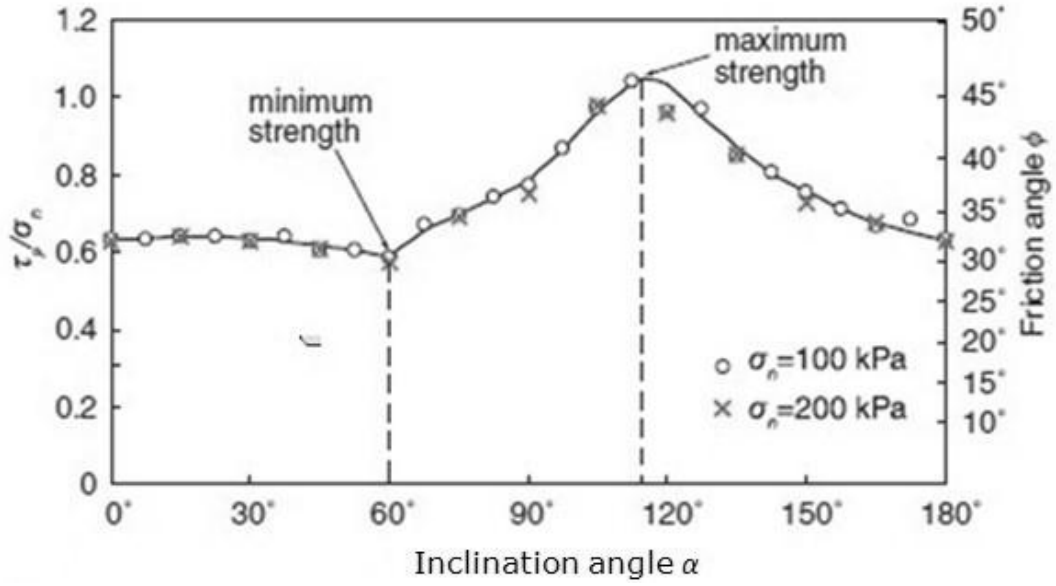

Fig. 2.8 Variation of peak strength with inclination angle (after Fu and Dafalias, 2011)

Li and Yu (2009) investigated the influence of loading direction on the behaviour of anisotropic granular material by two-dimensional DEM simulations. The strength anisotropy curves were consistent to that reviewed in Fig. 2.5(a) for the initially anisotropic sample and to that shown in Fig. 2.5(b) for the pre-loaded sample. For the initially anisotropic sample, the strength anisotropy was explained from microscopic observations that strength decreased slightly when loading direction a located within $\left(0^{\circ}, 30^{\circ}\right)$ due to both similar degrees of contact normal fabric anisotropy and contact force anisotropy developed. When a increased further, $30^{\circ} < a \leq 60^{\circ}$, it was observed that degree of contact normal anisotropy decreased significantly and degree of normal contact force decreased as well, and the deviation angle between the principal direction of contact normal and the principal direction of

normal contact force became larger, resulting in a smaller stress ratio at larger inclination angle. However, when a varied from 60º to 90º, the anisotropy degree of contact normal was found to decrease further while the anisotropy degree of normal contact force increased slightly, resulting in slower decreasing stress ratio, and even increasing slightly. For the pre-loaded sample, the fabric anisotropy and contact force anisotropy were found to decrease with increasing tilting angle a, leading to continuous decrease of strength.

Li and Yu (2009) also discussed the non-coaxial behaviour between the major principal stress and major principal strain increment directions, as shown in Fig. 2.9 and Fig. 2.10, where the solid straight line represented the fixed strain increment direction and the line with symbols referred to the observed principal stress direction. Microscopically, the degree of non-coaxiality was dependent on the deviation between principal directions of contact force and contact normal, as well as the anisotropic degrees. The anisotropy degree of contact normal was small for the initially anisotropic sample and the principal contact force direction was close to the loading direction, resulting in negligible degree of non-coaxiality. For the pre-loaded sample, the degree of contact normal anisotropy was large and the degree of non-coaxiality was observed to be significant when the loading direction deviated more from the initial principal fabric direction. However, the degree of non-coaxiality generally decreased as shearing continued and the principal direction of strain increment vector coincided with the principal stress direction at large deformation due to the principal fabric direction approaching the loading direction gradually.

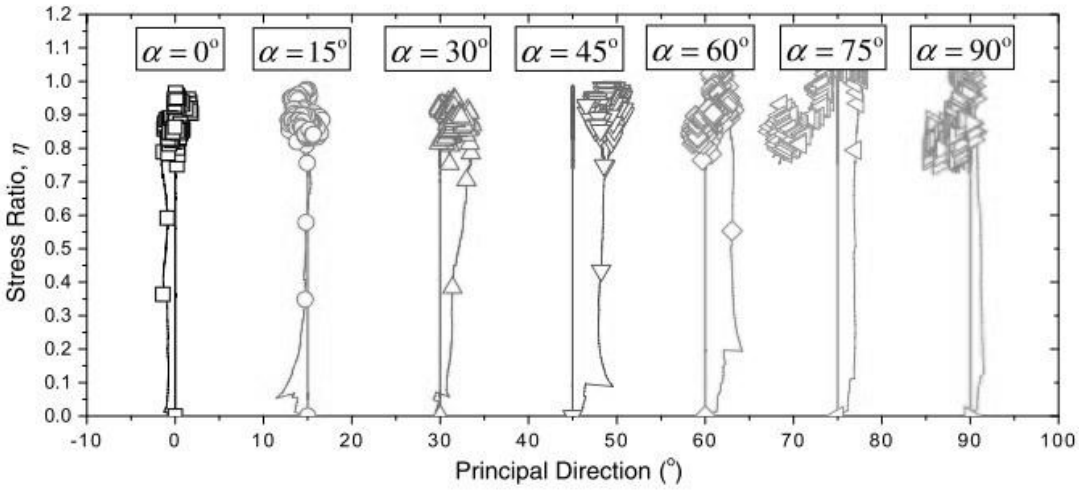

Fig. 2.9 Non-coaxial behaviour observed on the initially anisotropic sample (after Li and Yu, 2009)

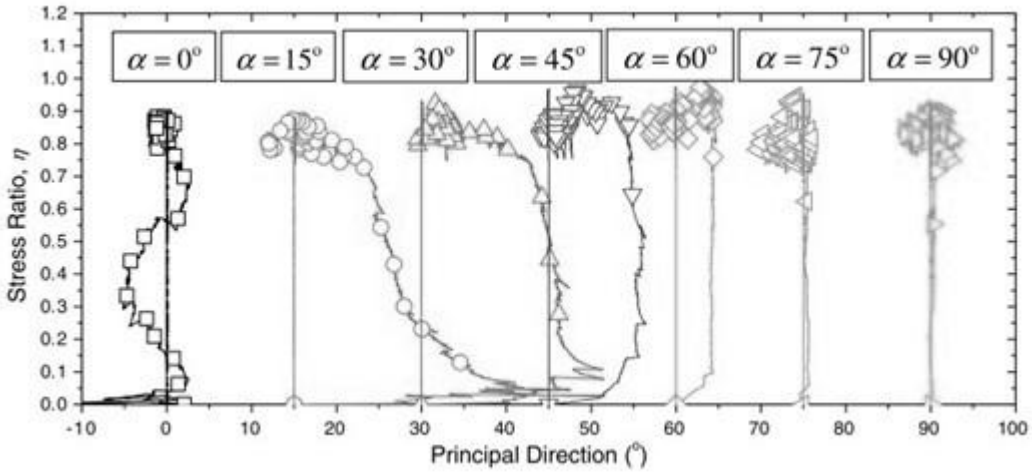

Fig. 2.10 Non-coaxial behaviour observed on the pre-loaded sample (after Li and Yu, 2009)

The two-dimensional DEM simulation of granular material under rotational shear has also been investigated by Li and Yu (2010). The material internal structure was found to rotate along the stress rotation continuously, the larger the internal structure size, the greater deformation generated. The dense and loose sample approached the same ultimate state with the same void ratio after large number of cycles due to the same size of internal structure reached. The effect of stress ratio on

rotational shear response was observed as the higher the stress ratio, the greater the deformation owing to the larger size of internal structure.

Those DEM results enhance the understanding of granular material micromechanics. However, most of them are two-dimensional simulations, where the intermediate principal stress is missing. Limited DEM results have been reported under general three-dimensional stress path to investigate anisotropic granular material behaviour. This is probably due to the difficulty in realising the general three-dimensional loading paths in numerical simulation. In this study, a virtual experiment model will be developed to realise general loading paths for multi-scale investigation of three-dimensional granular material behaviours.

2.4 Particle-scale statistics and stress-force-fabric relationship

With the DEM simulation, the microscopic study on granular material becomes possible. The micro-scale information, e.g., discrete contact force vector and contact normal vector, is of interest and it has thousands of such data in a granular system. To investigate the macroscopic granular material behaviour and apply the particle-scale observations to the continuum-scale constitutive relationships, the statistical characterisation of particle-scale directional data linking the two worlds is essential. The global stress tensor is related to the contact forces and branch vectors (e.g., Bagi, 1996). The stress tensor can be further expressed as a function of the contact force tensors and fabric tensors, termed as stress-force-fabric relationship. Hence, the micro-scale quantities of contact force and fabric are directly

related to the global material stress state and it can be interpreted to explain the macroscopic strength-deformation characteristics.

In this section, special focus is placed on the tensorial characterisation of contact force vectors and contact normal vector distributions by second-rank tensors. The contact density is described by the coordination number. By doing so, the granular material microstructural anisotropy is described by the invariants of second-rank contact force tensors and fabric tensors and their principal directions. The formulations and symbols defined in this section will be extensively used in the thesis, hereafter, to conduct particle-scale analysis.

2.4.1 Fabric quantification

2.4.1.1 Coordination number

A scalar parameter coordination number w is defined to describe the average density of contacts per particle within a granular assembly as:

$$w = \frac{2N_c - N_c^w}{N_p} \tag{2.2}$$

where N_c is the total number of contacts and N_c^w is the total number of contacts formed between particles and boundary walls. N_p is the total number of particles.

2.4.1.2 Directional distribution of contact normal orientations

Kanatani (1984) established a mathematical theory to describe the directional distributions of orientations. In his work, three kinds of directional tensor have been defined for directional distribution of orientations. In characterising the statistics of

directional data with tensors, the fundamental quantities of these directional data are various averages of them. The moment tensor has been defined to characterise the average of those directional data up to second-order as:

$$N_{ij} = \frac{1}{N}\sum_{k=1}^{N} n_i^k n_j^k \tag{2.3}$$

where n_i^k is the k^{th} directional data and N is the total number of directional data. N_{ij} is symmetric.

In microscopic investigation of three-dimensional granular material, the discrete contact normal vector distribution can be approximated by Eq. (2.3). Up to the second order approximation, the probability density function $E(\mathbf{n})$ of contact normal distribution can be expressed as:

$$E(\mathbf{n}) = \frac{1}{4p}\left(1 + D_{ij} n_i n_j\right) \tag{2.4}$$

The deviatoric tensor D_{ij} is used for characterising the contact normal fabric distribution in this study. The relation between D_{ij} and the second-order moment tensor N_{ij} is expressed by integrating the probability density function $E(\mathbf{n})$ over the Euler space to give:

$$D_{ij} = \frac{15}{2}\left(N_{ij} - \frac{1}{3} d_{ij}\right) \tag{2.5}$$

It has three principal values D_1, D_2, D_3 and three corresponding principal directions $\mathbf{n}_i^D$, where D_1, D_2, D_3 are the major, intermediates and minor principal fabric values. The deviator fabric D_F is defined to describe the contact normal fabric

anisotropy and the intermediate fabric ratio b_F is used to describe the relative magnitudes of three principal fabric values as:

$$\begin{cases} D_F = \sqrt{\left[\left(D_1 - D_2\right)^2 + \left(D_2 - D_3\right)^2 + \left(D_1 - D_3\right)^2\right] / 2} \\ b_F = \left(D_2 - D_3\right) / \left(D_1 - D_3\right) \end{cases} \tag{2.6}$$

2.4.2 Directional distribution of vectors

Orientations of vector can be represented by unit vectors whose magnitudes are always 1. For micro-scale analysis, however, it may require characterising the directional distribution of probability density for contact force vectors and branch vectors, which should be described by a unit vector representing its direction and a representative value representing its magnitude. The directional distribution of contact force has been discussed in literature (Ouadfel and Rothenburg, 2001, Li and Yu, 2011b). The basic ideas are the same as that used for formulating directional distribution of orientations.

2.4.2.1 Directional distribution of contact force vectors

In three-dimensional microscopic study of granular material, the contact force vector can be decomposed into the normal contact force component and the tangential contact force component. The directional distribution of normal contact force vectors f_i^n and tangential contact force vectors f_i^t can be approximated by the second rank tensor K_{ij}^n and K_{ij}^t. The K_{ij}^n and K_{ij}^t are calculated from the pre-determined directional distribution of contact normal density $E\left(\mathbf{n}\right)$ up to the second-order approximation and discrete contact force vectors as:

$$K_{ij}^{n} = \frac{1}{N}\sum_{c=1}^{N}\frac{f^{n}n_{i}^{c}n_{j}^{c}}{E\left(n_{i}^{c}\right)} \tag{2.7}$$

$$K_{ij}^{t} = \frac{1}{N}\sum_{c=1}^{N}\frac{f_{i}^{t}n_{j}^{c}}{E\left(n_{i}^{c}\right)} \tag{2.8}$$

where N is the total number of contacts, f^{n} is the magnitude of normal contact force at contact c and f_{i}^{t} is the tangential contact force vector at contact c . n_{i}^{c} is the contact vector at contact c.

The mean normal contact force f_{0} can then be expressed as:

$$f_{0} = \frac{1}{4p}K_{ii}^{n} \tag{2.9}$$

Then, the deviatoric second rank tensors G_{ij}^{n} and G_{ij}^{t}, which are used for characterising contact forces distribution in this research, can be determined as:

$$G_{ij}^{n} = \frac{15}{2}\left(\frac{K_{ij}^{n}}{m_{0}} - \frac{d_{ij}}{3}\right) \tag{2.10}$$

$$G_{ij}^{t} = 5\frac{K_{ij}^{t}}{m_{0}} \tag{2.11}$$

where $m_{0} = K_{ii}^{n}$.

The symmetric and deviatoric tensor G_{ij}^{n} can be expressed as three principal values $G_{1}^{n}, G_{2}^{n}, G_{3}^{n}$, which are termed as the major, intermediate and minor principal normal forces ($G_{1}^{n} \geq G_{2}^{n} \geq G_{3}^{n}$), and the principal directions. The deviator normal contact force G_{d}^{n} is defined to describe the anisotropy of normal contact force and

the intermediate force ratio b_n is defined to reflect the relative magnitude of three principal values as:

$$\begin{cases} G_d^n = \sqrt{\dfrac{\left(G_1^n - G_2^n\right)^2 + \left(G_2^n - G_3^n\right)^2 + \left(G_1^n - G_3^n\right)^2}{2}} \\ b_n = \dfrac{\left(G_2^n - G_3^n\right)}{\left(G_1^n - G_3^n\right)} \end{cases} \tag{2.12}$$

Similarly, the symmetric and deviatoric tensor G_{ij}^t can be described by its invariants G_d^t , b_t and principal directions. The invariants G_d^n and b_t are used to describe the tangential contact force anisotropy and intermediate tangential force ratio calculated as:

$$\begin{cases} G_d^t = \sqrt{\dfrac{\left(G_1^t - G_2^t\right)^2 + \left(G_2^t - G_3^t\right)^2 + \left(G_1^t - G_3^t\right)^2}{2}} \\ b_t = \dfrac{\left(G_2^t - G_3^t\right)}{\left(G_1^t - G_3^t\right)} \end{cases} \tag{2.13}$$

where G_1^t, G_2^t, G_3^t are the major, intermediate and minor principal tangential forces ($G_1^t \geq G_2^t \geq G_3^t$).

2.4.2.2 Directional distribution of branch vector

The branch vector, connecting the centres of two contacting particles (e.g., Fig. 2.11), has a representative orientation and magnitude. For an assembly of spherical particle system, the direction of branch vector at a contact is the same with the contact normal direction while its magnitude depends on the particles size. The

branch vector direction of two non-spherical particles contact entities generally differs from the contact normal direction.

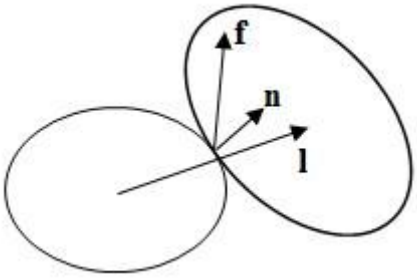

Fig. 2.11 Illustration of contact force vector f , contact normal vector n **and branch vector** l **in a contact**

The directional characterisation of branch vector is in analogy to that of contact force vectors, simply replacing the normal and tangential contact force vectors in Eqs. (2.7) and (2.8) by normal and tangential branch vector components, respectively. In this study, the tensorial characterisation of branch vector is described by B_{ij}^{n} and B_{ij}^{t}, representing the distribution of normal and tangential components respectively. The mean length of normal branch vector is determined as:

$$l_0 = \frac{1}{4p} B_{ii}^{n} \tag{2.14}$$

Similarly, the branch vector tensors B_{ij}^{n} and B_{ij}^{t} can be further expressed as the deviatoric tensors C_{ij}^{n} and C_{ij}^{t} in analogy to Eqs (2.10) and (2.11):

$$C_{ij}^{n} = \frac{15}{2}\left(\frac{B_{ij}^{n}}{B_{ii}^{n}} - \frac{d_{ij}}{3}\right) \tag{2.15}$$

$$C_{ij}^{t} = 5\frac{B_{ij}^{t}}{B_{ii}^{n}} \tag{2.16}$$

Similar to the definition of the fabric tensor invariants D_F and contact force tensor invariant G_d^n, the symbols C_d^n and C_d^t are used to describe the normal and tangential branch vector anisotropy.

2.4.3 Stress-force-fabric relationship

The continuum-scale stress tensor is related to contact force and branch vector in micro-level. Different considerations are followed to re-define the stress tensor for granular material, such as the volume average of external load acting on boundary, volume average of contact forces acting on discrete particles, virtual work principal. However, the stress tensors have been derived to be the same expression, irrespective of theoretical considerations under quasi-static conditions with body force and moments ignored, formulated in Eq. (2.17) as (Drescher and Jong, 1972, Christoffersen et al., 1981, Bagi, 1996, Li et al., 2009b)

$$s_{ij} = \frac{1}{V}\sum_{c=1}^{M} l_i^c f_j^c \tag{2.17}$$

where V is volume of assembly and M is the total contact numbers. l_i^c is the branch vector connecting the centres of two grains forming contact c. f_j^c is the contact force at contact c.

Starting from the micromechanical stress tensor definition in Eq. (2.17), the stress-force-fabric (SFF) relationship was first formulated by Rothenburg and Bathurst (1989) to relate the macroscopic strength to the microscopic contact force anisotropy and fabric anisotropy. The simplified three-dimensional SFF relationship

has been developed from the micromechanical parameters as (Ouadfel and Rothenburg, 2001, Li, 2006, Sitharam et al., 2009):

$$s_{ij} = \frac{w f_0 l_0}{3} \left\{ \begin{array}{l} d_{ij} + \frac{2}{5}\left(D_{ij} + G_{ij}^{n} + C_{ij}^{n}\right) + \frac{3}{5}\left(G_{ij}^{t} + C_{ij}^{t}\right) \\ + G_{ik}^{t} C_{kj}^{t} + \frac{2}{5} D_{pj} G_{pi}^{t} + \frac{8}{35}\left[D_{ik}\left(G_{kj}^{n} - G_{kj}^{t}\right)\right] \end{array} \right\} \tag{2.18}$$

where w is the coordination number, f_0 is the average normal contact force in the assembly, l_0 is the average branch vector length. d_{ij} is the Kronecker delta. The tensor C_{ij}^{n} and C_{ij}^{t} characterises the normal and tangential components of branch vector distribution, of which anisotropy is generally negligible compared to fabric anisotropy and contact force anisotropy.

It is clear from the expression that the stress tensor is related to the microstructural tensors. Thus, the micro-scale observations on contact forces tensors and fabric tensor can be used to explain the macro-scale strength characteristics. The deviatoric stress capacity of a granular assembly is dependent on the developed anisotropic degree of contact normal and contact forces and relative principal directions of stress tensor and microstructural tensors. The prediction of stress ratio using stress-force-fabric relationship showed good agreement with the measured values under both proportional loading and non-proportional loading paths (Rothenburg and Bathurst, 1989, Sitharam et al., 2002, Li and Yu, 2011a, Hosseininia, 2013, Li and Yu, 2013a).

2.5 Summary

Besides the state parameter determining the granular material dilatancy behaviour, anisotropy is another important parameter affecting the dilatancy rate. The granular material anisotropy is normally categorised as inherent anisotropy and induced anisotropy. The inherent anisotropy is formed with preferred direction of particle long axes perpendicular to the sedimentary direction. The induced anisotropy refers to the anisotropic microstructure induced whenever granular material subjected to anisotropic loading. The granular material anisotropy is mainly due to the internal fabric anisotropy.

The sand response is loading path dependent. Significant impact of b value on the strength-deformation behaviour has been observed in laboratory true triaxial tests. However, the true triaxial test does not purely show the effect of b value on sand behaviour but combined with material anisotropy unless the specimen is initially isotropic. The sand specimen prepared in laboratory is generally inherently anisotropic. In considering material anisotropy, the three-dimensional failure surface shows to be cross-anisotropic in the deviatoric stress plane. This clearly indicates that the anisotropic material behaviour is loading direction dependent. The sand performs a lower strength and presents more contractive behaviour when sheared at a greater inclination a . Significant non-coaxiality has been observed before failure. Under non-proportional rotational shear with constant stress invariants, significant volume contraction generates, even tested on dense sample. The flow deformation is generally non-coaxial during rotational shear.

Although the interesting observations have been widely reported in experimental tests, the fundamental mechanism is not well understood. Alternatively, the micromechanical investigation provides fundamental insights into the observed complex behaviour. The DEM has gained increasingly usage in multi-scale investigation of granular material behaviour, in order to overcome the limitations of experimental micromechanics with micro-scale information easily accessed. The DEM simulations can reproduce qualitatively consistent results to a laboratory study, though the idealised particle shape and limited particle numbers are used in numerical simulation. However, most of DEM results studying material anisotropy rest on the two-dimensional simulations, where the intermediate principal stress is missing. This is probably due to the difficulty in realising the general loading paths in three dimensions. Hence, it is necessary to conduct the three-dimensional DEM simulation, at least for confirmation of two-dimensional results, and the effect of intermediate principal stress can be examined.

The micro-scale information, e.g., contact normal vectors and contact force vectors, is discrete data with directional distribution. To apply the particle-scale observations in continuum scale, the statistics of directional data is characterised by the second-rank symmetric and deviatoric tensor. The contact normal vector distribution is described by the fabric tensor D_{ij}. The normal and tangential contact force vectors are characterised by the tensor G_{ij}^{n} and G_{ij}^{t}, respectively. This definition will be followed in hereafter of this research. Starting from the micromechanical stress tensor definition, the stress tensor can be further described as a function of microstructrual fabric tensor and contact force tensors. This is termed

as the stress-force-fabric (SFF) relationship. It is clear from the SFF that the deviatoric stress ratio capacity of granular assembly is dependent on the anisotropic degree and principal directions of the developed microstructural fabric tensor and contact force tensors. Accordingly, through the SFF relations, the granular material macroscopic strength-deformation characteristics can be explained by examining the microscopic contact force tensors and fabric tensor in the following research, under both proportional loading and non-proportional loading conditions.

Chapter 3 Discrete element method

3.1 Introduction of DEM

The continuum mechanics investigates the phenomenal behaviour of granular material and propose constitutive models to fit the experimental observations by introducing additional material constants, which sometimes have no clear physical meanings. However, a granular assembly is discontinuous with discrete particles inter-acting each other and the local contact behaviour is quite simple. Alternatively, the distinct element method investigates granular material behaviour with particle arrangement modelled explicitly. Although DEM simulates granular assembly with finite number of particles and idealised particle shape, it can reproduce typical stress-strain behaviour as observed for soil and provides insight of micro-scale particle arrangement (Rothenburg and Bathurst, 1989, Thornton, 2000, Ng, 2005, Li and Yu, 2009).

The recent distinct element method (DEM) was first developed by Cundall (1971) for analysis of rock mass problems and later applied to granular materials by Cundall and Strack (1979). It has been extensively used to for multi-scale investigation of granular material behaviour. The advantages of DEM include:

- Preparing initially isotropic and anisotropic samples with different initial fabric easily and the same numerical sample can be tested repeatedly with influence of sample variation reduced, which is difficult to prepare exactly the same sample in laboratory.
- Particle-scale information, difficult to be obtained in a real experiment, can be accessed conveniently at any shearing level without disturbing sample, such as individual particle orientation, displacement, rotation, contact normal direction, contact force et al.

In this research, the commercial software, Particle Flow in Three Dimensions (PFC3D) (Itasca, 1999), is used to carry out DEM simulations, which is user-friendly and has been widely applied for multi-scale study by researchers (Li and Yu, 2009, Yimsiri and Soga, 2010, Guo and Zhao, 2013).

3.2 Principles of PFC3D

The particle flow model is composed of distinct particles that displace independent of one another and interact only at contacts or interfaces between the particles. The PFC3D particle-flow model has the following assumptions:

1. The particles are treated as rigid bodies.
2. The contact points occur over a vanishingly area.
3. The rigid particles can overlap one another at contact points based on a soft-contact approach.

4. The magnitude of the overlap is determined by the contact force via the force-displacement law. However, all overlaps are small compared to particle sizes.
5. All particles are spherical except clump logic, which allows the creation of arbitrary shape by several overlapping particles that behaves as a rigid body with a deformable boundary.

In PFC3D, the ball and the wall are the two basic entities. Walls allow one to apply velocity boundary conditions to assemblies of balls for purposes of compaction and confinement. The balls and walls interact with one another via the forces that arise at contacts. PFC3D is suitable for modelling the stress-strain response of a granular material, which deformation results primarily from the sliding and rotation of the rigid particles and the interlocking at particle interfaces.

3.2.1 Calculation cycle

The calculation cycle in PFC3D starts from the application of Newton's second law to each particle followed by a force-displacement law at contacts as showed in Fig. 3.1. The motion of each particle is calculated from Newton's second law by a set of equilibrium equations of resultant force and moment at the mass centre of each particle. However, the equations of motion are not satisfied for each wall since the boundary walls are treated as no mass physics, which means forces acting on a wall do not influence its motion. Therefore, velocity for each wall can be specified by the user for the purposes of compaction and confinement.

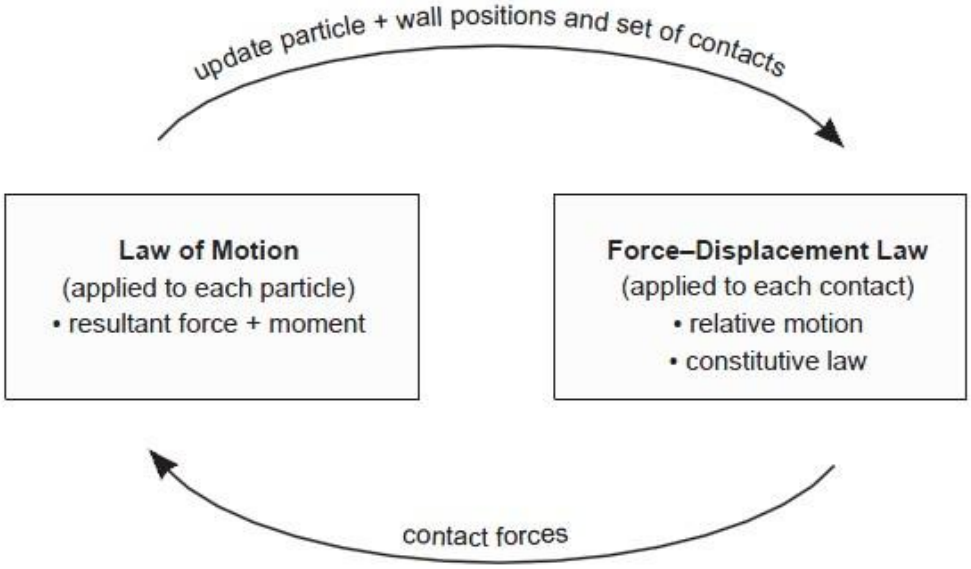

Fig. 3.1 Calculation cycle in PFC3D (Itasca, 1999)

Force-displacement law:

The force-displacement law relates the relative displacement between two entities at a contact to the contact force acting on the entities. The contact force comprises of normal and shear components with respect to the contact plane as

$$F_i = F_i^n + F_i^s \tag{3.1}$$

The normal contact force vector is determined by

$$F_i^n = K^n U^n n^i \tag{3.2}$$

where K^n is the secant normal contact stiffness determined by the defined contact model, n^i is unit normal defining contact plane and U^n is the overlap of contact entities.

The normal stiffness K^n is a secant modulus relating total displacement and force while the shear stiffness k^s is a tangent modulus relating incremental

displacement and force. Thus, the shear contact force is computed in an incremental fashion. When a contact is formed, the total shear contact force is initialised to zero.

Each shear force increment resulting from relative shear displacement increment ΔU_i^s at a contact is added to the current value, which can be described as:

$$\begin{cases} \Delta F_i^s = -k^s \Delta U_i^s \\ F_i^s = (F_i^s)_{old} + \Delta F_i^s \end{cases} \tag{3.3}$$

The resultant force and moment acting on the contact entities are then updated to determine motion of particles.

Law of motion:

The law of motion determines translational velocity and rotational velocity for a single rigid particle from resultant force and moment, respectively.

The translational motion is related to resultant force to be:

$$F_i = m(\ddot{x}_i - g_i) \tag{3.4}$$

where F_i is the resultant force, m is the total mass of the particle, $\ddot{x}_i$ is acceleration and g_i the body force acceleration vector.

The equation of rotational motion can be written as:

$$M_i = \dot{H}_i \tag{3.5}$$

where M_i is the resultant moment and $\dot{H}_i$ is the angular momentum of the particle.

The equations of motion are integrated using a centred finite difference procedure involving a timestep of Δt. The translational and rotational velocity quantities are computed at mid-intervals of $t \pm n\,\Delta t/2$, while displacement, acceleration and force quantities are computed at the primary intervals of $t \pm n\Delta t$.

3.2.2 Mechanical timestep determination

The equations of motion expressed by Eqs. (3.2) and (3.3) will remain stable only if the timestep does not exceed a critical timestep, which is related to the minimum eigenperiod of the total system. The critical timestep is estimated at the start of each cycle.

The simplified estimation procedure considers a one-dimensional mass-spring system described by a point mass, m, and spring stiffness, k. The motion of point mass is governed by the differential equation: $-kx = m\ddot{x}$. The critical timestep for this equation is given by Bathe and Wilson (1976):

$$t_{crit} = \frac{T}{p}, \quad \text{where} \quad T = 2p\sqrt{m / k} \tag{3.6}$$

where T is the period of the system.

It can be extended to a system of infinite series of point masses and springs. The mass, m, is replaced by inertia moment, I, for rotational motion of the same system. Thus, the critical timestep for the generalised multiple mass-spring system can be expressed as:

$$t_{crit} = \begin{cases} \sqrt{m/k^{tran}} \\ \sqrt{I / k^{rot}} \end{cases} \tag{3.7}$$

where k^{tran} and k^{rot} are the translational and rotational stiffnesses respectively.

3.2.3 Damping

Energy supplied to the particle system dissipates through frictional sliding. However, sliding mechanism may not be active in a contact and even if active, it may not be sufficient to achieve a steady state within a reasonable calculation time. This research focuses on the simulation of quasi-static granular material behaviour. Therefore, the mechanical damping is introduced to dissipate energy by damping particle motions. There are a few damping models available in PFC3D while the local damping is employed in this study.

The local damping adds a damping force to the equations of motion in Eqs. (3.4) and (3.5) . The damped equations of motion can be written as:

$$\begin{aligned} &F_i + F_i^d = mA_i; \qquad i = 1...6 \\ &mA_i = \begin{cases} m\ddot{x}_i, & \text{for } i = 1...3 \\ I\dot{\omega}_{i-3}, & \text{for } i = 4...6 \end{cases} \end{aligned} \tag{3.8}$$

where F_i, M_i, A_i are the generalised force, mass and acceleration components respectively; F_i^d is the damping force

$$\begin{aligned} &F_i^d = -x\,|F_i|\,sign(V_i); \qquad i = 1...6 \\ &sign(x) = \begin{cases} 1, & \text{if } x > 0; \\ -1, & \text{if } x < 0; \\ 0, & \text{if } x = 0 \end{cases} \end{aligned} \tag{3.9}$$

The magnitude of damping force is controlled by the damping coefficient x, of which default value 0.7 is used in all the simulations presented in this study.

The advantages of this form of damping are:

- Only accelerating motion is damped and no erroneous damping force arise at steady state motion.
- The damping coefficient is non-dimensional.
- The damping is equally applied to the whole assembly independent of local frequency.

3.2.4 Contact model

The DEM defines the local contact behaviour without any further assumptions. In PFC3D, the constitutive model acting at a particular contact without bonding consists of two parts: a stiffness model and a slip failure model. The stiffness model defines the elastic relationship between normal contact force and relative displacement at a contact. The slip model enforces a relation between normal and tangential contact forces so that the two contacting bodies may slip relative to each other.

There are two kinds of contact-stiffness model available in PFC^{3D}, a linear model and a simplified Hertz-Mindlin model. The Hertz-Mindlin model defines more accurate contact mechanics behaviour with curvature surface from the well-known elastic contact mechanics theory (Johnson, 1985) while it is less computational efficiency for DEM simulation. On the other hand, although the linear

contact model defines a simplified linear force-displacement law, it, macroscopically, still can reproduce the elasto-plastic behaviour as observed for sand (Thornton, 2011). Accordingly, the linear contact model has been selected for all simulations in this study.

The contact stiffnesses relate the contact forces and relative displacement in the normal and shear directions as shown in Eqs. (3.2) and (3.3). For linear contact model, the contact normal secant stiffness is given by

$$K^n = \frac{k_n^A k_n^B}{k_n^A + k_n^B} \tag{3.10}$$

And the contact shear tangent stiffness is given by

$$k^s = \frac{k_s^A k_s^B}{k_s^A + k_s^B} \tag{3.11}$$

where the superscripts *A* and *B* denote the two contacting entities. For linear contact model, the normal secant stiffness is equal to the normal tangent stiffness.

3.3 Numerical sample specifications

3.3.1 Particle shape specification

In PFC^{3D}, the particle shape can be spherical or arbitrary shaped non-spherical. Spherical particle is generated by directly specifying particle centre position and radii of individual particle.

The clump logic is used to define non-spherical clump particles. A clump can be formed by two or more overlapping spherical particles to serve as a rigid body

without considering internal contact force arising from these balls itself. Particles within a clump may overlap to any extent. Particles comprising the clump possess the same motion, in which the clump particle will not break apart.

In this study, the non-spherical clump particle is specified by two identical overlapping balls to form a clump-shaped particle. The shape of a clump particle is described by the ratio $R_a = d/(2R)$ (e.g., Fig. 3.2). The value of R_a varies from 1 (fully overlapped) to 2 (just in contact) and various ratio values indicate different clump geometry. In this study, the ratio R_a is selected to be equal to 1.7.

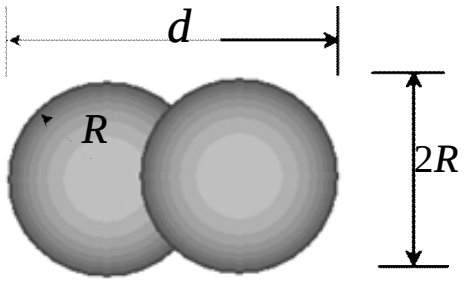

Fig. 3.2 Geometry of non-spherical particle

3.3.2 Choice of sample size

The granular material is naturally heterogeneous. To investigate three-dimensional behaviour of granular material with DEM, the number of particles used in numerical simulations should be sufficiently large so that the granular assembly can serve as a representative volume element. However, the number of particles cannot be infinitely large due to the limitation of computational power. Hence, it is required to make a comprise choice of sample size with limited number of particles,

which can still produce typical stress-strain behaviour within an acceptable computation time.

Four samples with different size have been generated to study the influence of sample size on the stress-strain behaviour. The initially isotropic samples were prepared with similar initial void ratios. The particle size was randomly distributed with radii between $0.3mm$ and $0.5mm$. The particle density was set to be $r = 2700\,kg/m^3$. The linear contact model was employed with normal and tangential stiffness to be $k_n = k_s = 1\times10^5\ N/m$. The simulation details are shown in Table 3.1 and the detail of initial sample are summarised in Table 3.2.

Table 3.1 Simulation details

Particle solid density r	$2700\,kg/m^3$
Spherical particle radius r	$[0.3, 0.5]\,mm$
Normal stiffness for ball and wall	$k_n = 1\times10^5\ N/m$
Tangential stiffness for ball and wall	$k_s = 1\times10^5\ N/m$
Friction coefficient for ball and wall	$m = 0.5$
Time-step Δt	$1.02\times10^{-6}s$
Damping coefficient x	0.7

Table 3.2 Samples with different size

No. of particles N_p	Initial void ratio e_0
512	0.601
1462	0.591
2948	0.606
5053	0.604

The triaxial compression tests have been conducted on four samples with constant mean normal stress $p = 500kPa$. The stress-strain behaviour is plotted in Fig. 3.3. It shows that the sample with 512 particles performs the highest peak stress ratio and most dilative, followed by the sample with 1462 particles. And the other two samples with more particles show a smaller peak stress ratio and less dilative. The sample with 2948 particles gives almost identical behaviour to that of sample with 5053 particles. It indicates that the granular assembly consisting of 2948 particles can produce acceptable simulation results and the stress-strain behaviour would not change significantly by further increasing sample size. However, it still may be better to use as many number of particles as possible under reasonable computational effort. Therefore, the sample size chosen in this research contains number of particles around 5000 or larger, which should be enough to serve as a representative volume for investigation of granular material behaviour.

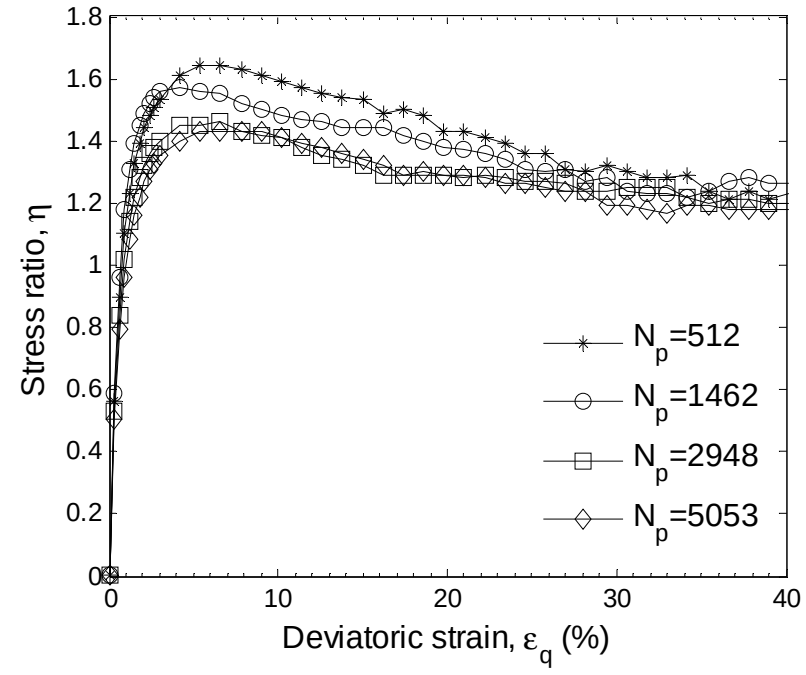

(a)

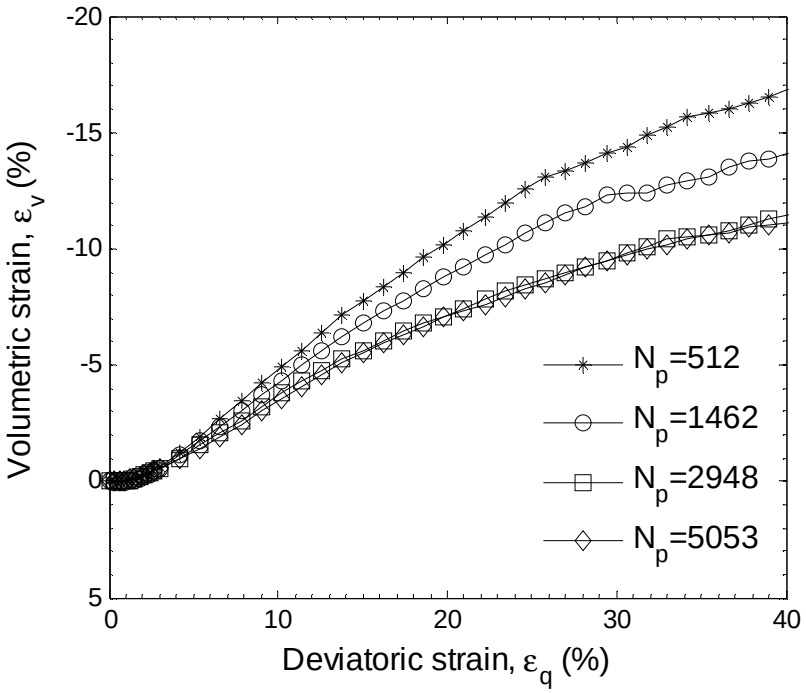

(b)

Fig. 3.3 Effects of sample size on (a) stress-strain behaviour (b) volume change behaviour

3.4 Parameters for contact model

As introduced in Section 3.2.4, the linear contact model presents simple constitutive relations to model the local contact behaviour. It only requires three inputting parameters, normal contact stiffness, tangential contact stiffness and friction coefficient, respectively. The frictional coefficient is selected to be $m = 0.5$, as it is normally used in DEM simulation of granular materials (Li and Yu, 2009, Thornton and Zhang, 2010, Guo and Zhao, 2013). The selection of a realistic stiffness differs from different DEM simulations. In this section, it introduces the selection of realistic contact stiffness for numerical simulation.

3.4.1 Estimation of contact stiffness by Hertz theory

For a granular assembly with average particle radius $\overline{R}$ and confining pressure p, the average contact force F is estimated as the multiplication of p and area projection A as:

$$F = pA \approx 4p\overline{R}^2 \tag{3.12}$$

The mechanical parameter E refers to Young's modulus and n is Poisson's ratio. The average contact displacement under contact force F is determined according to Hertz-Mindlin contact model (Johnson., 1985):

$$d = \left(\frac{9F^2}{16\overline{R}E^{*2}} \right)^{\frac{1}{3}} \tag{3.13}$$

where $E^* = \frac{E}{2(1-n^2)}$, d is the normal contact displacement.

Then, the contact normal stiffness is determined as the ratio of contact force F over normal contact displacement d :

$$k_n = \frac{F}{d} = \left(\frac{16\overline{R}E^{*2}F}{9} \right)^{\frac{1}{3}} \tag{3.14}$$

Substituting Eq. (3.12) into Eq.(3.14), resulting in the normal stiffness only a function of confining pressure for a specific material with known specific average particle size $\overline{R}$ and mechanical properties (E and n):

$$k_n = 4\overline{R}\left(\frac{pE^{*2}}{9} \right)^{\frac{1}{3}} \tag{3.15}$$

The sand is chemically composed of silicon dioxide in the form of quartz, e.g., toyoura sand (90%). The mechanical Young's modulus of quartz is around 70GPa. In DEM simulation, the particle size of numerical sample is randomly distributed with diameter within $\left[0.6,1\right]mm$. By setting $E = 70GPa, v = 0.3$ $\overline{R} = 0.0004m$, the relationship between normal contact stiffness and confining pressure according to Eq. (3.15) is shown in Fig. 3.4.

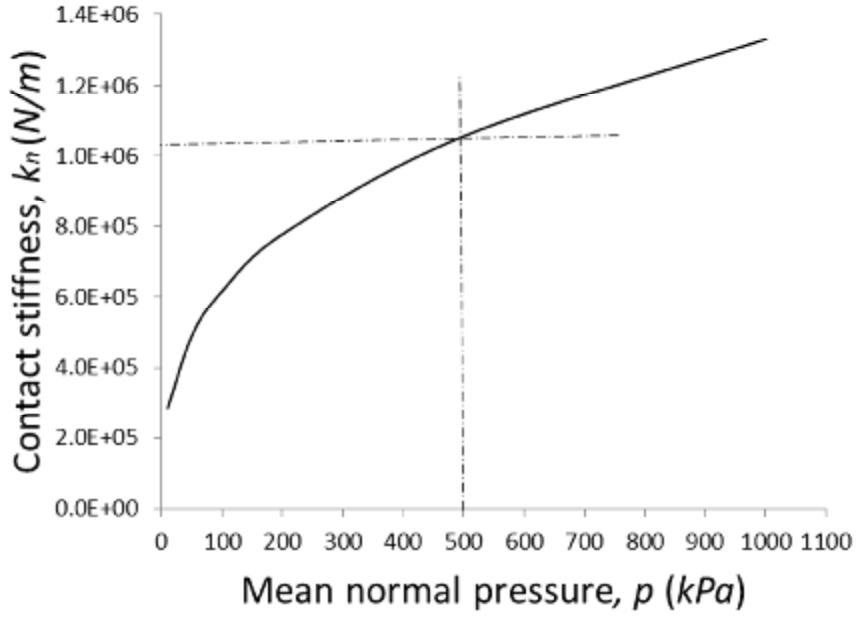

Fig. 3.4 Relations between contact stiffness and mean normal pressure

Fig. 3.4 suggests a normal stiffness of $1\times10^6 N/m$ at the confining pressure of 500kPa. The influence of k_s/k_n ratio on stress-strain response was presented by Li (2006) and no significant effect of k_s/k_n ratio on material behaviour was observed if only $k_s/k_n \neq 0$. For simplicity, taking the tangential stiffness equal to normal stiffness $k_n = k_s = 1\times10^6 N/m$, the initially isotropic dense and loose samples were prepared and isotropically consolidated to the initial confining pressure of $p = 10MPa$. Then, undrained triaxial compression tests have been carried out on two samples with initial void ratio 0.49 (dense) and 0.68 (loose), respectively. The stress ratio reaches the critical value at $e_q = 50\%$ as shown in Fig. 3.5(a). It can be seen from Fig. 3.5(b) that the confining pressure increases for both samples at large deformation. This is similar to the pore pressure build-up in laboratory undrained tests. At $e_q = 70\%$, the confining pressure almost approaches constant value.

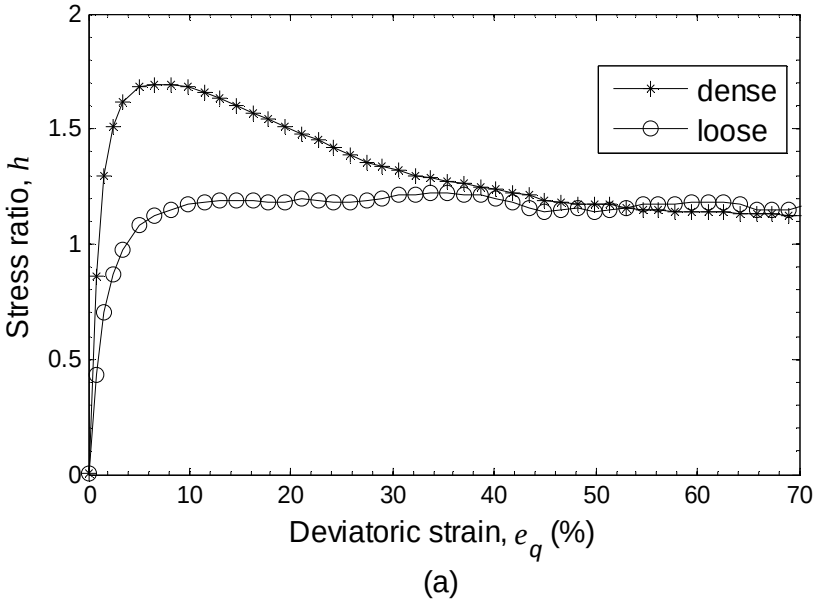

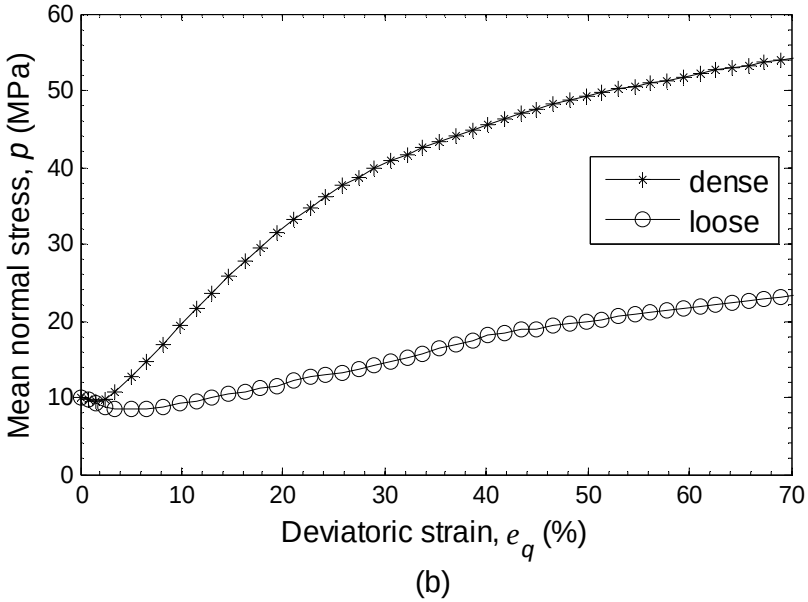

Fig. 3.5 Simulation results of undrained shear (a) stress-strain response (b) evolution of mean normal stress

Fig. 3.5(b) indicates that the samples approach critical state with deviatoric strain larger than 70%, where the material would experience deformation failure in a real laboratory test and the result is not reliable at such large deformation level. On the other hand, it means the material is far from the critical state line at the initial

state of confining pressure $p = 10MPa$. Assuming the critical state line is straight for this particular material and the void ratio would not decrease significantly with increasing confining pressure, the initial confining pressure should be increased to prepare a sample with initial state closer to the critical state, e.g., $p = 30MPa$.

3.4.2 Estimation of stiffness by dimensionless parameter

The confining pressure roughly performs a linear relationship with selected stiffness under otherwise the same condition as linear contact model employed. To obtain similar stress-strain behaviour at different confining pressures, the dimensionless parameter p/k, the ratio of confining pressure over the contact stiffness, should keep constant. Therefore, to perform the same or at least similar stress-strain behaviour at $p_1 = 500kPa$ as that obtained with $k_2 = 1\times10^6\ N/m$, $p_2 = 30MPa$, the stiffness k_1 at $p_1 = 500kPa$ should satisfy the conditions: $\frac{p_1}{k_1} = \frac{p_2}{k_2}$. It suggests a stiffness value of $k_1 = 1.6\times10^4\ N/m$ approximately.

3.4.3 Numerical simulations with different stiffness k_n

The contact stiffness estimated from Hertz contact theory and dimensionless estimation at $p = 500kPa$ was considered as the upper bound and lower bound of stiffness selection, respectively. Three samples were prepared by three different stiffnesses, $k_n = 2\times10^4\ N/m$, $k_n = 1\times10^5\ N/m$, $k_n = 1\times10^6\ N/m$, respectively.

The samples consisted of 5500 particles approximately. The three samples were sheared under triaxial compression at constant mean normal stress $p = 500kPa$.

Table 3.3 makes a comparison of effect of the selected contact stiffness on the secant modulus and the calculation speed. The desktop computer processor is *Intel(R) Core(TM)2 Quad CPU Q9650 @ 3.00GHz*, with *4.00 GB RAM*. The G_{50} indicates the secant shear modulus at 50% of the peak stress ratio as $G_{50} = \left(q/e_q\right)_{50}$. The sample with greatest contact stiffness with $k_n = 1\times10^6\ N/m$ gives the highest secant modulus, which is considerably larger than that of sand, normally $10MPa \sim 80MPa$, e.g., the secant Young's modulus of toyoura sand $E_{50} = 40MPa$ (Oda, 1972a), and unacceptable calculation time while the sample with the lowest value of normal contact stiffness performs too soft (e.g., Fig. 3.6). However, the sample with the middle value of contact stiffness produces reasonable secant modulus in between and acceptable calculation time.

Accordingly, the choice of stiffness is a compromise of values determined by Hertz contact theory and dimensionless analysis, selecting $k_n = k_s = 1\times10^5\ N/m$. The sample with stiffness of $k_n = k_s = 1\times10^5\ N/m$ produces typical stress-strain behaviour of sand in drained triaxial compression test with constant confining pressure $p = 500kPa$, i.e., Fig. 3.6. Therefore, the selected stiffness for numerical simulation is $k_n = k_s = 1\times10^5\ N/m$. When the sample with the selected stiffness is isotropically consolidated to mean normal stress of $500kPa$, the mean contact force is around $0.3N$ and the ratio of contact overlap Δu over particle size $\overline{D}$ is

$\frac{\Delta u}{\overline{\overline{D}}} = \frac{0.3}{1\times10^5 \times 0.0008} = 0.375\%$, which is sufficiently small to consider the contact point as a vanishingly area.

Table 3.3 Comparison of selected stiffness on simulations

Contact stiffness $k_n = k_s$	Void ratio e_0	Secant modulus $G_{50}(MPa)$	Time-step Δt	Calculation time to $e_q = 30\%$ (days)
$1\times10^6\ N/m$	0.6	720	$3.2\times10^{-7}\ s$	> 30
$1\times10^5\ N/m$	0.61	71	$1\times10^{-6}\ s$	4
$2\times10^4\ N/m$	0.63	8	$2.3\times10^{-6}\ s$	1

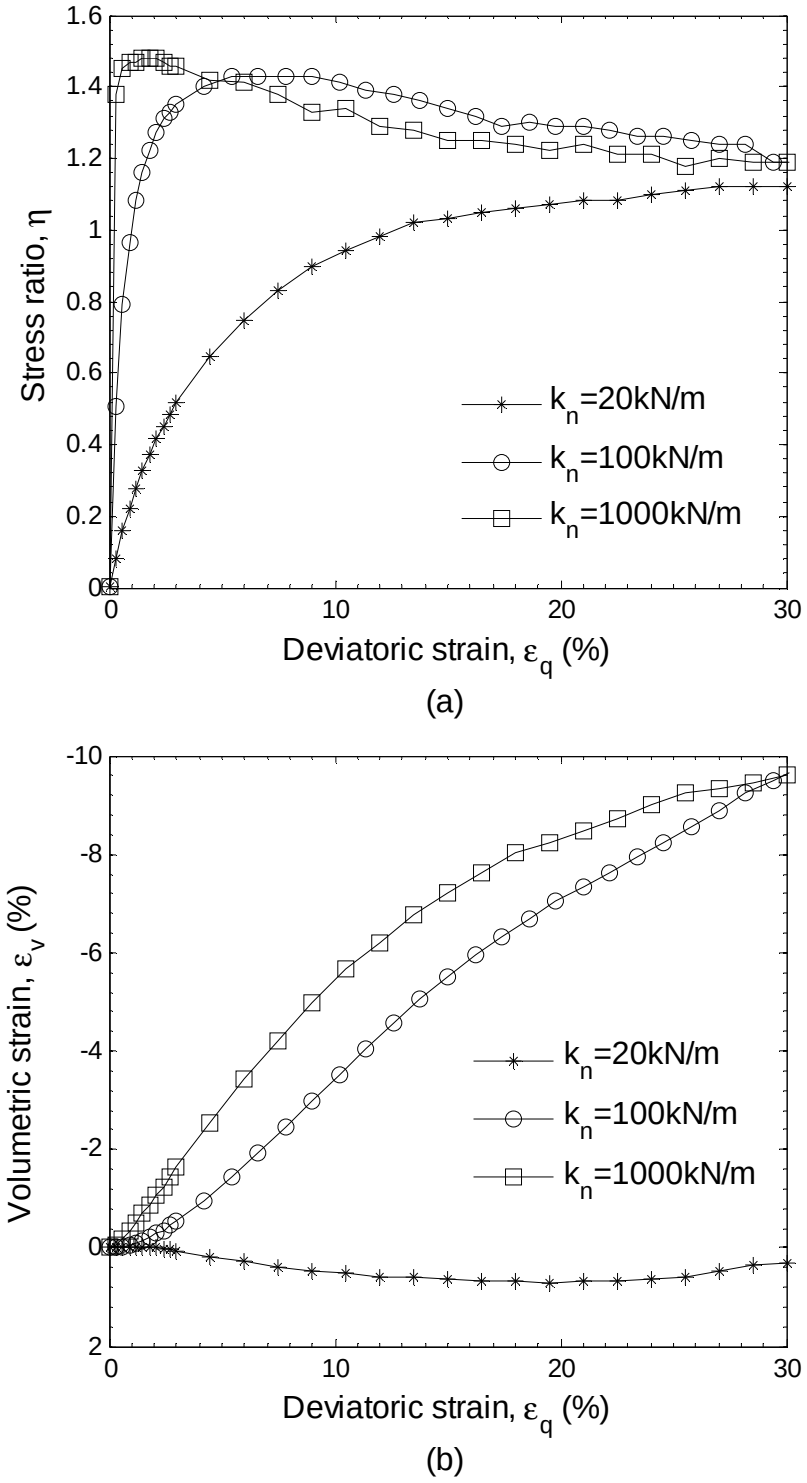

Fig. 3.6 Effects of contact stiffness on granular material response (a) stress-strain behaviour (b) volumetric strain

3.5 Summary

The commercial software PFC3D has been employed for multi-scale study on granular material behaviour. The PFC3D models the movement and interaction of particles assembly. The behaviour at contacts is modelled by a soft-contact approach, which allows vanishing small (e.g., a point) overlapping between rigid particles. The particles shape can be spherical or arbitrary shaped non-spherical. For simulations presented in this research, the radius of spherical particles consisting of numerical sample is randomly distributed between $0.3mm$ and $0.5mm$. For the non-spherical clump particle shape, the value of R_a (long axis of two overlapping spheres over ball diameter) is 1.7. The size of a clump particle is determined by the replaced ball of diameter randomly distributed among $[0.6, 1.0]\,mm$.

The linear contact model is assumed to describe the local contact behaviour. The frictional coefficient is selected to be $m = 0.5$. The parametric study suggests the stiffness to be $k_n = k_s = 1\times10^5\ N/m$ to produce typical stress-strain behaviour within an acceptable calculation period. By selecting the particle density as $r = 2700\,kg/m^3$, the mechanical time-step is $\Delta t \approx 1\times10^{-6}\,s$. The damping coefficient employs the default value $x = 0.7$, unless otherwise stated. The sample size consisting of over 3000 particles seems to produce typical stress-strain behaviour and further increase of sample size would not affect material response significantly. Hence, the sample with more than 3000 particles is sufficient to serve as representative volume.

Chapter 4 Virtual experiment set-up and testing

4.1 Introduction

The stress-strain behaviour of granular material, e.g., sand, is loading path and loading history dependent. To conduct multi-scale investigation with DEM simulations, it is essential to realise various loading paths in DEM. DEM simulations are reported in literature mimicing conventional laboratory tests to reproduce both the stress conditions and boundary conditions, e.g., triaxial test on cylindrical sample (Cui et al., 2007), true triaxial test on cubic sample (Thornton, 2000). DEM simulations have also been reported to prepare and simulate elementary behaviour of granular material with circular shaped boundary (Rothenburg and Bathurst, 1992, Hosseininia, 2012). However, limited three-dimensional DEM simulations on granular material elementary behaviour have been demonstrated with independent control of both principal stresses magnitudes and their principal directions.

Li et al. (2013) proposed a virtual experiment technique to realise general loading path with DEM, both proportional and non-proportional, and it was successfully implemented in 2D DEM simulations for monotonic shearing and rotational shearing (Li and Yu, 2009, Li and Yu, 2010). The numerical simulations

presented in this research implement the same technique proposed by Li et al. (2011) in three-dimensional spaces within the commercial software PFC3D. Material responses undergoing various loading paths will be simulated, including both proportional loading and non-proportional loading.

The key features of the developed numerical model can be summarised as:

1. The rigid massless boundary walls form a polyhedral shape with obtuse angle between every two neighbouring walls to minimise arching effect and to enhance specimen uniformity.
2. Finite strain definition is adopted for accurate description of volumetric strain.
3. The general loading path involving principal stress rotation can be realised by control of boundary conditions, specifying translational and rotational motions of boundary walls.

This chapter introduces the implementation of the numerical simulation technique within PFC3D and presents a few examples to demonstrate the capability of the proposed numerical model in studying granular material behaviour under general loading paths.

4.2 Virtual experiment set-up

In this research, the rigid massless walls are used to form the boundary of a numerical sample. A set of infinite walls are specified to form a polyhedral-shaped boundary, in order to enhance sample uniformity. The polyhedron is defined by only two parameters n and R, where n is the number of sides of the top regular polygon

wall surface and R is the radius of the polyhedron inscribed sphere. And n defines the shape of the polyhedron and R controls the size of the polyhedron. More details about the polyhedron definition and generation within PFC3D can be found in appendix B.2. An example of such polyhedron with $n = 8$ is shown in Fig. 4.1. Further increase of n value would not affect simulation results significantly but computational effort does increase dramatically.

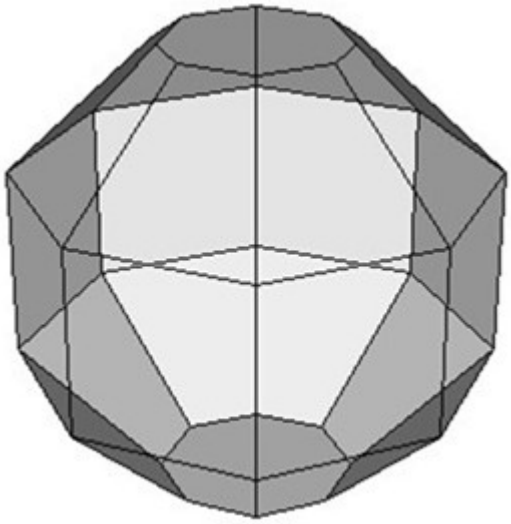

Fig. 4.1 Polyhedral boundary shape with $n = 8$

The stress and strain tensors of the polyhedral sample are evaluated from the forces acting on the boundary walls and relative displacement of the vertices forming the boundary walls, respectively. The sign convention is taken to be consistent with that defined for stress and strain in soil mechanics, where the positive mean normal stress and volumetric strain increment indicate compression of specimen.

In testing soil, the loading path is usually controlled by stress invariants or strain invariants instead of tensorial component forms for investigating soil behaviour, e.g., strength and volume change behaviour. To realise general loading

path, the boundary wall motions are determined from the strain increment in tensorial form in each loading cycle so that it is required to transform the stress or strain tensor to its invariants form and compared to the specified loading path to check if boundary conditions satisfied. Therefore, it is required to inter-transform the stress/strain state in tensorial form and in invariants form. The stress and strain tensor determination and inter-transformation between stress and strain tensor and their invariants are introduced in detail in Appendix B.3.

In this research, the stress invariants are described as mean normal stress p, intermediate principal stress ratio b and deviatoric stress q, which is determined from the three principal stresses $s_i \left(i = 1, 2, 3\right)$ as follows:

$$\begin{cases} p = \dfrac{s_1 + s_2 + s_3}{3} \\ b = \dfrac{s_2 - s_3}{s_1 - s_3} \\ q = \sqrt{\dfrac{\left(s_1 - s_2\right)^2 + \left(s_2 - s_3\right)^2 + \left(s_1 - s_3\right)^2}{2}} \end{cases} \tag{4.1}$$

The stress ratio is defined as $h = q/p$. The strain invariants include the volumetric strain e_v, deviatoric strain e_q and intermediate principal strain ratio b_e, which are expressed from three principal strains $e_i \left(i = 1, 2, 3\right)$ as:

$$\begin{cases} e_v = e_1 + e_2 + e_3 - e_1 e_2 - e_2 e_3 - e_1 e_3 + e_1 e_2 e_3 \\ e_q = \dfrac{2}{3}\sqrt{\left(e_1 - e_2\right)^2 + \left(e_2 - e_3\right)^2 + \left(e_1 - e_3\right)^2} \\ b_e = \dfrac{e_2 - e_3}{e_1 - e_3} \end{cases} \tag{4.2}$$

It is worth noting that the volumetric strain definition in finite strain definition is different from the summation of the three principal strains given in the infinitesimal deformation theory. The latter induces a significant error when the deformation is finite and large. The above strain and strain invariants definition are used in this research hereafter.

In laboratory soil testing, the loading control can be classified to be strain controlled; stress controlled and mixed control boundary conditions. In numerical simulations, however, the loading is applied by specifying boundary walls motions to achieve an accurate strain increment and it is inherently strain controlled. Therefore, a strain controlled loading path can be realised directly by specifying translational and rotational velocities to achieve a target strain increment while the stress controlled loading requires a servo-control mechanism to achieve a target stress increment. In view that the boundary walls work as an integrated set to impose the desired loading, the movements of boundary walls are determined synchronically and are calculated based on the specified change in a unified way. More details can be found in Appendix B.4.1 for strain-controlled loading conditions and in Appendix B.4.2 for stress-controlled loading conditions.

In numerical simulations, the target boundary conditions and static equilibrium state can not be exactly satisfied. Therefore, the numerical test control is set to monitor the sample stress/strain conditions. This is introduced in detail in Appendix B.4.3.

4.3 Sample preparation method

For numerical simulations, the particle and wall properties are summarised in detail in Table 4.1. The initially isotropic samples are prepared with spherical particles used, of which radius r is randomly distributed within $[0.3, 0.5]\,mm$. The linear contact model is employed and the contact stiffness is chosen to be $k_n = k_s = 1\times10^5\ N/m$. Those simulations parameter values are suitable for all simulations presented throughout the thesis unless otherwise stated.

Table 4.1 Numerical simulation details

Particle solid density r	$2700\ kg/m^3$
Spherical particle radius r	$[0.3, 0.5]\,mm$
Normal stiffness for ball and wall	$k_n = 1\times10^5\ N/m$
Tangential stiffness for ball and wall	$k_s = 1\times10^5\ N/m$
Friction coefficient for ball and wall	$m = 0.5$
Time-step Δt	$1.02\times10^{-6}\,s$
Damping coefficient x	0.7

4.3.1 Radius expansion for isotropic sample preparation

The radius expansion method is used to generate initially isotropic samples with varying initial void ratios. The procedures of sample preparation are as follows:

1. A set of infinite boundary walls are generated to form the closed polyhedron boundary shape as introduced in Appendix B.2. The inputting parameters n and R are chosen to be 8 and 0.01m, respectively.
2. The number of spherical particles is determined based on the target void ratio e_g and particle size distribution. The particles are generated within the volume enclosed by the polyhedron boundary walls and are positioned randomly in the specific volume with radius reduced by 1.5 times of their normal value so that no contact forces arised between any two particles (e.g., Fig. 4.2(a)).
3. After all particles are positioned, the particles radii are restored. Simulations are carried out to achieve sample equilibrium. At this stage, the initial pressure p_0 is controlled and different values of friction coefficient m_g are set for preparing samples with various initial void ratios (e.g., Fig. 4.2(b)). If the non-spherical clump particles are used, then the individual spherical particle is replaced by two identical overlapping balls to serve as a clump particle (e.g., Fig. 3.2). Then, simulations are carried out to reach equilibrium (e.g., Fig. 4.2(c)). Otherwise, skip to step 4.
4. The friction coefficient m is then restored to 0.5 and the sample is isotropically consolidated to the target confining pressure of $500kPa$.

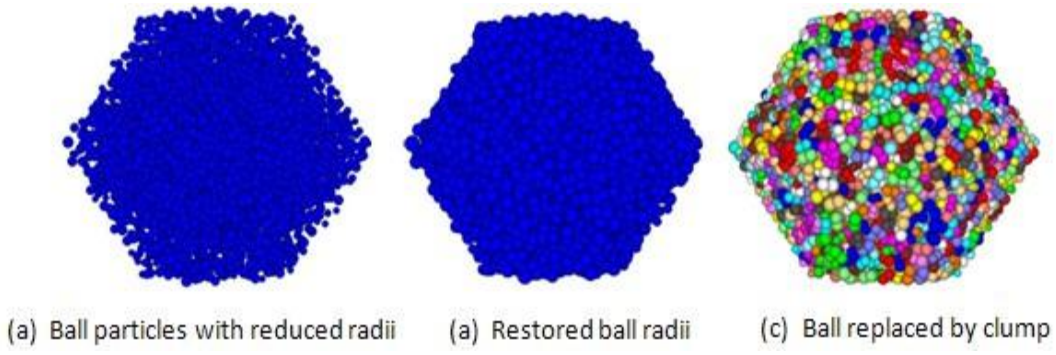

Fig. 4.2 Isotropic sample preparation by the radius expansion method

The radius expansion method of sample preparation is advantageous to the isotropic compression method of which full sized particles are generated and the boundary walls moves inward till the target confining pressure or target void ratio achieved. The uniformity would not be achieved as the presence of large pores in central part of sample due to boundary effect for wall-moving isotropic compression method, even worse for generating loose sample (Jiang et al., 2003). On the other hand, the radius expansion method results in more uniform specimens with less computational effort to reach equilibrium.

The initial confining pressure p_0 obtained after the particle radii restored is mainly dependent on the friction coefficient m_g and target void ratio e_g during the generation process. However, the final void ratio e_0 obtained after the isotropic consolidation to a target mean normal stress is only dependent on the friction coefficient m_g. Fig. 4.3 shows the influence of m_g on the obtained void ratio e_0 after isotropic consolidation to $p = 500kPa$. It can be seen that the void ratio e_0 initially increases with a greater m_g and then keeps steady when $m_g \geq 0.5$. Hence,

the initially isotropic samples with three different void ratios can be prepared by specifying different m_g values ($0 \leq m_g \leq 0.5$), respectively.

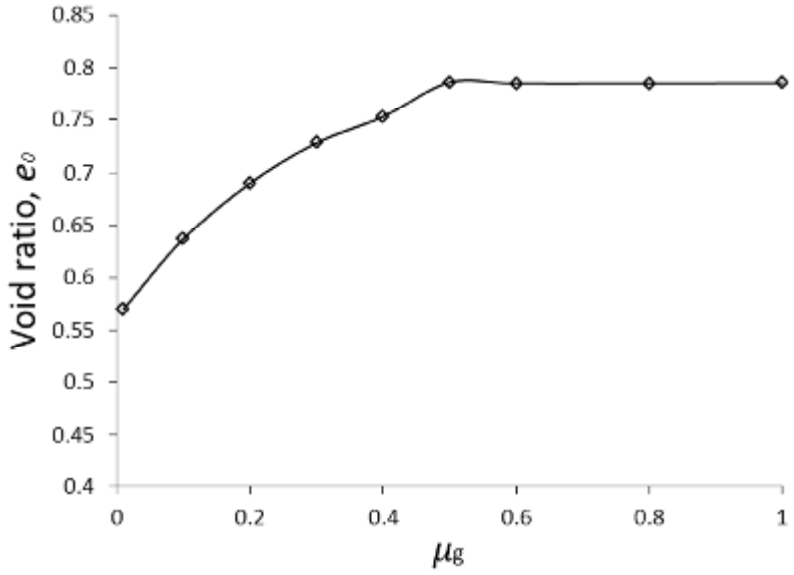

Fig. 4.3 Variation of void ratio *e* with m_g

Three initially isotropic samples consisting of spherical particles were prepared using this method. After the required particle radius was restored and static equilibrium condition was achieved, during which the frictional coefficients were kept unchanged as m_g. Then, the frictional coefficient was restored to their normal value, $m = 0.5$, and the samples were isotropically consolidated to the confining pressure of $500kPa$, where the void ratio e_0 was recorded as the initial void ratio of the prepared sample. The number of particles within three samples was more than ten thousand, which was sufficient to represent as a representative volume for numerical simulation. Information on the prepared initially isotropic samples has been given in Table 4.2. The samples are labelled by a string of characters for simple identification throughout the thesis, where the first letter 'S' indicates that the sample

consists of spherical particles; the second and third characters 'RE' represents the Radius Expansion method for preparing initially isotropic sample; and the fourth letters 'D', 'M', 'L' refer to the sample termed as dense, medium and loose, respectively. The last two characters 'TT' indicate that the sample is going to be simulated under True Triaxial loading in the following. A detailed introduction of the entire numerical sample label in this research can be found in Appendix C.

Table 4.2 Details of prepared isotropic samples of spherical particles

Sample preparation method	m_g	e_g	Void ratio, e_0 ($p = 500kPa$)	No. of particles	Target loading path	Sample label
Radius Expansion (RE)	0.1	0.64	0.64 (Dense)	11090	True triaxial (TT)	SRED_TT
	0.3	0.74	0.73 (Medium)	10446		SREM_TT
	0.5	0.79	0.78 (Loose)	10151		SREL_TT

4.3.2 Gravitational deposition method

The gravitational deposition method is used to prepare initially anisotropic sample, similar to the process of granular assembly, e.g. sand, formed naturally by physical sedimentation under gravity force. It consists of following procedures:

1. Create a box with a height 8 times of the target specimen height, which has the same mechanical properties with particles. Then, randomly generate spherical particles within the box without contact force arising between any

two particles and friction coefficient m_g is specified to each particle (e.g., Fig. 4.4(a)). The number of particles generated is nearly 3 times of target sample size. At this stage, the void ratio of box sample is close to 8.

2. If non-spherical particles are used, the spherical particle is then replaced by two identical overlapping balls to serve as a clump particle, which has the same volume to the replaced spherical particle and the orientations of non-spherical particles are randomly distributed (e.g., Fig. 4.4(b)). Otherwise, skip to step 3.

3. Gravitational acceleration field $g = -100\, m/s^2$ is assigned to each particle and damping coefficient x is modified to a smaller value $x = 0.2$, to save computational time. Then, carry out numerical simulation to allow particles falling freely under gravitational force to achieve a static equilibrium state, (e.g., Fig. 4.4(c)).

4. Delete the box boundary walls created in step 1 and generate walls to form the polyhedral boundary shape (e.g., marked by yellow line in Fig. 4.4(d)). Then, delete particles positioned outside of the polyhedral boundary.

5. Finally, remove the gravitational field and restore damping coefficient to 0.7. The inter-particle friction coefficient is then reset to representative value $m = 0.5$. Then, carry out simulation to achieve equilibrium state, (e.g., Fig. 4.4(e)). At this stage, the sample has an initial pressure p_0. The sample is finally isotropically consolidated to target mean normal stress of $500kPa$.

Due to a few particles deleted in step 4, the number of particles generated in step 1 is larger than the target sample size. Though the gravitational field is enlarged

to be $g = -100\, m/s^2$ to accelerate the deposition process, it does not affect the prepared sample, e.g., initial void ratio, fabric anisotropy, significantly. The gravitational deposition method would generate initially anisotropic sample with more contacts oriented in the vertical deposition direction due to gravitational force. Similar to that of the radius expansion method, the initially anisotropic samples with various initial void ratios e_0 can be achieved by specifying different frictional coefficient m_g, a smaller m_g leads to a lower initial void ratio e_0.

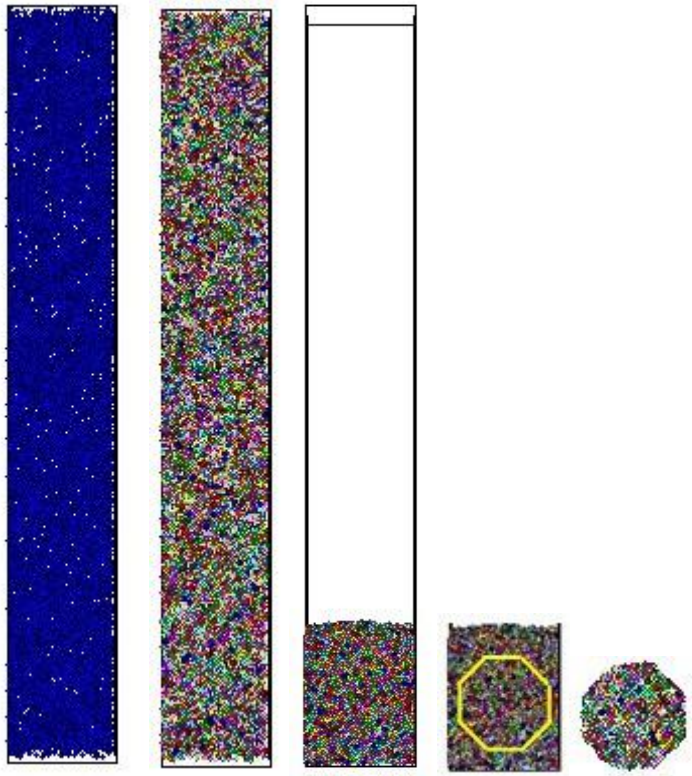

Fig. 4.4 Sample preparation by gravitational deposition method (a) ball generation (b) ball replaced by clump particle (c) gravitational deposition (d) polyhedron boundary generation (e) isotropic consolidation

4.4 Typical simulation results

This section presents the detailed realisation of three particular loading paths, which represent the strain-controlled, stress-controlled and mixed-controlled boundary conditions, also including proportional and non-proportional loading. Moreover, typical simulation results are illustrated to demonstrate the applicability of the proposed DEM model for multi-scale investigating granular material behaviour under general stress paths.

4.4.1 Undrained simple shear

In soil testing, the laboratory Cambridge-type simple shear test apparatus has been designed for widely use in obtaining soil parameters (Roscoe et al., 1967, Budhu and Britto, 1987). The simple shear configuration is illustrated in Fig. 4.5. It illustrates that the volumetric strain is equal to the vertical strain. The simple shear test is either drained with constant vertical normal stress or undrained with zero vertical strain. In undrained simple shearing, only the shear strain component e_{zx} increases continuously while all the other strain components are kept zero. It is purely strain-controlled non-proportional loading conditions. In each loading step, the strain increment Δe_{zx} is applied by specifying boundary walls velocities using Eqs. (30) and (31) (more details in appendix B.4.1).

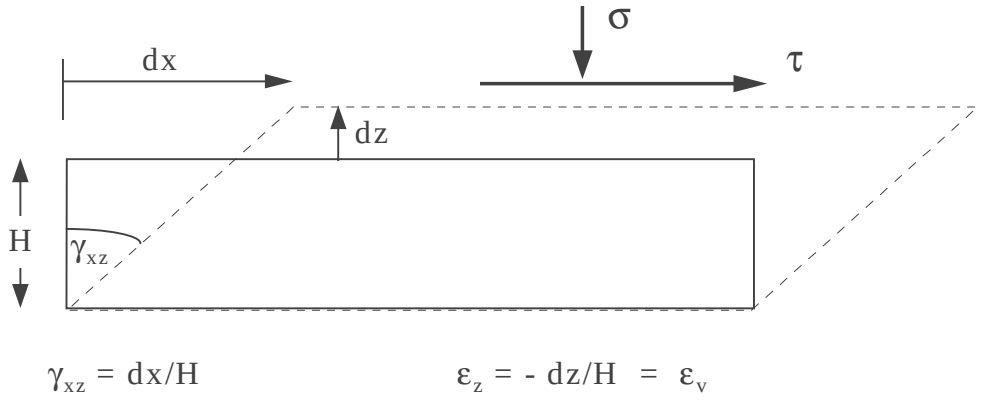

Fig. 4.5 Configuration of simple shear boundary conditions

The numerical undrained simple shear tests have been simulated under constant volume $e_v = 0$. The shear strain increment e_{zx} is applied by rigid wall rotations about its centre. Similar scheme of DEM simulation of drained simple shear can be found in literatures (Thornton and Zhang, 2006, Langston et al., 2013). The numerical simulations have been conducted on samples with various initial $K_0 = s_{xx}/s_{zz}$ conditions, $K_0 = 0.5, 1.0, 2.0$ respectively. The sample of initial $K_0 = 1$ is the initially isotropic dense sample SRED_TT. For the other two samples with initial $K_0 \neq 1$ conditions, the initially isotropic dense sample SRED_TT is loaded at constant $s_{xx} = 500kPa$ and $e_{yy} = 0$, by increasing s_{zz} or decreasing s_{zz} to $s_{zz} = 1000kPa$ or $s_{zz} = 250kPa$, corresponding to initial $K_0 = 0.5$ and $K_0 = 2$, respectively. The pre-loading process is the plane strain loading path with mixed controlled boundary conditions. The prepared three samples for undrained simple shear are labelled as SRED_PSK05_SS, SRED_PSK10_SS and SRED_PSK20_SS, with initial K_0 being 0.5, 1.0 and 2.0 respectively. The prepared samples for simple shear simulations are shown in Table 4.3. More details about the sample label refer to Appendix C.

Table 4.3 Samples of spherical particles for undrained simple shear

Sample preparation		K_0 value	Void ratio	Numerical simulations	Sample label
Sample SRED_TT	Pre-shear by Plane Strain (PS)	0.5	$e_0 = 0.62$	Undrained simple shear (SS)	SRED_PSK05_SS
		1.0	$e_0 = 0.64$		SRED_PSK10_SS
		2.0	$e_0 = 0.65$		SRED_PSK20_SS

Fig. 4.6 shows the evolution of the volumetric strain (e_{zz}) during the designed undrained simple shear loading. It is clear that the target loading path has been well maintained with zero dilation against increasing shear strain. The stress paths in simple shear are shown in Fig. 4.7, which is consistent to the laboratory undrained simple test (Yoshimine et al., 1998). It turns out that the simulations can reproduce the undrained behaviour of sand qualitatively.

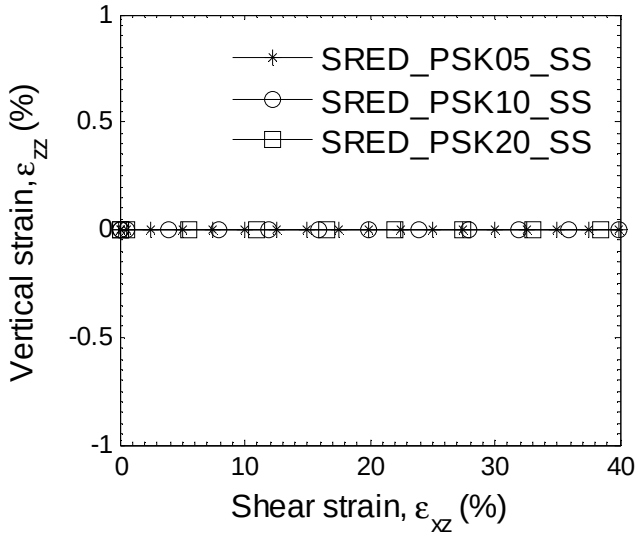

Fig. 4.6 Evolution of volumetric strain in undrained simple shear

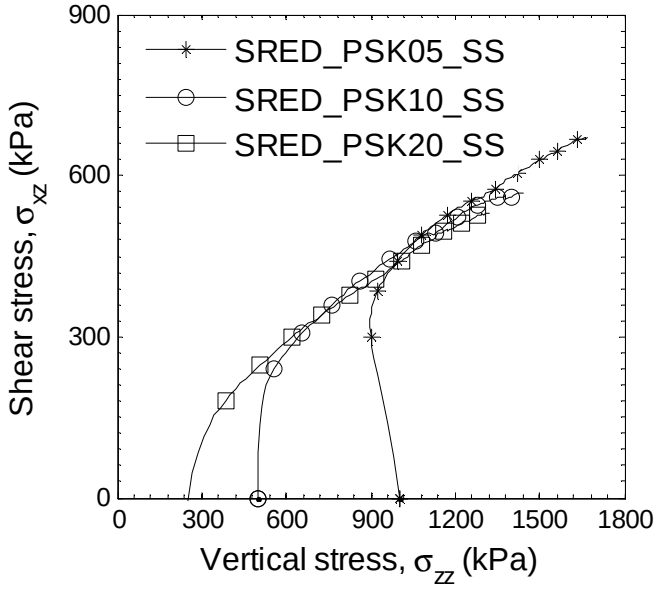

Fig. 4.7 Stress paths in undrained simple shear with various K_0 conditions

The evolution of ratio of horizontal stress over vertical stress is illustrated in Fig. 4.8. Initially, it starts from different values, corresponding to various initial K_0 conditions. Upon shearing, the value of s_{xx}/s_{zz} approaches the same value, i.e., $s_{xx}/s_{zz} \approx 0.9$, at large deformation, irrespective of initial K_0 values.

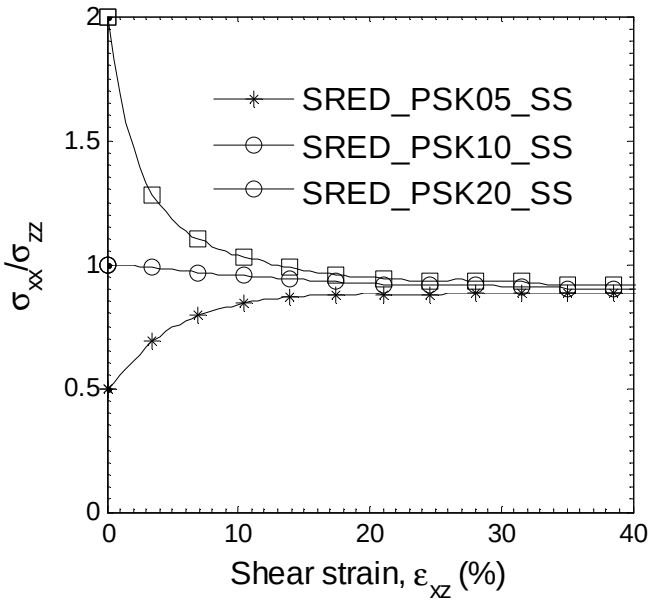

Fig. 4.8 Stress-strain behaviour in undrained simple shear

If one intends to compare simple shear results to other test results, i.e., plane strain test, knowledge of the complete stress state will be required. It was found that the post-failure simple shear behaviour was similar to the plane strain test under similar stress conditions (*b* value and *a*) (Pradhan et al., 1988, Yoshimine et al., 1998). Fig. 4.9 demonstrates the evolution of *b* value during simple shear. Initially, the *b* value is greater in the sample of larger K_0 value. It may be seen that the b value reaches the same value at large deformation, irrespective of initial K_0 values, and remains constant for further shearing. The ultimate value is around $b \approx 0.32$. The ultimate *b* value was found to be 0.25 in experimental undrained simple shear, regardless of material initial void ratio and consolidation stress ratios (Pradhan et al., 1988, Yoshimine et al., 1998).

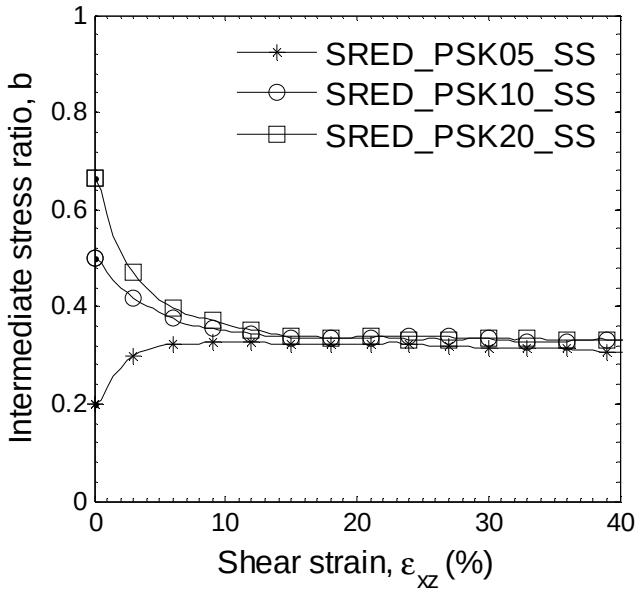

Fig. 4.9 Evolution of *b* value during simple shear under varying intial K_0

The rotation of the major principal stress direction during simple shear is illustrated in Fig. 4.10. The solid straight line without symbol represents the applied principal strain increment direction $g_{\Delta e}$, which is always in the *x*-*z* plane and keeps

an angle of 45^{o} to the vertical *z*-axis. The major principal stress direction is represented by the angle a , which is the direction of major principal stress direction vector projected in the *x*-*z* plane relative to the vertical *z*-axis direction. Initially, for sample with initial $K_0 = 0.5$, the major principal stress direction is in the vertical direction ($a = 0^{o}$). For sample with initial $K_0 = 2$, the major principal stress direction is in the horizontal direction ($a = 90^{o}$). For the initially isotropic sample with $K_0 = 1$, the major principal stress direction is not defined. Upon shearing, it can be seen from the figure that the principal stress direction is generally coaxial with the strain increment direction ($a \approx g_{\Delta e} = 45^{o}$) when $K_0 = 1$. When $K_0 \neq 1$, significant degree of non-coaxiality is observed and the major principal stress directions approach the strain increment direction gradually as shearing continues. After 15% shear strain, the degree of non-coaxiality becomes quite small and the general coaxial behaviours are observed, irrespective of initial K_0. It is noted that the ultimate principal stress direction is $a \approx 41.4^{o}$, deviating a few degrees from the strain increment direction $g_{\Delta e} = 45^{o}$. This is consistent to the experimental observation of the ultimate principal stress direction $a = 40^{o} \sim 45^{o}$ in undrained simple shear regardless of initial stress conditions (Yoshimine et al., 1998). The principal stress rotation has also been reported in drained laboratory simple shear test and DEM simulations (Roscoe et al., 1967, Thornton and Zhang, 2006, Langston et al., 2013). However, the mechanism of the principal stress rotation is not well explained in their numerical work.

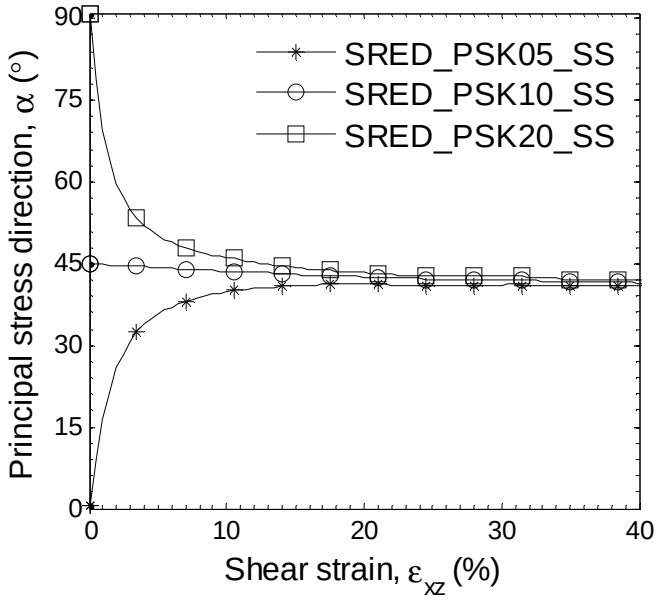

Fig. 4.10 Rotation of major principal stress direction in undrained simple shear

4.4.2 Drained true triaxial test

4.4.2.1 Simulation details

The numerical experiment model can control the individual stress invariant independently, both magnitudes and principal directions. The drained true triaxial loading path keeps stress invariants p, b and principal stress directions $\mathbf{n}_i^s$ unchanged while deviatoric strain e_q continuously increases. It is mixed controlled boundary, with partially stress-controlled and partially strain-controlled. It simulates the laboratory true triaxial test, with loading path shown in Fig. 4.11. It is worth noting that there is no restriction of the principal stress direction being vertical only.

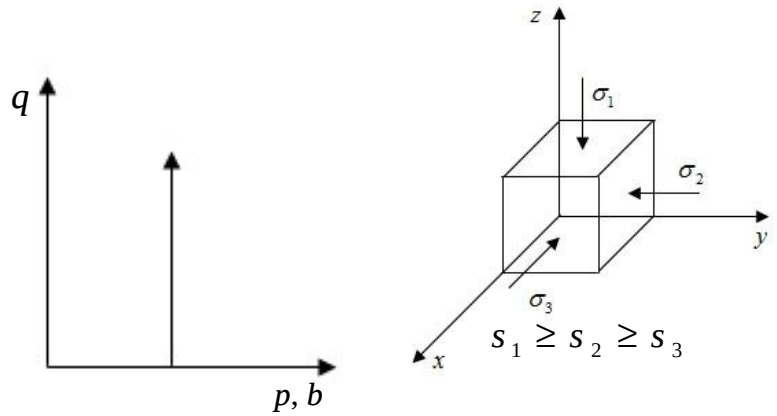

(a) (b)

Fig. 4.11 Illustration of drained true triaxial loading path

During numerical implementation, the target stress state s_{ij}^{t} can be determined by transforming stress invariants p, b, q into stress tensor as introduced in Appendix B.3.2, where q is the current deviatoric stress of the sample. The current stress state s_{ij} can be determined from contact forces acting on boundary walls as expressed in Eq. (20) in Appendix B.3.2. Accordingly, the stress increment is the difference between the current stress state and the target stress state, $\Delta s_{ij} = s_{ij}^{t} - s_{ij}$.

Then, the strain increment Δe_{ij} can be estimated according to Eq. (32), shown in appendix B.4.2. The strain increment can be expressed as its invariants $\Delta e_v, \Delta e_q, b_{\Delta e}$ and principal strain directions $\mathbf{n}_i^{\Delta e}$. If the boundary conditions are not satisfied, the strain increment Δe_{ij} is applied till target stress boundary conditions achieved through servo-control mechanism.

Otherwise if the boundary conditions are satisfied, the modified deviatoric strain increment Δe_q^m is applied by introducing an additional deviatoric strain increment Δe_q^{inc} as $\Delta e_q^m \leftarrow \Delta e_q + \Delta e_q^{inc}$ with other strain increment invariant Δe_v, $b_{\Delta e}$ and $\mathbf{n}_i^{\Delta e}$ unchanged. Then, a modified strain increment tensor Δe_{ij}^m can be determined by transformation of the strain invariants $\Delta e_v, \Delta e_q^m, b_{\Delta e}, \mathbf{n}_i^{\Delta e}$ into strain tensor Δe_{ij}^m as introduced in appendix B.3.3. The strain increment Δe_{ij}^m is applied to boundary walls by specifying velocities according to Eqs. (30) and (31).

4.4.2.2 True triaxial simulation results

The drained true triaxial simulations have been conducted on the initially isotropic dense sample SRED_TT and loose sample SREL_TT to demonstrate the validity of the numerical simulation technique. The information of the initially isotropic samples can be found in Table 4.2. The drained true triaxial simulations controls constant mean normal stress $p = 500kPa$ and intermediate stress ratio $b = 0.5$, with fixed major principal stress direction in the vertical direction. Only the deviatoric strain e_q increases continuously.

Fig. 4.12 presents of the evolution of stress invariants during true triaxial simulation. It shows that the target mean normal stress and b value have been accurately controlled at constant values. This clearly indicates that the required mixed-controlled true triaxial loading path is satisfied.

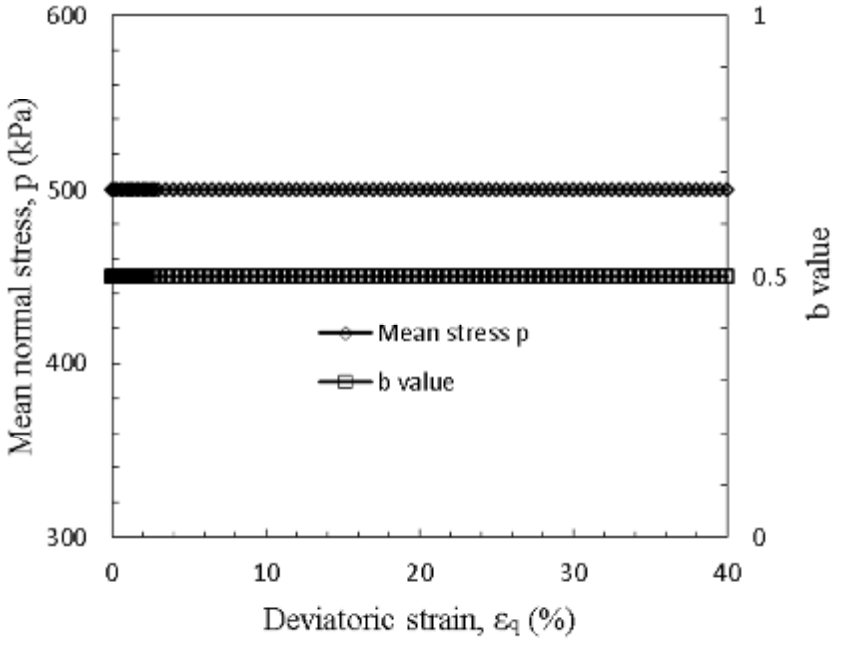

Fig. 4.12 Evolution of target stress invariants during true triaxial simulation

The typical stress-strain behaviour is shown in Fig. 4.13. The numerical simulation results show qualitatively good agreement with the laboratory observations on sand behaviour (Verdugo and Ishihara, 1996). When tested under otherwise the same boundary conditions, the dense sample SRED_TT performs strain hardening and softening behaviour while the loose sample SREL_TT hardens continuously. The dense sample SRED_TT dilates with increasing void ratio and the loose sample SREL_TT contracts with decreasing void ratio. At large deformation, both samples would eventually approach the same state with similar stress ratios and void ratios. It indicates that the DEM can be employed for multi-scale investigation of the void ratio effect on dilatancy behaviour of granular material.

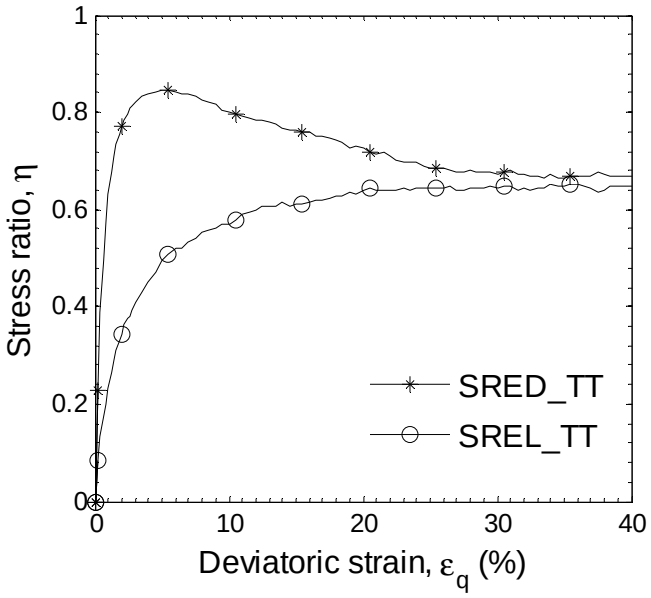

(a)

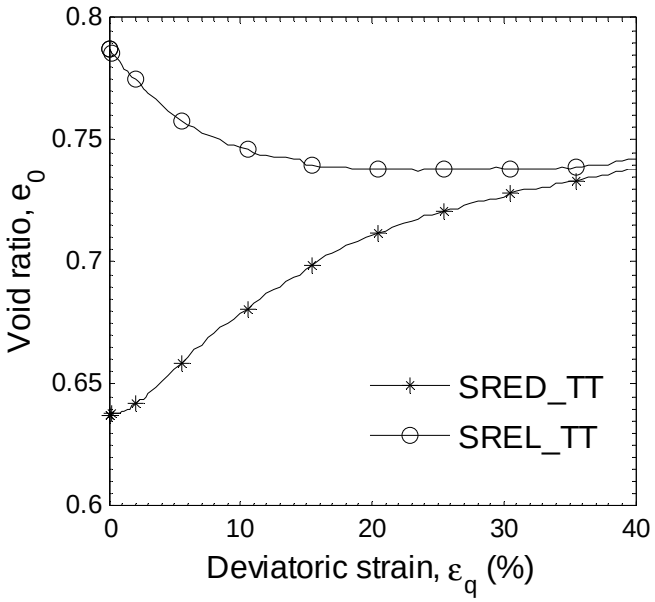

(b)

Fig. 4.13 Drained true triaxial simulations (*b*=0.5) on isotropic dense and loose samples of spherical particles (a) stress-strain (b) volume change

4.4.3 Drained rotational shear

4.4.3.1 Simulation procedures

The stress path involving principal stress rotation can be in many different ways. To study the granular material response under pure principal stress rotation, however, one stress path presented in this study is to mimic the pure stress rotation in a laboratory test using hollow cylinder apparatus. It is a purely stress-controlled loading path. The stress path in the deviatoric plane is a circle (e.g., Fig. 4.14) due to constant magnitudes of stress invariants and the stress vector from the origin point has a angle of $2a$, twice the angle of the major principal stress s_1 to the vertical direction. Limited DEM results employing this kind of non-proportional loading path have been reported. The numerical drained rotational shear has been investigated in two-dimensional conditions (Li and Yu, 2010) , which uses the same virtual experiment method as it is followed in this research. However, the intermediate principal stress is missing in 2D simulation and it is necessary to conduct the 3D simulations, at least, for confirmation of 2D observations.

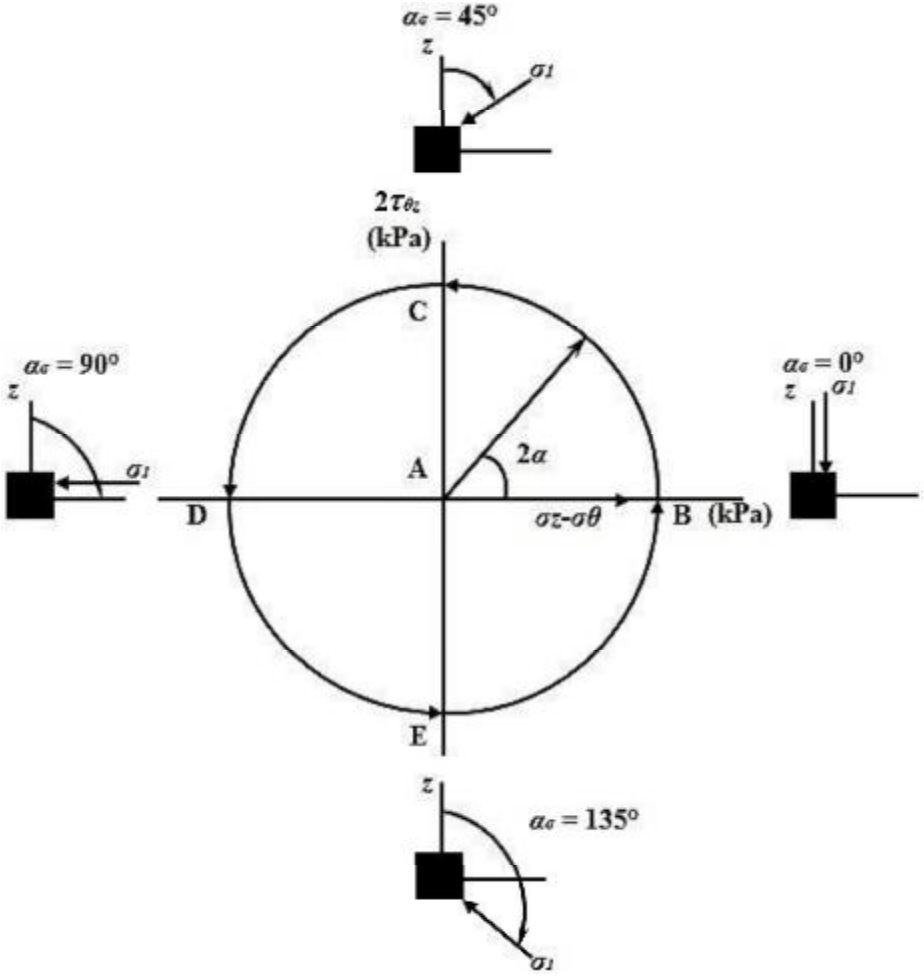

Fig. 4.14 Stress paths in X-Y stress space for rotational shear (after Nakata et al., 1998)

The principal stress rotational shear is purely stress controlled loading path with magnitudes of stress invariants p^t, h^t, b^t constant while the major principal stress directions rotates continuously in the *x*-*z* plane as shown in Fig. 4.15. Meanwhile, the intermediate principal stress direction is fixed along the *y*-axis. The angle a is the target major principal stress direction $\mathbf{n}_1^t$ relative to the positive *z*-axis direction. The target principal stresses direction vectors are expressed in a matrix with the first row and last row corresponding to the major principal stress direction vector and the minor principal stress direction vector:

$$n_{ij}^{s\,t} = \begin{bmatrix} \sin a & 0 & \cos a \\ 0 & 1 & 0 \\ \cos a & 0 & -\sin a \end{bmatrix} \tag{4.3}$$

Then, the target stress tensor s_{ij}^{t} can be calculated from its invariants as introduced in appendix B.3.2. A stress increment tensor Δs_{ij} can then be determined as the difference of the target stress tensor and current stress tensor s_{ij} determined from Eq. (20), $\Delta s_{ij} = s_{ij}^{t} - s_{ij}$. Accordingly, a strain increment tensor Δe_{ij} can be estimated by Eq. (32) in Appendix B.4.2. This strain increment is applied to the sample by specifying translational and rotational velocities of boundary walls according to Eqs. (30) and (31), as shown in appendix B.4.1. As the applied strain increment does not necessarily lead to the required stress increment Δs_{ij}, the servo-control mechanism is employed till the target boundary stress conditions satisfied. After the boundary conditions have been satisfied, an increment of the principal stress direction is applied by specifying $a \leftarrow a + \Delta a$, where the major principal stress direction increment is small $\Delta a = 3^{o} \times 10^{-4}$ in one calculation cycle. By repeat doing so, the continuous principal stress direction rotation can be realised.

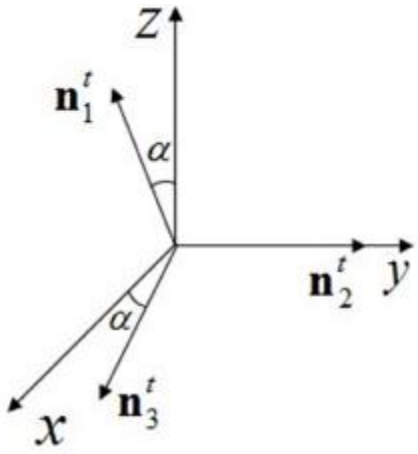

Fig. 4.15 Illustration of principal stress rotation in Cartesian system

Before conducting rotational shearing, the initial sample has to be monotonically sheared to the target boundary stress conditions p^t, h^t, b^t. This drained pre-shearing process keeps constant p, b and fixed major principal stress direction in the vertical *z*-axis. The deviatoric strain e_q increases till the target stress ratio h^t has been reached. The initially isotropic samples SRED_TT and SREL_TT have been pre-sheared to $h = 0.5$ at constant $p = 500kPa, b = 0.5$, to study the effect of void ratio on material behaviour under rotational shear. The response of the samples to the pre-shearing loading path can be found in Fig. 4.13. When pre-sheared to $h = 0.5$, the sample SRED_TT dilates with slightly increasing void ratio and the sample SREL_TT contracts with void ratio decreased. The void ratio of the pre-sheared samples at $h = 0.5$ is summarised in Table 4.4. And the samples are labelled as 'SRED_B05Y05_RS' and 'SRED_B05Y05_RS', referring to the dense and loose samples of spherical particles for rotational shear, respectively. The meaning of those label characters can be found in Appendix C.

Table 4.4 Samples information for rotational shear

Initial sample	Pre-loading		Sample label	Void ratio e_0
SRED_TT	True triaxial ($b = 0.5$)	$h = 0.5$	SRED_B05Y05_RS	0.64
SREL_TT		$h = 0.5$	SREL_B05Y05_RS	0.75

The evolution of stress invariants and principal stress direction during rotational shear is plotted in Fig. 4.16. It can be found that the mean normal stress, deviatoric stress and *b* value have been well kept at constant target values (e.g., Fig. 4.16(a)) and the principal stress direction *a* varies periodically with one cycle

relating to 180º rotation of the major principal stress direction (e.g., Fig. 4.16(b)). Consequently, it shows the desired stress paths have been well maintained during rotational shear.

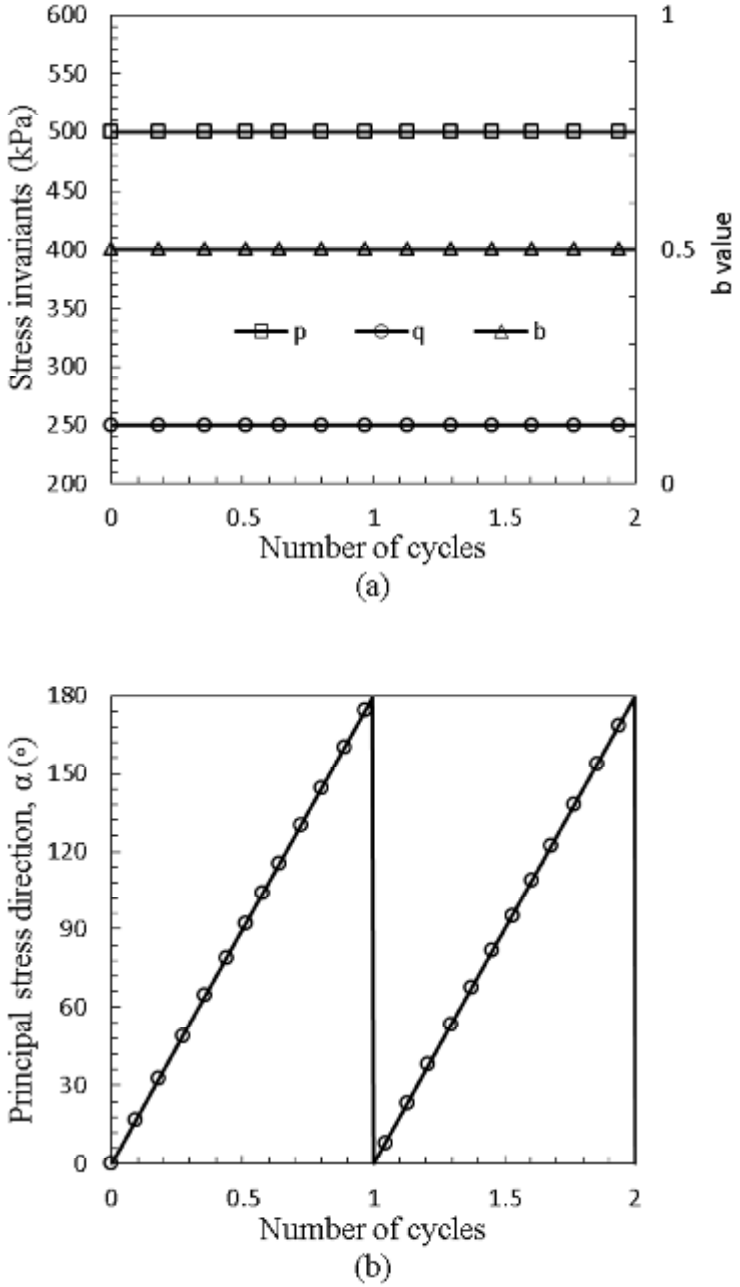

Fig. 4.16 Evolution of stress invariants and principal stress direction during rotational shear

Fig. 4.17(a) plots the variations of stress components of the sample SRED_B05Y05_RS during pure principal stress rotation. It shows that the stress components s_{xx}, s_{zz}, s_{xz} varies periodically. The stress components along the direction of *y*-axis keep constant with $s_{yy} = 500kPa, s_{xy} = s_{yz} = 0$, which demonstrates that the intermediate principal stress direction has been well maintained in the target direction of *y*-axis. The stress trajectory in the deviatoric plane is a circle as shown in Fig. 4.17(b). Similar variations of stress components can be found in a hollow cylinder rotational shear test (Tong et al., 2010, Yang, 2013).

The principal directions of stress and strain increment in the deviatoric plane are illustrated in Fig. 4.18. As the stress path is a circle, the vector connecting from the centre to any point on the circle represents the stress vector. The principal directions of stress vector and strain increment vector are described by the angle a and $g_{\Delta e}$, respectively. For the second order symmetric strain increment tensor Δe_{ij}, which is determined within a small increment of the principal stress direction, i.e., $\Delta a \approx 2^{\circ}$, the principal direction vector $\mathbf{n}_{\Delta e}$ of the strain increment tensor can be calculated as introduced in appendix B.3.1. Then the angle $g_{\Delta e}$ of the principal strain increment direction vector $\mathbf{n}_{\Delta e}$ relative to the vertical *z*-axis can be determined as:

$$g_{\Delta e} = \mathbf{tan}^{-1}\left(\frac{n_x}{n_z}\right) \tag{4.4}$$

where n_x, n_z are the components of the vector $\mathbf{n}_{\Delta e}$.

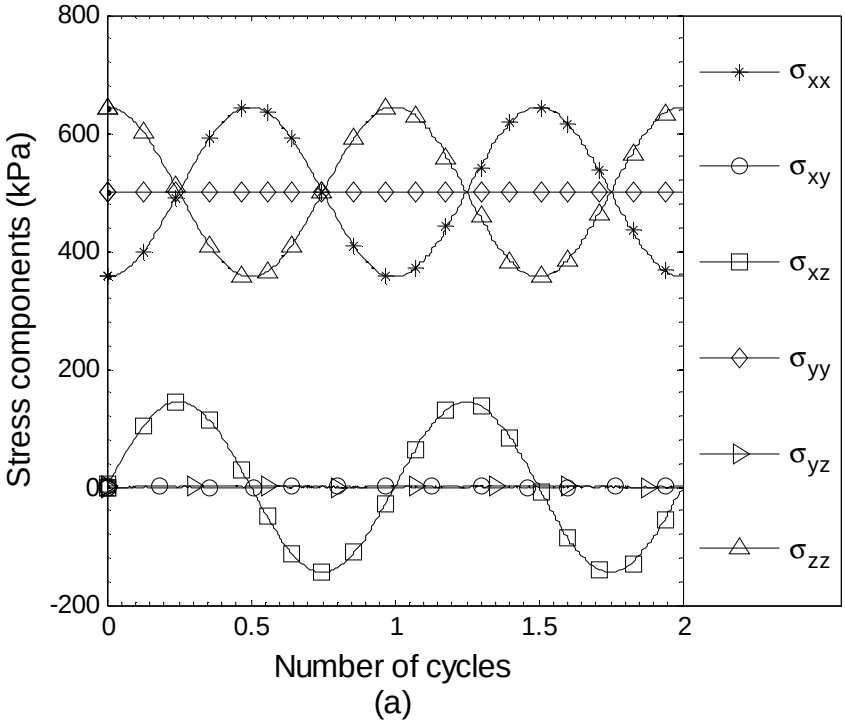

(a)

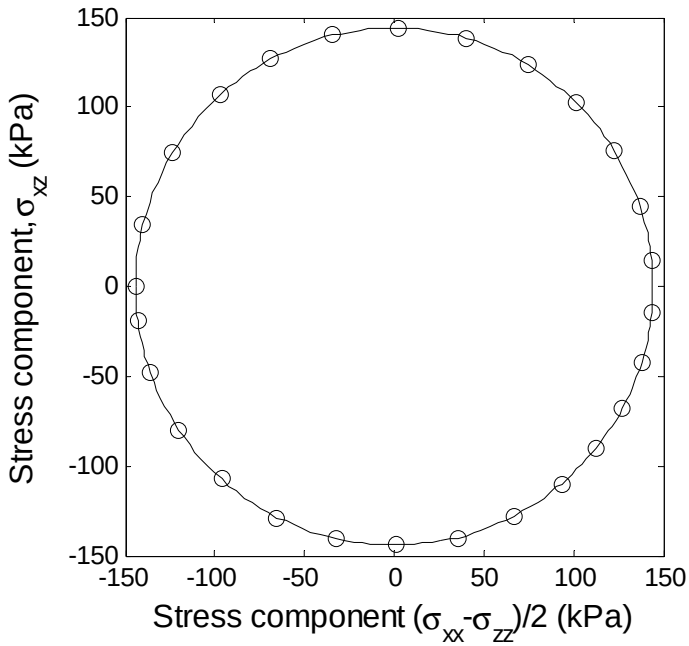

(b)

Fig. 4.17 Stress path in rotational shear (a) variation of stress components (b) stress trajectory

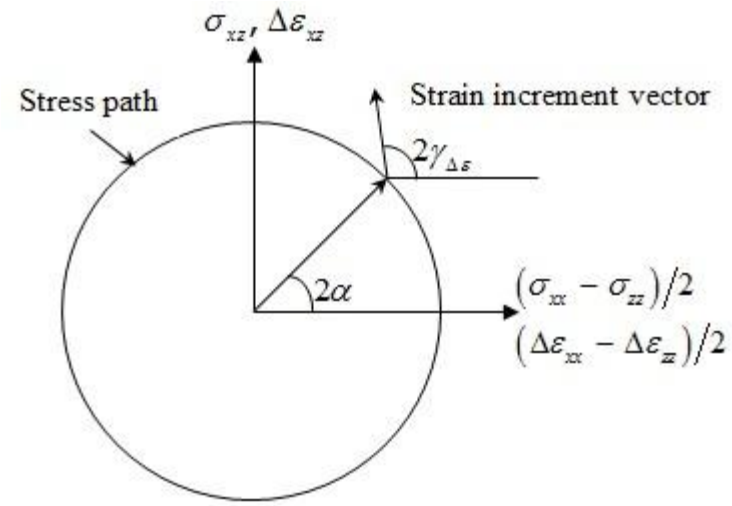

Fig. 4.18 Illustration of principal directions

4.4.3.2 Material response

Fig. 4.19 shows the strain trajectory of dense sample SRED_B05Y05_RS and loose sample SREL_B05Y05_RS in rotational shear under constant stress invariants $p = 500kPa, b = 0.5, h = 0.5$. Significant deformation can be observed on two samples, even though the magnitudes of stress invariants are kept constant. This is qualitatively consistent to the laboratory observations on sand response to rotational shear (Miura et al., 1986, Nakata et al., 1998, Tong et al., 2010). It is observed that, unlike the circle of stress trajectory, the strain paths are spiral. The size of the circular strain path becomes smaller with increasing number of cycles for loose sample. After a large number of cycles, the strain paths stabilise to be a circle. The difference of strain trajectory for dense and loose samples is that the size of the strain path is larger for sample SREL_B05Y05_RS in the first few cycles. This is consistent with the two-dimensional DEM observations on the effect of void ratio on size of strain trajectory under rotational shear (Li and Yu, 2010).

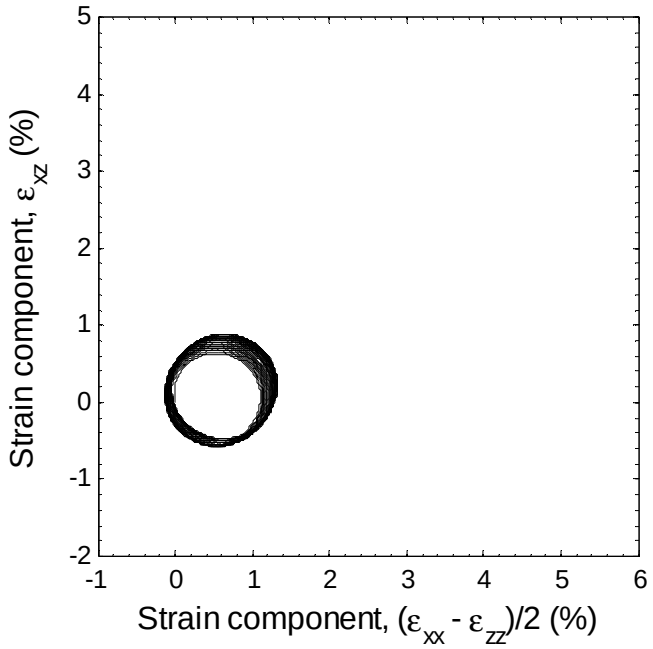
Strain component, ε_{xz} (%)
Strain component, $(\varepsilon_{xx} - \varepsilon_{zz})/2$ (%)

(a)

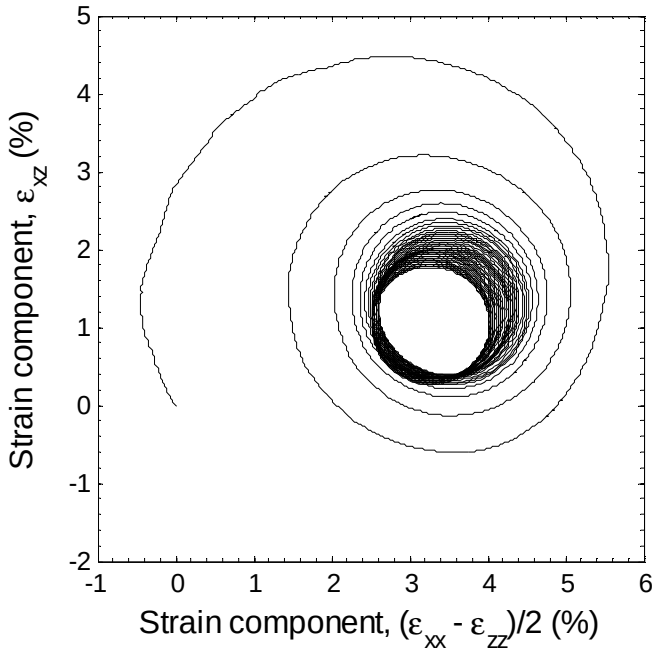
Strain component, ε_{xz} (%)
Strain component, $(\varepsilon_{xx} - \varepsilon_{zz})/2$ (%)

(b)

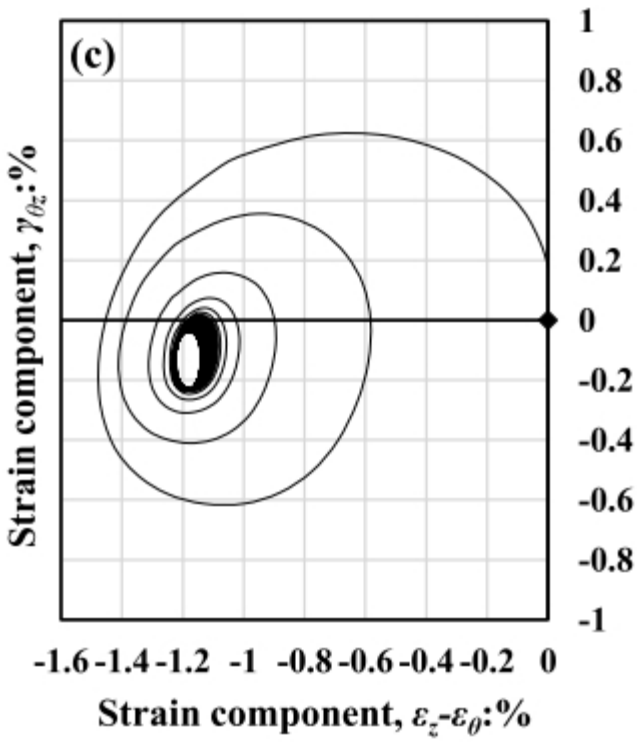

Fig. 4.19 Strain trajectory in deviatoric plane (a) dense sample SRED_B05Y05_RS (b) loose sample SREL_B05Y05_RS (c) experimental results in hollow cylinder test (after Yang, 2013)

Though the intermediate stress is kept constant, both the magnitude and principal direction, significant intermediate strain e_{yy} has been generated for both samples during rotational shear as shown in Fig. 4.20. The positive strain e_{yy} indicates contraction along the *y*-direction in order to maintain constant intermediate stress. The strain e_{yy} is much larger in the loose sample than that in the dense sample. The intermediate strain contraction is reported as positive radial strain generated in laboratory drained hollow cylinder test (Yang, 2013).

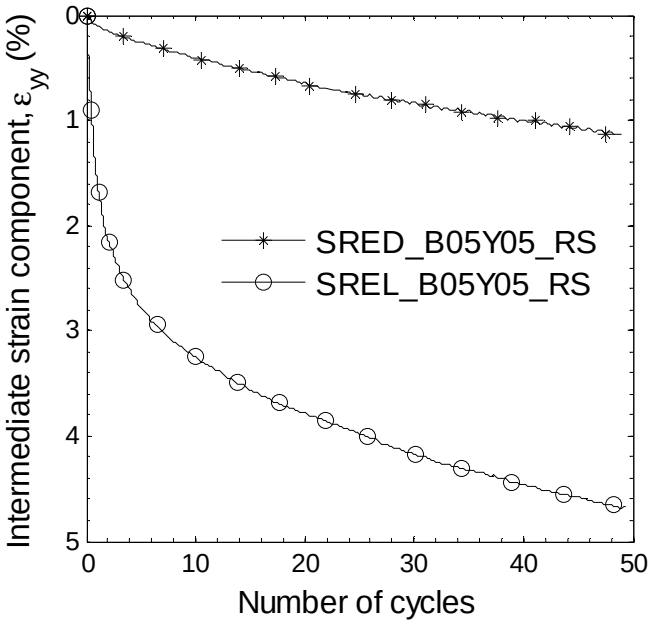

Fig. 4.20 Intermediate strain response

The volume change behaviour is presented in Fig. 4.21 in terms of void ratio variation. The increase of void ratio refers to volume dilation and decrease of void ratio indicates volumetric contraction. It can be seen that the void ratio of dense sample remains constant during rotational shear. For the loose sample, however, the void ratio decreases significantly with increasing number of cycles. And most of volume contraction is generated in the first few cycles. It is interesting to observe that the materials approach the same ultimate state to achieve similar void ratio under rotational shear, irrespective of initial void ratios. This confirms the 2D DEM results of the same ultimate void ratio obtained in rotational shear (Li and Yu, 2010).

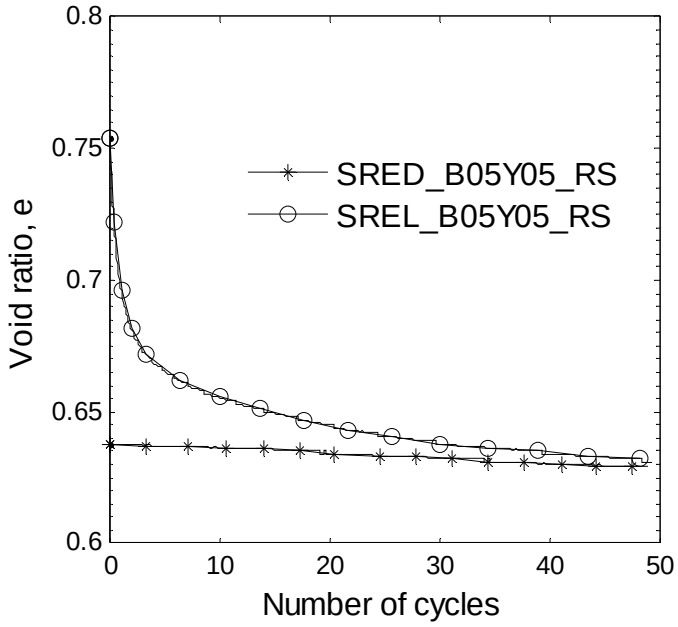

Fig. 4.21 Evolution of void ratio during rotational shear

The degree of non-coaxiality between the major principal stress direction and the major principal strain increment direction is plotted in Fig. 4.22. The total strain increment $d\varepsilon_{ij}$ is obtained within a small increment of stress direction with $\Delta a \approx 1^{o}$. The strain increment direction angle $g_{\Delta e}$ is determined according to Eq. (4.4). It is clear from the figure that the degree of non-coaxiality $g_{\Delta e} - a$ generally decreases slightly for the dense sample and it increases in the first a few number of cycles for the loose sample. It shows that the degree of non-coaxiality is slightly larger in the dense sample than in the loose sample while the gap becomes smaller with increasing number of cycles. This is similar to the 2D DEM observations (Li and Yu, 2010). The non-coaxial behaviour has also been observed on sand materials under rotational shear (Miura et al., 1986, Gutierrez et al., 1991).

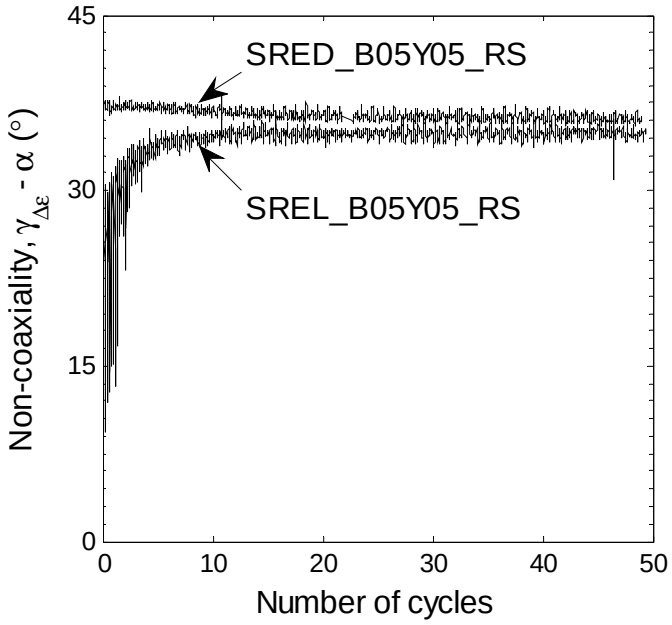

Fig. 4.22 Non-coaxiality between the principal stress and the principal strain increment direction

4.5 Summary

This chapter presents a standard numerical technique to conduct virtual experiments on the elementary behaviour of granular materials using the discrete element method (DEM). Various loading paths can be applied using the proposed numerical model. In particular, the importance of accurate volume measurement and control on the test material behaviour has been emphasized. The error in evaluating the volumetric strain by summing up the normal components of the engineering strain could be significant, which would lead to dramatic change in pore water pressure under undrained conditions. Hence, the adoption of finite strain definition and evaluating volumetric strain based on the Jacobian determinant are necessary. The Cauchy stress and the Biot strain have been used to characterise the stress and strain state of the sample. Based on the assumption of a uniform field, their

expressions in terms of the particle interactions with the boundary walls and the relative displacements between the boundaries vertices have been derived and provided as Eqs. (20) and (21).

The numerical technique applies loading on a granular assembly through boundary consisting of rigid mass-less walls. It is suggested that the boundary walls form a polyhedral shape with the angle between two neighbouring walls being obtuse to enhance sample uniformity. Such a loading application scheme is inherently strain-controlled. In the simulation of the material elementary behaviour, the boundary motions are monitored in synchronized way. Strain-controlled boundary is achieved by directly specifying the translational and rotational velocities of the walls. A servo-control mechanism of stress boundary conditions is developed and can be combined with strain boundary conditions to achieve mixed loading conditions. The developed numerical technique is advantageous in applying general loading paths and various loading conditions, including fully strain controlled, fully stress controlled and partially strain controlled and partially stress controlled. Loading paths are described in terms of the changes in the invariants and the principal directions of the stress and strain tensors.

The proposed algorithm has been implemented in three-dimensional discrete element codes. The results of numerical simulations of undrained simple shear, true triaxial simulation and rotational shear, typical loading paths in laboratory tests, have been presented. The observation on the principal stress rotation in simple shear and the significant volume contraction and deformation non-coaxiality during continuous major principal stress rotation are in qualitative accordance with the laboratory

findings over various sand. This qualitatively supports the application of the discrete element method (DEM) and confirms the capability of the developed numerical technique as a useful tool to facilitate multi-scale investigations on the constitutive theories of granular materials.

Chapter 5 Influence of intermediate principal stress on granular material behaviour

5.1 Introduction

In engineering practice, the magnitudes of three principal stresses are generally non-equal ($s_1 \geq s_2 \geq s_3$). The relative magnitude of the intermediate principal stress s_2 plays significant influence on strength of granular material. This chapter simulates the behaviour of initially isotropic samples, eliminating the effects of initial anisotropy in a real laboratory test. Spherical particles are used in this chapter. Special focus is placed on the influence of $b = (s_2 - s_3)/(s_1 - s_3)$ value on the strength characteristics of granular material.

Based on the macro-micro relation, the stress tensor is defined on the micro-scale contact force vectors and branch vectors, as shown in Eq. (2.17). The distribution of contact force vector and contact normal vector at discrete contact points can be statistically characterised by directional tensors. In this chapter, the microscopic information on internal structure and particle interaction are characterised by the second-order contact normal fabric tensor D_{ij}, normal contact

force tensor G_{ij}^{n} and tangential contact force tensor G_{ij}^{t}, which is informative sufficiently for micro-scale analysis without considering higher-order (e.g., fourth-order) tensors. The microstructural tensors are calculated from the average of discrete vectors at contacts. More details on the tensors determination can be found in Section 2.4. Together with the stress-force-fabric relationships in Eq. (2.18), the macroscopic strength-deformation characteristics will be explained in terms of the microscopic observations.

5.2 Numerical samples and test procedures

5.2.1 Testing materials

In numerical simulations, the samples consist of rigid spherical particles, of which radius is randomly distributed within $\left[0.3, 0.5\right] mm$. The solid particle density is selected to be $r = 2700\, kg/m^3$. The linear contact model is used to describe the local contact behaviour. The particle-wall properties and parameters for the contact model are summarised in detail in Table 4.1. The initially isotropic samples with three varying initial void ratios were prepared by the radius expansion method, which was introduced in detail in Section 4.3.1. The same samples have been used for numerical simulation as presented in Section 4.4. The initial samples information can be found in Table 4.2.

5.2.2 Simulation procedures

The drained true triaxial loading path keeps stress invariants p, b and principal stress directions $\mathbf{n}_i^s$ unchanged while deviatoric strain e_q continuously increases. It is mixed controlled boundary in mimicing the laboratory true triaxial test. More numerical implementation details have been introduced in Section 4.4.2. In this chapter, the true triaxial simulations keep constant $p = 500kPa$. The b value is constant in individual simulation. The major principal stress direction is fixed along the vertical *z*-axis and the intermediate principal stress direction is fixed along the *y*-axis.

The drained triaxial compression ($b = 0$) tests have been carried out in three samples to investigate the influence of initial void ratios on material behaviour. The true triaxial simulation results presented in Section 4.4.2 corresponds to $b = 0.5$. The samples SRED_TT and SREL_TT are also tested undergoing true triaxial shearing paths ($0 \le b \le 1$) to investigate the effect of b value on granular material behaviour with varying b value from 0 to 1 with 0.2 intervals. The numerical simulation plan is shown in Table 5.1.

Table 5.1 True triaxial simulations plan on initially isotropic samples

True triaxial simulations	Initial isotropic sample of spherical particles ($p = 500kPa$)		
	SRED_TT	SREM_TT	SREL_TT
b value	$0 \le b \le 1$, 0.2 interval	$b = 0$	$0 \le b \le 1$, 0.2 interval

5.3 Effect of void ratio on material response

5.3.1 Drained material behaviour

The drained triaxial compression simulations have been carried out on three samples of various initial void ratios. The stress-strain behaviour of initially isotropic samples is plotted in Fig. 5.1(a). The strain hardening behaviour has been observed in the dense sample SRED_TT, with a peak stress ratio obtained and followed by strain softening behaviour. The stress ratio increases quickly and then remains constant for the medium sample SREM_TT. The loose sample SREL_TT exhibits continuous strain hardening behaviour. Upon the same shearing strain, e.g., $e_q = 3\%$, a higher stress ratio is observed in sample with smaller initial void ratio, indicating the material performing stronger at a lower initial void ratio. At large shear strain level with e_q up to 40%, the stress ratio reaches the same values for all the three samples and remains constant for further shearing, which is termed as critical stress ratio $h_c = 0.79$ according to the critical state soil mechanics definition.

The corresponding volumetric strain behaviour is shown in Fig. 5.1(b). It can be seen that the dense sample dilates with negative volumetric strain and the loose sample contracts with positive volumetric strain while the volume change of medium sample is close to zero. This clearly shows the effect of void ratio on granular material dilatancy behaviour. At large shear strain, the volumetric strains continue to be steady for all three samples as the material approaches the critical state, where the critical void ratio $e_c = 0.74$ is achieved as shown in Fig. 5.1(c), irrespective of

initial void ratios. Similar observations of the void ratio on sand responses have also been reported by Verdugo and Ishihara (1996).

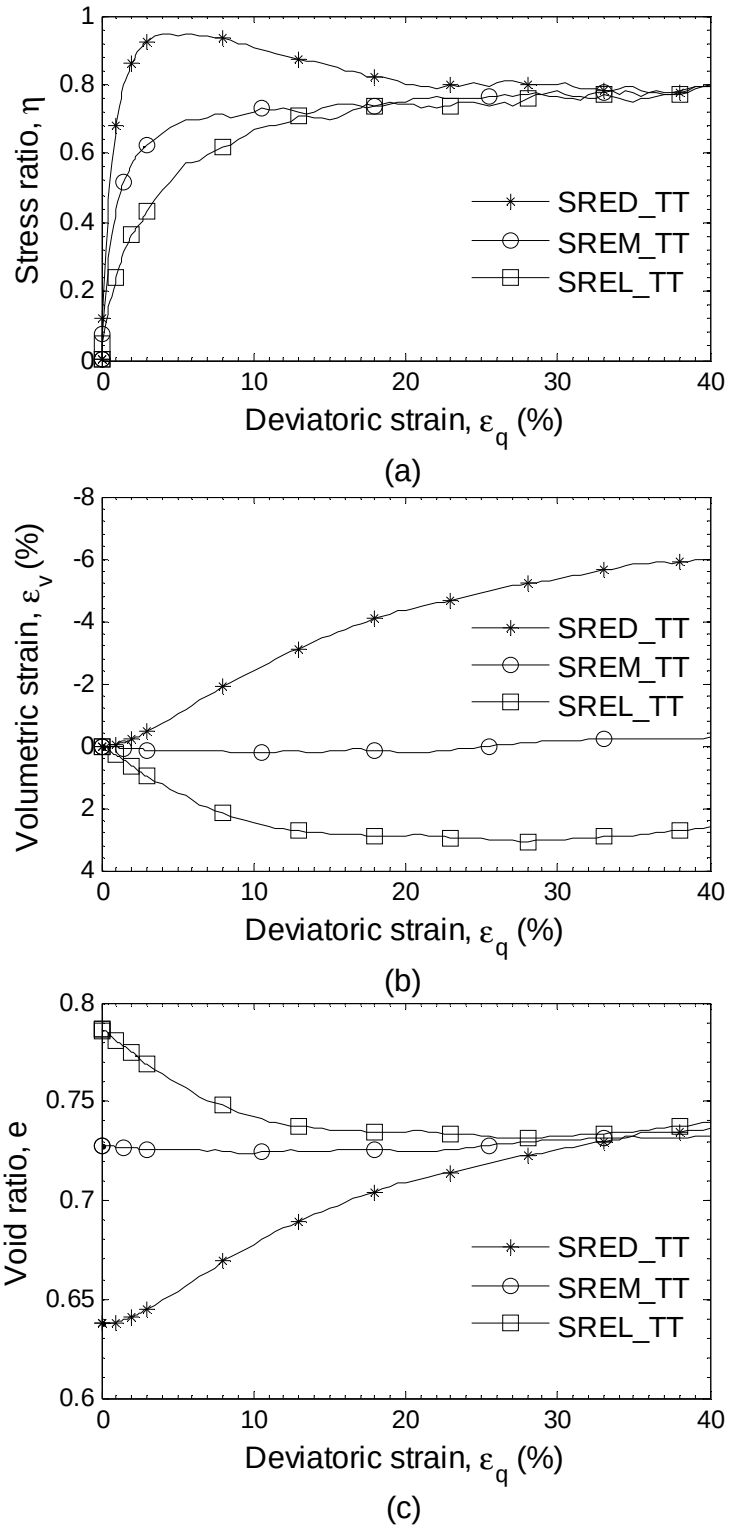

Fig. 5.1 Effects of initial void ratio on initial isotropic samples behaviours

5.3.2 Micro-scale observations

5.3.2.1 Contact normal evolution

The coordination number w is defined as the average number of contacts per particle possessing within the sample as shown in Eq. (2.2). It is related to the macroscopic material initial void ratio, with higher w value corresponding to a smaller initial void ratio. Fig. 5.2 shows the evolution of the coordination number against shearing. Initially, the sample with smaller void ratio has a greater coordination number, referring to a particle in sample with smaller void ratio gaining more contacts support from its neighbouring particles. It is obvious that the coordination number decreases quickly to the constant value for the dense and medium samples, corresponding to large dilation of samples with increasing void ratio. It increases slightly and remains steady for the loose sample, corresponding to the decrease of initial void ratio with volume contraction. At large deformation, all three samples possess the same coordination number, $w = 4.5$. Thornton (2000) has reported similar observations on the coordination number evolution in samples with various void ratios, where the material reached the constant $w = 5.2$ under asymmetric triaxial compression. The slightly larger coordination number is probably due to the more uniform distributed spherical particle diameter in Thornton's simulation and his numerical sample has a much smaller void ratio. The decrease of coordination number is due to the larger rate of contact disruption than the rate of contact creation (Kuhn, 2010, Kruyt, 2012). The contact disruption rate decreases rapidly against shearing till it becomes equal to the rate of contact creation. Accordingly, the coordination number remains steady.

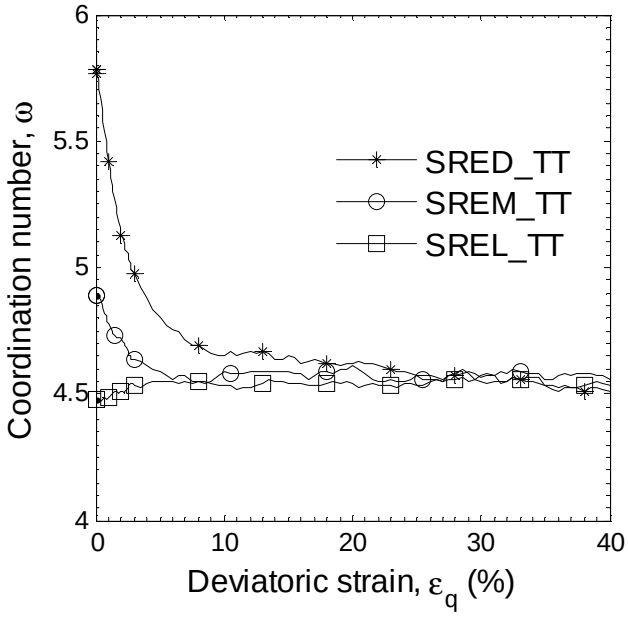

Fig. 5.2 Effect of void ratio on coordination number during triaxial compression

The deviatoric fabric tensor D_{ij} is used to characterise the directional distribution of contact normal vectors and the material internal structure anisotropy is defined as $D_F = \sqrt{3D_{ij}D_{ij}/2}$. The relative magnitude of three principal fabric values is described by $b_F = \left(D_2 - D_3\right)/\left(D_1 - D_3\right)$, where D_1, D_2, D_3 are the major, intermediate and minor principal fabric. Fig. 5.3(a) demonstrates the effect of initial void ratio on fabric anisotropy evolution during shearing. Before shearing, the deviator fabric anisotropy D_F is close to zero as expected for initially isotropic samples. As shearing occurs, the external loading induce anisotropic internal structure developed, with more contacts oriented in the major principal stress direction owing to more contacts disrupted in minor stress directions (Kruyt, 2012). Hence, the fabric tensor becomes anisotropic with the deviatoric invariant $D_F > 0$. The deviator fabric increases fastest in the dense sample to the peak and is then followed by slight decreasing. The deviator fabric increases gradually with a

decreasing rate in the medium and loose samples. The deviator fabric is slightly larger in the sample of medium void ratio than that in the loose sample at small strain, e.g., $e_q < 10\%$. At large strain levels, the deviator fabric is observed to be similar among all the three samples, which may be considered as critical fabric anisotropy, $D_c = 0.6$. Accordingly, the critical stress ratio is achieved. Similar results can also be found in literatures (Thornton, 2000, Kruyt, 2012). During asymmetric triaxial compression, the internal structure is also found to be asymmetric with isotropic fabric distribution in the horizontal direction. This is termed as the intermediate fabric ratio b_F close to zero as shown in Fig. 5.3(b).

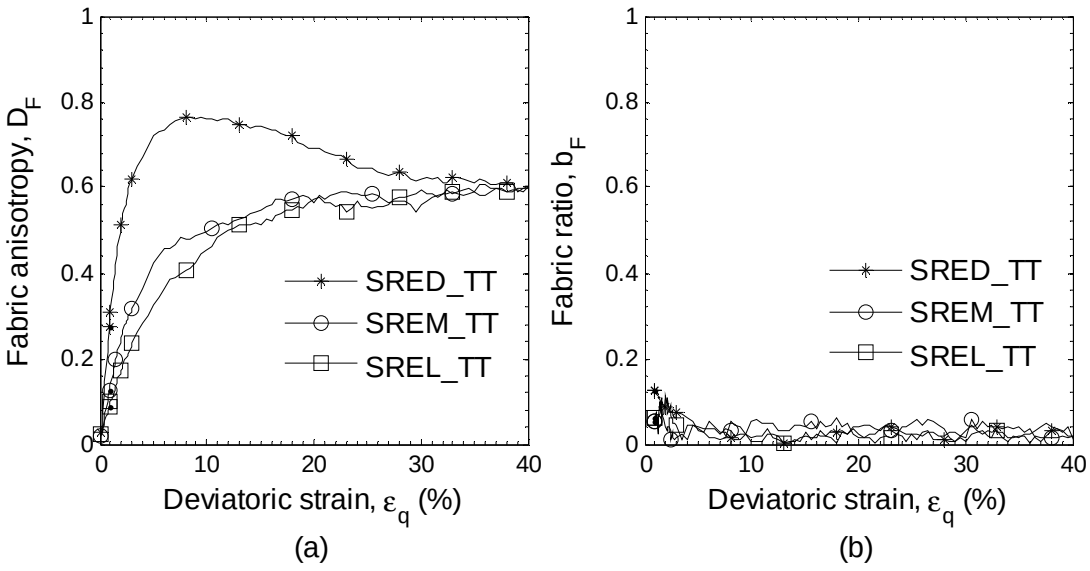

Fig. 5.3 Effects of initial void ratio on fabric evolution in triaxial compression

The internal principal fabric direction is determined by the angle of the principal fabric direction vector relative to the vertical *z*-axis as $g_F = \arccos(n_z)$, where n_z is the component of the unit direction vector. The evolution of principal fabric direction is shown in Fig. 5.4. It is clear that the angle g_F is close to 0^o,

indicating the principal fabric direction being coaxial with the major principal stress direction in the vertical axis.

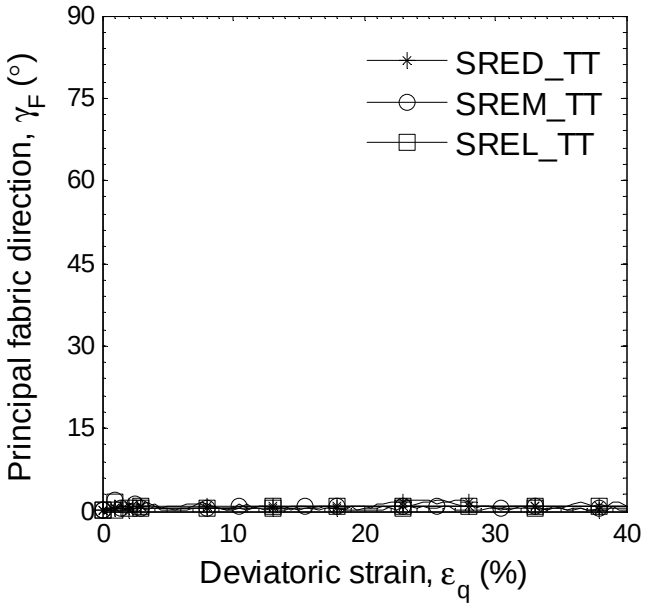

Fig. 5.4 Evolution of principal fabric direction during triaxial compression

5.3.2.2 Contact forces evolution

The evolution of mean normal force f_0, which has been defined in Eq. (2.9), is presented in Fig. 5.5. Before shearing, the samples are isotropic. The material mean normal stress can be expressed as microscopic parameters as $p = w f_0 l_0 / 3$ by simplifying the SFF relations in Eq. (2.18). As three samples have the same mean normal stress and particle size distribution (i.e., identical l_0), the initial mean normal force f_0 is inversely proportional to the coordination number w. This is observed as a smaller value of initial f_0 in samples of smaller void ratio, corresponding to the larger coordination number (e.g., Fig. 5.2). At larger deformation, the mean normal force reaches the same value, irrespective of initial void ratio.

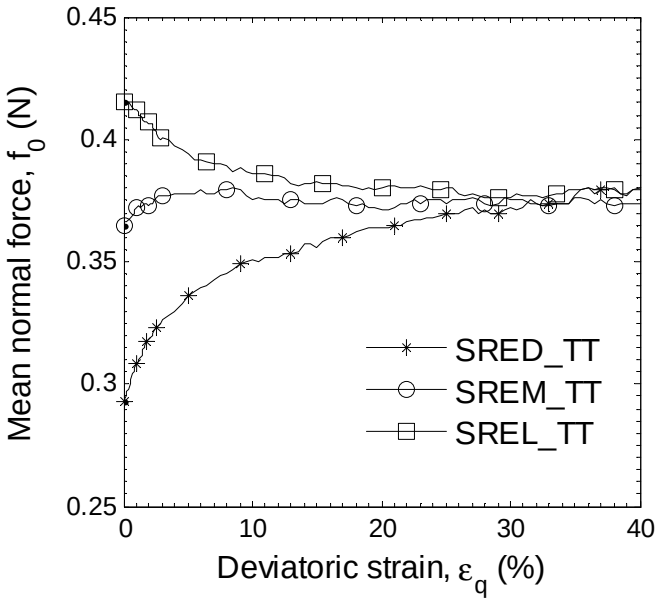

Fig. 5.5 Mean normal contact force evolution

Against deviatoric loading, the contact force distribution becomes anisotropic in the sample. The deviatoric contact forces tensors G_{ij}^n and G_{ij}^t are used to characterise the microstructural discrete normal contact force and tangential contact vector, respectively (more detail in Eqs. (2.12) and (2.13)). The anisotropic contact force distribution is described by the invariants $G_d^n = \sqrt{3G_{ij}^n G_{ij}^n / 2}$ and $G_d^t = \sqrt{3G_{ij}^t G_{ij}^t / 2}$. Fig. 5.6 demonstrates the evolution of normal contact force anisotropy G_d^n and tangential contact force anisotropy G_d^t. For the dense sample SRED_TT, the deviator contact forces anisotropy G_d^n and G_d^t reach peak value rapidly as $G_d^n = 1.27$ and $G_d^t = 0.4$ at $e_q = 3\%$ with strong force chains build up. It is then followed by a quick decrease as shearing continues to its ultimate steady value due to buckling of strong force chains, corresponding to strain softening behaviour. For the medium sample SREM_TT, G_d^n and G_d^t increases to its

maximum value as $G_d^n = 0.93$ and $G_d^t = 0.22$ at $e_q \approx 4\%$, which, however, is smaller than that observed in the dense sample. For the loose sample SREL_TT, the contact force anisotropy parameters G_d^n and G_d^t increase gradually to the steady value at large deformation. At large deformations, where the critical stress ratio is obtained, the values of G_d^n and G_d^t are observed to be similar in three samples, regardless of initial void ratios. This value may be considered as critical contact force anisotropy $G_d^n = 1.1$, $G_d^t = 0.24$. In addition, it is shown that the normal contact force anisotropy G_d^n is nearly four times larger than that of the tangential contact force anisotropy G_d^t for the same sample during shearing, indicating the normal contact force anisotropy is the major contribution to contact force anisotropy. This is confirmed by Thornton and Antony (1998), where the stress tensor was found to be the major contribution of normal contact force.

The intermediate force ratio is defined as $b_n = \left(G_2^n - G_3^n\right) \Big/ \left(G_1^n - G_3^n\right)$ and $b_t = \left(G_2^t - G_3^t\right) \Big/ \left(G_1^t - G_3^t\right)$, where G_i^n and G_i^t ($i = 1, 2, 3$) represent the major, intermediate and minor principal values of normal contact force and tangential contact force, respectively. The evolution of intermediate force ratio is plotted in Fig. 5.7. It can be seen that both b_n and b_t remains zero during shearing, which demonstrates that the contact forces distribution is isotropic in horizontal direction.

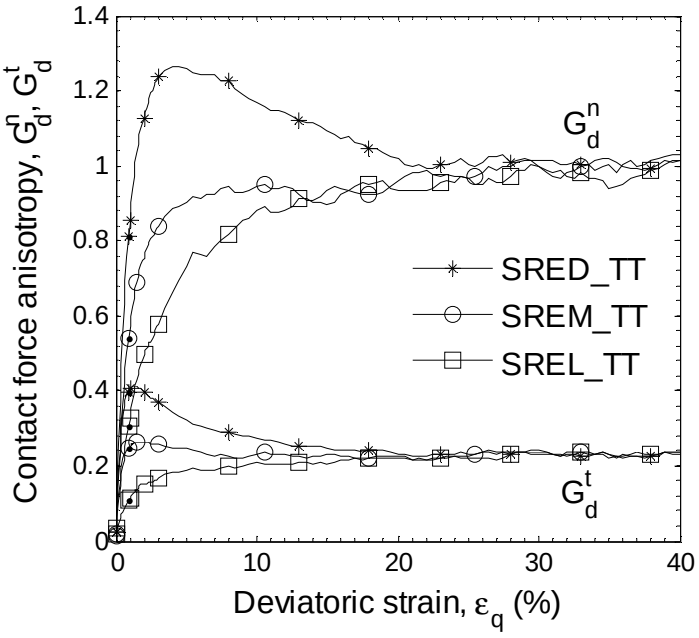

Fig. 5.6 Effect of initial void ratio on evolution of contact force anisotropy

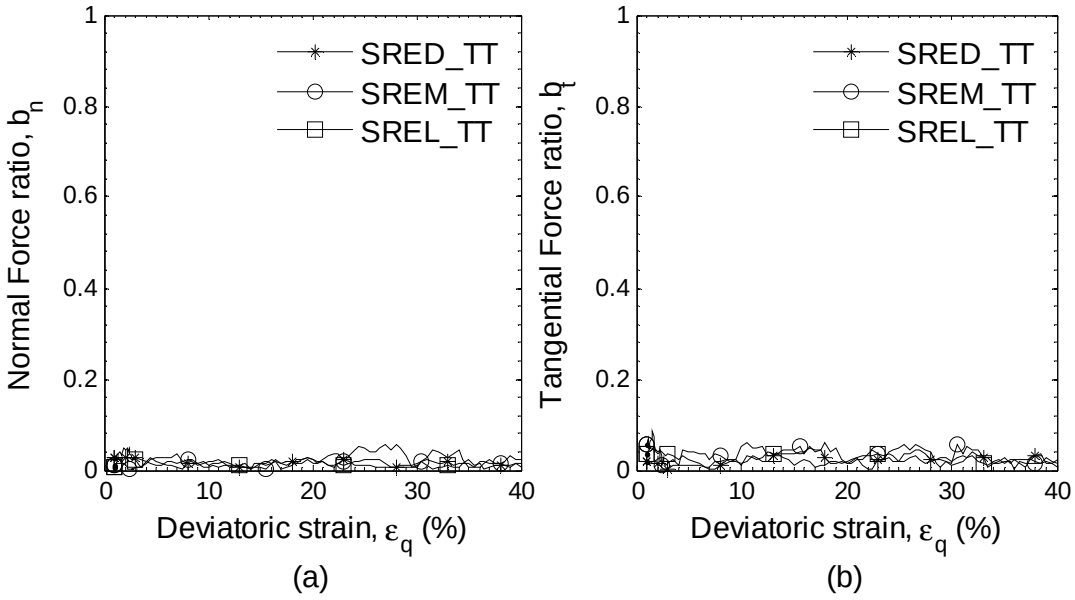

Fig. 5.7 Evolution of intermediate principal force ratio

5.3.2.3 Observations on the strong and weak force chains

In deviatoric shearing, the contact force transmission via interparticle contacts within the granular assembly is not distributed uniformly. Experimental

photoelastic study showed that the external load was carried by heavily stressed chains of particles with contact forces above average contact force and the rest particles were slightly loaded (Drescher and Jong, 1972, Oda and Konishi, 1974, Majmudar and Behringer, 2005). The contact force network was partitioned into two: the column network of strong force chains, contact force larger than average value $f/\langle f \rangle > 1$, forms in the direction of major principal stress and the weak force network; and the weak force chains, contact force below average value $f/\langle f \rangle \leq 1$, provides support to the strong force chains in lateral direction (Radjai et al., 1997, Azéma and Radjaï, 2012). Thornton and Antony (1998) found that the deviatoric stress was mainly contributed by contacts with $f/\langle f \rangle > 1$ while contacts with $f/\langle f \rangle \leq 1$ mainly contributed to mean normal stress and the contribution to deviator stress was negligible.

Fig. 5.8(a) shows the evolution of strong normal contact force anisotropy and weak normal contact force anisotropy, which is calculated from the discrete contact force vector using Eq. (2.7) with summation only on contacts with $f^n/\langle f^n \rangle > 1$ and $f^n/\langle f^n \rangle \leq 1$, respectively. It can be seen that the strong force distribution G_s^n is highly anisotropic while the weak force anisotropy G_w^n is quite small, correlating to the significantly anisotropic fabric structure D_F^s in contacts with $f^n/\langle f^n \rangle > 1$ (i.e., Fig. 5.8(b)) and negligible fabric anisotropy D_F^w in weak contacts (e.g., $f^n/\langle f^n \rangle \leq 1$). This indicates that the anisotropic stress is mainly carried by the anisotropic strong force chains, supported by the nearly isotropic weak force chains.

The sample of a smaller void ratio develops more anisotropic strong force chain network and fabric anisotropy. At large deformation, however, it reaches the same degree of anisotropy, irrespective of initial void ratios.

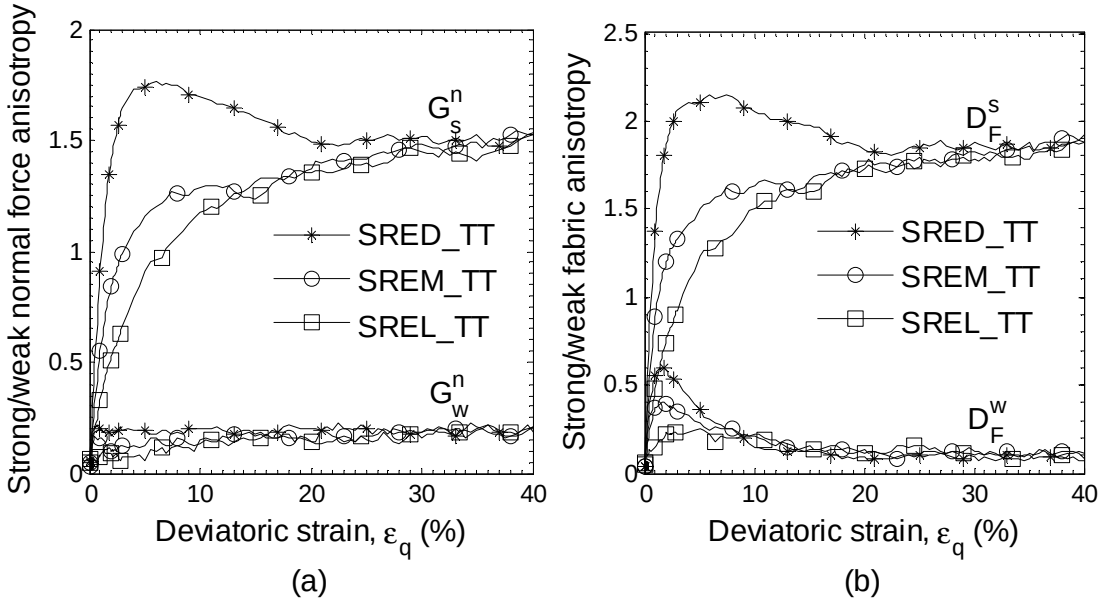

Fig. 5.8 Microstructural evolution, (a) strong and weak normal contact force anisotropy (b) strong and weak fabric anisotropy

5.3.2.4 Stress-force-fabric relations in triaxial loading

Under triaxial compression loading, and the material microstructure is transversely isotropic, the principal directions of microstructrual tensors are coaxial with the external loading direction. The anisotropic tensors can be represented by one variable characterising its anisotropy degree. For example, the fabric tensor D_{ij} can be expressed as:

$$D_{ij} = \begin{bmatrix} -D_F/3 & 0 & 0 \\ 0 & -D_F/3 & 0 \\ 0 & 0 & 2D_F/3 \end{bmatrix} \tag{5.1}$$

Hence, the stress ratio h can be expressed in the following simplified form using the stress-force-fabric relations in Eq. (2.18):

$$h = \frac{2}{5}\left(D_F + G_d^n + C_d^n\right) + \frac{3}{5}\left(G_d^t + C_d^t\right) \tag{5.2}$$

where C_d^n and C_d^n are the normal and tangential branch vectors anisotropy due to non-uniform particle size distribution, which is negligible and ignored in this study.

It is clear from Eq. (5.2) that the stress ratio capacity in samples with different initial void ratios is strongly dependent on the microscopic quantities G_d^n, G_d^t and D_F. For the sample with a smaller void ratio, it has larger G_d^n, G_d^t and D_F before reaching the critical values, resulting in higher stress ratio in the sample of smaller void ratio at the same shear strain. At the large deformation level, all the microscopic parameters approach similar critical values. Hence, the critical stress ratio is achieved, irrespective of initial void ratios. The strain hardening or strain softening behaviour against shearing is dominated by the formation of anisotropic contact force chains or buckling of force chains, particularly the normal contact force.

5.4 Effect of *b* value on material response

The true triaxial loading path is illustrated in Fig. 5.9. Fig. 5.9(a) denotes the triaxial compression test ($b = 0$) with the intermediate principal stress s_2 equal to the minor principal stress s_3. Fig. 5.9(c) denotes the triaxial extension test ($b = 1$) with the major principal stress s_1 equal to the intermediate principal stress s_2. Otherwise, it denotes the true triaxial tests ($0 < b < 1$) with independent control of three principal stresses as shown in Fig. 5.9(b). The monotonic shearing keeps stress

invariants p, b and principal stress directions n_i^s constant while the deviatoric strain e_q increases continuously (e.g., Fig. 5.9(d)).

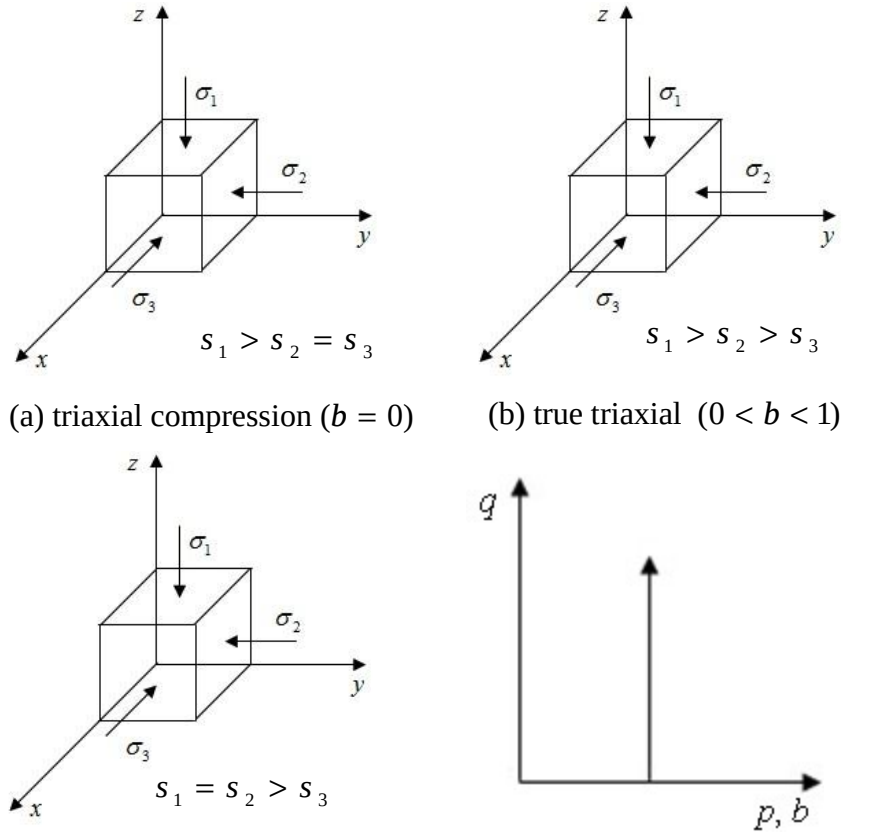

(a) triaxial compression ($b = 0$) (b) true triaxial ($0 < b < 1$)

(c) triaxial extension ($b = 1$) (d) constant p,b loading path

Fig. 5.9 Illustration of drained true triaxial loading paths

5.4.1 Macro-scale material response

Fig. 5.10(a) and Fig. 5.11(a) show the stress-strain behaviour for the dense sample SRED_TT and the loose sample SREL_TT under true triaxial simulations. It can be seen that the dense sample reaches the peak stress ratios in simulations with different b values, followed by strain softening to critical stress ratios. The loose sample shows continuous strain hardening with decreasing rate to critical stress

ratios. Up to the same deviatoric strain, a lower stress ratio is observed in simulation with greater b value for both samples.

The influence of b values on the volumetric strain responses is shown in Fig. 5.10(b) and Fig. 5.11(b). The dense sample starts to dilate at the beginning of shearing and the loose sample tends to contract during shearing. More dilative behaviour is observed at a greater b value, though the variation is small. At large deformation, the increment rate of volumetric strain becomes small and the volumetric strain approaches a steady value, where the critical state may be considered to be achieved. Similar experimental investigations on effects of b value on sand behaviour have been reported for dense samples in the literature (Sutherland and Mesdary, 1969, Lade and Duncan, 1973, Ochiai and Lade, 1983). However, the sand samples prepared in a laboratory were initially anisotropic. The test results may be affected not only by the b value but also by the material anisotropy.

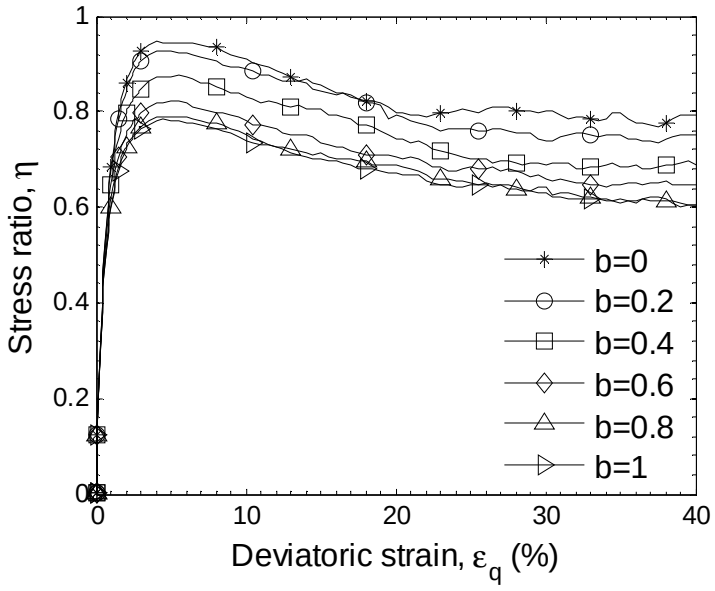

(a)

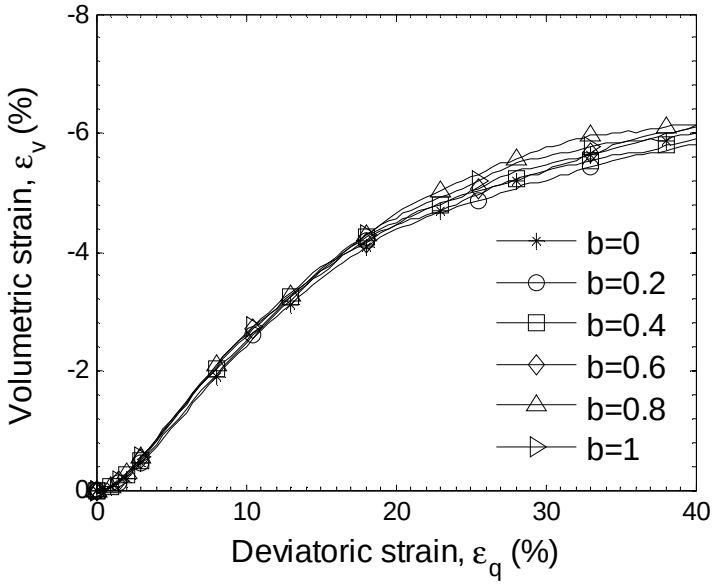

(b)

Fig. 5.10 Effects of b value on response of isotropic dense sample SRED_TT (a) stress-strain relations (b) volume change behaviour

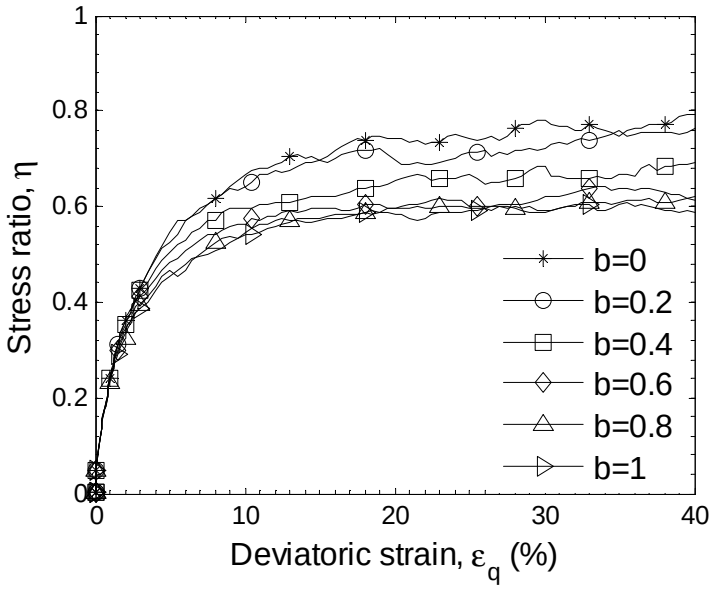

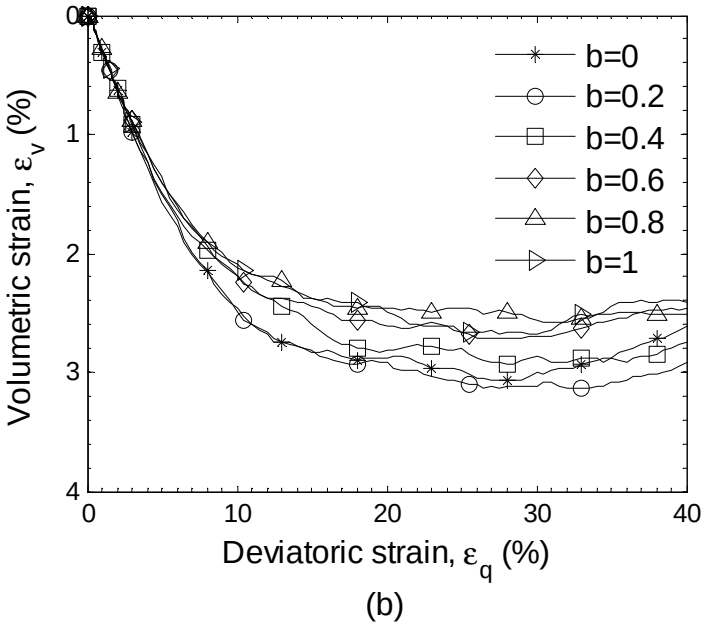

Fig. 5.11 Effects of b value on response of isotropic loose sample SREL_TT (a) stress-strain behaviour (b) volume change behaviour

The response of the intermediate strain increment ratio $b_{\Delta e} = \left(\Delta e_2 - \Delta e_3\right)/\left(\Delta e_1 - \Delta e_3\right)$, where $\Delta e_1, \Delta e_2, \Delta e_3$ are the principal values of total strain increment δ_{ij}, is shown in Fig. 5.12 with five different deviatoric strain

levels, which represent the regions of elastic, pre-failure, failure, post-failure and critical state, respectively. The strain increment is obtained within a small deviatoric strain increment (e.g., $d\varepsilon_q = 0.1\%$ when $e_q \leq 3\%$ and $d\varepsilon_q = 0.5\%$ when $e_q > 3\%$). It is observed that $b_{\Delta e}$ generally keeps constant and is close to intermediate stress ratio b values, in asymmetric loading conditions ($b = 0$ and $b = 1$) for both samples. For simulations of the dense sample with $0 < b < 1$, the value of $b_{\Delta e}$ is larger than the intermediate stress ratio b during shearing, where the dashed line describes the equality of $b_{\Delta e}$ and b. The deviation is larger in the middle range of b values. And the value of $b_{\Delta e}$ increases slightly at a greater shear strain e_q in constant b simulation. Similar observations have also been reported in DEM simulations (Thornton and Zhang, 2010).

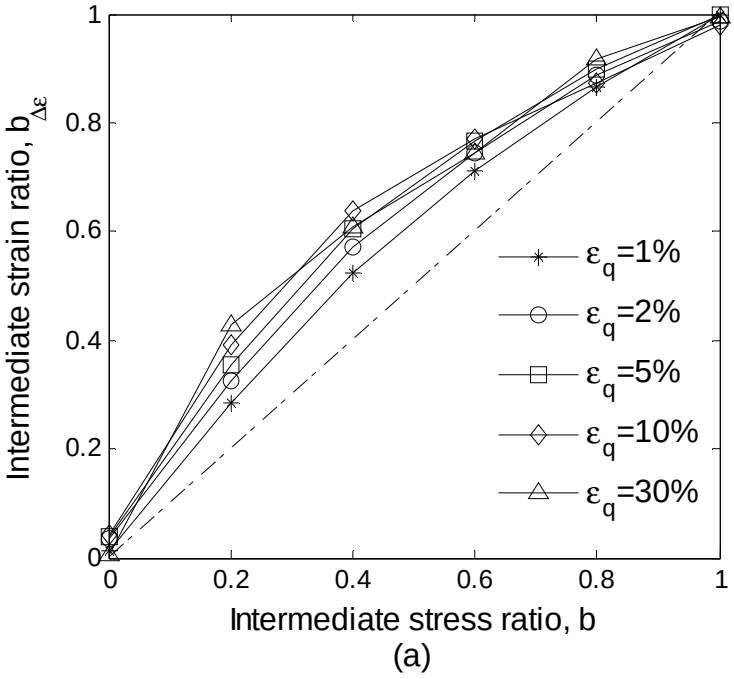

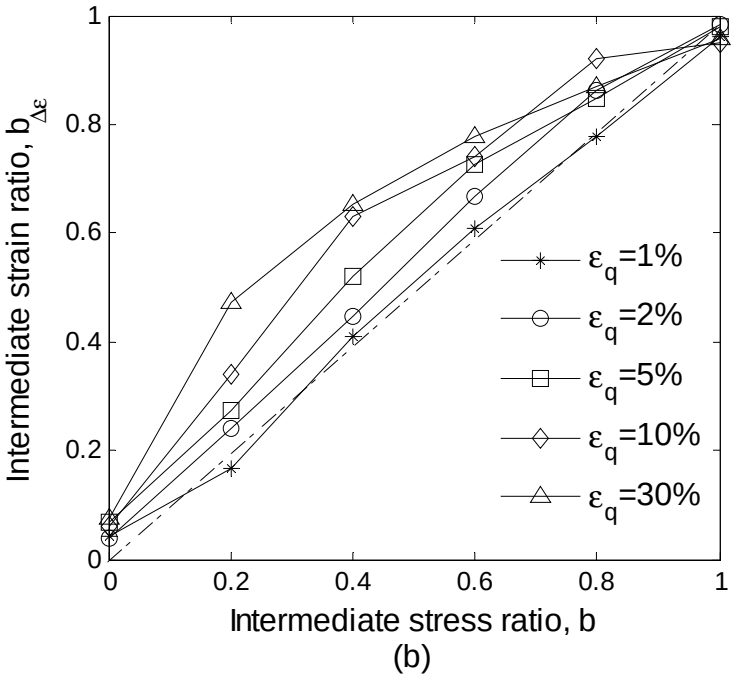

Fig. 5.12 Relationship between intermediate stress ratio b and intermediate strain rate ratio $b_{\Delta e}$ (a) dense sample SRED_TT (b) loose sample SREL_TT

5.4.2 Micro-scale observations

5.4.2.1 Evolution of internal structure

Fig. 5.13 shows the evolution of coordination number w during true triaxial tests for dense and loose samples. It can be seen that the dense sample SRED_TT initially has a larger coordination number $w = 5.8$ than that of loose sample SREL_TT with $w = 4.5$. As shearing occurs, the w value decreases quickly for the dense sample owing to contact disruption while it increases slightly for the loose sample due to contact creation during the initial 5% deviatoric strain. As shearing continues, the coordination number does not change significantly due to the same rate of contact disruption and contact creation. It can be seen that the influence of the b value on the evolution of w is negligible. The ultimate coordination number is approximately $w = 4.5$ for both dense and loose samples.

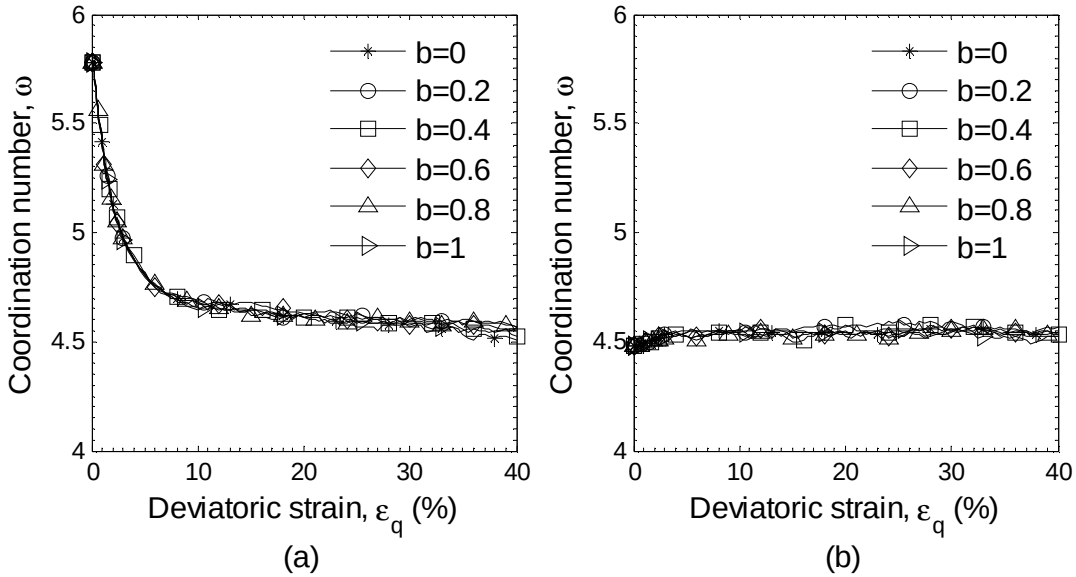

Fig. 5.13 Effect of *b* value on coordination number evolution during true triaxial shearing (a) dense sample SRED_TT (b) loose sample SREL_TT

The influences of b values on the evolution of fabric anisotropy D_F are plotted in Fig. 5.14. For initially isotropic dense sample SRED_TT, Fig. 5.14(a) shows that a higher peak deviator fabric is achieved with greater b value, which shows a reverse trend of the effects of b on the stress-strain behaviour as shown in Fig. 5.10. The deviator fabric decreases gradually at post-peak shearing with different b values. At large deformation, the values of deviator fabric are nearly constant but differ from each other at different b values. This is consistent with the DEM results of larger fabric anisotropy at greater b_e value in the dense sample reported by Thornton and Zhang (2010).

The influence of b values on the evolutions of deviator fabric is not significant for the loose sample SREL_TT, as shown in Fig. 5.14(b). The deviator fabric increases continuously with a decreasing rate to its ultimate values. At large shear strain, e.g., $e_q = 40\%$, the values of D_F do not change significantly as shearing continues and the critical fabric anisotropy D_c is considered to be obtained. The variations of D_c are quite small for various b values. However, it may be summarised that D_c generally decreases with an increasing b value as shown in Fig. 5.15, where D_c is the average value of D_F in the last 5% of deviatoric strain. For simulations with the same b value, the same D_c is reached in both samples, irrespective of initial void ratios.

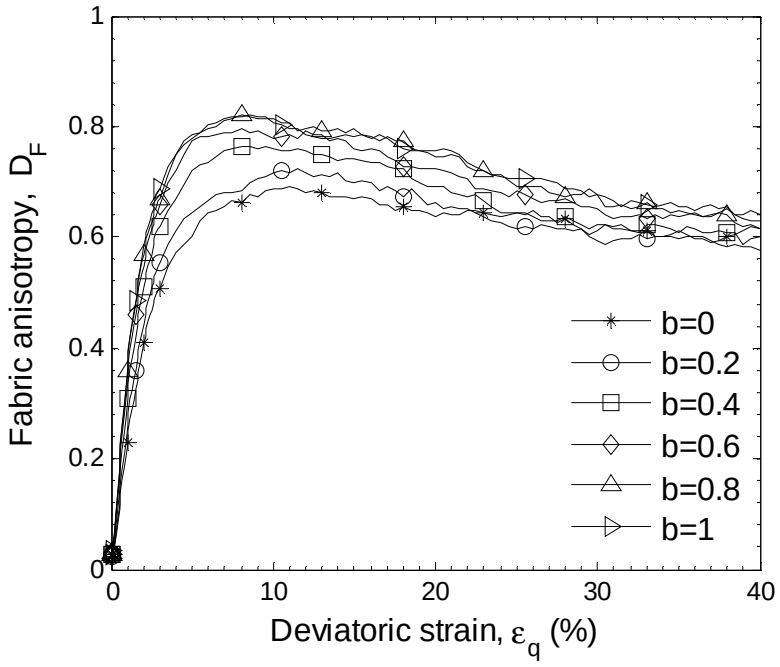

(a)

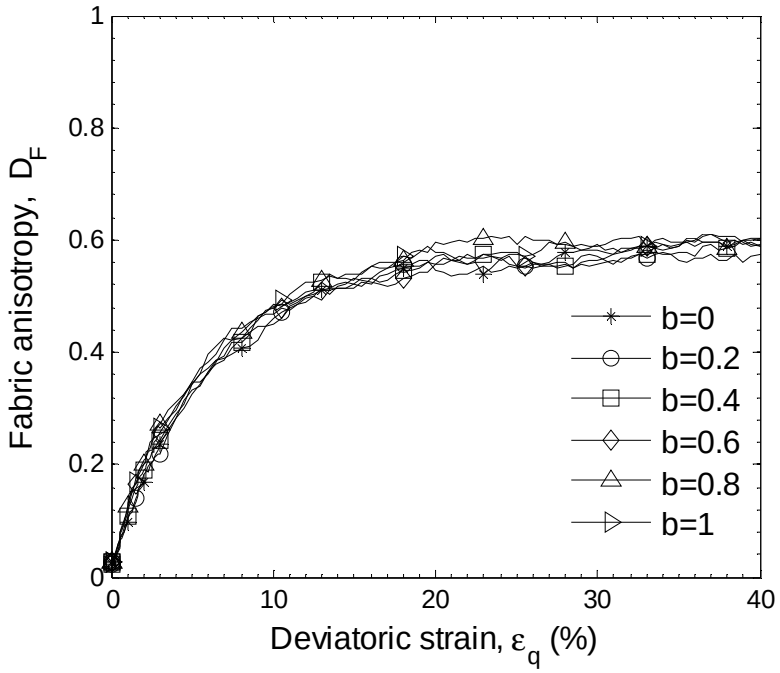

(b)

Fig. 5.14 Effect of *b* value on fabric anisotropy (a) dense sample SRED_TT (b) loose sample SREL_TT

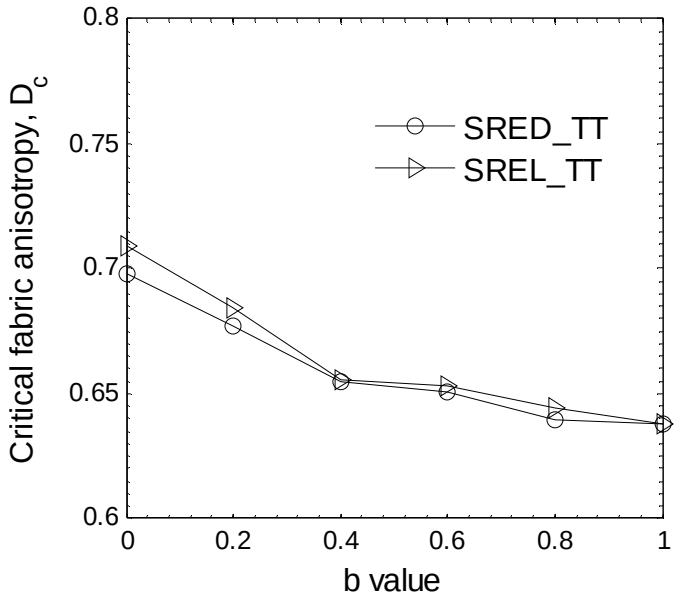

Fig. 5.15 Effect of *b* value on critical fabric anisotropy

Fig. 5.16 illustrates the evolution of intermediate fabric ratio b_F for dense and loose samples at different deviatoric strain levels. The dashed line describes the linear equality between b_F and b . In the triaxial compression and extension simulations ($b = 0$ and $b = 1$), the intermediate fabric ratio b_F is generally close to the intermediate stress ratio b for both samples. In simulations with other b values ($0 < b < 1$), however, b_F is larger than b at various deviatoric strain levels for both samples and b_F is nearly constant after 10% of deviatoric strain. The large deviation of b_F from b at smaller deviatoric strain $e_q \leq 2\%$ is probably due to the fabric anisotropy being small, as shown in Fig. 5.14, where b_F is quite sensitive.

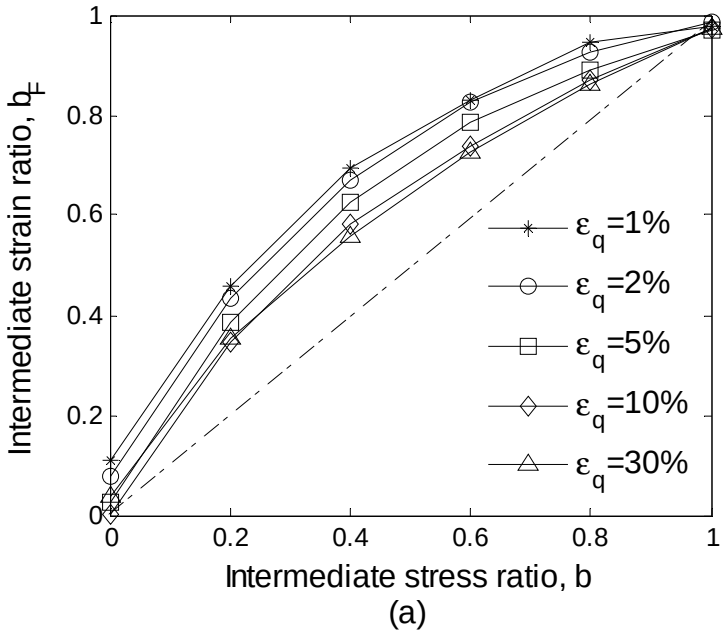

Fig. 5.16 Effects of *b* value on intermediate fabric ratio (a) dense sample SRED_TT (b) loose sample SREL_TT

Fig. 5.17 gives the evolution of principal fabric direction in simulations with various b values of dense and loose samples. The angle g_F is defined as the major principal fabric direction relative to the vertical axis. It clearly shows that the angle

g_F is close to zero during shearing for various b values, which indicates the major principal contact fabric direction is coaxial with the applied major principal stress direction in the vertical *z*-axis.

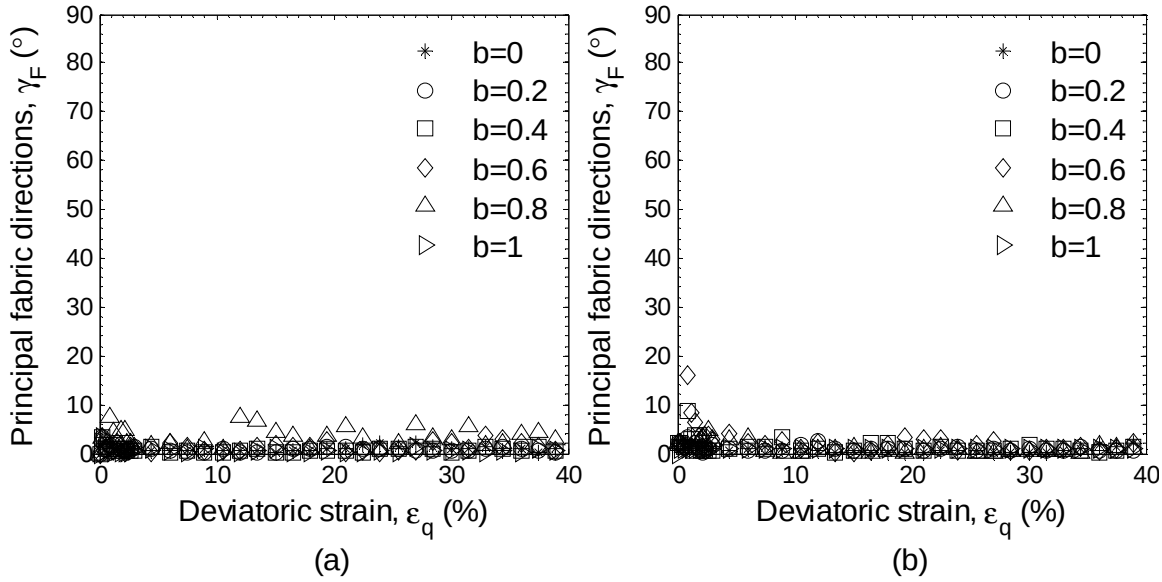

Fig. 5.17 Evolution of principal fabric direction (a) dense sample SRED_TT (b) loose sample SREL_TT

5.4.2.2 Evolution of contact force

Fig. 5.18 shows the effects of b value on the evolution of mean normal force f_0 under constant mean normal stress simulations. Against shearing, the mean normal force f_0 increases to constant value at large deformation in the dense sample and it decreases slightly to be steady for the loose sample. At the same deviatoric strain, it shows negligible effect of b value on f_0 in both samples, correlated with little difference of coordination number (e.g., Fig. 5.13) at various b value simulations.

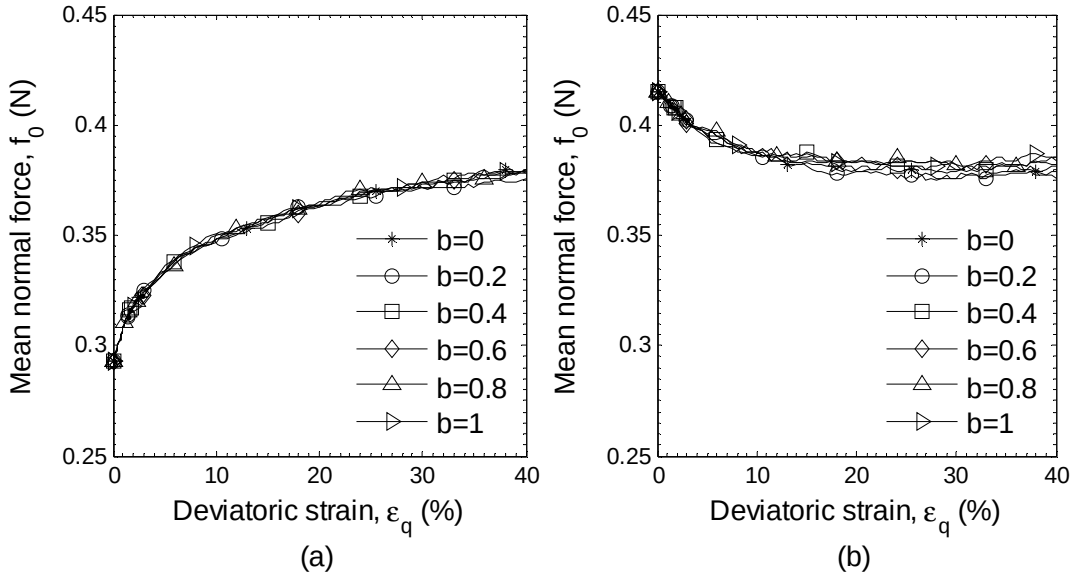

Fig. 5.18 Effects of *b* value on mean normal force evolution (a) dense sample SRED_TT (b) loose sample SREL_TT

The influence of b values on the evolution of contact force anisotropy is shown in Fig. 5.19. Higher normal contact force anisotropy G_d^n and tangential contact force anisotropy G_d^t are observed in simulation at smaller b value in both samples, resulting in a greater stress ratio at lower b value. This is more obvious when $b \leq 0.6$ and the difference is small for $b = 0.8$ and $b = 1$. The variation of G_d^n is larger than that of G_d^t at different b values. Additionally, the normal contact force anisotropy G_d^n is much larger that the tangential contact force anisotropy G_d^t, indicating more contribution to deviator stress from G_d^n than that from G_d^t.

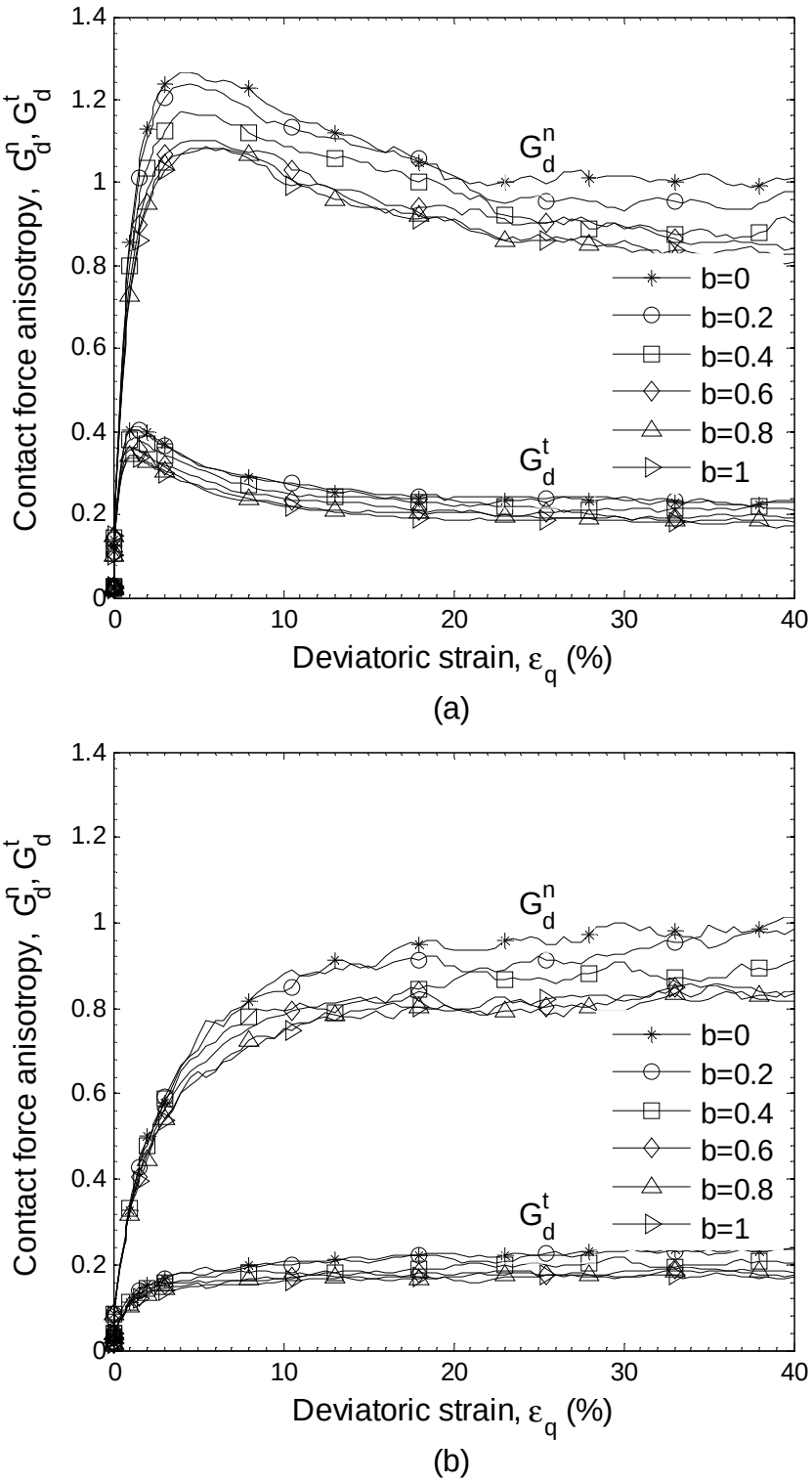

Fig. 5.19 Effects of *b* value on normal and tangential contact force anisotropy (a) dense sample SRED_TT (b) loose sample SREL_TT

The evolution of the intermediate normal contact force ratio b_n and intermediate tangential contact force ratio b_t are presented in Fig. 5.20 for the dense sample and Fig. 5.21 for the loose sample. It can be seen that b_n is generally close to the intermediate stress ratio b for both samples. However, the tangential force ratio b_t is found to be smaller than the intermediate stress ratio b.

The principal directions of normal and tangential contact forces are shown in Fig. 5.22 for the dense sample and Fig. 5.23 for the loose sample. g_n and g_t are the relative angles of the major principal normal contact force direction vector and the principal tangential contact force direction vector to the positive *z*-axis, respectively. It can be seen that the angles of g_n and g_t are close to zero in simulations of both samples with various b values, which implies that the principal contact force directions are coaxial with the external applied loading direction.

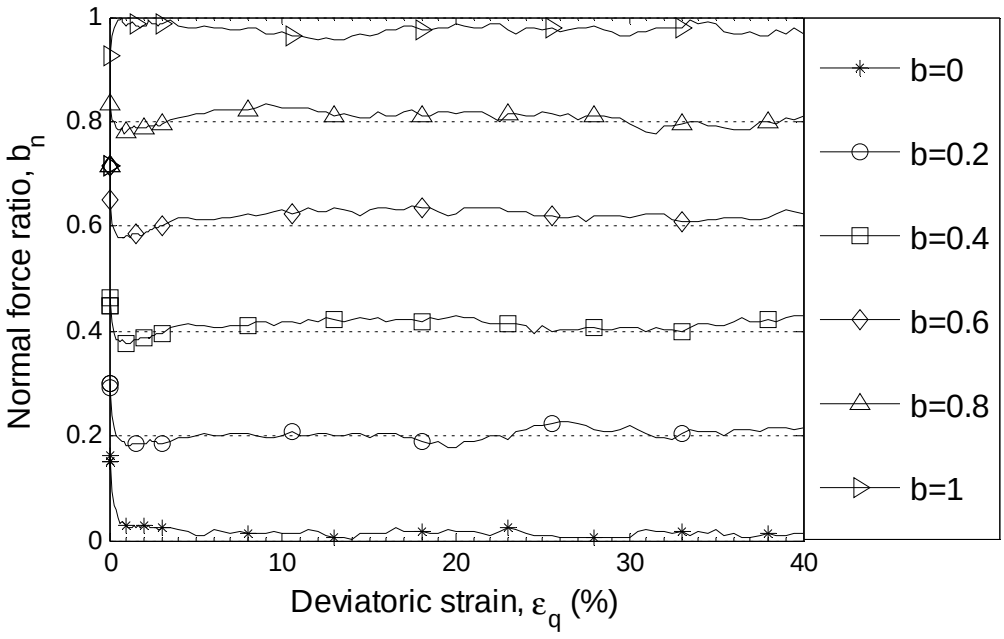

(a)

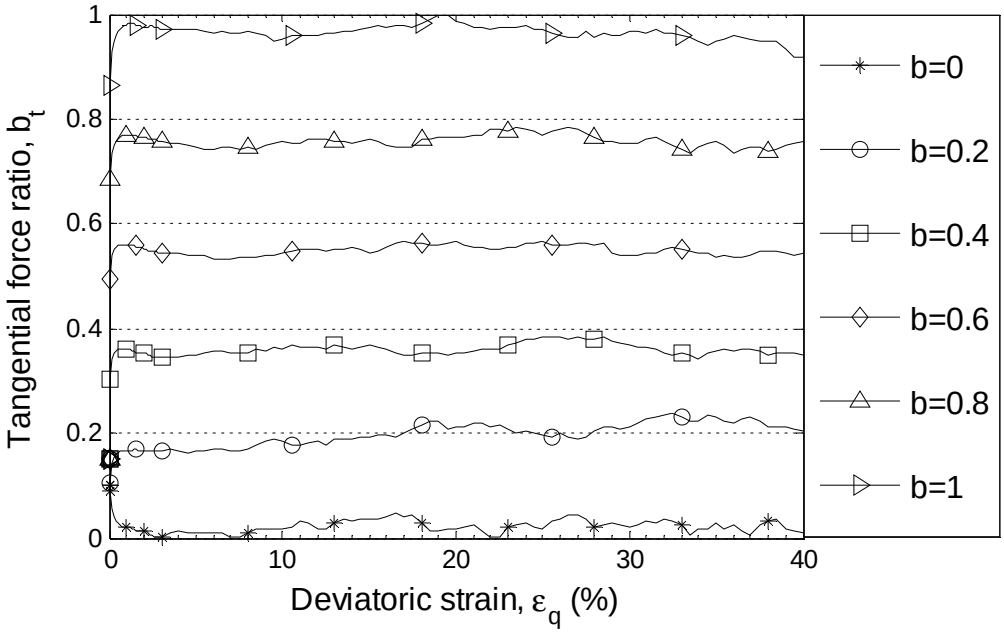

(b)

Fig. 5.20 Effects of *b* value on intermediate contact force ratio in dense sample SRED_TT (a) normal force ratio b_n (b) tangential force ratio b_t

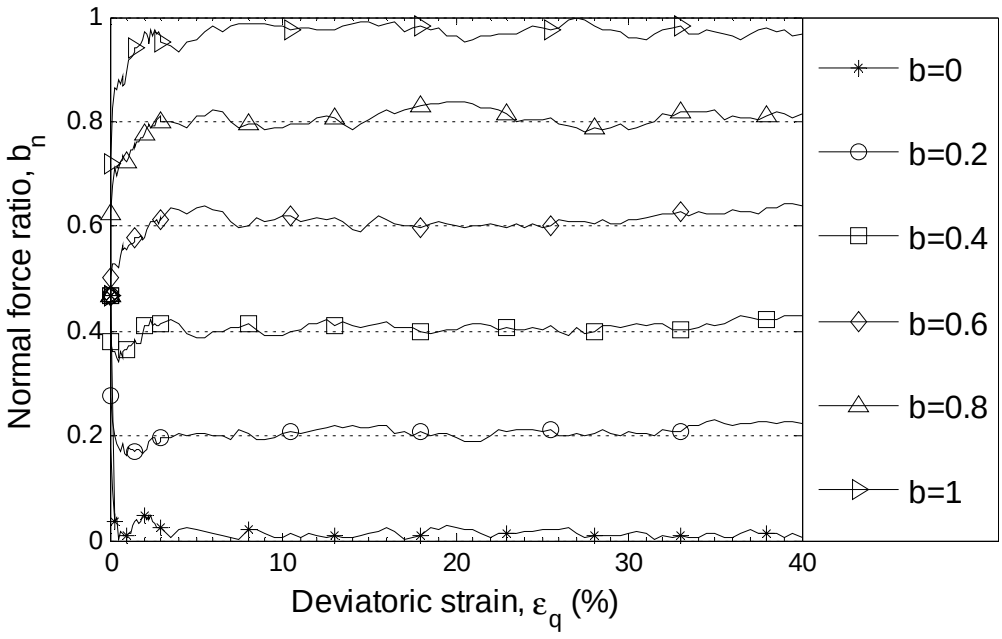

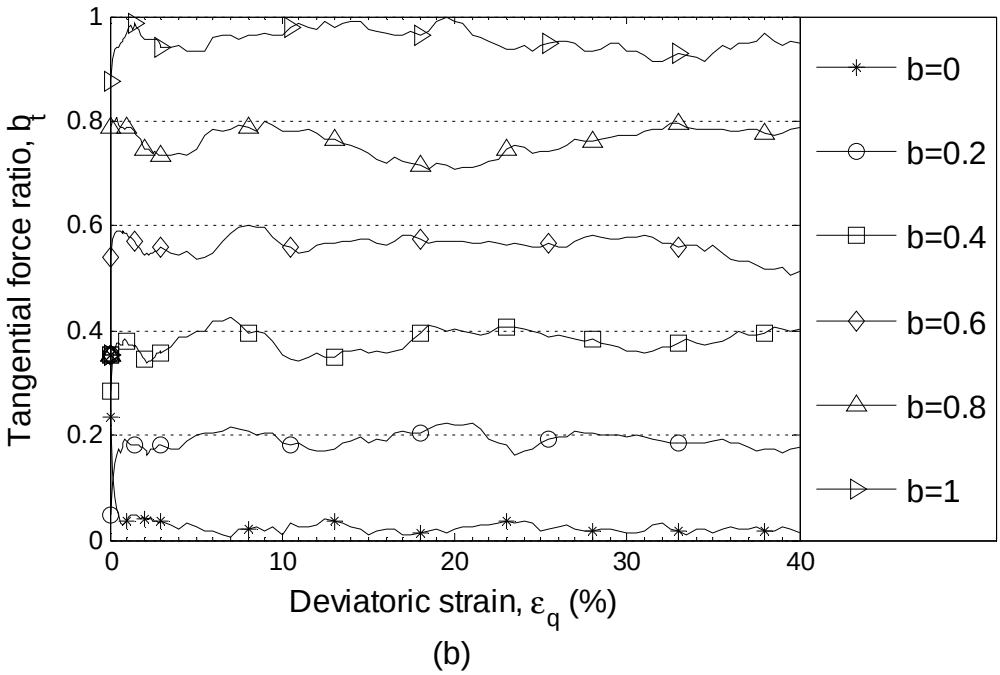

Fig. 5.21 Effects of *b* value intermediate contact force ratio in loose sample SREL_TT (a) normal force ratio b_n (b) tangential force ratio b_t

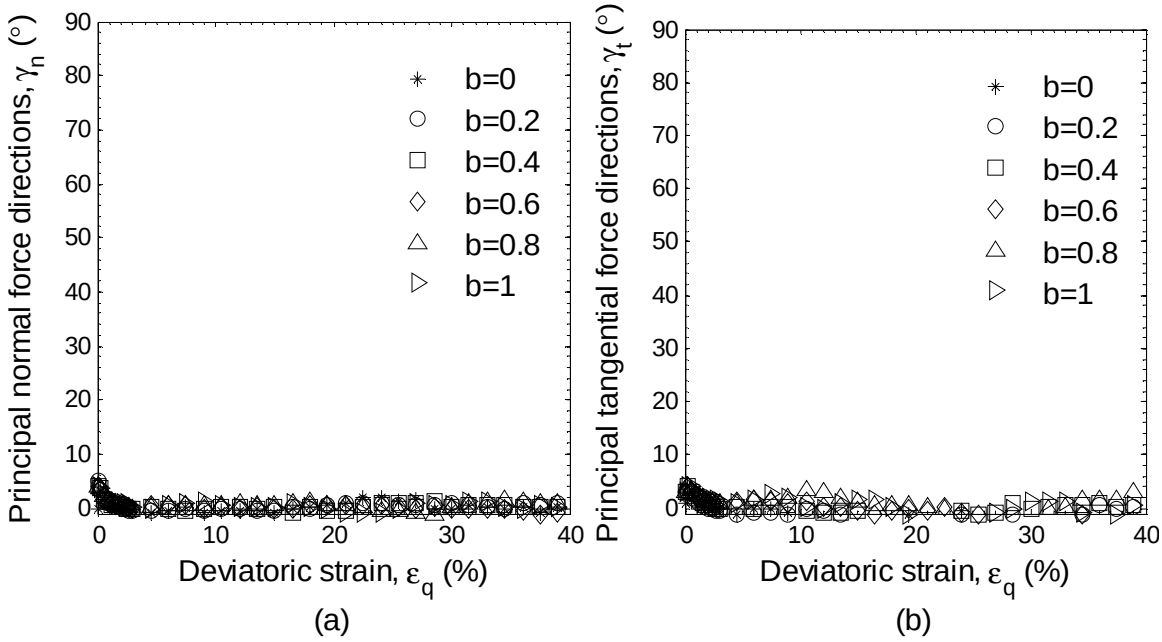

Fig. 5.22 Evolution of principal directions of contact force in dense sample SRED_TT (a) normal contact force (b) tangential contact force

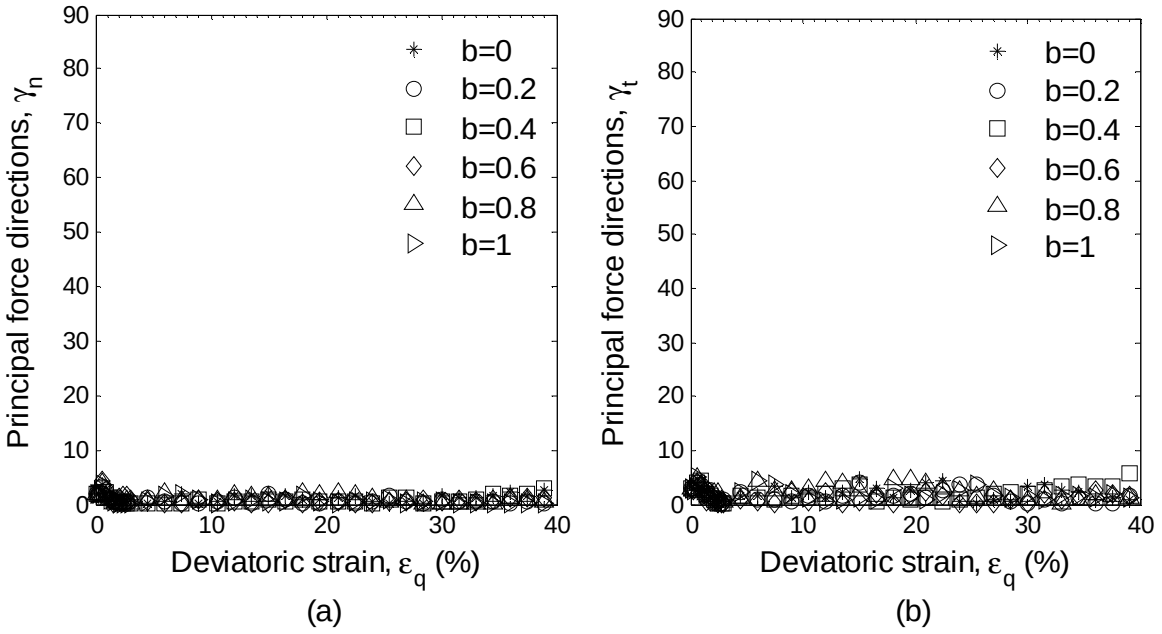

Fig. 5.23 Evolution of principal directions of contact force in loose sample SREL_TT (a) normal contact force (b) tangential contact force

5.5 Discussions

5.5.1 Failure criterion and strain increment direction

In soil mechanics, the friction angle, $f = \sin^{-1}\left(s_1 - s_3\right)/\left(s_1 + s_3\right)$, is used to define the mobilised shear strength (Wood, 1991). Fig. 5.24 illustrates the effect of b value on the mobilised peak friction angle f_{max} of the dense sample SRED_TT and the critical friction angle f_c of both dense and loose samples in the $f - b$ diagram. The symbols represent the DEM results and the solid line is the prediction of isotropic failure criterion proposed by Lade (1977), of which model parameter is obtained from the triaxial compression simulation (b=0). It shows that the peak friction angle initially increases to reach the maximum at $b \approx 0.5$. Then, it decreases as b increases further to 1. The minimum f_{max} is obtained from the triaxial compression test ($b = 0$). The difference between the maximum f_{max} ($b \approx 0.5$) and minimum f_{min} ($b = 0$) is approximately 5^{o}. The peak friction angle of the dense sample can be well captured by Lade's failure criterion. It is worth noting that the peak friction angle obtained from triaxial compression ($b = 0$) is lower than that obtained from triaxial extension ($b = 1$), which does not support the failure criterion proposed by Matsuoka and Nakai (1974). Their failure criterion predicts the same peak friction angle under triaxial compression and triaxial extension. This observation is supported by experimental results (Lade and Duncan, 1973, Arthur et al., 1977, Yamada and Ishihara, 1979). The dense and loose samples give the same critical friction angle f_c in simulations with the same b value. With

increasing b values, f_c initially increases and then decreases. The minimum f_c is obtained at triaxial extension ($b = 1$). It is also shown that Lade's failure criterion significantly overestimates the f_c, which indicate that Lade's failure criterion may not be good to serve as a yield criteria.

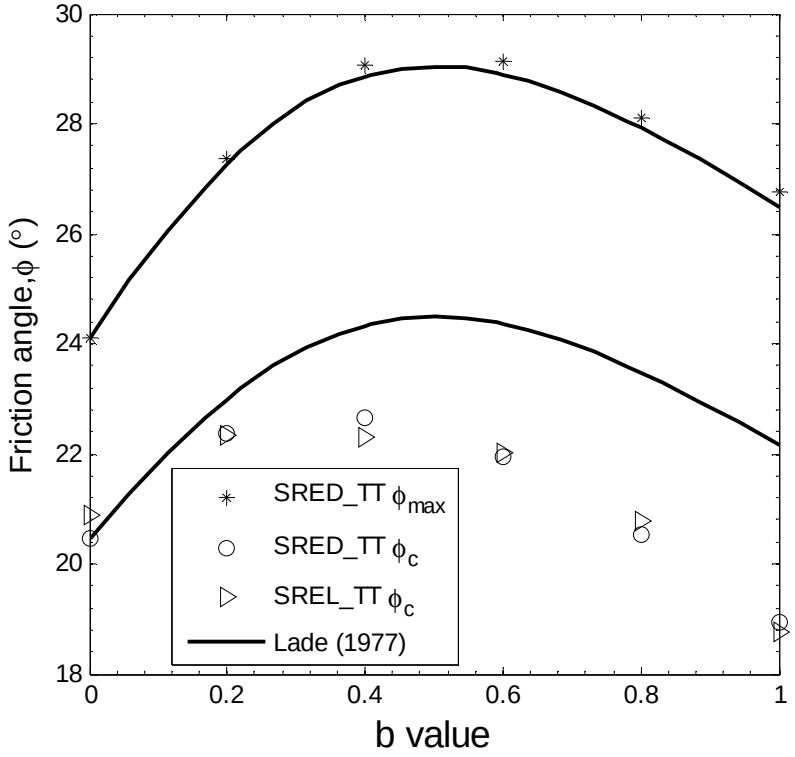

Fig. 5.24 Effects of *b* value on friction angle

Fig. 5.25 demonstrates the peak stress ratio (square symbols) obtained in the sample SRED_TT in simulations at various b values on the octahedral plane. The loose sample SREL_TT, presenting continuous strain hardening (no peak stress ratio observed), is not included. It is clear that the DEM failure envelop shows excellent agreement with Lade's failure criterion. The non-equality between b and $b_{\Delta e}$ (i.e., Fig. 5.12) reflects the non-coincidence of the strain increment direction and the stress direction in the octahedral plane. The solid arrow vector in Fig. 5.25 represents the

total strain increment direction at the peak stress ratio, where the total strain increment $\delta\varepsilon_{ij}$ (i.e., $\delta\varepsilon_q = 0.5\%$) is considered to be plastic as the stress increment is negligible, resulting in a negligible elastic strain increment. The direction of the strain increment vector is determined by the strain lode angle $q_{\Delta e}$ relative to the vertical symmetry axis as $q_{\Delta e} = \tan^{-1}\left(\sqrt{3}b_{\Delta e}/\left(2 - b_{\Delta e}\right)\right)$. The dashed arrow represents the stress vector direction in the octahedral plane, which is fixed due to constant b simulation and points from the intersection point between the hydrostatic axis and the octahedral plane to the failure stress point (square symbols). It is found that the strain increment direction deviates from the stress direction except in asymmetric loading conditions ($b = 0$ and $b = 1$). Similar observations of non-coincidence between strain increment direction and stress vector direction in the octahedral plane have also been reported in laboratory tests of sand soils (Lade and Duncan, 1973, Ochiai and Lade, 1983, Sun et al., 2008).

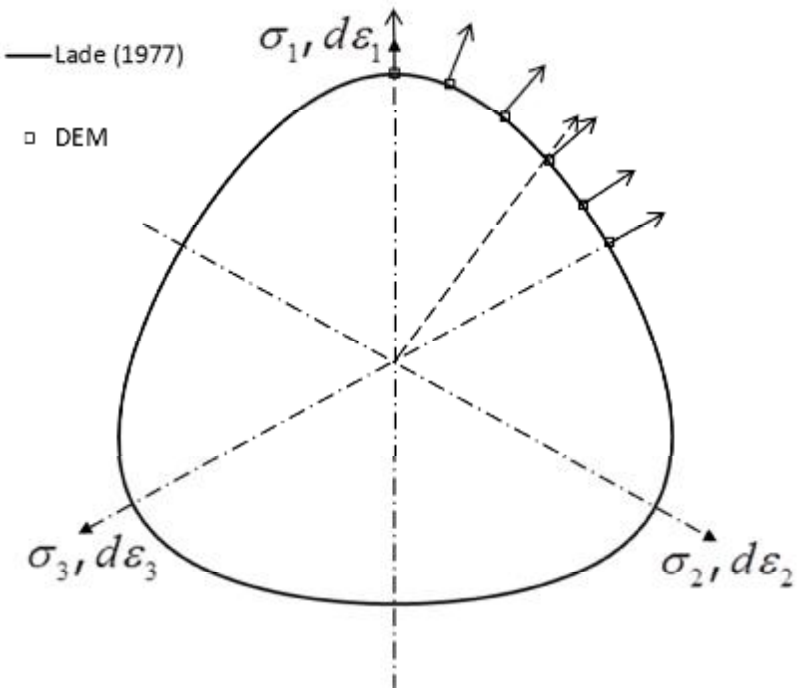

Fig. 5.25 Failure surface and strain increment vectors on octahedral plane

5.5.2 Micromechanical interpretation

With the stress-force-fabric (SFF) relationship in Eq. (2.18), the stress tensor can be expressed by the microstructural tensors, including fabric tensor D_{ij}, normal contact force tensor G_{ij}^{n}, tangential contact force tensor G_{ij}^{t} and branch vector tensor C_{ij}. The assumption that negligible contributions of higher order tensors, i.e., fourth order tensors, to stress tensor has been made. As the spherical particles are used for numerical simulations, the branch vector tensor anisotropy is quite small and it produces negligible contribution to the deviator stress. Accordingly, the stress state of the sample is only dependent on the microstructural fabric tensor and contact force tensors. This is confirmed by the good agreement of the stress ratio calculated from Eq. (2.17) and that determined from the SFF relationship using Eq.(2.18), as shown in Fig. 5.26, where the solid line refers to the stress ratio determined from boundary forces and the hollow symbols represent the stress calculated using the SFF relationship. The stress ratio from SFF is slightly larger than that from Eq. (2.17) at large deformation, which is probably due to the stress non-uniformity.

As shown in Fig. 5.17, Fig. 5.22 and Fig. 5.23, the principal directions of microstructure tensors $D_{ij}, G_{ij}^{n}, G_{ij}^{t}$ are coaxial with the principal stress direction in simulations of various b values. Accordingly, with the stress-force-fabric relationships in Eq. (2.18), the stress ratio capacity is dependent on the deviatoric anisotropy of the fabric tensor and contact force tensors. Thus, the effect of b values on material strength is dependent on the developed anisotropy degrees D_F, G_d^{n}, G_d^{t} of microstructural tensors. The peak stress ratio h and corresponding anisotropy values

of D_F, G_d^n, G_d^t are shown in Fig. 5.27. It clearly shows the contact force anisotropy G_d^n and G_d^t at failure is larger at a smaller b value, corresponding to a larger peak stress ratio at a lower b value. The fabric anisotropy D_F, however, increases for a greater b value. The normal contact force anisotropy is largest compared to the fabric anisotropy and tangential force anisotropy. It indicates that the normal contact force anisotropy G_d^n is dominant on the peak stress ratio obtained at various b values, while the contribution of fabric anisotropy to stress ratio is secondary.

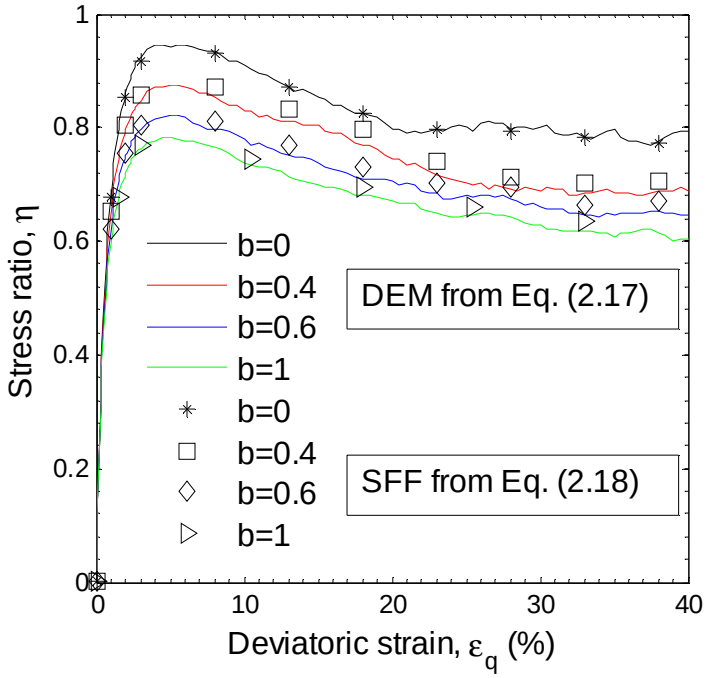

Fig. 5.26 Comparison of stress determined from DEM and analytical SFF relations for dense sample SRED_TT in true triaxial simulations

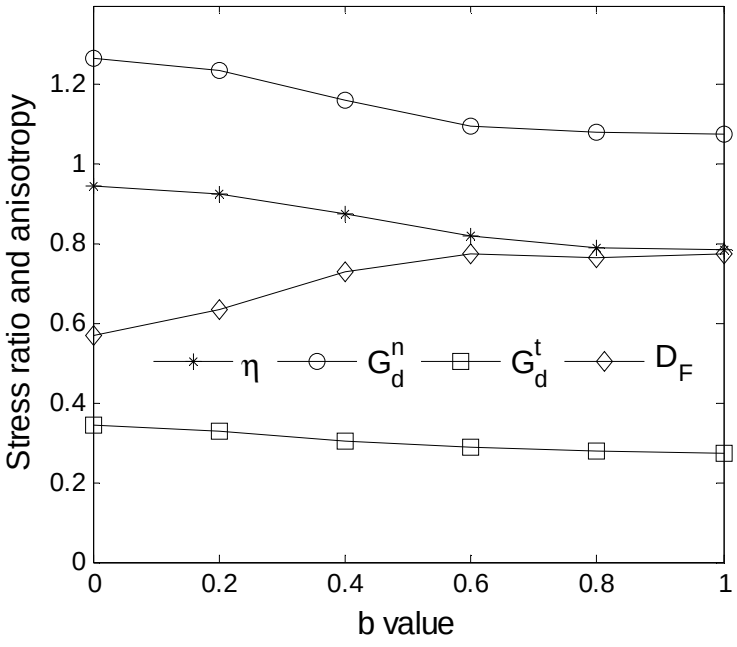

Fig. 5.27 Contribution of microstructural anisotropy degree to peak stress ratio according to Eq. (5.2) in sample SRED_TT at various *b* values

In constant b simulation, the intermediate fabric ratio b_F is larger than b (e.g., Fig. 5.16), correlated with the intermediate tangential force ratio being generally smaller than b value (e.g., Fig. 5.20). Therefore, the non-equality of intermediate stress ratio b and intermediate principal strain increment ratio $b_{\Delta e}$ is due to the non-equality of b and b_F. Accordingly, the constitutive relationship between the stress lode angle and the strain lode angle is recommended to be linked by the intermediate fabric ratio b_F, which has a clear physical meaning.

5.6 Summary

This chapter produces the DEM simulation results of samples with spherical particles. The influences of initial void ratio and b value on the granular material response have been examined. With the stress-force-fabric relationship, the stress

tensor of granular material is related to the microscopic parameters, i.e., coordination number w, fabric tensor D_{ij} and contact force tensors G_{ij}^n, G_{ij}^t. This is confirmed by that the stress ratio calculated using the SFF relation shows good agreement with that determined from the forces acting on boundary walls.

For the initially isotropic samples in true triaxial simulations, the principal directions of the internal fabric tensor and contact force tensors are coaxial with the loading direction, and the deviator stress developed in the assembly is dependent on the micro-scale scalar quantities, w, D_F, G_d^n, G_d^t. The material performs stiffer and more dilative with a smaller initial void ratio due to larger values of w, D_F, G_d^n, G_d^t. At large deformation, the critical stress ratio is achieved as micro-scale quantities w, D_F, G_d^n, G_d^t reaching critical values, irrespective of initial void ratios.

The true triaxial simulation results show the stress ratio decreases with an increasing b value for both dense and loose samples since the contact force anisotropy G_d^n, G_d^t is dominant in contribution to the deviatoric stress compared to that of fabric anisotropy D_F. The contact force anisotropy G_d^n, G_d^t is greater at a smaller b value, leading to a higher stress ratio achieved at a lower b value. It is observed that the direction of strain increment vector is not coaxial with the direction of stress increment vector ($b_{\Delta e} \neq b$) when illustrated in the octahedral plane. Microscopically, this is due to the intermediate fabric ratio b_F being bigger than the intermediate stress ratio b.

Chapter 6 Influence of loading direction on anisotropic material behaviour

The granular material is generally initially anisotropic and its behaviour is loading direction and loading history dependent. The material anisotropy may affect the strength-deformation characteristics significantly when the principal stress axes deviate from the material symmetric axes, known as loading direction dependent behaviour. In this chapter, the numerical simulations have been carried out on the initially anisotropic sample and the pre-loaded sample under various loading directions. The anisotropic stress-strain behaviour and non-coaxial deformation will be interpreted from the micro-scale observations.

6.1 Numerical simulation procedures

6.1.1 Preparation of anisotropic samples

The initially anisotropic sample was prepared by the gravitational deposition method as introduced in Section 4.3.2. The spherical particles were randomly generated without contact force arising in the large box. The frictional coefficient

during the deposition process was set to be $m_g = 0.1$ and the gravitational field was set to be $g = -100 m / s^2$ along the vertical direction (z-axis). After all particles were positioned and reached a state of equilibrium, the polyhedron boundary walls were generated by setting $n = 8$ and $R = 0.0068$. The box boundary walls and particles detected outside of the polyhedron boundary were deleted. Then, the frictional coefficient was restored to the representative value $m = 0.5$ for both particles and boundary walls and simulations were carried out to reach equilibrium. At this stage, the confining pressure p_g of the sample was recorded. Finally, the sample was isotropically consolidated to target confining pressure $p = 500kPa$, and the void ratio e_0 was recorded as the initial void ratio.

The pre-loaded sample was prepared by triaxial compression of the initially anisotropic sample to the deviatoric strain $e_q = 10\%$ with the major principal stress direction fixed at the deposition direction and constant mean normal stress $p = 500kPa$. Then, the sample was unloaded to the isotropic stress state. The loading history of the pre-loaded sample is illustrated in Fig. 6.1.

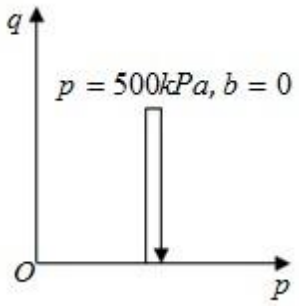

Fig. 6.1 Illustration of pre-loading hisory

The prepared anisotropic samples are given in detail in Table 6.1. The two samples are labelled by string of characters, with more details referred to Appendix C. The difference in the void ratio between the initially anisotropic sample SDEM_TT and the pre-loaded sample SDEM_TC_TT is small. The sample consisting of 5302 particles is sufficient to serve as a representative volume for investigating granular material behaviour.

Table 6.1 Information of anisotropic samples of spherical particles

Anisotropic sample	m_g	Void ratio e_0	No. of particles
SDEM_TT	0.1	0.72	5302
SDEM_TC_TT	Pre-loaded by triaxial compression	0.71	

6.1.2 Numerical simulation procedures

The numerical tests have been conducted on the initially anisotropic sample and the pre-loaded sample with varying major principal stress directions. In individual simulation, the confining pressure p was kept unchanged at $500kPa$. The intermediate principal stress ratio b was constant. The intermediate principal stress direction $\mathbf{n}_2$ was fixed to be coaxial with the coordinate axis of *y*-axis. The principal stress direction $\mathbf{n}_1$ was fixed with an angle a relative to the *z* axis in the *x*-*z* plane, as shown in Fig. 6.2. The tilting angle a varies from the vertical $a = 0^{o}$ to the

horizontal $a = 90^{o}$ with 15^{o} intervals. Only the deviatoric strain e_q increased continuously.

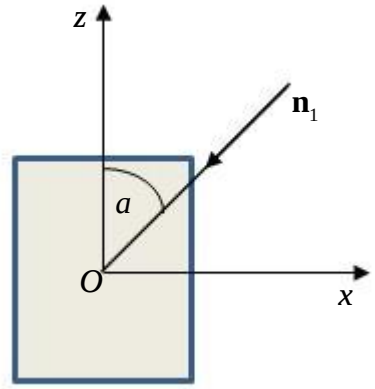

Fig. 6.2 Illustration of loading direction a

Table 6.2 Numerical simulations plan

Numerical sample	Constant p, varying loading direction a $\left(0^{o},15^{o},30^{o},45^{o},60^{o},75^{o},90^{o}\right)$		
	b value		
SDEM_TT	b=0	b=0.4	b=1
SDEM_TC_TT	b=0	b=0.4	b=1

6.2 Results on initially anisotropic sample

6.2.1 Influence of anisotropy on material behaviour

The simulation result on the sample SDEM_TT is illustrated in Fig. 6.3. It is shown that a slightly lower stress ratio at the small strain level, i.e., $e_q = 5\%$ and

greater initial volume contraction have been observed with increasing tilting angle a . This clearly indicates initially anisotropic microstructure formed during the deposition process. At large deformation, the stress ratio is equal and the difference of volumetric strain becomes small, showing the effect of initial anisotropy being wiped out. Similar anisotropic stress-strain behaviours have been produced in laboratory tests of sand at different loading directions (Oda, 1972a, Oda et al., 1978, Lam and Tatsuoka, 1988).

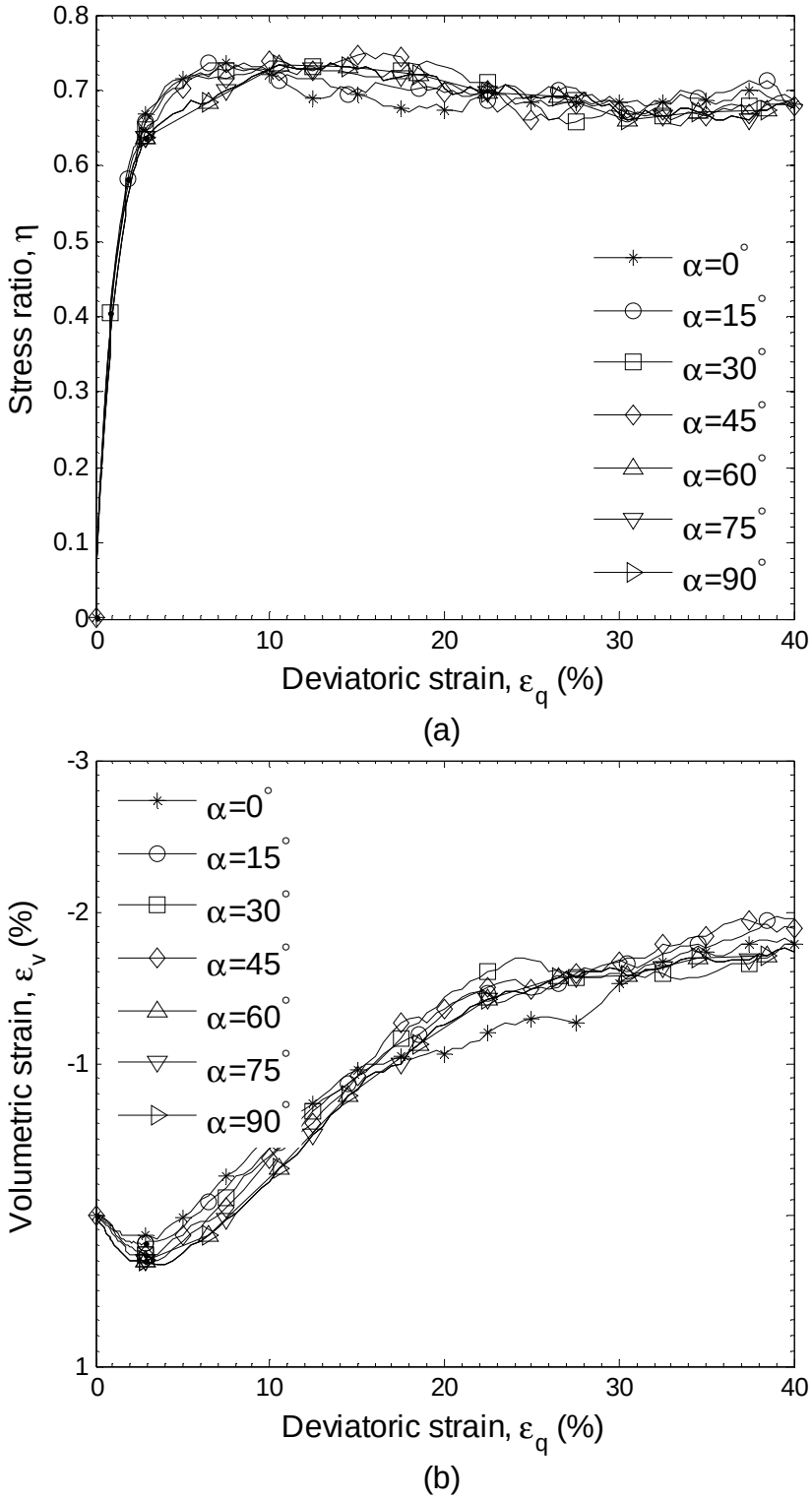

Fig. 6.3 Effect of loading direction a on initially anisotropic sample SDEM_TT without pre-loading at $b = 0.4$ (a) stress-strain (b) volume change behaviour

6.2.2 Influence of b value on stress-strain behaviour

The effect of b value on stress-strain behaviour of the sample SDEM_TT is given in Fig. 6.4. Regardless of various loading direction a , it is shown that the greatest stress ratio h occurs in asymmetric compression ($b = 0$) and the lowest stress ratio is obtained from asymmetric extension ($b = 1$). This is similar to the observation of effects of b stress-strain behaviour of the initially isotropic sample SRED_TT, as shown in Fig. 5.10, where the stress ratio decreases with increasing b value.

Fig. 6.5 plots the effect of b value on the stress-strain behaviour of sample SDEM_TT. It seems that the difference of volumetric strain at various b values is small. The slightly more volumetric contraction is observed at a greater b value in the small strain level, more obviously in simulations with $a = 0^{o}$. The experimental undrained shear results of Toyoura sand demonstrated that a higher excess pore water pressure developed at greater b value, indicating more contractive sand behaviour at larger b value (Yoshimine et al., 1998). However, this is different to the observation of effects of b values on the volume change behaviour of initially isotropic samples SRED_TT and SREL_TT as shown in Fig. 5.10 and Fig. 5.11, where the material is more contractive at a lower b value. It clearly indicates other factors, e.g. initial anisotropy, also affect the volume change behaviour. At large deformation, the variation of e_v is quite small and it may be considered that the critical state void ratio is achieved at the end of shearing.

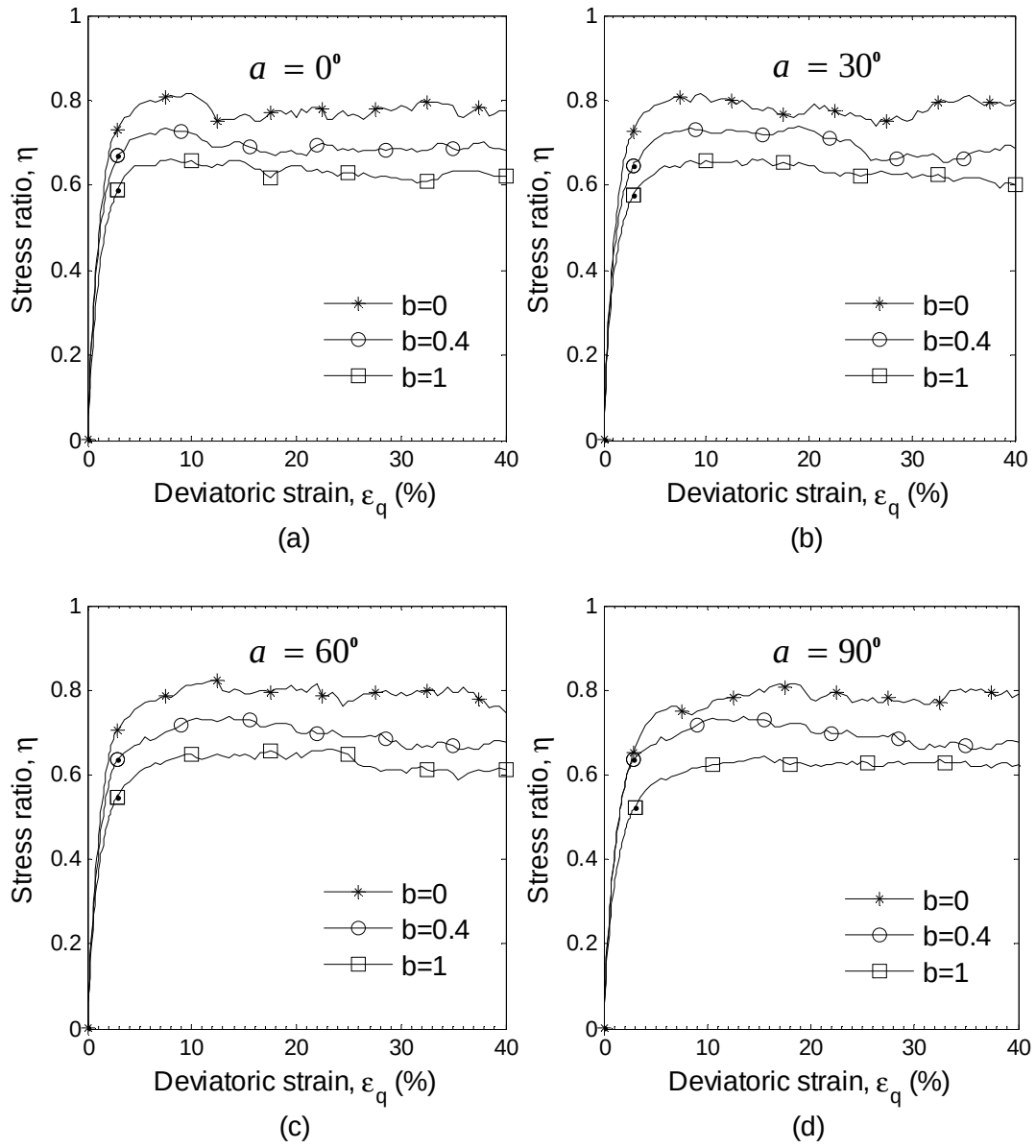

Fig. 6.4 Effect of b value on stress-strain behaviour of initial anisotropic sample SDEM_TT without pre-loading (a) $a = 0^{o}$ **(b)** $a = 30^{o}$ **(c)** $a = 60^{o}$ **(d)** $a = 90^{o}$

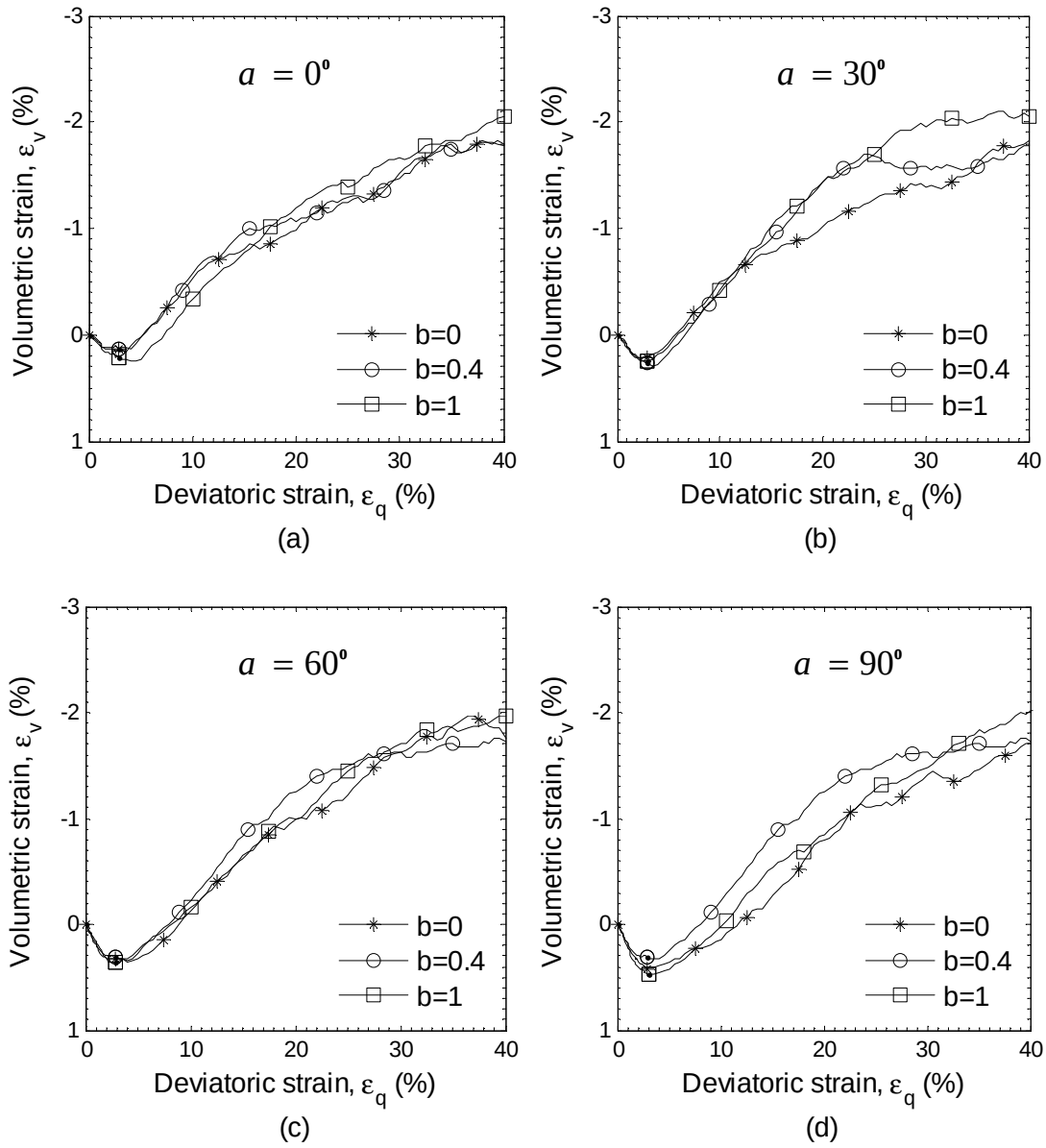

Fig. 6.5 Effect of b value on volumetric strain behaviour of initial anisotropic sample SDEM_TT (a) $a = 0^{o}$ **(b)** $a = 30^{o}$ **(c)** $a = 60^{o}$ **(d)** $a = 90^{o}$

6.2.3 Non-coaxiality

Fig. 6.6(a) shows the evolution of $g_{\Delta e}$ in simulation at $b = 0$, which is the angle of the principal strain increment direction vector $\mathbf{n}^{\Delta e}$ relative to the positive *z*-axis in the *x*-*z* plane determined by $g_{\Delta e} = \mathbf{tan}^{-1}\left(n_x^{\Delta e} / n_z^{\Delta e}\right)$. The strain increment δ_{ij}

is calculated within a small increment of deviatoric strain $d\varepsilon_q = 0.5\%$. The solid straight line represents the fixed major principal stress direction α. The hollow symbols show the evolution of corresponding principal strain increment direction $\gamma_{\Delta\varepsilon}$. It can be seen that the degree of non-coaxiality between principal stress direction and principal strain increment direction is quite small, indicating the material response is generally coaxial. Slightly larger deviation up to 5° is observed at $\alpha = 60°$ and the deviation is towards the bedding plane. Similar observations can be found in simulations with $b = 0.4$ (Fig. 6.6(b)) and $b = 1$ (Fig. 6.6(c)). This is consistent with the results of 2D DEM simulations from Li et al., (2009). The non-coaxial behaviour has also been reported in experimental results while the deviation of principal strain increment direction is always towards $\alpha = 45°$ (Miura et al., 1986, Gutierrez et al., 1991).

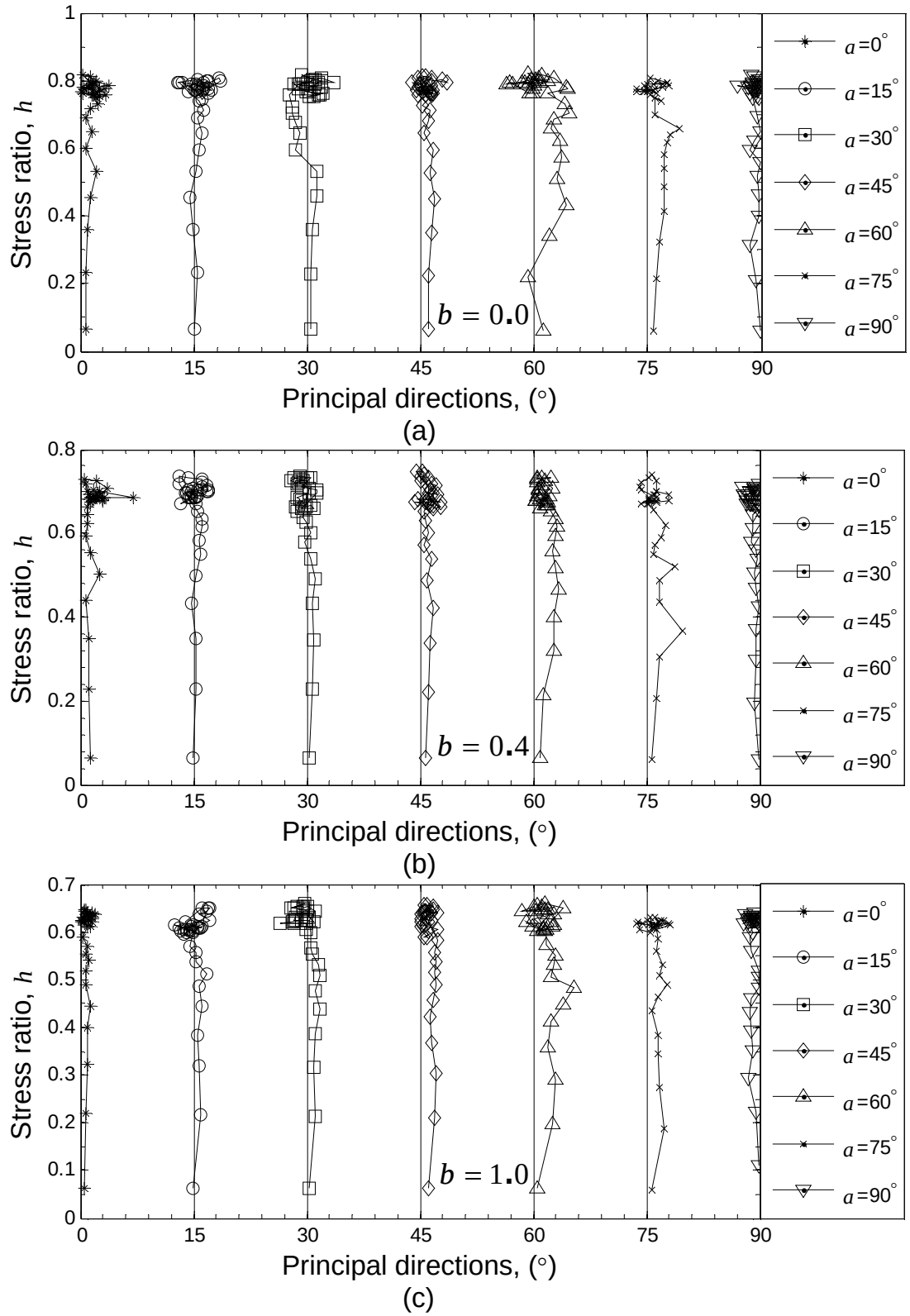

Fig. 6.6 Non-coaxial behaviour for initially anisotropic sample SDEM_TT without pre-loading (a) $b = 0$ **(b)** $b = 0.4$ **(c)** $b = 1$

6.2.4 Microscopic observations on initially anisotropic sample

6.2.4.1 Fabric evolution

The evolution of coordination number w is presented in Fig. 6.7 for initially anisotropic sample SDEM_TT. The coordination number does not show much difference at different loading directions, corresponding to similar volume change behaviour at varying loading direction (e.g., Fig. 6.3). It decreases during the initial 10% deviatoric strain as the sample dilates with increasing void ratio. For further shearing, the same critical value $w = 4.6$ is obtained independent of a, which is the same as that obtained for initially isotropic sample SRED_TT at various b value simulations (e.g., Fig. 5.13). This indicates that the critical coordination number is independent of material initial void ratio, material anisotropy and loading paths under constant mean normal stress simulations.

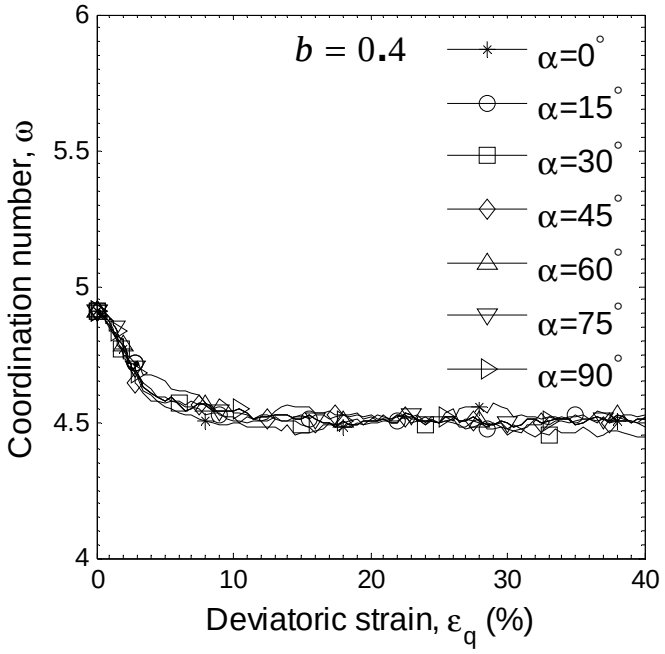

Fig. 6.7 Effect of loading direction a on coordination number for SDEM_TT

The evolution of contact normal fabric anisotropy of the sample SDEM_TT is shown in Fig. 6.8 in terms of D_F and principal direction g_F under constant $b = 0.4$ simulation. The initial degree of fabric anisotropy is $D_F = 0.13$ with the principal fabric direction in the vertical deposition direction ($g_F = 0^o$). It clearly shows the anisotropic structure developed during the deposition process. As shearing occurs, the contact normal anisotropy increases when $a \leq 45^o$. At $a \geq 60^o$, it initially decreases to its minimum value and then starts to increase due to fabric reorganisation, with the principal fabric direction rotating gradually to the loading direction. It is observed (e.g., $e_q = 5\%$) that a slightly larger D_F developed at a smaller a value, corresponding to the small variations of anisotropic stress-strain behaviour observed in Fig. 6.3.

In addition, the principal fabric direction evolves to the loading direction rapidly at a small shear strain, e.g., $e_q = 3\%$. For further shearing, the principal fabric direction is coaxial with the loading direction. Thus, though the principal fabric direction initially deviates from the loading direction, the general coaxial behaviour is obtained due to a small fabric anisotropy D_F at small shear strain.

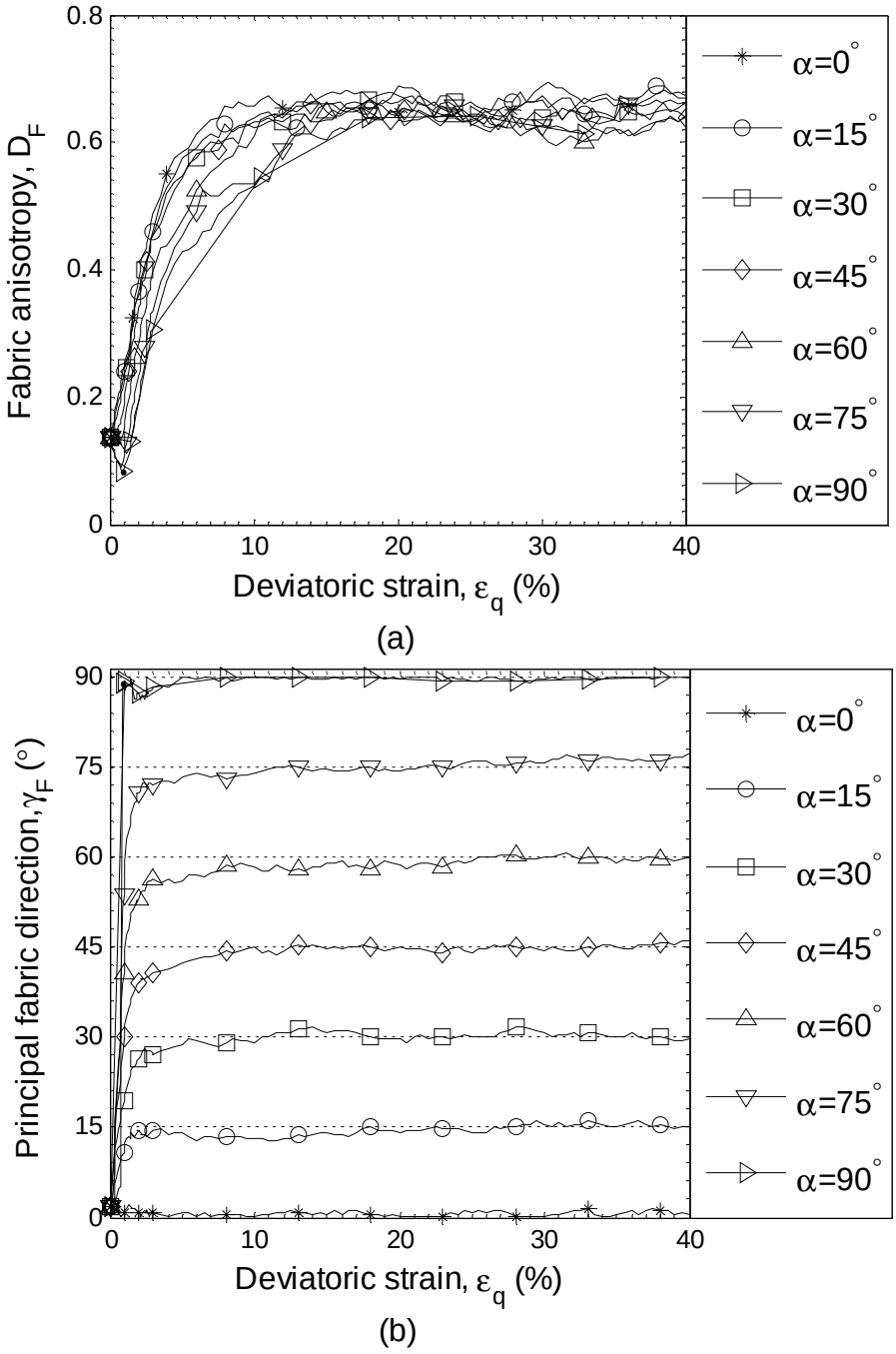

Fig. 6.8 Effect of loading direction on fabric evolution of sample SDEM_TT without pre-loading at $b = 0.4$ (a) deviator fabric (b) principal fabric direction

6.2.4.2 Effect of *b* value on fabric evolution

The influence of the b value on the fabric evolution of sample SDEM_TT at different loading directions is plotted in Fig. 6.9. Generally speaking, a slightly

greater D_F is observed at a larger b value, similar to that observed on the initially isotropic sample SRED_TT sheared at different b values (e.g., Fig. 5.14). The principal fabric direction presents no significant difference at various b values (Fig. 6.10).

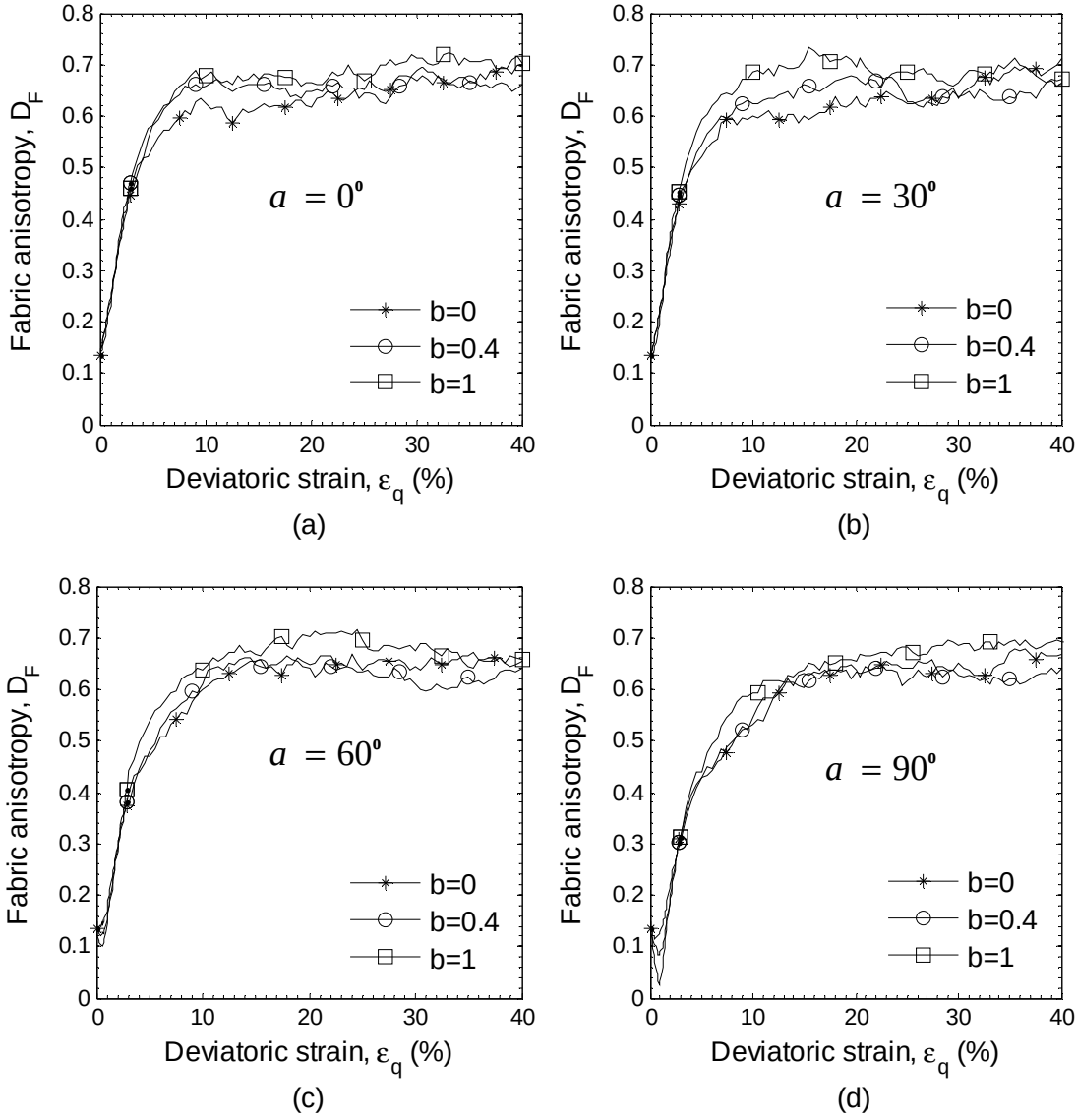

Fig. 6.9 Effects of b on fabric evolution of initial anisotropic sample SDEM_TT at different loading directions (a) $a = 0^o$ **(b)** $a = 30^o$ **(c)** $a = 60^o$ **(d)** $a = 90^o$

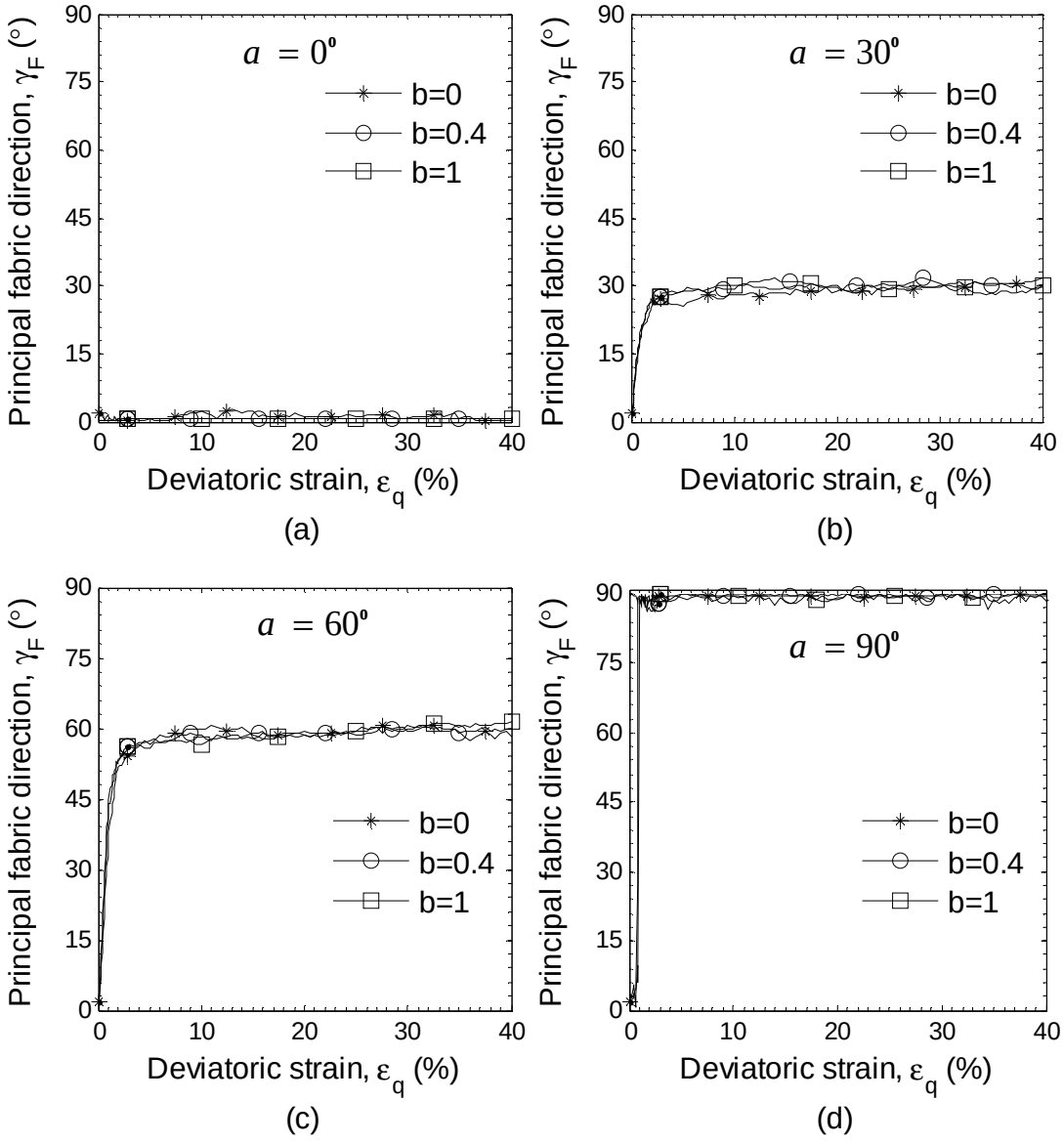

Fig. 6.10 Effects of *b* value on principal fabric direction for initially anisotropic sample SDEM_TT sheared at various loading directions

6.3 Results on pre-loaded sample

6.3.1 Effect of anisotropy on stress-strain behaviour

The stress-strain behaviour of the pre-loaded sample SDEM_TC_TT is shown in Fig. 6.11 under various loading directions, under constant $p = 500kPa$ and $b = 0.4$ simulation. A lower stress ratio and larger initial contraction are observed at small strain level, i.e., $e_q = 4\%$ as the loading direction rotates from the vertical direction $a = 0^o$ to the horizontal direction $a = 90^o$. At the large shear strain level, the stress ratio shows little difference, and variation of volumetric strain becomes small. Compared to the stress-strain behaviour of the initially anisotropic sample SDEM_TT (e.g., Fig. 6.3), the influence of loading direction on stress-strain response is more significant in the pre-loaded sample. This indicates that the pre-loading history has a significant effect on granular material behaviour.

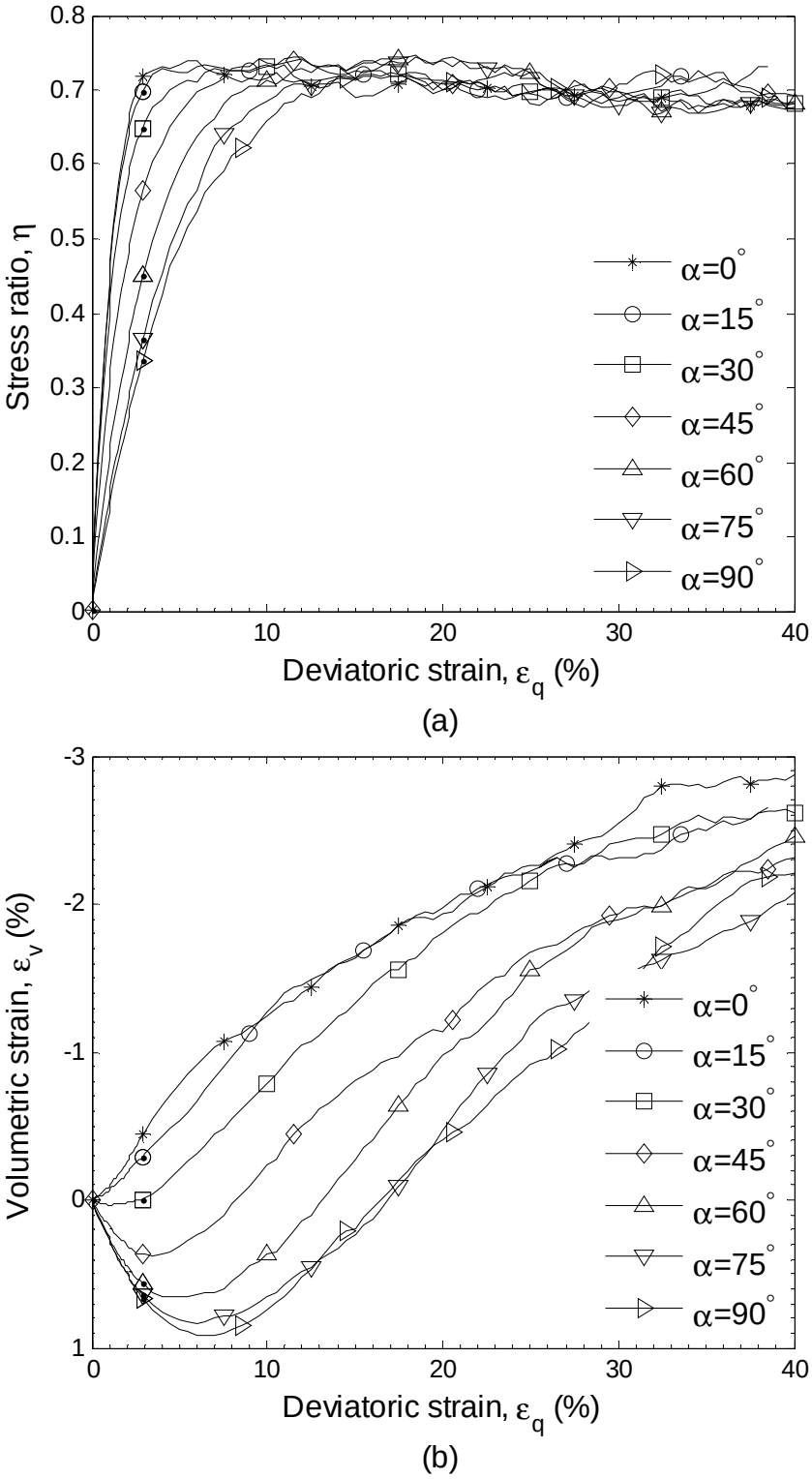

Fig. 6.11 Results on pre-loaded sample SDEM_TC_TT at $b = 0.4$ (a) stress-strain behaviour (b) volume change behaviour

6.3.2 Effect of *b* value on stress-strain behaviour

Fig. 6.12 shows the effects of the b value on stress-strain behaviour in simulations with fixed a . The stress ratio is larger at a lower b value (similar observations in simulations at other a values). This is similar to effect of b value on stress-strain behaviour of the initially isotropic sample SRED_TT, as shown in Fig. 5.10.

The effect of b value on the volumetric strain is demonstrated in Fig. 6.13. It shows that the sample SDEM_TC_TT performs more contractive with increasing b value during the initial small shearing strain, i.e., up to $e_q = 20\%$, irrespective of loading direction a . This is consistent to the observation of larger pore pressure build-up at a greater b value in experimental undrained shear (Yoshimine et al., 1998). However, the volumetric strain curves converge to similar values of e_v at large deformation, indicating the effect of fabric anisotropy on dilatancy behaviour disappeared. This observation is different to the effect of b values on the volume change behaviour of the initially isotropic samples, as shown in Fig. 5.10 and Fig. 5.11, where the sample is more contractive at a lower b value. This clearly shows the combined effects of b and material anisotropy on volumetric strain response of the pre-loaded sample. The reason is that the pre-loaded sample performs most contractively when $a = 90^{\circ}$ due to anisotropy, where the principal stress direction is within the bedding plane, as is shown in Fig. 6.11. As b increases from 0 to 1, the magnitude of intermediate principal stress increases and the intermediate principal stress direction is parallel with the bedding plane. Thus, the effect of material

anisotropy on the volumetric strain behaviour is dominant than the magnitude of intermediate stress (b value). Compared to the initially anisotropic sample SDEM_TT, the effect of anisotropy on the volume change behaviour is not so significant as that of the pre-loaded sample due to a lower degree of fabric anisotropy D_F in the sample SDEM_TT, which is supported by less initial maximum volume contraction at various loading directions in the sample SDEM_TT (Fig. 6.3) than in the pre-loaded sample (Fig. 6.11).

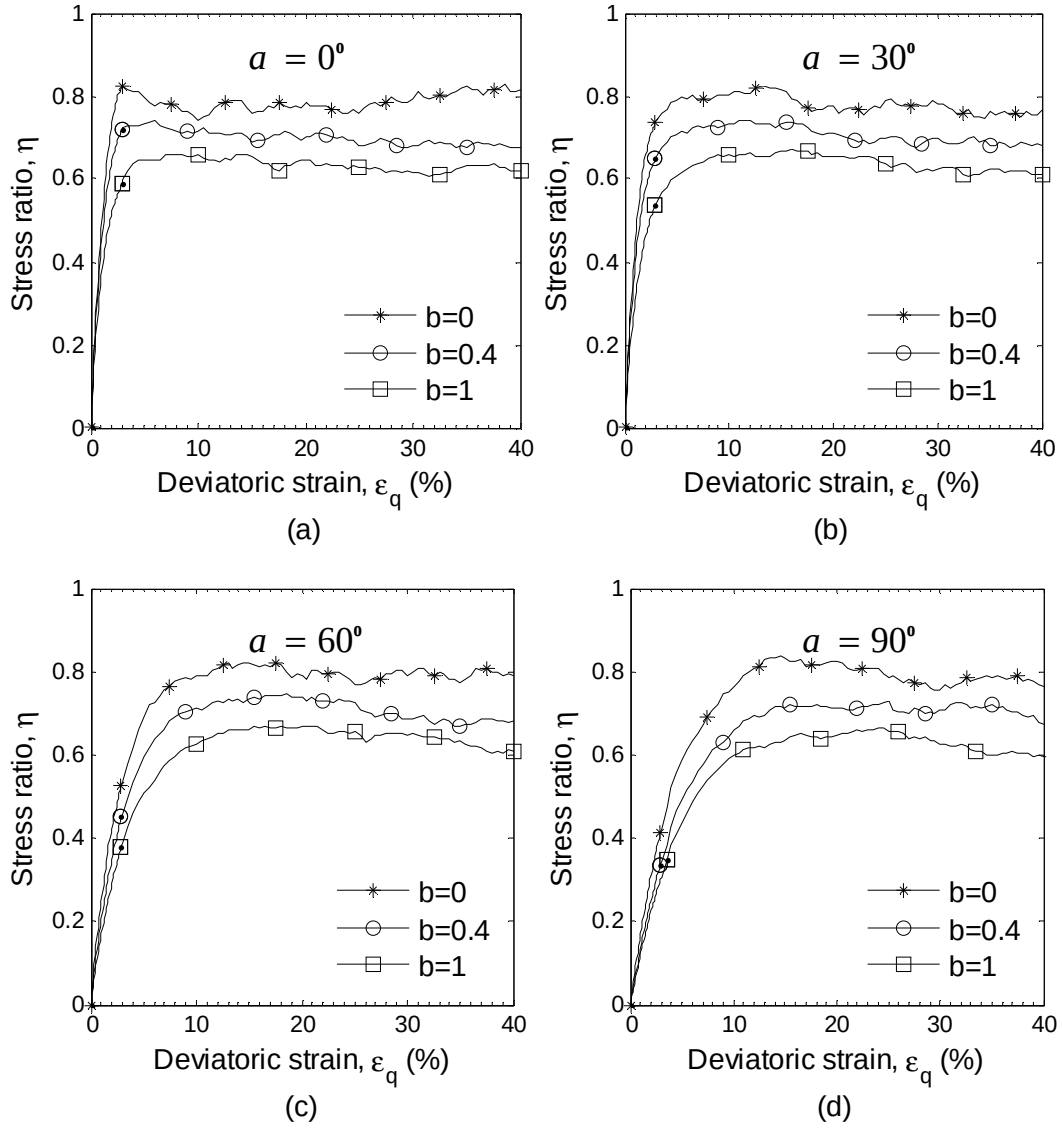

Fig. 6.12 Effect of b value on stress-strain behaviour of pre-loaded sample SDEM_TC_TT

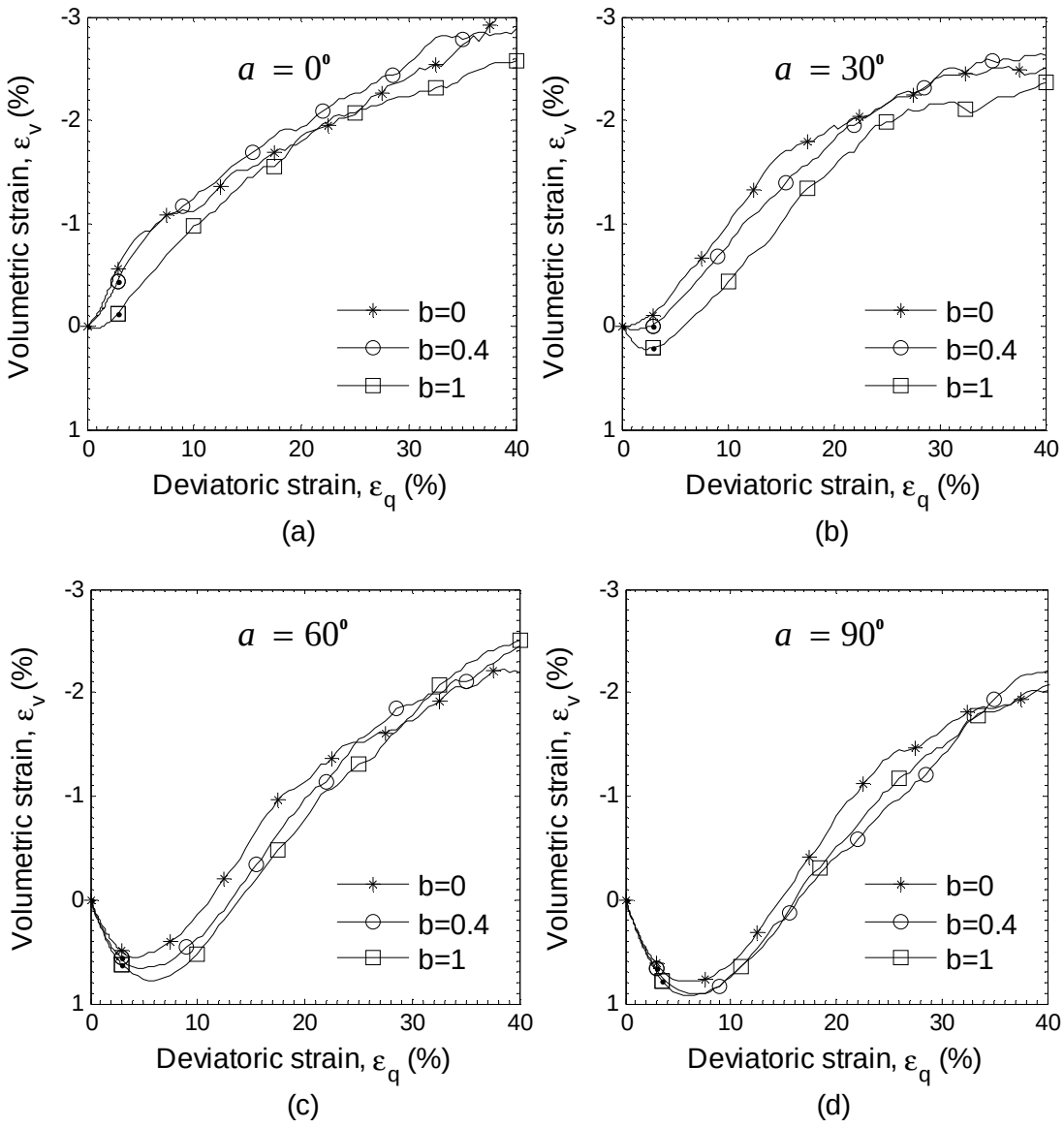

Fig. 6.13 Effect of b value on volumetric strain behaviours of pre-loaded sample SDEM_TC_TT (a) $a = 0^{o}$ **(b)** $a = 30^{o}$ **(c)** $a = 60^{o}$ **(d)** $a = 90^{o}$

6.3.3 Non-coaxiality

Fig. 6.14(a) shows the evolution of $g_{\Delta e}$, which is the angle of principal strain increment direction vector relative to the positive *z*-axis in the *x*-*z* plane. The strain increment $d\varepsilon_{ij}$ is calculated within a small increment of deviatoric strain $d\varepsilon_q = 0.5\%$. The solid straight line represents the major principal stress direction a, which was fixed during loading. It can be found that $g_{\Delta e}$ is close to the loading direction when $a = 0^o$ and $a = 90^o$. At other a values, however, significant non-coaxiality between the major principal stress and the principal strain increment directions is observed. The non-coaxiality is larger when the principal stress direction deviates more from the vertical direction, i.e., $a = 60^o$. However, the degree of non-coaxiality decreases as shearing continues and the material behaviour becomes coaxial at large deformation. Similar observations have also been produced in simulations at $b = 0.4$ and $b = 1$, as shown in Fig. 6.14(b) and Fig. 6.14(c). The non-coaxial behaviour has also been reported in experimental study on sand, e.g., Fig. 6.15 (Miura et al., 1986, Gutierrez et al., 1991, Cai et al., 2013). However, the effect of the b value on non-coaxiality is not presented in experimental study. The influence of the b value on degree of non-coaxiality is shown in Fig. 6.16. No significant difference of non-coaxiality degree is found in simulations at different b values with fixed a.

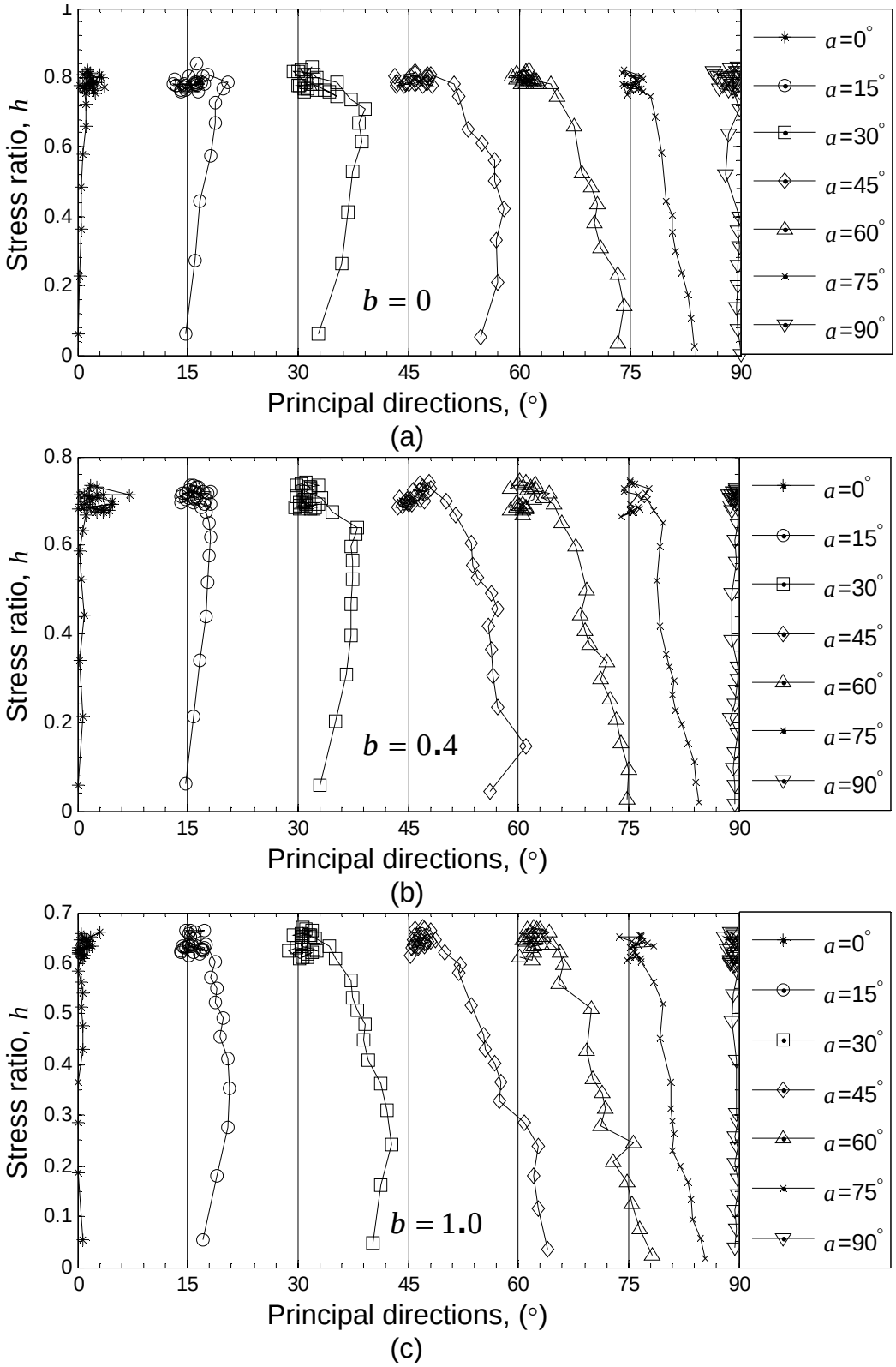

Fig. 6.14 Non-coaxial behaviour for the pre-loaded anisotropic sample of SDEM_TC_TT (a) $b = 0$ **(b)** $b = 0.4$ **(c)** $b = 1$

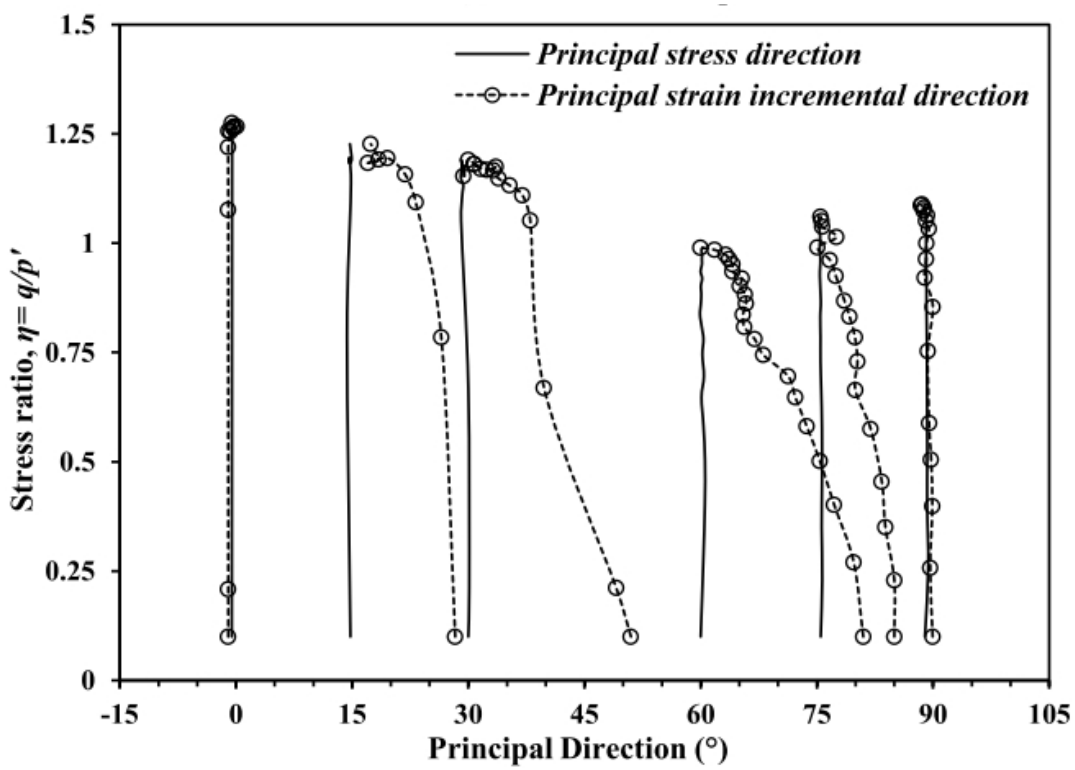

Fig. 6.15 Non-coaxial behaviour observed in laboratory test on sand sheared at different loading directions (after Yang, 2013)

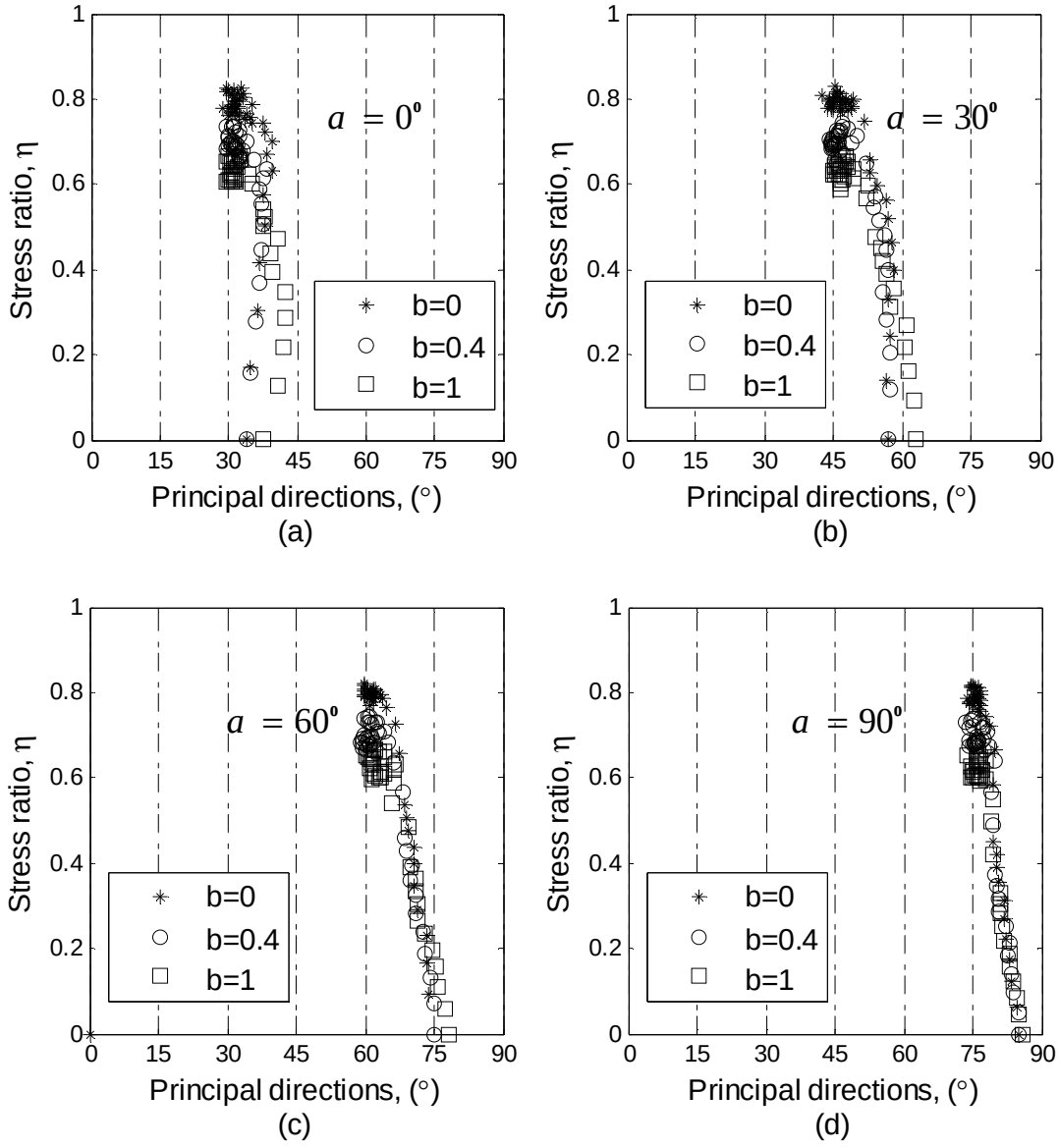

Fig. 6.16 Effects of b value of non-coaxiality for pre-loaded sample SDEM_TC_TT (a) $a = 30^{o}$ **(b)** $a = 45^{o}$ **(c)** $a = 60^{o}$ **(d)** $a = 75^{o}$

6.3.4 Microscopic observations on the pre-loaded sample

6.3.4.1 Fabric evolution

The evolution of coordination number w is presented in Fig. 6.17 in simulation at $b = 0.4$ for the pre-loaded sample SDEM_TC_TT. The coordination

number does not show big difference at different loading directions. A slightly larger w is observed at a greater tilting angle a at the initial 10% deviatoric strain, relating to the greater initial volume contraction with decreasing void ratio. For further shearing, the same critical $w = 4.6$ is obtained independent of a, which is the same as that obtained for initially isotropic sample at various b simulations (e.g., Fig. 5.13). This indicates that the critical coordination number is independent of material initial void ratio, material anisotropy and loading paths under constant mean normal stress simulations.

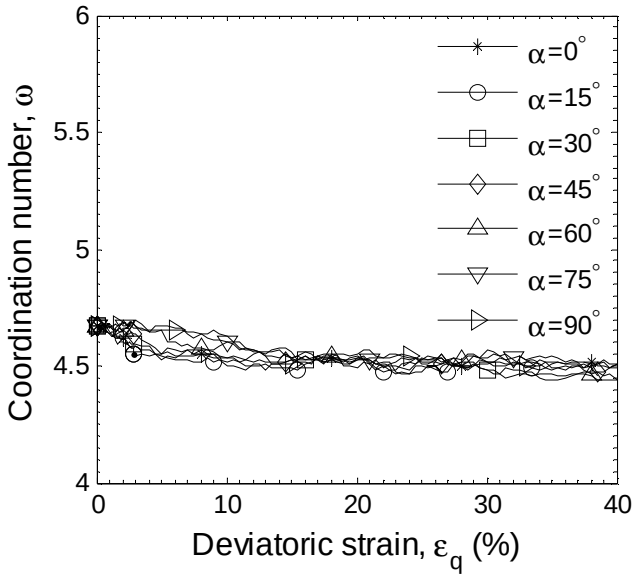

Fig. 6.17 Effects of loading direction on coordination number for the pre-loaded sample SDEM_TC_TT, *b*=0.4

The effect of loading direction on fabric anisotropy is shown in Fig. 6.18 at constant $b = 0.4$ simulation. It can be seen from Fig. 6.18 that the initial degree of contact normal anisotropy is $D_F = 0.22$, which is larger than that of the initially anisotropic sample SDEM_TT of which $D_F = 0.13$, and the principal fabric direction is in the vertical deposition direction ($g_F = 0^o$). It indicates the pre-loading

history results in a more anisotropic structure in the pre-loaded sample SDEM_TC_TT. As shearing occurs, the fabric anisotropy D_F increases from the very beginning when $a \leq 45^{\circ}$. At $a \geq 60^{\circ}$, it initially decreases to the minimum value and then start to increase gradually. Before reaching the mobilised peak stress ratio at various loading directions, the fabric anisotropy D_F is generally larger at a smaller a and the principal fabric direction approaches to the loading direction during the shearing. However, at large deformation, the fabric anisotropy reaches similar values and the principal fabric direction is coaxial with loading direction at various loading directions. This demonstrates that the initial internal structure has been destroyed due to applied loading.

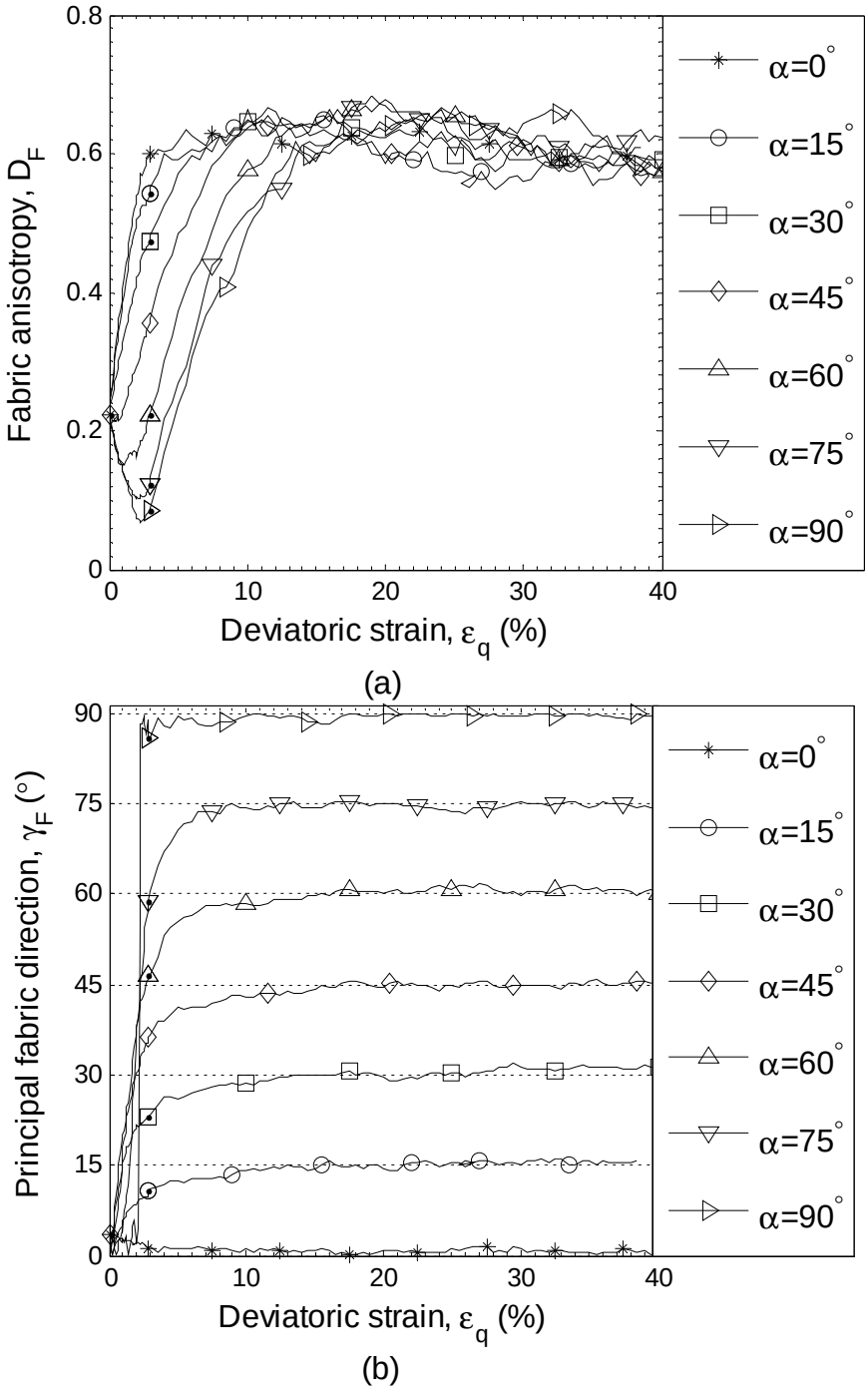

Fig. 6.18 Effect of a on fabric evolution in the pre-loaded anisotropic sample SDEM_TC_TT at b=0.4 (a) fabric anisotropy (b) principal fabric direction

6.3.4.2 Contact force evolution

Fig. 6.19 shows the effect of a on the mean normal force f_0. It can be found that similar value $f_0 = 0.38N$ is obtained despite of loading direction. A slightly larger mean normal force has been observed at a smaller tilting angle a due to smaller coordination number at smaller a in constant mean normal stress simulation (i.e., Fig. 6.17).

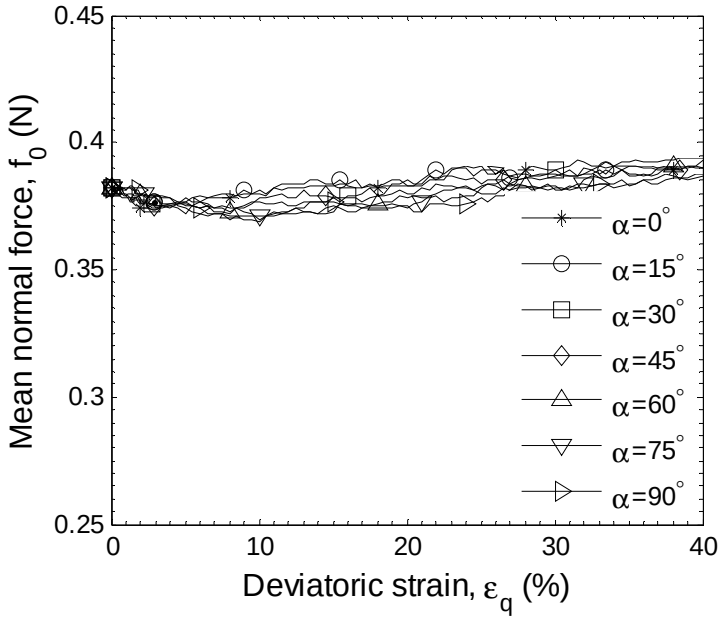

Fig. 6.19 Effect of loading direction on mean normal force for the pre-loaded sample SDEM_TC_TT, *b*=0.4

The evolution of normal contact force anisotropy at various loading directions is shown in Fig. 6.20. The normal contact force anisotropy G_d^n increases as shearing, with anisotropic force chains developed to carry external load. Before reaching the mobilised peak stress ratio at various loading directions, A smaller degree of normal force anisotropy is observed at larger tilting angle a, correlated to the smaller fabric anisotropy D_F. However, at large deformation, the contact force

anisotropy G_d^n reach similar values despite of different loading directions, indicating the effect of initial fabric anisotropy being wiped out. The principal direction g_n of normal contact force anisotropy is found to be generally coaxial with the applied loading direction.

In the initially isotropic stress state, the anisotropic fabric (preferred contact orientations in the vertical direction) results in anisotropic tangential contact force distribution with the preferred direction in horizontal direction ($g_t = 90^o$), as shown in Fig. 6.21. As shearing occurs, the tangential force anisotropy G_d^t start to increase from the very beginning when $a \leq 45^o$. At $a \geq 60^o$, they initially decrease to the minimum value and then start to increase quicklly to reach steady values. The tangential force anisotropy G_d^t shows little difference at different loading directions. The principal direction g_t of tangential force distribution rotates gradually to the loading direction after 15% of deviatoric strain, correlated to the rotation of principal fabric direction shown in Fig. 6.18.

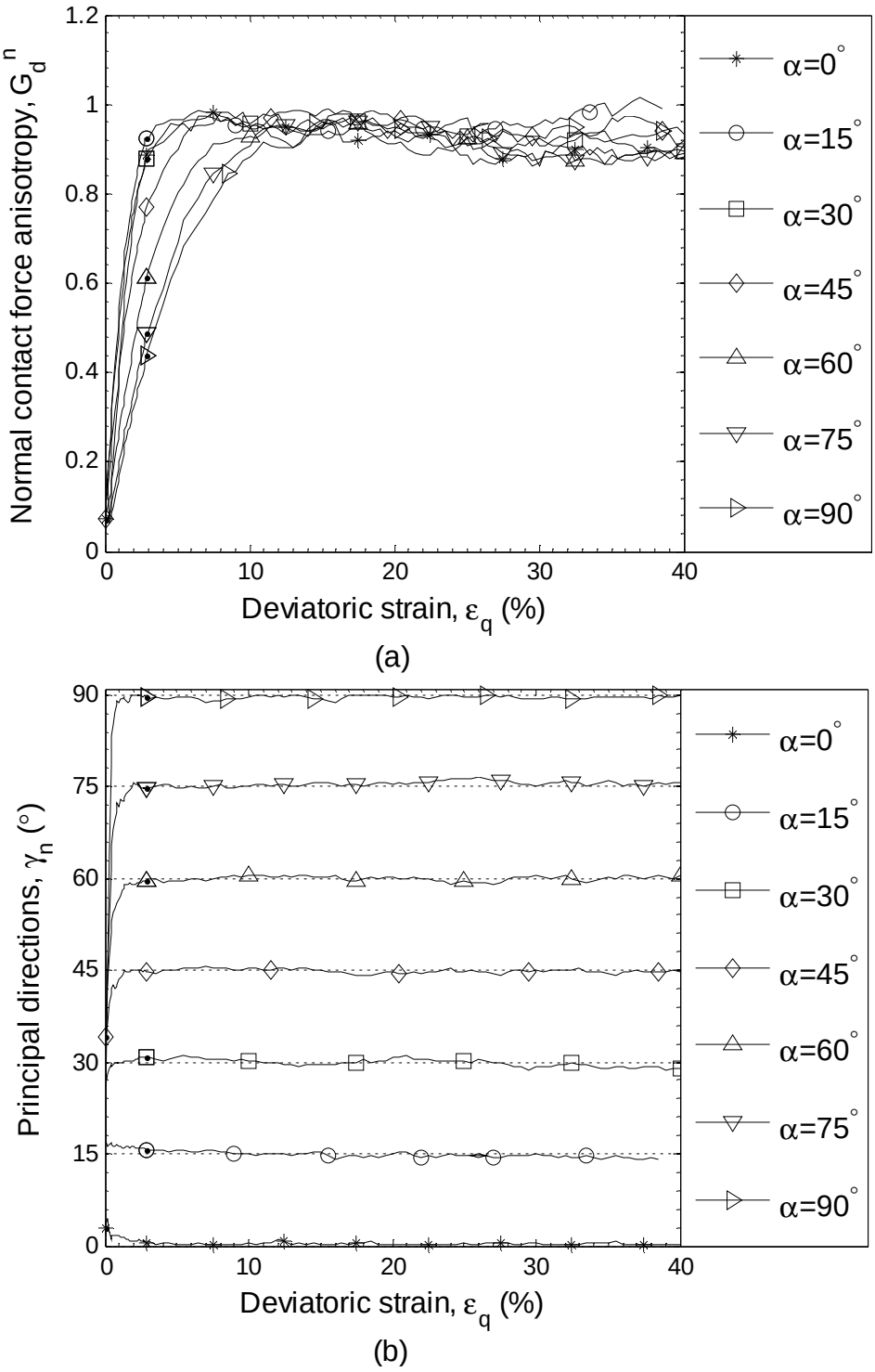

Fig. 6.20 Effect of a on normal contact force anisotropy for the pre-loaded sample SDEM_TC_TT at b=0.4 (a) anisotropy degree (b) principal direction

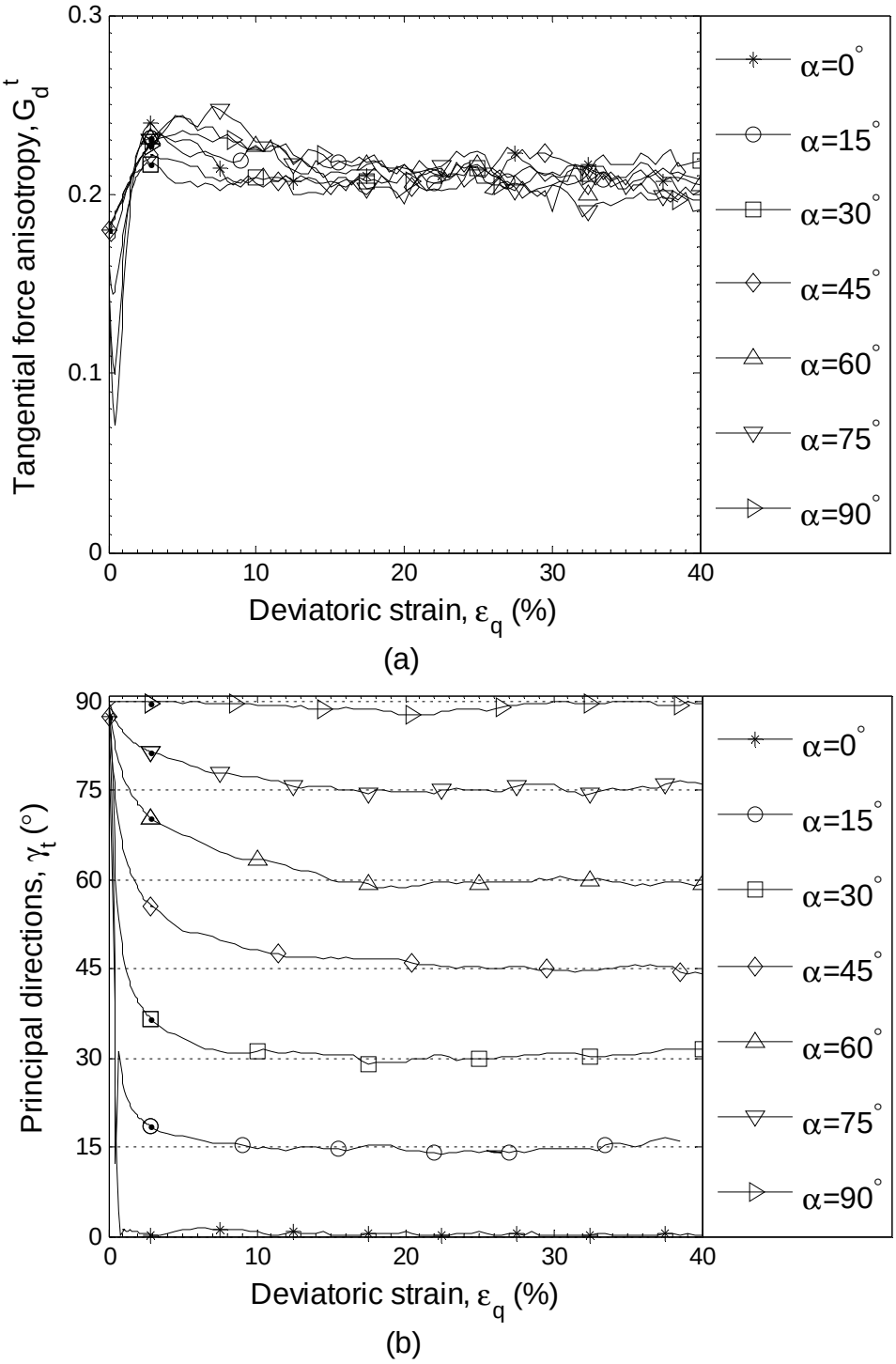

Fig. 6.21 Effect of a on tangential contact force evolution for the pre-loaded sample SDEM_TC_TT at b=0.4 (a) anisotropy degree (b) principal direction

6.3.4.3 Effect of *b* value on fabric evolution

The influence of the b value on the fabric evolution of the pre-loaded sample at different loading directions is plotted in Fig. 6.22. At the initial stage of small shearing, the difference of D_F is not obvious at $a \leq 30^{\circ}$ (see Fig. 6.22(a) and Fig. 6.22(b)). The increasing b value results in more initial decrease of D_F to its minimum value when $a \geq 60^{\circ}$. Upon further shearing, the curves fluctuate significantly. It, however, may be seen that slightly greater D_F is observed at a larger b value with deviatoric strain in the range of $15\% \sim 30\%$.

The degree of non-coaxiality is dependent on the relative directions of principal stress and principal fabric, and relative anisotropy degrees of fabric and contact force (Li and Yu, 2013b). The effect of the *b* value on the non-coaxiality degree is negligible, as shown in Fig. 6.16. Microscopically, the reason is the evolution of fabric anisotropy and principal fabric direction presents no significant difference at various *b* values (e.g., Fig. 6.22 and Fig. 6.23).

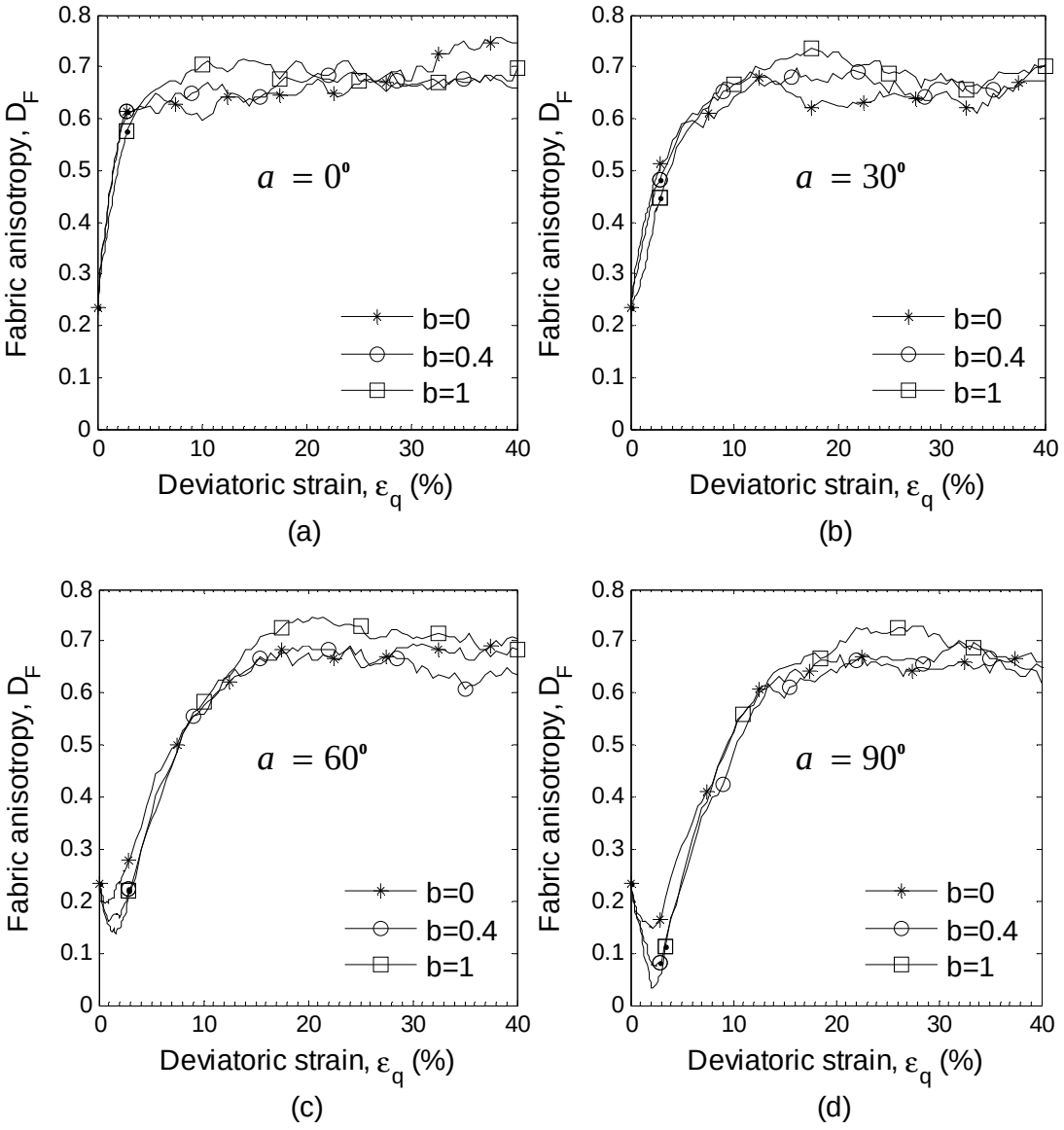

Fig. 6.22 Effects of *b* on fabric evolution of pre-loaded sample SDEM_TC_TT at different loading directions (a) $a = 0^o$ **(b)** $a = 30^o$ **(c)** $a = 60^o$ **(d)** $a = 90^o$

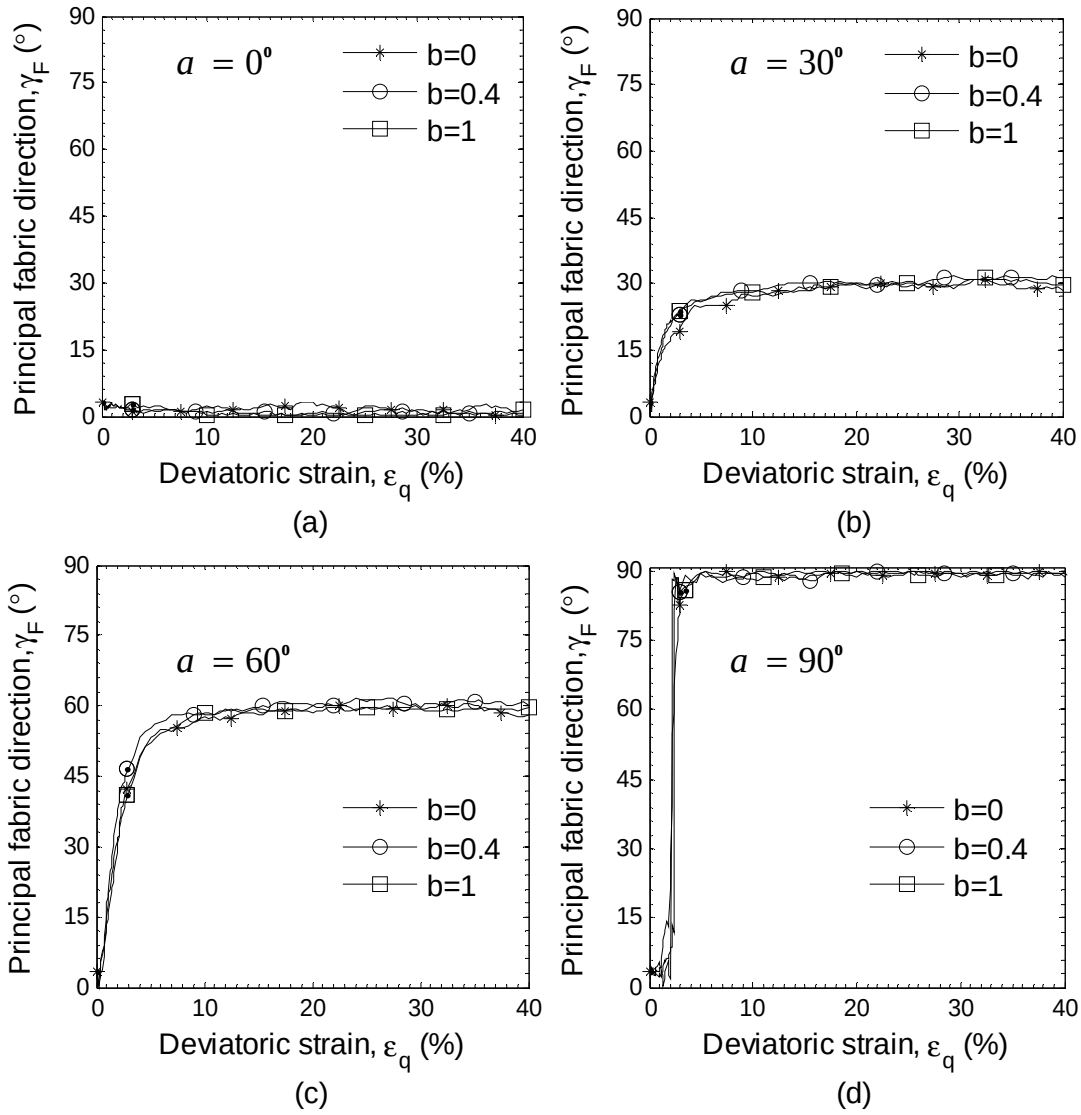

Fig. 6.23 Effects of *b* on principal fabric direction of pre-loaded sample SDEM_TC_TT at different loading directions (a) $a = 0^o$ **(b)** $a = 30^o$ **(c)** $a = 60^o$ **(d)** $a = 90^o$

6.4 Discussion

The non-coaxial behaviour can be explained in terms of the micro-scale contact force and fabric evolution. The non-coaxial behaviour is due to non-coincidence between the major principal fabric direction and the major principl

stress direction, resulting in non-coincidence between the principal tangential force direction and the principal stress direction. The normal contact force is found to be coaxial with loading direction (e.g., Fig. 6.20(b)) while the tangential force direction rotates gradually to the loading direction during shearing (Fig. 6.21(b)). The degree of non-coaxiality is dependent on the principal directions of contact normal fabric and contact force, as well as the degree of contact normal anisotropy and contact force anisotropy. Therefore, more deviation of the contact normal principal direction from the principal stress direction and higher degree of contact normal fabric anisotropy would results in more non-coaxial behaviour (Li and Yu, 2009).

Initially, the principal fabric direction is in the vertical deposition direction ($\psi_F = 0^o$). Upon shearing, the principal fabric direction is close to 0^o in similations with $\alpha = 0^o$, leading to coaxiality between the principal strain increment direction and principal stress direction. In simulations with $15^o \le \alpha \le 75^o$, the principal fabric direction gradually approaches the loading direction as shearing, resulting in non-coaxial deformation. And the principal fabric direction deviates more from the loading direction with the increasing α. Therefore, a higher degree of non-coaxiality is observed at greater tilting angle. When α further increases from 75^o to 90^o, however, the deviator fabric anisotropy D_F is smaller with increasing α in spite of a larger deviation between ψ_F and α. Thus, a smaller degree of non-coaxiality has been observed with further increasing α. At $\alpha = 90^o$, the principal fabric direction remains in the vertical direction ($\psi_F \approx 0^o$) during the initial 3% of deviatoric strain and then it nearly follows the loading direction with $\psi_F \approx 90^o$ by a

sudden change. Though the g_F initially deviates from the loading direction $a = 90^{o}$ significantly, the fabric anisotropy D_F decreases to a small value. Thus, the general coaxial behaviour is also observed. At large deformation, the principal fabric direction coincides with the loading direction, resulting in general coaxial behaviour at various loading directions.

Although the non-coaxial behaviour has been explained in the 2D DEM simulation, of which the intermediate principal stress is missing (Li and Yu, 2009). The 3D simulation, at least, confirms their observations. In addition, the b value has little influence on the degree of non-coaxiality since the fabric anisotropy and principal fabric direction remain similar at different b values (e.g., Fig. 6.23).

The critical state theory has been defined as the material reaches the constant stress ratio (critical stress ratio) and deforms continuously without volume change (constant void ratio) (Roscoe et al., 1958). Fig. 6.24 demonstrates the critical stress ratio for the sample SDEM_TT and the pre-loaded sample SDEM_TC_TT at various loading directions. The symbol with red solid line represents the results of sample SDEM_TT and the symbol with dark solid line refers to the results from pre-loaded sample. It is clear from Fig. 6.24 that the h_c shows little difference in both samples at different loading directions with constant b. This indicates the pre-loading history and loading direction have negligible influence on the critical stress ratio. Microscopically, the critical stress ratio is reached due to the microstructural tensors reaching critical anisotropy D_F, G_d^n, G_d^t and the principal directions of microstructural tensors being coaxial with loading direction, (e.g., Fig. 6.8 and Fig. 6.18). And the

critical fabric anisotropy D_F is independent of material anisotropy, with the same value $D_F \approx 0.6$ obtained at constant $b = 0.4$ simulation for samples SDEM_TT (Fig. 6.8) and SDEM_TC_TT (Fig. 6.18).

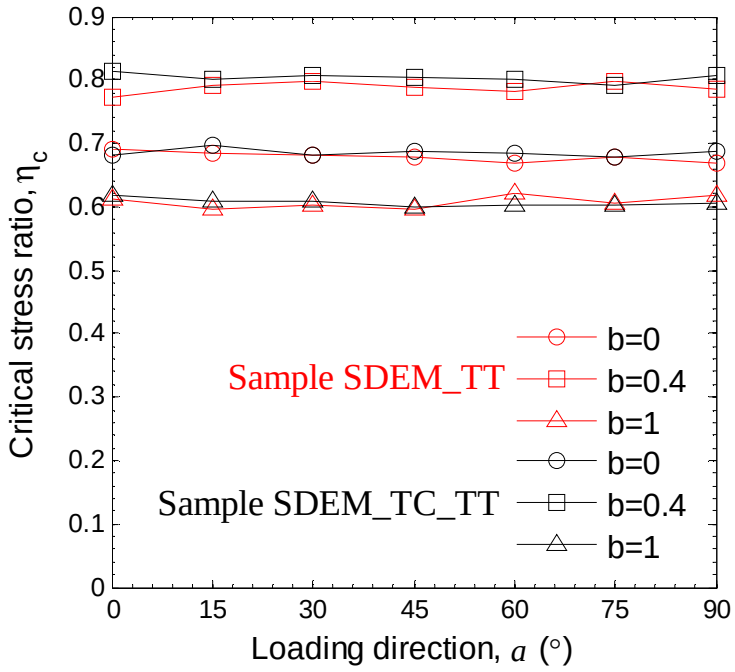

Fig. 6.24 Critical stress ratio of initial anisotropic sample SDEM_TC_TT and pre-loaded sample SDEM_TC_TT

The uniqueness of the critical state line due to anisotropy effect is controversial (Vaid and Chen, 1985, Yin and Chang, 2009, Dafalias and Li, 2013). In numerical simulations, the critical constant void ratio of the pre-loaded sample has not been achieved at 40% deviatoric strain as the volumetric strain seems to increase against further shearing (Fig. 6.11). However, the variation of volumetric strain at $e_q = 40\%$ becomes smaller compared to that at $e_q = 10\%$. If shearing continues, it is plausible to assume that the same critical void ratio may be achieved at various angle a, if it exists, or at least only with a tiny difference as that observed in the initially anisotropic sample (e.g., Fig. 6.3). Hence, the anisotropy effect on critical

state void ratio may not be significant. However, the deformation characteristics are strongly dependent on the loading direction before reaching critical state, where severer volume contraction has been observed at greater tilting angle a . By assuming the unique critical state exists, this is interpreted as when the anisotropic sample is sheared at various loading directions, the sample is considered to have different initial state fabric anisotropy in reference to the unique critical state fabric anisotropy. It indicates that the granular material initial state is not only dependent on the initial void ratio, e.g., state parameter proposed by Been and Jefferies (1985), but also the initial fabric relative to the critical state fabric. The DEM results support the anisotropic critical state theory proposed by Li and Dafalias (2012), where the critical state is constrained by the constant stress ratio, critical void ratio and critical fabric anisotropy, in terms of both its magnitude and principal direction.

6.5 Summary

This chapter presents the simulation results of the anisotropic sample with spherical particles under various loading directions. The anisotropic microstructure has been produced with more contacts oriented in the vertical deposition direction under gravitational field. The pre-loading history of the initially anisotropic sample results in a more anisotropic microstructure in terms of larger fabric anisotropy D_F .

When the initially anisotropic sample and the pre-loaded sample sheared at different loading directions a , the samples perform stiffer and more dilative at a smaller a . The anisotropic stress-strain behaviour is more obvious in the pre-loaded sample than the initially anisotropic sample. The deviator stress ratio capacity is

mainly dependent on the developed fabric anisotropy D_F, contact forces anisotropy G_d^n, G_d^t and their relative principal directions. Upon the same deviatoric strain, e.g., $e_q = 5\%$, the fabric anisotropy and normal contact force anisotropy are smaller at a greater tilting angle a. Hence, the anisotropic stress-strain behaviour has been observed before reaching mobilised stress ratios. However, both fabric anisotropy and contact force anisotropy approach similar values after large deformation, irrespective of loading directions. And the principal directions of the microstructural tensors become coaxial with the external loading direction. Thus, the effect of material anisotropy on stress-strain behaviour disappears and a similar critical stress ratio has been achieved.

The principal strain increment direction and the principal stress direction are generally coaxial for the initially anisotropic sample while significant non-coaxial behaviour is observed for the pre-loaded sample. The non-coaxial behaviour is due to the non-coincidence between the fabric tensor principal directions and stress tensor principal directions. The degree of non-coaxiality is dependent on the relative directions and relative magnitudes of fabric anisotropy and contact force anisotropy. For the initially anisotropic sample, the fabric anisotropy is small and the principal fabric direction evolves rapidly to the loading direction, although the initial fabric direction is not coaxial with the loading direction. Accordingly, the general coaxial behaviour is observed. For the pre-loaded sample, the fabric anisotropy is larger and the fabric direction rotates gradually to the loading direction. Hence, significant non-coaxiality is observed. After large deformation, the principal fabric direction becomes coaxial with loading direction, leading to coaxial behaviour.

Chapter 7 Influence of particle shape on granular material behaviour

7.1 Introduction

The previous chapters present the simulation results on samples of spherical particles, where the idealised particle shape is used. The real granular material, e.g., sand, generally consists of non-spherical particles. In this chapter, the numerical simulations results are presented on samples with non-spherical clump particles and are compared to the results on sample with spherical particles, to investigate the effect of particle shape on granular material behaviour. The observations on material responses under triaxial compression and simulations with tilting principal stress directions are qualitatively compared to each other.

7.2 Sample preparation

The initially isotropic samples prepared by the radius expansion method have been introduced in Section 4.3.1. The individual non-spherical clump particle has been defined in Section 3.3.1. The initially isotropic dense sample CRED_TT is

prepared with non-spherical particles randomly positioned within the polyhedral boundary ($n = 8$ and $R = 0.0065m$). Details of prepared initial samples are summarised in Table 7.1. The sample size, over 3000 particles, is sufficient to produce typical stress-strain behaviour, as validated in Section 3.3.2. The mechanical parameters used for numerical simulation are the same as that used for spherical particles in Table 4.1. It can be seen that the sample CRED_TT of non-spherical particles has a lower initial void ratio ($e_0 = 0.59$) than the sample SRED_TT of spherical particles ($e_0 = 0.64$) under otherwise the same generation procedures. The prepared samples are used for simulation results presented in Section 7.3.

Table 7.1 Samples information of initially isotropic dense sample with different particle shapes

Sample	m_g	e_g	Initial pressure $p_g\ (kPa)$	Void ratio e_0	No. of particles
CRED_TT	0.1	0.59	447	0.6	5053
SRED_TT	0.1	0.64	450	0.64	11090

The initially anisotropic samples of non-spherical particles were generated by the gravitational deposition method as introduced in Section 4.3.2. The cubic box had the three dimensions (length, width, height) of $0.0192m \times 0.0192m \times 0.133m$, resulting in 18876 particles generated. Two samples with different initial void ratios have been prepared by setting the frictional coefficient $m_g = 0.01$ and $m_g = 0.5$ during the deposition process. After the deposition process completed and material

equilibrium satisfied, the polyhedral boundary walls were generated by selecting $n = 8, R = 0.0066$ for the dense sample CDED_TT and $n = 8, R = 0.0068$ for the loose sample CDEL_TT. Then, the particles outside the boundary walls were deleted and the friction coefficient was restored to the normal value $m = 0.5$. Finally, simulation was carried out to achieve static equilibrium and the samples were isotropically consolidated to the mean normal stress of $500kPa$. At this stage, the void ratio e_0 is recorded as initial void ratio. The details of the prepared samples are summarised in Table 7.2.

Table 7.2 Initially anisotropic samples of non-spherical clump particles

Anisotropic sample	m_g	Initial pressure $p_g\ (kPa)$	Void ratio e_0	No. of particles
CDED_TT	0.01	440	0.64	5188
CDEL_TT	0.5	416	0.77	5178

7.3 Effect of particle shape on isotropic material behaviour

7.3.1 Macro-scale material behaviour

The triaxial compression tests ($b = 0$) have been conducted on the isotropic samples with different particle shapes under constant mean normal stress $p = 500kPa$ and fixed principal stresses directions along coordinate axis. The

stress-strain behaviour of two samples with different particle shape is shown in Fig. 7.1. Both samples exhibit strain hardening and strain softening behaviours. The dilative volumetric expansion is also observed in the two samples. Despite the common observations, it is clear that the sample CRED_TT performs stiffer and more dilative than the sample SRED_TT. A much higher peak stress ratio is obtained in the sample CRED_TT. At large deformation, the sample SRED_TT is approaching the critical state with constant volumetric strain while the sample CRED_TT seems to dilate further as shearing continues. Macroscopically, this is well understood as the granular assembly with angular particles being more shearing resistant and dilative than that with rounded particles since the particle sliding and rotation mechanism can occur more easily between rounded particles. In addition, excess particle rotation could happen in DEM simulation in assembly of spherical particles, which is unrealistic. And it is suggested that the rolling resistance should be incorporated into DEM simulations (Iwashita and Oda, 1998, Jiang et al., 2005). However, this topic is not considered in this study.

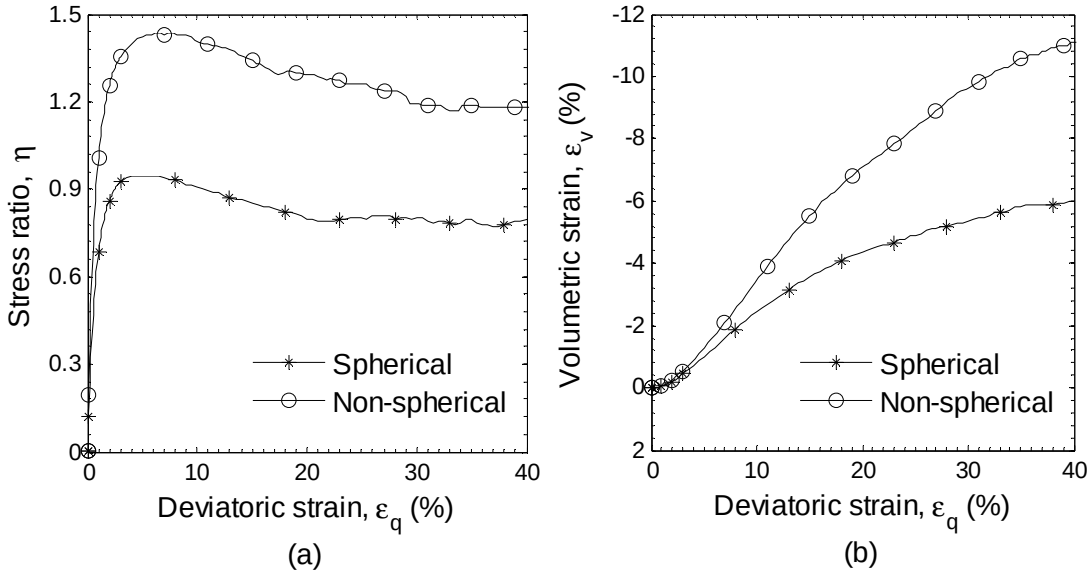

Fig. 7.1 Effects of particle shape on material response during triaxial compression ($b = 0$) (a) stress-strain behaviour (b) volumetric strain

7.3.2 Micro-scale observations

7.3.2.1 Fabric evolution

The influence of particle shape on the evolution of microscopic parameters during triaxial compression, i.e., coordination number w and contact normal anisotropy D_F, is plotted in Fig. 7.2. It shows that the sample CRED_TT initially has a larger coordination number than the sample SRED_TT with a difference of $w = 2.6$. It indicates the non-spherical particles assembly are closer packed and individual particle gains more contact support from its neighbours, corresponding to the smaller void ratio in the sample CRED_TT. The coordination number of both samples reduces significantly during the initially 10% of deviatoric strain due to volumetric dilation and the difference of w between two samples is narrowed to 1.5. This difference remains constant for further shearing. Fig. 7.2(b) demonstrates the

developed contact normal anisotropy D_F during shearing. Initially, the fabric anisotropy is close to zero in both samples, corresponding to the initially isotropic internal structure. The evolution of D_F against shearing is similar for both samples. However, the fabric anisotropy D_F is much larger in the sample CRED_TT than the sample SRED_TT at the same deviatoric strain.

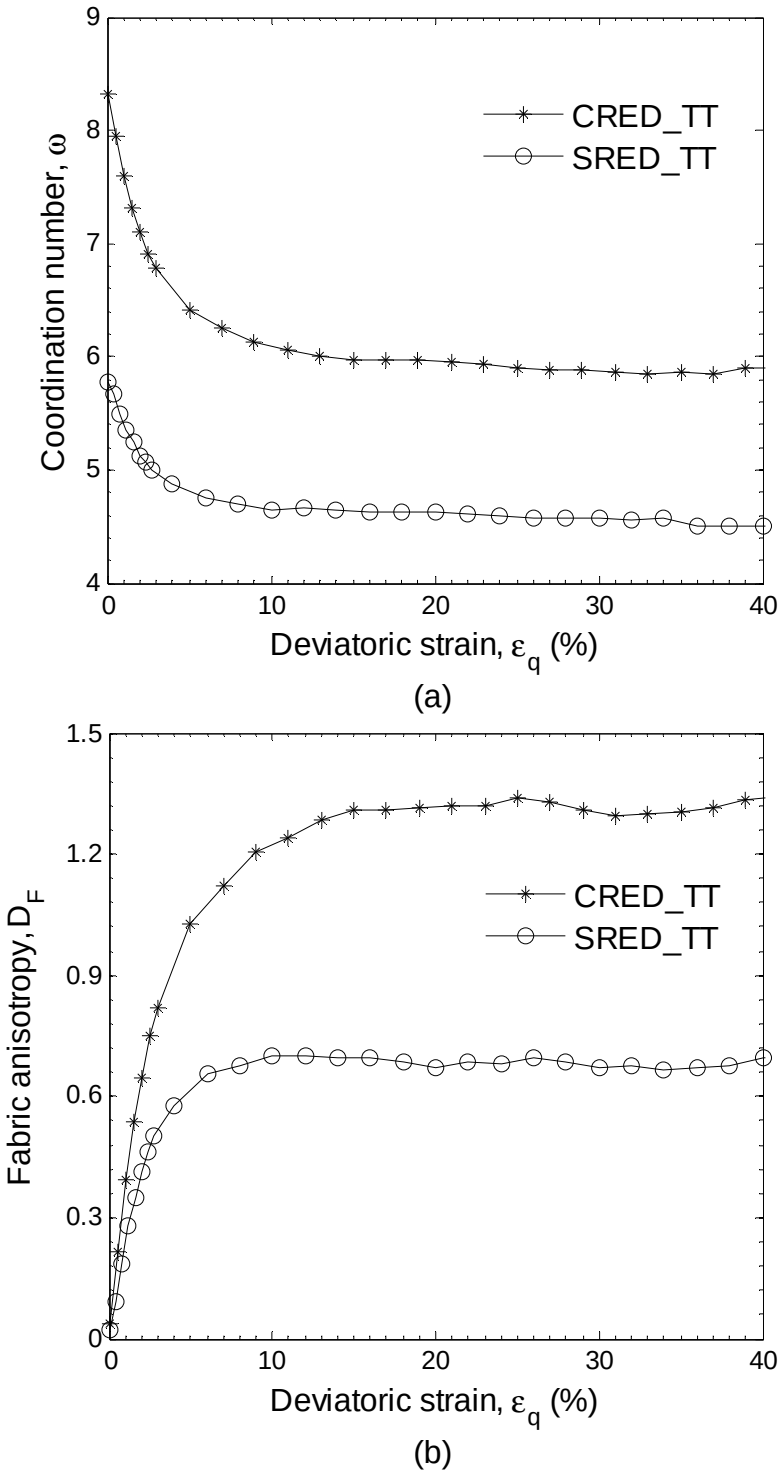

Fig. 7.2 Effects of particle shape on (a) coordination number (b) fabric anisotropy

7.3.2.2 Particle interaction force

The particle shape effect on mean normal force f_0 evolution is shown in Fig. 7.3. At the same deviatoric strain, the mean normal force in sample of spherical particles is 1.3 ~ 1.5 times larger than that in sample of non-spherical particles. As the mean normal stress is constant, the mean normal force is reversely proportional to the coordination number (e.g., Fig. 7.2(a)), where coordination number in sample of spherical particles is approximately 1.3 times less than that in sample of non-spherical particles.

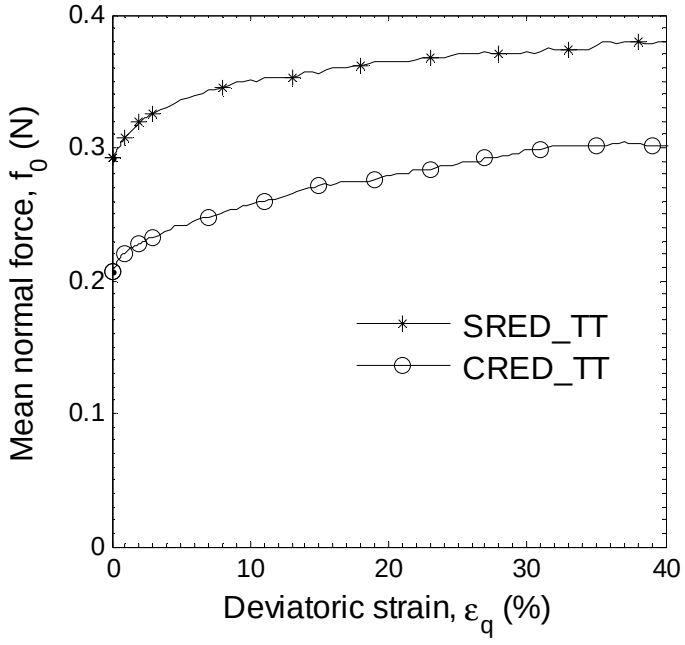

Fig. 7.3 Particle shape effect on mean normal force

The effect of particle shape on the contact force anisotropy is plotted in Fig. 7.4. The contact force anisotropy is partitioned into normal contact force anisotropy G_d^n and tangential contact force anisotropy G_d^t. It can be found that the normal and tangential contact force anisotropy increase rapidly against shearing to the peak value, corresponding to the strain hardening process in both samples. Then, the

contact force anisotropy decreases to the steady value owing to buckling force chains, dominating the strain softening behaviour. However, the normal and tangential contact force anisotropy is much larger in the sample with non-spherical particles than the sample with spherical particles.

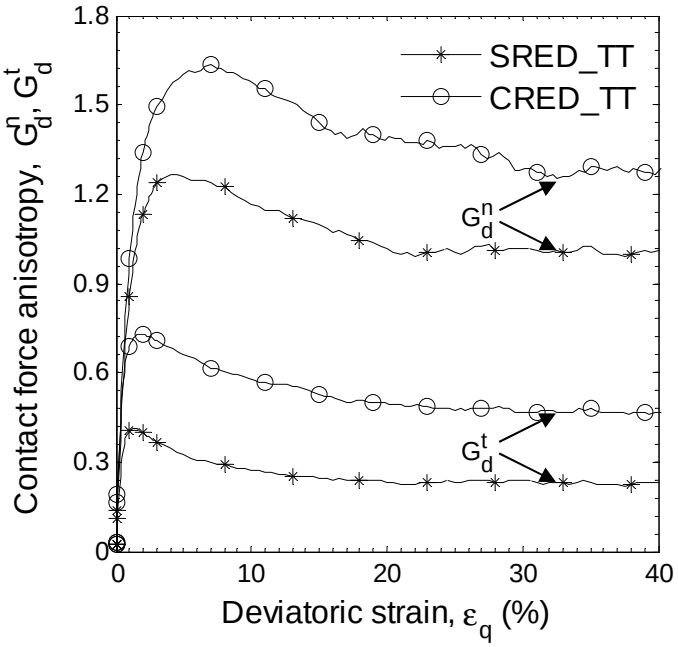

Fig. 7.4 Effects of particle shape on contact force anisotropy

The individual contact friction mobilisation coefficient is determined by the frictional force normalised by the normal contact force as $m_c = |f_t| / f_n$. The evolution of its average over all contacts $m_a = \langle |f_t| / f_n \rangle$ is shown in Fig. 7.5. It can be seen that the frictional mobilisation coefficient increases rapidly to the peak against shearing, corresponding to the anisotropic contact force distribution stabilised by frictional resistance. It is then followed by tiny decrease to steady value for both samples. The average friction mobilisation is much larger in the sample with non-spherical particles than that in the sample with spherical particles. Hence, the sample with non-spherical particles exhibits a higher strength characteristic due to

more anisotropic microstructure developed, in terms of greater fabric anisotropy and contact force anisotropy, and larger friction mobilisation.

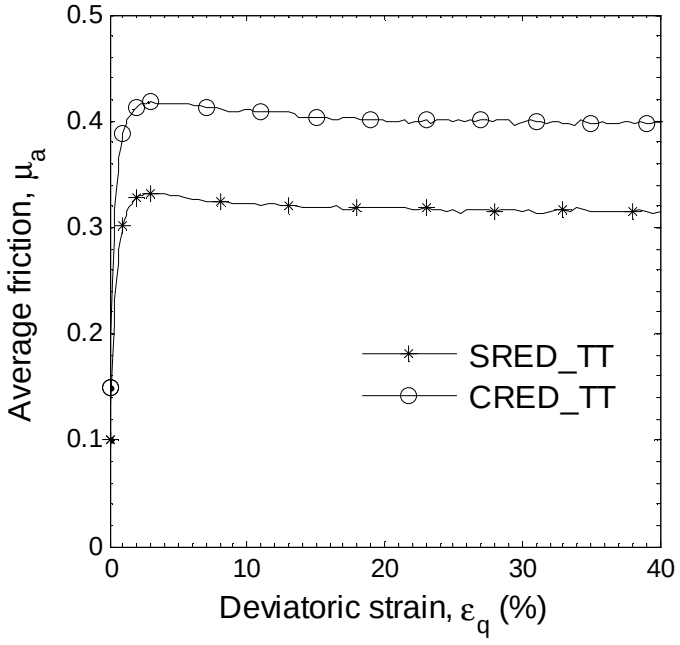

Fig. 7.5 Effect of particle shape on contact friction mobilisation coefficient

7.4 Combined effect of *b* value and cross-anisotropy

7.4.1 Numerical simulation procedures

The gravitational deposited samples have an initially cross-anisotropic internal structure with transversely isotropy in the horizontal bedding plane, i.e., the *x-y* plane in Fig. 7.6. The true triaxial loading paths on initially cross-anisotropic sample are illustrated in Fig. 7.6, in considering both the magnitude and principal directions of principal stresses. In sector I ($0^{o} \le q \le 60^{o}$), where $q = \tan^{-1}\left(\sqrt{3}b/(2-b)\right)$ is the stress lode angle, the major principal stress direction and intermediate principal stress direction are fixed along the *z*-axis ($a = 0^{o}$) and

the *y*-axis, respectively. In sector II ($60^o \le q \le 120^o$), the major principal stress direction and intermediate principal stress direction are fixed along the *y*-axis ($a = 90^o$) and the *z*-axis, respectively. In sector III ($120^o \le q \le 180^o$), the major principal stress direction and intermediate principal stress direction are fixed along the *x*-axis ($a = 90^o$) and the *y*-axis, respectively. In each sector, the intermediate stress ratio b varies from 0 to 1 with 0.2 intervals. The numerical true triaxial tests have been conducted on samples CDED_TT and CDEL_TT in three sectors to investigate the cross-anisotropic behaviour of granular material. The numerical simulations plan is shown in Table 7.3.

Table 7.3 True triaxial simulations plan on initially anisotropic samples of non-spherical particles

Anisotropic samples	Sector I $a = 0^o$ $0^o \le q \le 60^o$	Sector II ($a = 90^o$) $60^o \le q \le 120^o$	Sector III $a = 90^o$ $120^o \le q \le 180^o$
CDED_TT	$b \in [0,1]$ with 0.2 interval	$b \in [0,1]$ with 0.2 interval	$b \in [0,1]$ with 0.2 interval
CDEL_TT			

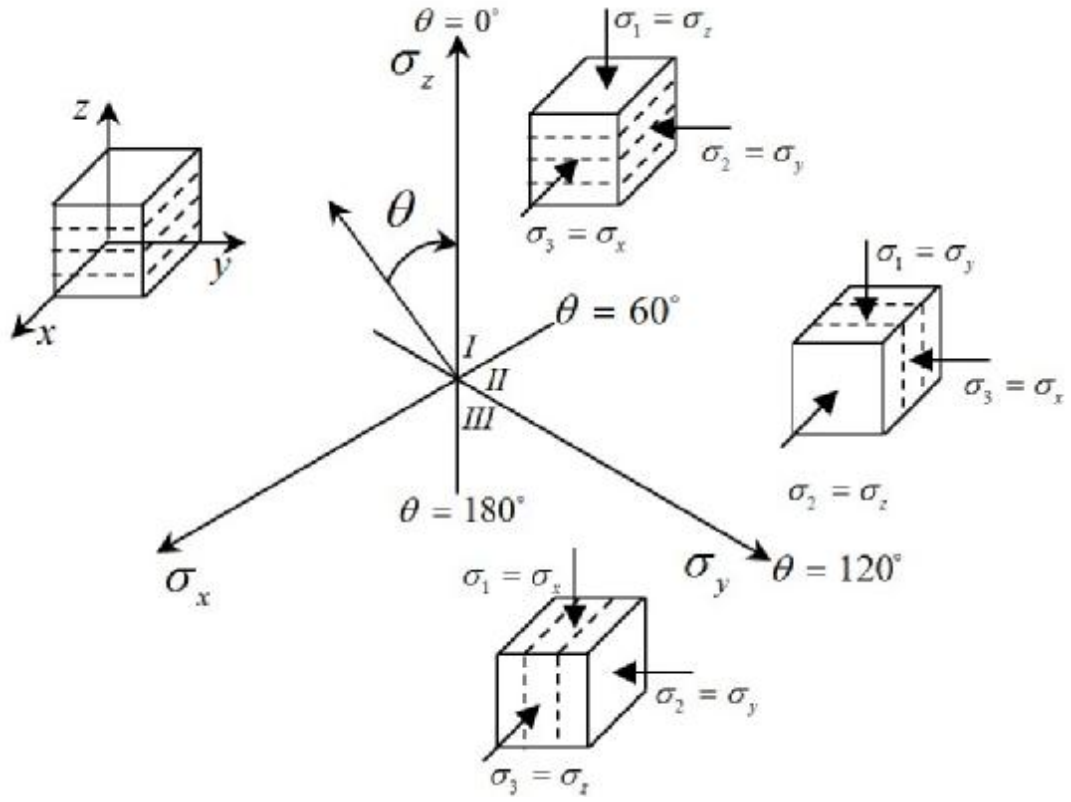

Fig. 7.6 Illustration of true triaxial tests in three sectors on octahedral plane with different combinations of relative directions of major, intermediate, minor principal stresses, s_1, s_2 and s_3 to bedding plane

7.4.2 True triaxial tests with on initially anisotropic samples

The effects of cross-anisotropy on the stress-strain behaviours of samples CDED_TT and CDEL_TT are demonstrated in Fig. 7.7. It shows that the dense sample CDED_TT exhibits strain hardening with a peak stress ratio reached, followed by strain softening behaviour. The loose sample CDEL_TT hardens continuously. In asymmetric loading conditions ($b = 0$, $b = 1$), the stress-strain behaviour are identical when triaxial compression ($b = 0$) conducted in Sector II and Sector III and triaxial extension ($b = 1$) conducted in Sector I and Sector II, which is due to the same loading path in considering material cross-anisotropy (or

transversely isotropy in horizontal plane). Under otherwise loading conditions, it is generally observed that the sample sheared in Sector I exhibits the highest stress ratio and the lowest stress ratio is obtained when sheared in Sector III, with middle values occurred in Sector II at the same deviatoric strain, e.g., $e_q = 5\%$, for both samples. And the samples perform most dilative in Sector I, followed by Sector II and Sector III, successively. Similar results are also reported on the anisotropic deformation characteristics of sand (Yamada and Ishihara, 1979, Haruyama, 1981). At large deformation, the effects of cross-anisotropy on the strength becomes small and the stress ratios reach similar values for both samples, regardless of loading directions at constant b simulation. It indicates that the critical stress ratio is independent of the initial void ratio and material anisotropy. The volumetric strain approaches the steady value but does not reach the same value at $e_q = 40\%$ in three Sectors.

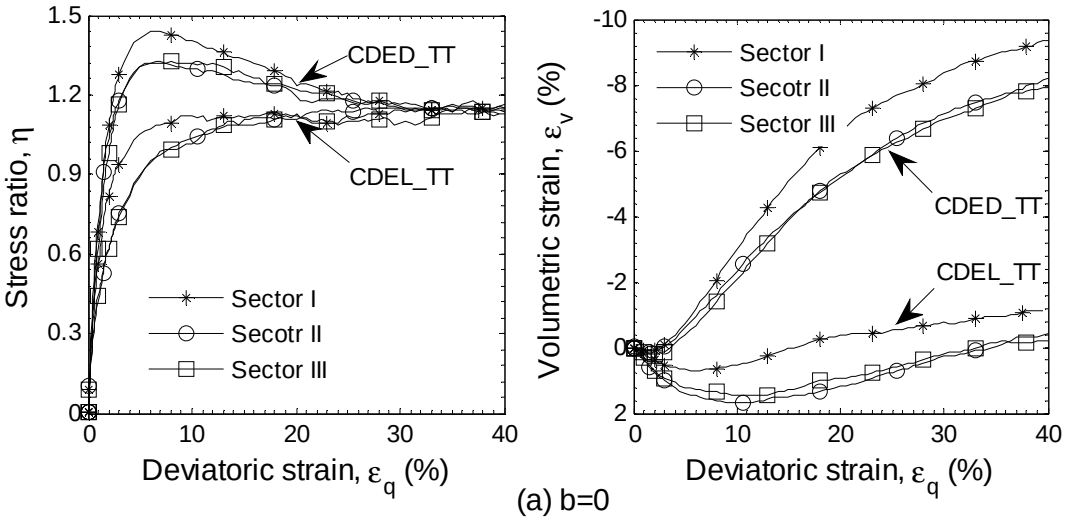

(a) b=0

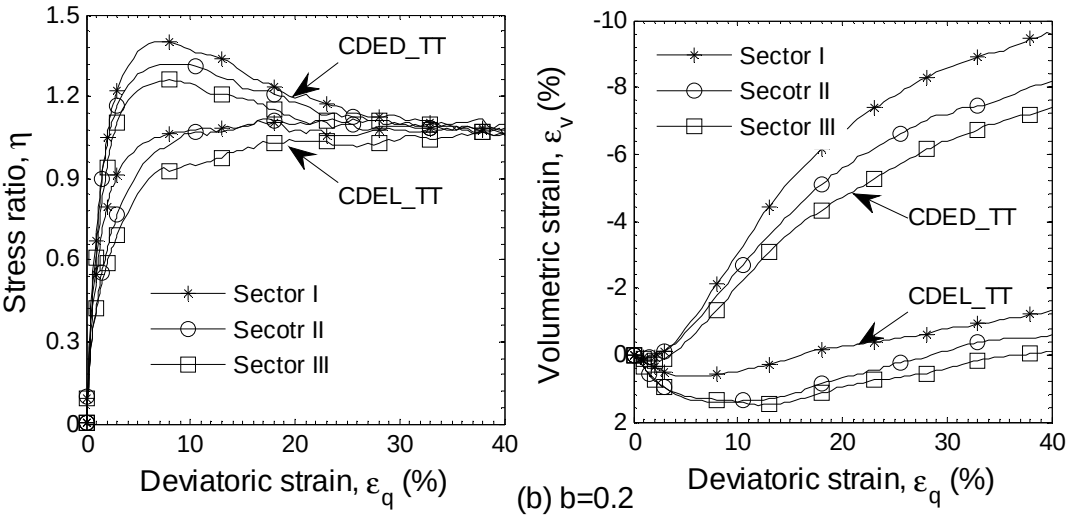

(b) b=0.2

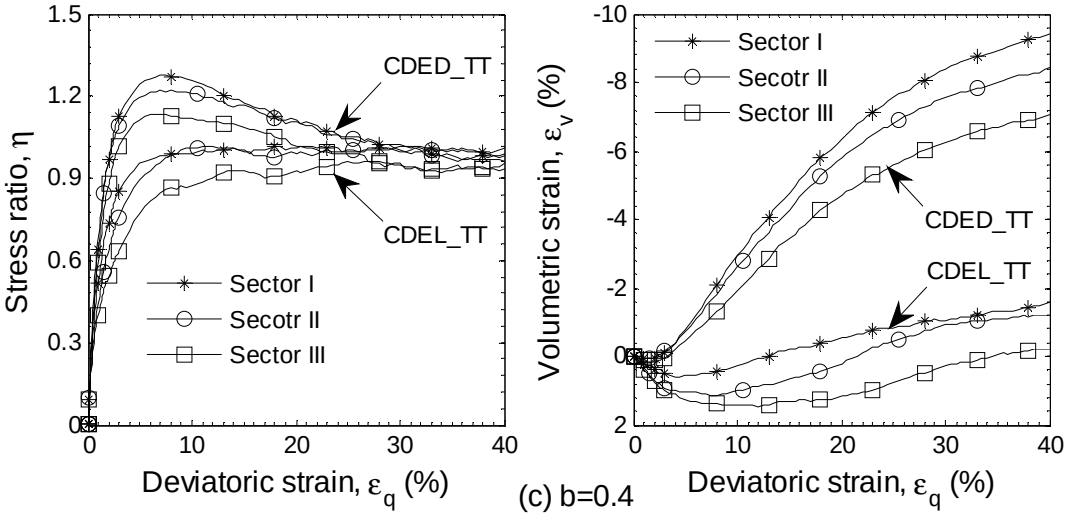

(c) b=0.4

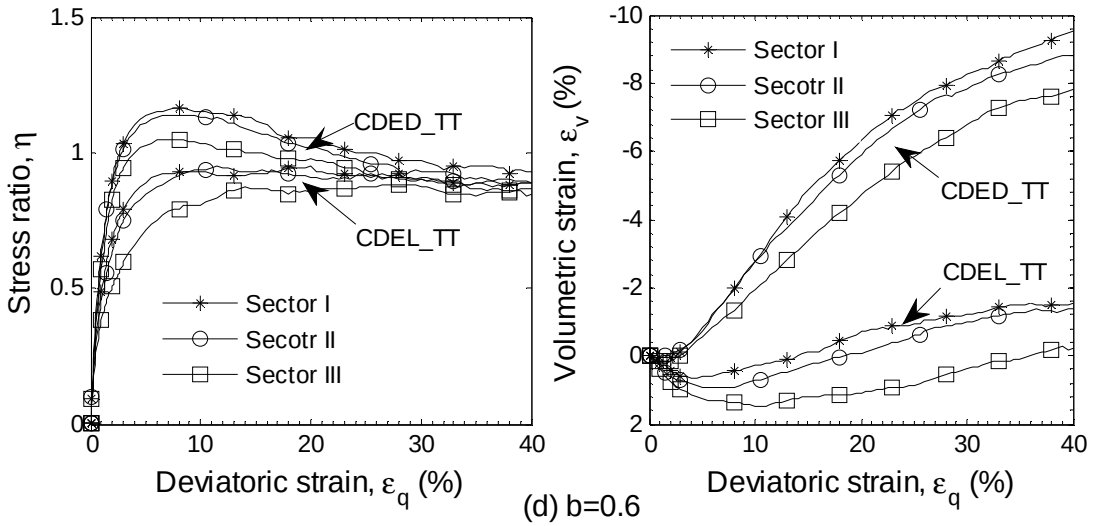

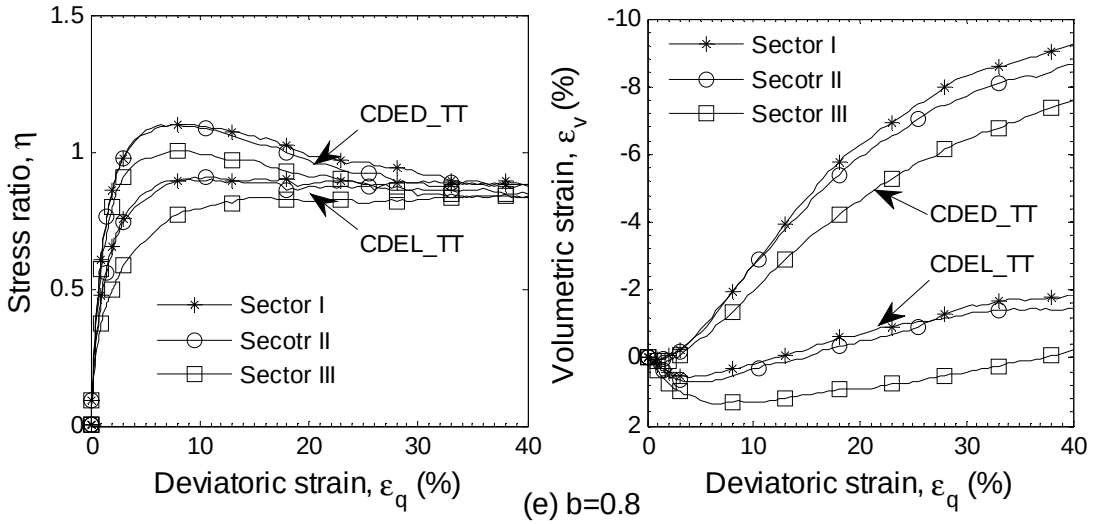

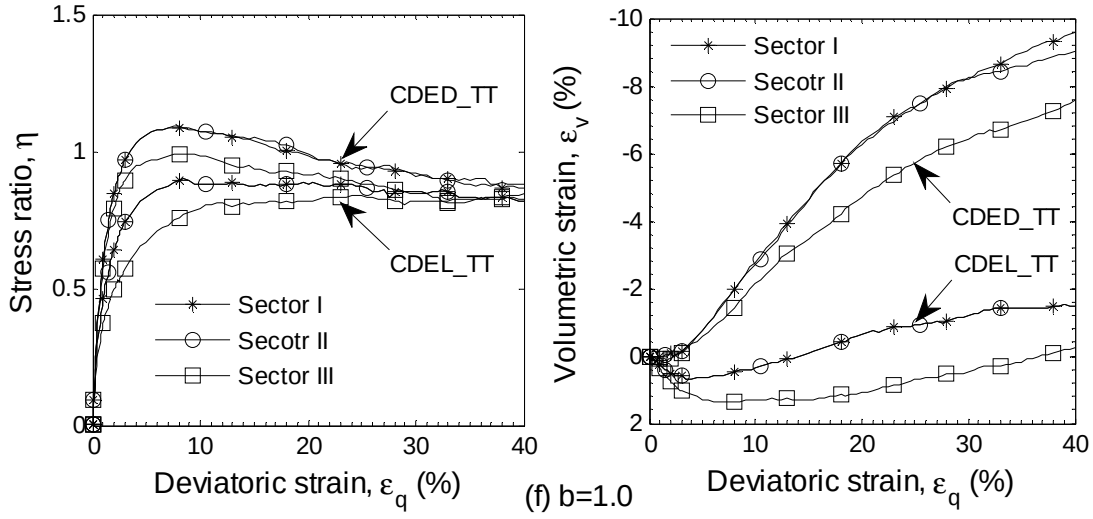

Fig. 7.7 Effects of cross-anisotropy on stress-strain behaviour in true triaxial tests in three sectors

The effects of cross-anisotropy on the dilatancy behaviour is interpreted as dilation angle as shown in Fig. 7.8. The dilation angle j is calculated as $\sin j = -\frac{d\varepsilon_v / d\varepsilon_1}{2 - d\varepsilon_v / d\varepsilon_1}$, where $d\varepsilon_v$ and $d\varepsilon_1$ are the total volumetric strain increment and major principal strain increment at the peak stress ratio and it is determined under small deviatoric strain increment $\Delta e_q = 0.5\%$ (Schanz and Vermeer, 1996, Lade and Abelev, 2003b) . It is clear from the figure that the dilation angle increases at a greater b value in each sector. This is more significant in the dense sample as the difference of j in the triaxial compression ($b = 0$) and the triaxial extension ($b = 1$) is around 9^o while it is about 4^o in the loose sample. At the same b value, the dilation angle is largest in Sector I and smallest in Sector III for the dense sample and the difference of j is up to 6^o at $b = 0.6$. Similar observations of cross-anisotropy on dilation angle can be seen for the loose sample except for small difference of j observed in three sectors when $b \le 0.4$. The maximum difference of j in three sectors is around 1.7^o at $b = 0.8$ for the loose sample. Similar results of anisotropic dilatancy behaviour can be found in the experimental study (Lade and Abelev, 2003b).

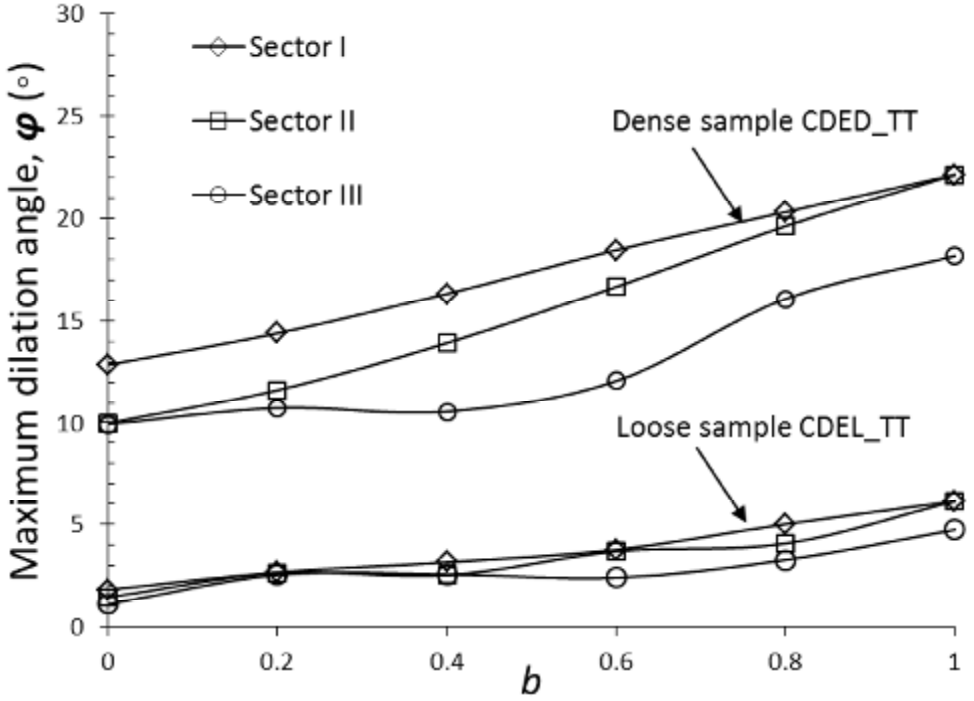

Fig. 7.8 Effects of cross-anisotropy on dilation angle

7.4.3 Micro-scale observations

The effect of cross-anisotropy on the contact normal fabric evolution is shown in Fig. 7.9 in simulations at different b values. Before shearing, the contact normal fabric anisotropy D_F is not equal to zero with $D_F = 0.42$ for the dense sample CDED_TT and $D_F = 0.51$ for the loose sample CDEL_TT. This clearly shows the anisotropic microstructure formed due to the gravitational deposition process. As shearing occurs, in sector I, it is observed that D_F increases to its maximum value in the dense sample, followed by continuous decrease to its ultimate steady value, and D_F shows continuous increase with decreasing rate to its ultimate value in the loose sample. In Sector II, D_F is found to decrease initially to its minimum value for both samples. Then, it starts to increase to reach its ultimate

steady value. In Sector III, the D_F initially decreases to its lowest value for both samples and the reduction is larger than that occurred in Sector II at the same b value. Then, it increases gradually to its ultimate constant value and no peak value has been observed. The initial decrease of D_F is due to the applied major principal stress direction is not coaxial with the major principal direction of initial fabric anisotropy. The initial fabric evolves gradually to orient itself to the principal stress direction. The minimum value of D_F is the turning point where the major principal fabric direction becomes coaxial with the loading direction.

Generally, the samples sheared in Sector I have the highest D_F at the same deviatoric strain, resulting in a higher stress ratio achieved in Sector I than the other Sectors even tested at the same b value. The difference of D_F in three sectors becomes smaller at large shearing strain level. At the end of shearing, the D_F reaches the similar constant value, termed as critical fabric anisotropy, in dense and loose samples in the same sector as seen in Fig. 7.14. The critical D_F is generally greatest in Sector I and lowest in Sector III. Accordingly, the difference of critical stress ratio achieved in three sectors (see Fig. 7.13) is small as the fabric anisotropy reaches similar values. The small variation of the critical stress ratio in the middle range of b values is related to the slightly larger critical fabric anisotropy in Sector I than in Sector III, as shown in Fig. 7.14.

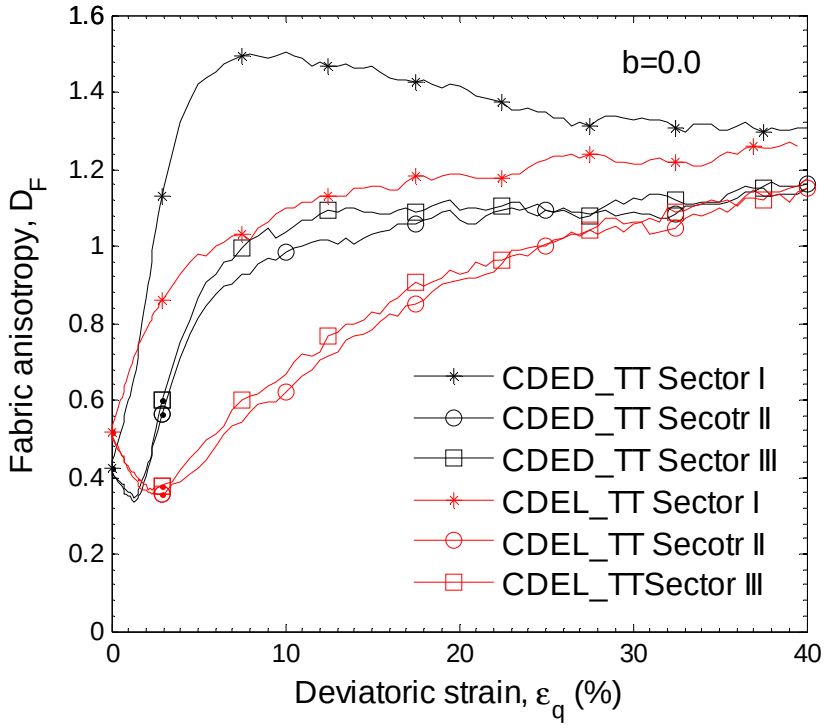
b=0.0
Fabric anisotropy, D_F
Deviatoric strain, ε_q (%)
CDED_TT Sector I
CDED_TT Secotr II
CDED_TT Sector III
CDEL_TT Sector I
CDEL_TT Secotr II
CDEL_TTSector III
0
0.2
0.4
0.6
0.8
1
1.2
1.4
1.6
0
10
20
30
40

(a)

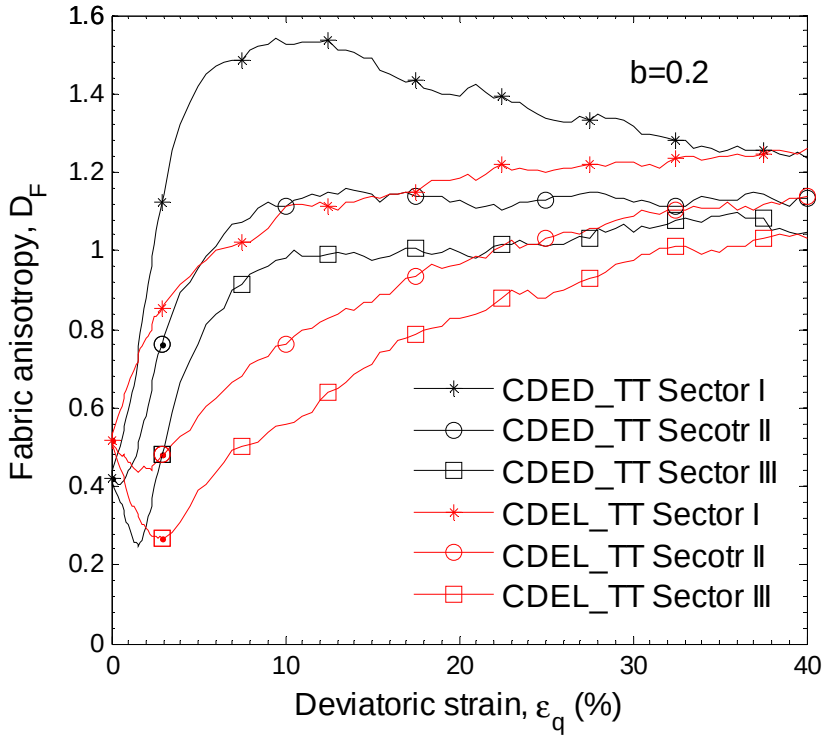
b=0.2
Fabric anisotropy, D_F
Deviatoric strain, ε_q (%)
CDED_TT Sector I
CDED_TT Secotr II
CDED_TT Sector III
CDEL_TT Sector I
CDEL_TT Secotr II
CDEL_TT Sector III
0
0.2
0.4
0.6
0.8
1
1.2
1.4
1.6
0
10
20
30
40

(b)

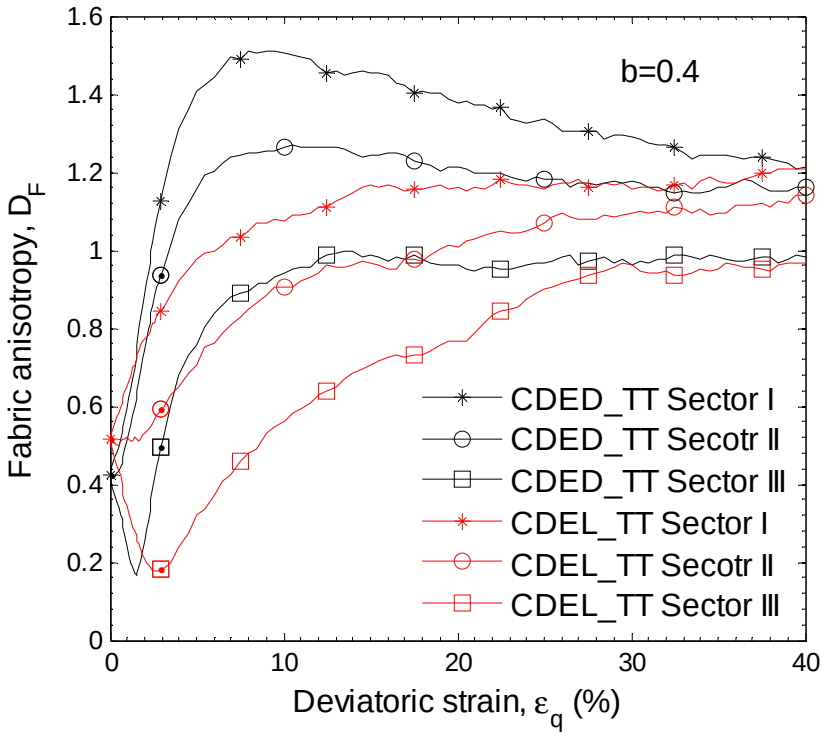
b=0.4
Fabric anisotropy, D_F
Deviatoric strain, ε_q (%)
CDED_TT Sector I
CDED_TT Secotr II
CDED_TT Sector III
CDEL_TT Sector I
CDEL_TT Secotr II
CDEL_TT Sector III
0
0.2
0.4
0.6
0.8
1
1.2
1.4
1.6
0
10
20
30
40

(c)

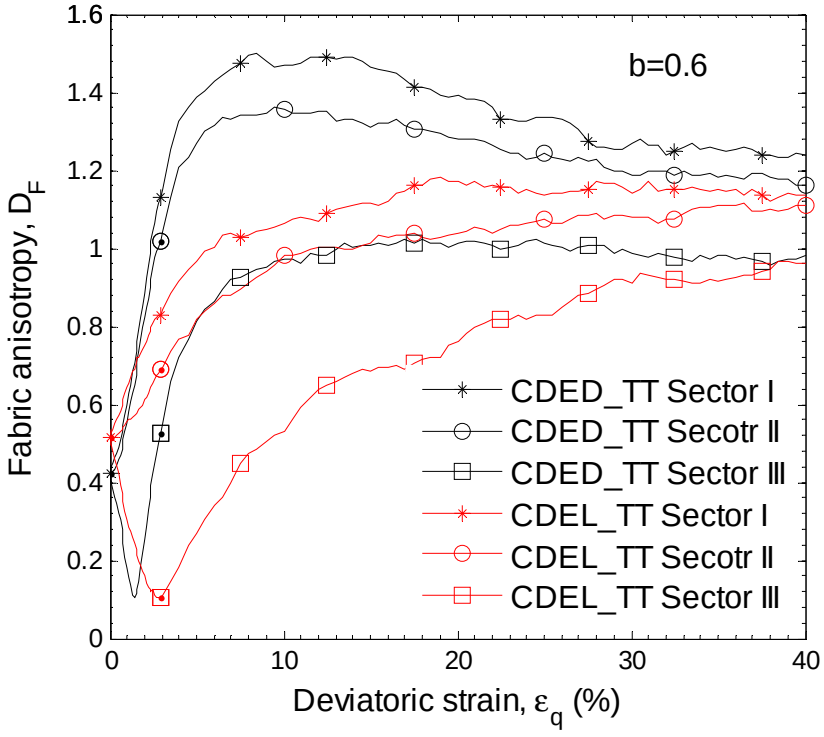
b=0.6
Fabric anisotropy, D_F
Deviatoric strain, ε_q (%)
CDED_TT Sector I
CDED_TT Secotr II
CDED_TT Sector III
CDEL_TT Sector I
CDEL_TT Secotr II
CDEL_TT Sector III
0
0.2
0.4
0.6
0.8
1
1.2
1.4
1.6
0
10
20
30
40

(d)

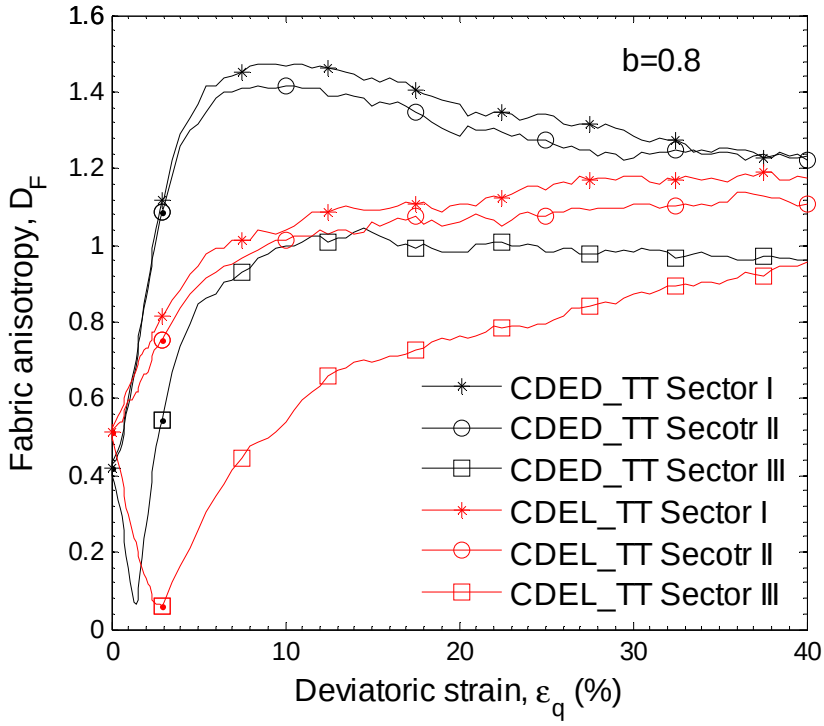

(e)

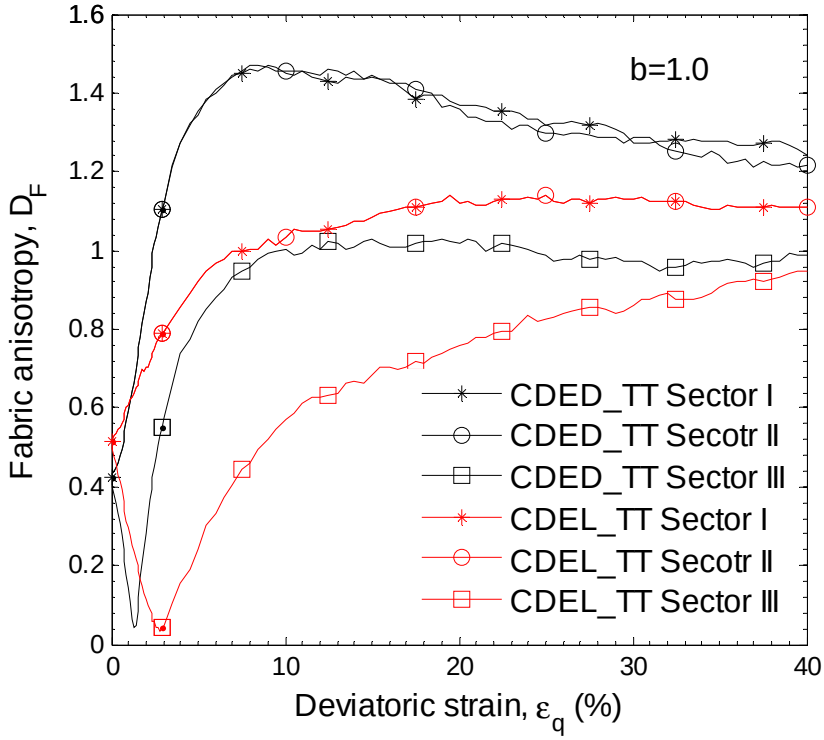

(f)

Fig. 7.9 Effects of cross-anisotropy on fabric anisotropy evolution in true triaxial simulations in three sectors

7.4.4 Discussion

To have a better view of the effects of initial cross-anisotropy on yielding and strength characteristics, Fig. 7.10 shows the maximum internal friction angle f_{max} of the dense sample CDED_TT obtained at peak stress ratio in three sectors and the internal friction angle f of the loose sample CDEL_TT at different deviatoric strain levels due to no softening behaviour for the loose sample. The curves with diamond, square and triangle symbols represent f obtained in Sector I, Sector II and Sector III, respectively. The peak strength f_{max} of the sample CDED_TT increases initially from $b = 0$ to $b \approx 0.5$. Then, it decreases slightly with the increasing b value to 1. Similar variations of $f - b$ relations for the loose sample CDEL_TT can be observed, though the variation is small at $e_q = 1\%$. At the same b, the friction angle of the dense sample at peak stress ratio or the loose sample at different shearing levels is generally larger in Sector I than in Sector II, with the lowest value obtained in Sector III. The difference of the f between Sector I and Sector II becomes small with increasing b value while it enlarges between Sector II and Sector III. Those results clearly show the significant effect of cross-anisotropy on the anisotropic failure strength or yielding behaviour of granular material. Similar observations have also been achieved by experimental study of cross-anisotropic sand behaviour (Yamada and Ishihara, 1979, Haruyama, 1981, Ochiai and Lade, 1983, Abelev and Lade, 2003a).

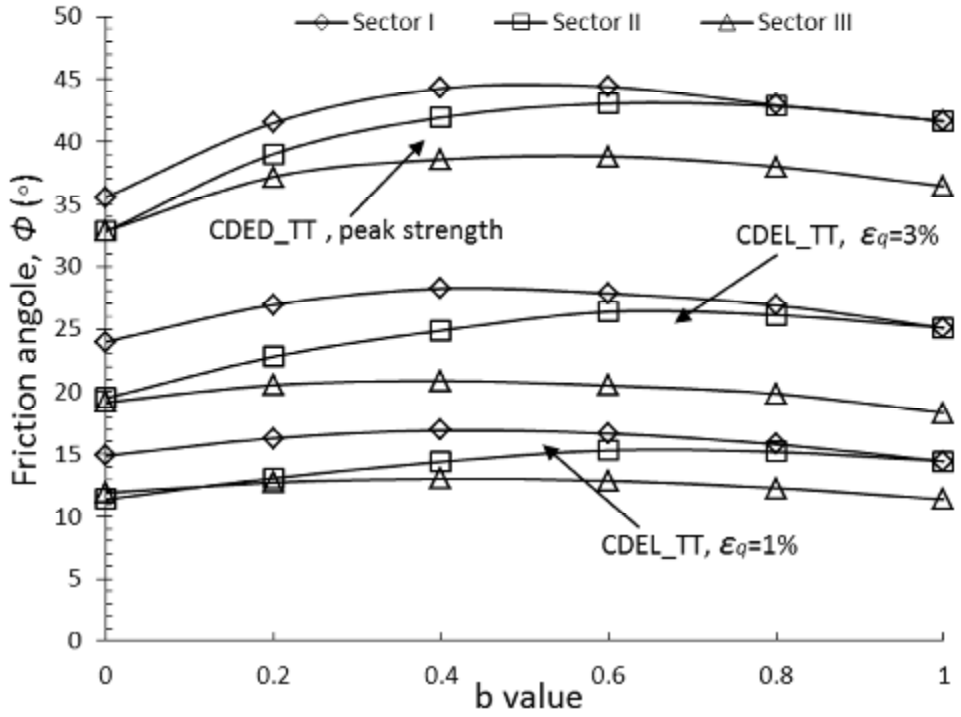

Fig. 7.10 Effects of cross-anisotropy on peak friction angle of the sample CDED_TT and friction angle of the sample CDEL_TT at different strain levels

The three-dimensional isotropic failure criterions have been formulated to predict the soil strength (Matsuoka and Nakai, 1974, Lade, 1977). However, the sand material is initially anisotropic and the failure strength may be different even tested with the same magnitude of stress conditions. The peak stress ratios of the dense sample CDED_TT obtained from true triaxial simulations are plotted in the octahedral plane as square hollow symbols, as shown in Fig. 7.11. The surface with solid line represents the isotropic failure surface proposed by Lade (1977), of which model parameter is determined from the triaxial compression simulation in Sector I. It can be seen that the DEM results cannot be captured by the isotropic failure criterion with significant overestimation of the peak stress ratio in Sector III. On the contrary, the DEM failure surface is cross-anisotropic in the octahedral plane and the

failure strength of the initially anisotropic sample CDED_TT is dependent on the applied principal stress directions.

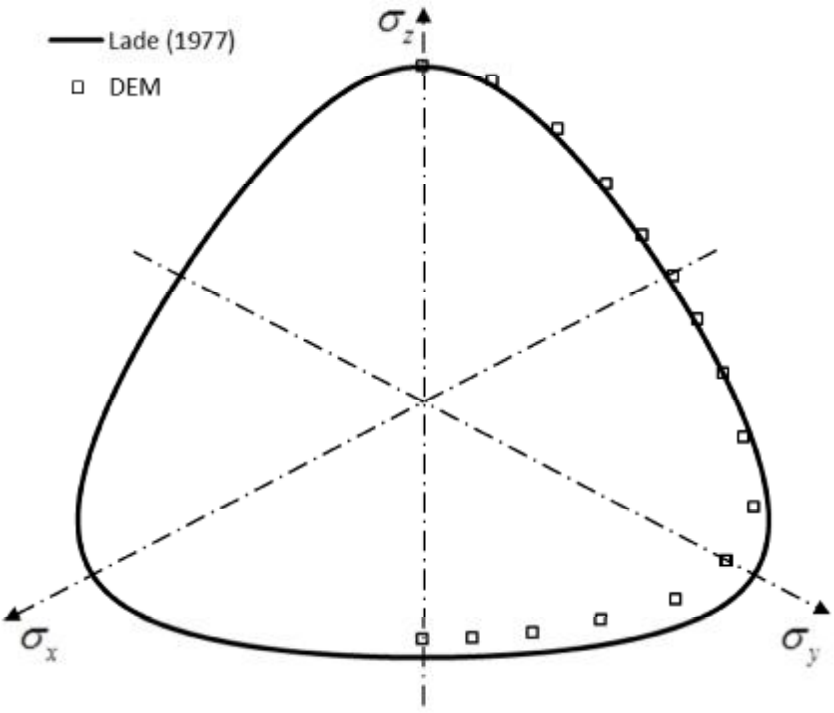

Fig. 7.11 Cross-anisotropic failure surface on the octahedral plane

The fabric anisotropy at peak stress ratio or particular strain level is illustrated in Fig. 7.12. The fabric anisotropy of the dense sample CDED_TT in three sectors is the value of D_F at the peak stress ratio and the fabric anisotropy of the loose sample CDEL_TT in three sectors is the value of D_F at $e_q = 1\%$, corresponding to the anisotropic failure or yielding, as shown in Fig. 7.10. It is clear that the anisotropic failure strength or anisotropic yielding is dependent on the anisotropic fabric anisotropy D_F developed in three sectors.

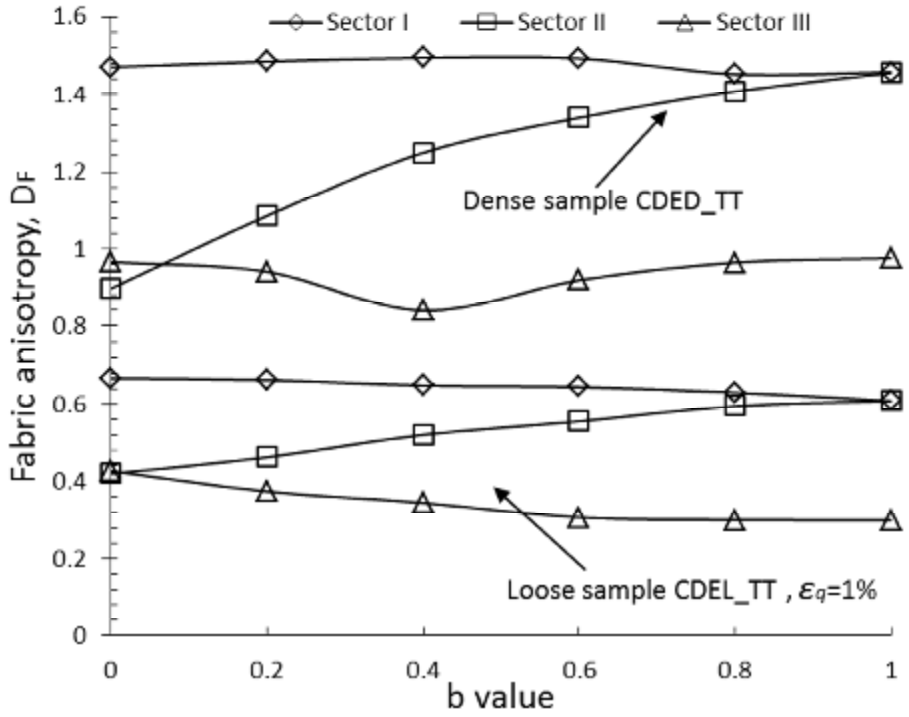

Fig. 7.12 Fabric anisotropy at failure point in the dense sample and $e_q = 1$% in the loose sample

Fig. 7.13 shows the critical stress ratio h_c, which is the average value of stress ratio at the last 5% of deviatoric strain for both samples. It can be seen that critical stress ratio decreases with the increasing b value. In simulations at the same b, h_c approaches similar values for dense and loose samples due to initial anisotropy effects disappeared at large deformation, irrespective of different sectors. This is microscopically explained that the materials approach similar critical internal structure anisotropy, as shown in Fig. 7.14.

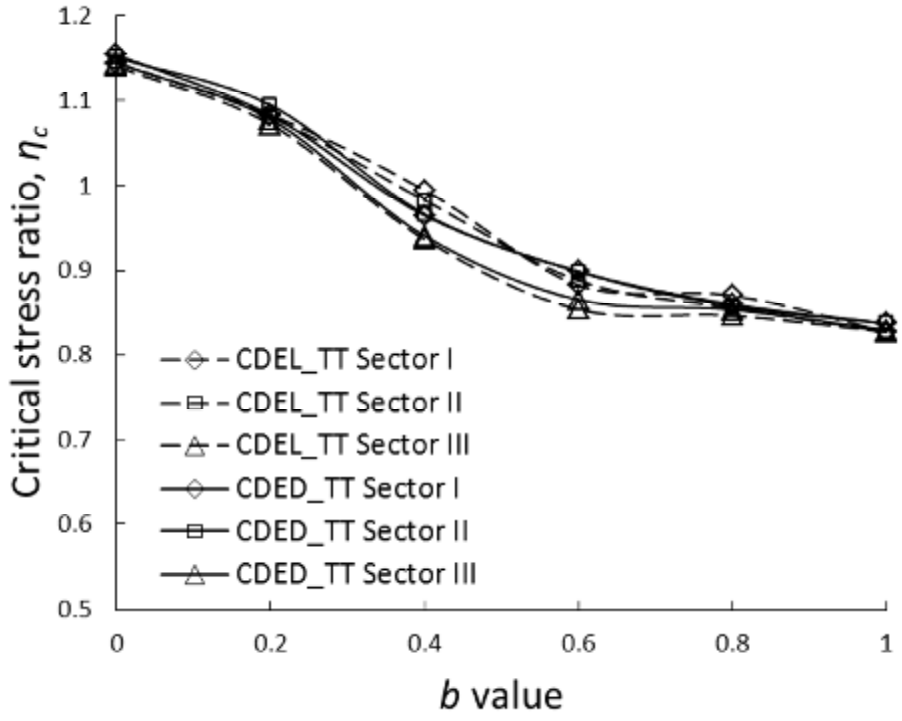

Fig. 7.13 Effects of initial cross-anisotropy on critical stress ratio

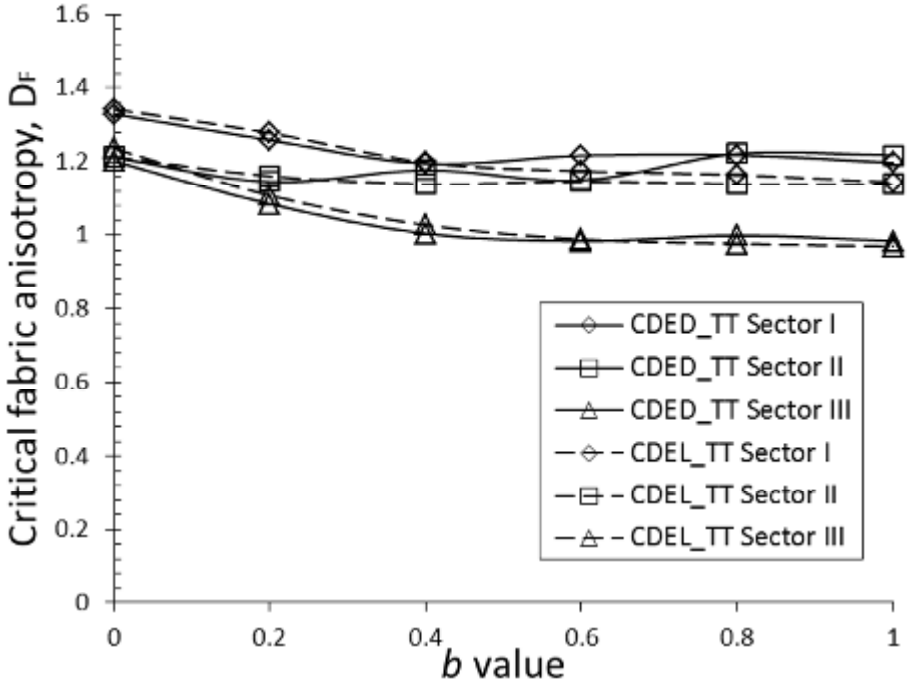

Fig. 7.14 Critical fabric anisotropy in three sectors

7.5 Effect of particle shape on anisotropic material behaviour

The true triaxial simulation results in three sectors may clearly indicate the loading direction dependent behaviour of anisotropic material, where the major principal stress direction is either vertical ($a = 0^{o}$) or horizontal ($a = 90^{o}$). Accordingly, the effect of loading direction a on anisotropic sample CDED_TT and pre-loaded sample CDED_TC_TT is investigated in this section and the results are qualitatively compared to those presented on samples with spherical particles in Chapter 6.

The initially anisotropic dense sample CDED_TT and the pre-loaded sample CDED_TC_TT are sheared at various loading directions at constant $b = 0.4$ and $p = 500kPa$. The pre-loaded sample was prepared by pre-loading the sample CDED_TT to the deviatoric strain $e_q = 10\%$ under triaxial compression loading path with the principal stress direction in the vertical deposition direction (e.g., Fig. 5.9). Then, the sample was un-loaded to isotropic stress state with confining pressure $p = 500kPa$. The prepared samples are summarised in Table 7.4. The pre-loaded sample has a slightly larger void ratio e_0 .

Table 7.4 Initially anisotropic and pre-loaded samples

Anisotropic samples	Void ratio e_0	No. of particles
CDED_TT	0.64	5188
CDED_TC_TT	0.65	5188

7.5.1 Stress-strain behaviour

The stress-strain behaviours of initially anisotropic sample CDED_TT and pre-loaded sample CDED_TC_TT at various loading directions a are shown in the Appendix A (Fig. A1 and Fig. A8). It shows that the material performs stiffer before reaching the peak stress ratio and severer initial volume contraction has been observed with the increasing tilting angle a . In addition, a lower peak stress ratio is obtained and larger deviatoric strain is required to reach failure at a greater tilting angle a . At large shear strain level, the stress ratio shows little difference and variation of volumetric strain becomes small. This is qualitatively similar to the observation of loading direction dependent stress-strain behaviour on samples with spherical particles as presented in Chapter 6.

7.5.2 Non-coaxiality

The non-coaxial behaviour of anisotropic samples is shown in the Appendix A (Fig. A3 and Fig. A9), where the solid straight lines represent the major principal stress direction of which is fixed in the *x*-*z* plane, described by the angle a . And the principal strain increment direction is determined by the relative angle $g_{\Delta e}$ between the principal strain increment direction and the vertical *z*-axis in *x*-*z* plane. The strain increment $d\varepsilon_{ij}$ is determined within a small increment of deviatoric strain $d\varepsilon_q = 0.5\%$. It can be seen that the initially anisotropic sample CDED_TT generally presents coaxial-behaviour while significant non-coaxial behaviour is

observed in the pre-loaded sample CDED_TC_TT. This is qualitatively similar to that observed on the initially anisotropic sample SDEM_TT and pre-loaded sample SDEM_TC_TT with spherical particles, as presented in Chapter 6. Consistent non-coaxial behaviour has also been observed in 2D DEM simulations on initially anisotropic sample and pre-loaded sample with non-spherical particles by Li et al., (2009).

7.5.3 Micro-scale observations

The microscopic tensors evolution of anisotropic samples with non-spherical particles is illustrated in the Appendix A. The effect of loading direction on evolution of fabric anisotropy and contact force anisotropy is generally observed to be qualitatively similar to that in samples with spherical particles. The detailed description of fabric tensor and contact forces tensors evolution has been introduced in Chapter 6 and it is not described in details in this section. Generally, the anisotropic stress-strain behaviour before failure at various loading directions corresponds to the different degrees of fabric anisotropy and contact forces anisotropy in both sample CDED_TT and pre-loaded sample CDED_TC_TT. During the strain softening regime, the contact forces anisotropy is similar and the fabric anisotropy becomes small at various loading directions, leading to similar stress-strain behaviours observed. The generally coaxial behaviour observed in initially anisotropic sample CDED_TT is due to the fabric anisotropy being small and the principal fabric direction approaches the loading direction rapidly. For the pre-loaded sample CDED_TC_TT, the principal fabric direction evolves gradually to

the loading direction due to large fabric anisotropy before shearing, resulting in significant non-coaxiality.

7.5.4 Discussion on strength anisotropy

The stress-force-fabric (SFF) has been validated to predict the stress ratio accurately in Section 5.5 on samples of spherical particles and itself has no restriction on particle shape. Fig. 7.15 shows the SFF relationship for the pre-loaded sample CDED_TC_TT in simulation at $b = 0.4$. The solid lines represent the stress ratio calculated from forces acting on boundary walls using Eq. (2.17). And the hollow symbols corresponds to the stress ratio determined from SFF relations using Eq. (2.18). It can be seen that stress ratio from SFF shows little difference to that calculated from boundary walls before reaching the peak stress ratio. However, the SFF predicts a greater stress ratio than that obtained from Eq. (2.17) during post-peak shearing. This is probably due to significant stress non-uniformity at large deformation. The stress is found to be larger within measurement sphere, which is an intrinsic function within PFC3D to measure stress tensor within granular assembly, in the central area of the sample than that determined from forces acting on rigid boundary walls due to no sufficient frictional resistance between particle-wall contacts. The other possible reason is the second-order approximation of internal structure may not be sufficient and higher-order approximation, e.g., fourth-order, may be more accurate. Nevertheless, the qualitative trend of the predicted stress ratio, at least, is similar to that calculated from the boundary forces at various loading directions. Thus, the microscopic information may still be used to interpret the anisotropic strength characteristics.

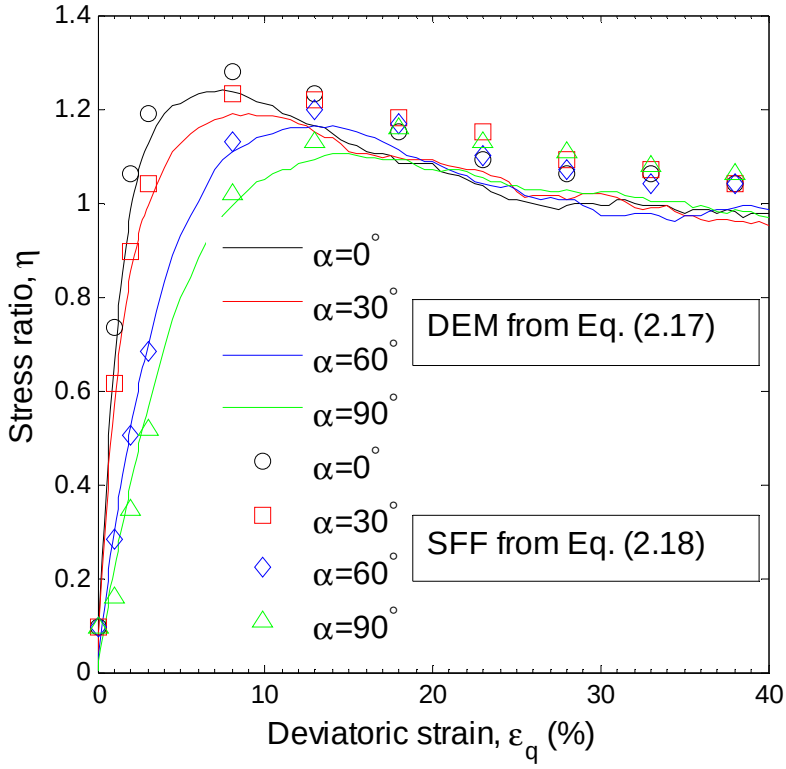

Fig. 7.15 Comparison of stress determined from DEM and SFF relations for pre-loaded anisotropic sample CDED_TC_TT of non-sphercial clump particles

To visualise the effects of loading direction on the anisotropic strength characteristics more clearly, the anisotropic strength of initially anisotropic dense sample CDED_TT and pre-loaded sample CDED_TC_TT are illustrated in Fig. 7.16, from simulation results at constant $b = 0.4$. In simulations with the same b value, it can be seen that the peak stress ratio decreases continuously with the increasing loading direction a for both samples. The pre-loaded sample generally gives slightly smaller peak stress ratio than the initially anisotropic sample at the same loading direction, suggesting the material slightly softened by the pre-loading history. Similar experimental results have also been reported on tests of anisotropic sand material (Oda, 1972, Arthur and Menzies, 1972, Lam and Tatsuoka, 1988).

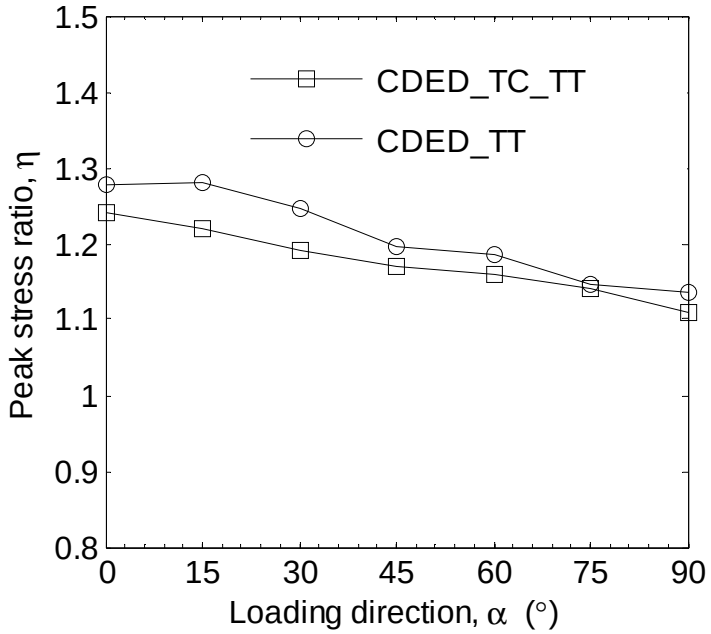

Fig. 7.16 Anisotropic strength in three dimensional stress conditions, *b*=0.4

The microstructural tensor anisotropy degree of the sample CDED_TT and the pre-loaded sample CDED_TC_TT at peak stress ratio, corresponding to Fig. 7.16, is plotted in Fig. 7.17. The solid red lines with hollow symbols indicate the results from the sample CDED_TT and the solid dark lines with symbols refer to the results from the pre-loaded sample CDED_TC_TT. The lines with triangle symbols represent normal contact force anisotropy. The lines with square symbols are the fabric anisotropy and those with circles refer to the tangential contact force anisotropy. It is clear from the figure that the normal contact force anisotropy and tangential contact force anisotropy show small variation with tilting angle a while the fabric anisotropy D_F decreases significantly as loading direction rotates from the vertical ($a = 0^o$) to the horizontal plane ($a = 90^o$). Hence, it is clear that the strength anisotropy is due to the effect of fabric anisotropy, with a smaller fabric anisotropy developed at greater tilting angle a.

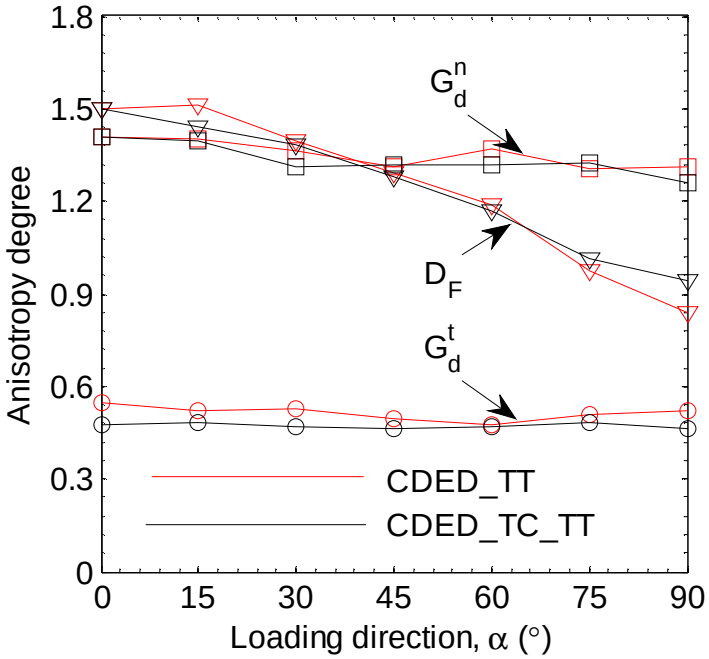

Fig. 7.17 Anisotropy degrees of microstructural tensors at peak stress ratio, *b*=0.4

At large deformation, where the critical stress ratio h_c is achieved in each simulation, it is clear from Fig. 7.18 that the h_c shows little difference in the initially anisotropic sample and the pre-loaded sample at different loading directions with constant $b = 0.4$. Microscopically, the fabric anisotropy D_F and contact forces anisotropy G_d^n and G_d^t approach the same value at large deformation under various loading directions (e.g., Appendix A). The principal directions of microstructural tensors are coaxial with the external stress direction. Hence, the same stress ratio is reached, irrespective of loading directions.

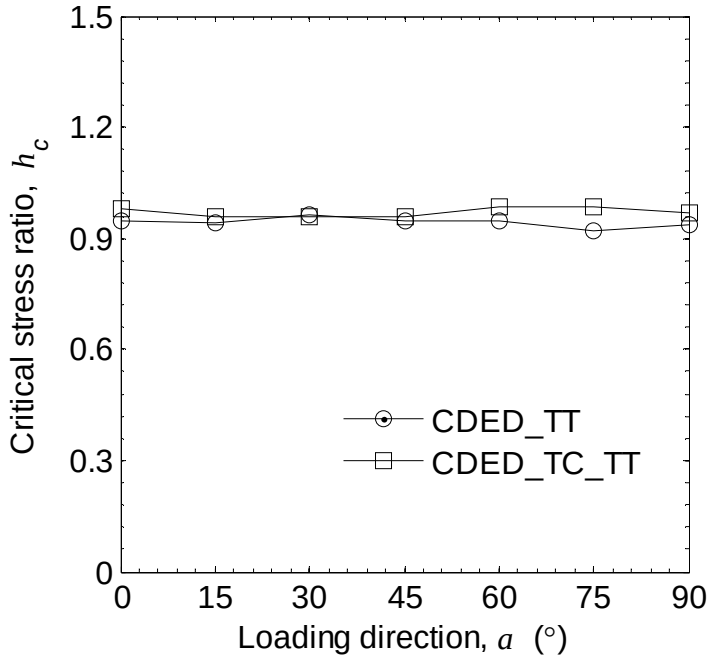

Fig. 7.18 Effects of loading direction on critical stress ratio, *b*=0.4

7.6 Discussion on particle shape effect on critical fabric anisotropy

Fig. 6.8 and Fig. 6.18 show the fabric evolution of the initially anisotropic sample and pre-loaded sample with spherical particles during monotonic shearing under different loading directions. It can be seen that at large deformation, where the critical stress ratio is achieved, the fabric anisotropy reaches similar values, irrespective of various loading directions. The principal fabric direction becomes coaxial with the loading direction. Accordingly, the critical fabric anisotropy is considered to be achieved.

Fig. A4 and Fig. A5 (e.g., Appendix A) show the fabric anisotropy evolution and principal fabric direction evolution of the initially anisotropic sample with non-

spherical particles. The fabric evolution of the pre-loaded sample with non-spherical particles is presented in Fig. A10. It is clear from the figures that the critical fabric anisotropy D_F has been achieved in the particular loading direction, independent of the initial void ratio and pre-loading history. However, the critical fabric anisotropy D_F obtained at different loading directions shows slight difference. The principal fabric direction approaches loading direction at large deformation but still a small gap.

The difference of critical fabric anisotropy obtained in the sample of spherical particles and in the sample of non-spherical particles is due to particle shape effect. Revisiting the stress tensor definition in Eq.(2.17), the stress tensor is dependent on the contact force vector and branch vector connecting the centres of two particles in contact. When the critical stress ratio is achieved, the contact forces anisotropy approach the same values, irrespective of loading direction, and the contact force principal directions become coaxial with loading direction as shown in Fig. 6.20 and Fig. 6.21. This is also observed on non-spherical particles assembly as presented in the Appendix A. Hence, the branch vector anisotropy must approach similar anisotropy degree at various loading directions and the principal direction of branch vector must be coaxial with loading direction at critical stress state. In the sample of spherical particles, the contact normal vector has the same direction as the branch vector in two contact entities. However, the contact normal vector generally differs from the branch vector direction in two contacting particles in the sample of non-spherical particles (e.g., Fig. 2.11). This is the main reason for the slight difference on the observed critical contact normal fabric anisotropy.

7.7 Summary

This chapter presents the simulation results of samples with non-spherical particles under various loading paths. And the results are compared to those of samples with spherical particles to stress the particle shape effect on granular material behaviour.

The initially isotropic sample CRED_TT has a lower initial void ratio and greater coordination number than the sample SRED_TT under otherwise the same generation procedures. In triaxial compression simulation, the sample CRED_TT performs stiffer, stronger and more dilative than the sample SRED_TT. Microscopically, this is due to a larger degree of fabric anisotropy and contact forces anisotropy developed and higher frictional mobilisation coefficient in the sample CRED_TT.

Under true triaxial tests in the initially anisotropic samples CDED_TT and CREL_TT (cross-anisotropy) at the same b value, the material performs stiffer and more dilative when sheared in Sector I than sheared in Sector III. The friction angle decreases continuously as stress lode angle q increases from 0^{o} to 180^{o}. The failure envelop on the deviatoric plane shows cross-anisotropic strength criterion, indicating the loading direction dependent strength characteristics. The different stress-strain behaviour in Sector II and Sector III, where the major principal stress directions are the same in the horizontal direction while the intermediate principal stress directions differ to be either in the vertical direction or in the horizontal direction, shows clear evidence of the combined effects of b value and material anisotropy on the initially

anisotropic granular material behaviour. Microscopically, the anisotropic strength characteristic is due to the effect of material cross-anisotropy. Upon the same shearing strain, the fabric anisotropy shows different evolution paths in three Sectors. At failure, the fabric anisotropy is found to be largest in sample sheared in Sector I while the lowest fabric anisotropy is obtained in sample sheared in Sector III.

In simulations with tilting principal stress directions on the initially anisotropic sample CRED_TT and the pre-loaded sample CRED_TC_TT, the loading direction dependent anisotropic stress-strain behaviour is qualitatively similar to that observed in sample with spherical particles as shown in Chapter 6, with significant effect of a before failure while negligible effect after failure. At the peak stress ratio, the internal fabric anisotropy D_F is lower at a greater angle a while the contact forces anisotropy G_d^n, G_d^t shows little variation at various loading directions. This clearly indicates that the anisotropic strength, decreasing peak stress ratio with larger angle a , is due to the lower fabric anisotropy developed at a greater angle a .

The non-coaxiality is negligible for the sample CRED_TT while significant non-coaxial behaviour is observed in the pre-loaded sample CRED_TC_TT. The non-coaxial behaviour is due to the initial non-coincidence of material internal structure direction, e.g., the principal fabric direction, relative to the loading direction. This is qualitatively similar to the non-coaxial behaviour observed in the sample SRED_TT and the pre-loaded sample SRED_TC_TT of spherical particles as presented in Chapter 6.

Comparing the fabric evolution in simulations under various loading directions in samples with spherical particles and non-spherical particles, the critical fabric anisotropy reaches similar values at different loading directions and the principal fabric direction becomes coaxial with loading direction in sample of spherical particles while a slight difference of critical fabric anisotropy is observed on sample of non-spherical particles and few degrees deviation exists between the principal fabric direction and the loading direction. The reason is that the contact normal vector direction coincides with the branch vector direction in contact between spherical particles while the direction of two vectors is generally different in contact between non-spherical particles.

Chapter 8 Material behaviour to rotational shear

8.1 Introduction

The simulation results of the anisotropic sample in the previous chapter clearly show the loading direction dependent deformation behaviour. Significant plastic deformation may be generated when anisotropic granular material experiences a stress path, even with constant magnitudes of stress invariants but purely continuous rotation of principal stress directions (i.e., rotational shear). In this chapter, the deformation characteristic of anisotropic samples of non-spherical clump particles is investigated under drained rotational shear. The effects of stress ratio and b value on the rotational shear behaviour are discussed. In addition, the effect of particle shape on material rotational shear response is also discussed, where the macroscopic results of sample with spherical particles has been presented in Section 4.4.3. The internal structure evolution, in terms of contact normal fabric evolution, will be examined to explain the macroscopic material deformation response.

8.2 Numerical simulation procedures

The rotational shear controls constant mean normal stress p, intermediate principal stress ratio b and stress ratio h. Only the principal stress direction rotates continuously within the *x*-*z* plane. More numerical implementation details have been introduced in Section 4.4.3. This specific loading path mimics the rotational shear involved in a laboratory hollow cylinder test.

The initially anisotropic dense sample CDED_TT, which is the one as shown in Table 7.2, has been pre-loaded to target boundary stress conditions for rotational shear. The control of pre-shearing loading is the drained true triaxial loading path as introduced in Section 4.4.2, with constant mean normal stress p, fixed b value and the major principal stress direction being vertical. The sample CDED_TT was pre-sheared at constant $p = 500kPa$, $b = 0.5$ to three different stress ratio levels, $h = 0.5, h = 0.7, h$ =0.9. The other group of samples was prepared by pre-shearing the initially anisotropic sample CDED_TT to the same stress ratio $h = 0.9$ at constant $p = 500kPa$ but various b values, $b = 0, b = 0.5, b = 1$ respectively. The detailed information of the pre-sheared numerical samples for rotational shear is summarised in Table 8.1. It can be seen that the prepared samples have similar initial void ratios.

After the initially anisotropic sample was pre-sheared monotonically to the target stress state, the samples were ready for rotational shear. During rotational shear, the major principal stress direction a was rotated with a small increment $3^{o} \times 10^{-4}$ in one calculation cycle only when the constant stress invariants satisfied.

Three series of simulations have been conducted. One was simulated at constant $p = 500kPa$, $b = 0.5$ and three different stress ratios h to investigate the influence of stress ratio h on the deformation characteristics of granular material under pure principal stress rotation. The other series was simulated at constant $p = 500kPa$, $h = 0.9$ and three various b values to examine the influence of b value on deformation behaviour during rotation of principal stress. The rotational shear has also been conducted on sample CRED_B05Y05_RS, which was prepared by radius expansion method and was initially isotropic. The results are compared to that obtained from sample CDED_B05Y05_RS to show the effect of initial anisotropy on internal structure evolution.

Table 8.1 Samples information for rotational shear

Simulations	Pre-loading		Sample label	Void ratio e_0
Series 1 Constant b value	True triaxial ($b = 0.5$)	$h = 0.5$	CDED_B05Y05_RS	0.645
		$h = 0.7$	CDED_B05Y07_RS	0.645
		$h = 0.9$	CDED_B05Y09_RS	0.645
Series 2 Constant stress ratio h	True triaxial ($h = 0.9$)	$b = 0.0$	CDED_B00Y09_RS	0.644
		$b = 1.0$	CDED_B10Y09_RS	0.646
Series 3 Initially isotropic sample CRED_TT	True triaxial ($b = 0.5$)	$h = 0.5$	CRED_B05Y05_RS	0.6

8.3 Influence of stress ratio on material response

The effects of stress ratio on the material response undergoing rotational shear at constant mean normal pressure $p = 500kPa, b = 0.5$ have been investigated. The intermediate principal stress was fixed in both magnitude and direction along *y*-axis. The major principal stress directions rotated continuously in the *x*-*z* plane. More details about the numerical implementation can be found in Section 4.4.3.

8.3.1 Stress path

The variation of stress components at $h = 0.5$ is exemplified in Fig. 8.1(a). It shows that the stress components along the *y*-axis direction keep constant with $s_{yy} = 500kPa, s_{yx} = 0, s_{yz} = 0$, corresponding to the target boundary conditions with fixed intermediate principal stress magnitude and principal direction along the *y*-axis. The stress components s_{xx}, s_{zz}, s_{xz} vary periodically every one cycle with 180^{o} variation of a. The stress trajectory in the deviatoric space is circled, as shown in Fig. 8.1(b). And the stress trajectory size is larger in rotational shear with a higher stress ratio. This shows that the desired stress path (i.e., Fig. 4.14) has been well maintained in numerical simulations.

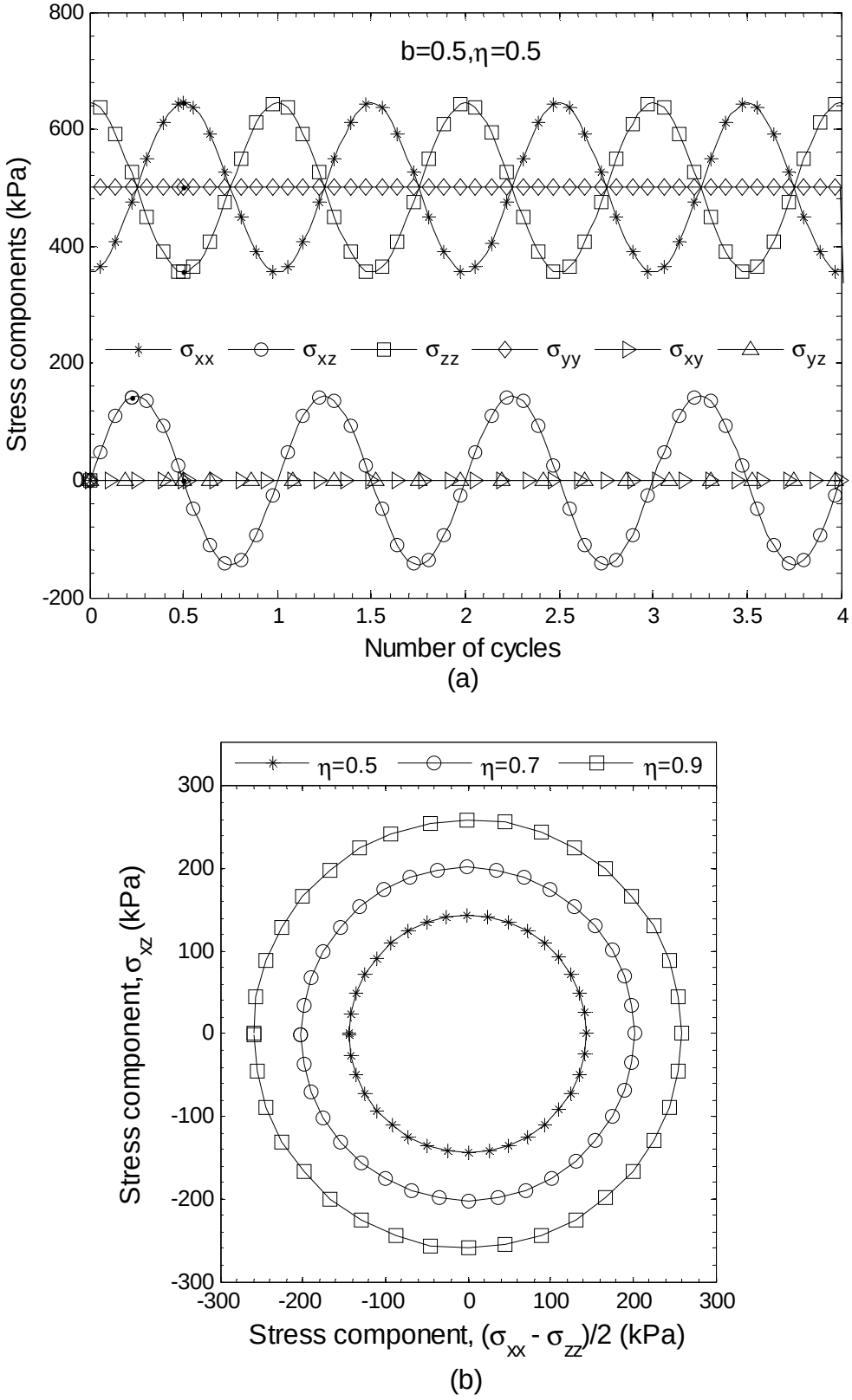

Fig. 8.1 Stress path (a) variation of stress components (b) stress trajectory

8.3.2 Strain response to various stress ratios

The variations of six strain components against the increasing number of cycles are illustrated in Fig. 8.2 (a) – (c). One cycle indicates a 180º variation of a. The three figures share the same legend, as shown in Fig. 8.2(a). In the figures, the positive value of strain along the vertical axis refers to compression and the negative value indicates extension. It is observed that the significant plastic strains are accumulated, regardless of constant magnitudes of the three principal stresses. This is inconsistent with the classic plasticity theory, which predicts no strain increment due to constant magnitudes of the three principal stresses. The strains e_{xx}, e_{xz}, e_{zz} are larger in the first a few cycles. As the number of cycle increases, the strain components e_{xx}, e_{xz}, e_{zz} vary periodically with decreasing oscillation amplitudes. Although the intermediate principal stress s_{yy} is kept constant throughout the simulations, the contractive strain e_{yy} generally accumulates with continuous cyclic major principal stress rotation. It is also observed that the strain components e_{yx}, e_{yz} are nearly zero, related to zero shear stress components s_{yz}, s_{yx} (e.g., Fig. 8.1(a)).

Other than the common observations of strain response under various stress ratios, it is found that larger plastic strain rates are induced in simulation with a higher stress ratio. The oscillation amplitudes of e_{xx}, e_{xz}, e_{zz} are larger at a greater stress ratio. Up to 30 cycles, the accumulated contractive intermediate strain e_{yy} is larger in simulation at a higher stress ratio, observed to be $e_{yy} = 0.7\%$ at $h = 0.5$, $e_{yy} = 1.9\%$ at $h = 0.7$ and $e_{yy} = 6.4\%$ at $h = 0.9$. Similar observations have

been presented on sand responses to rotational shear under various stress ratios (Yang, 2013).

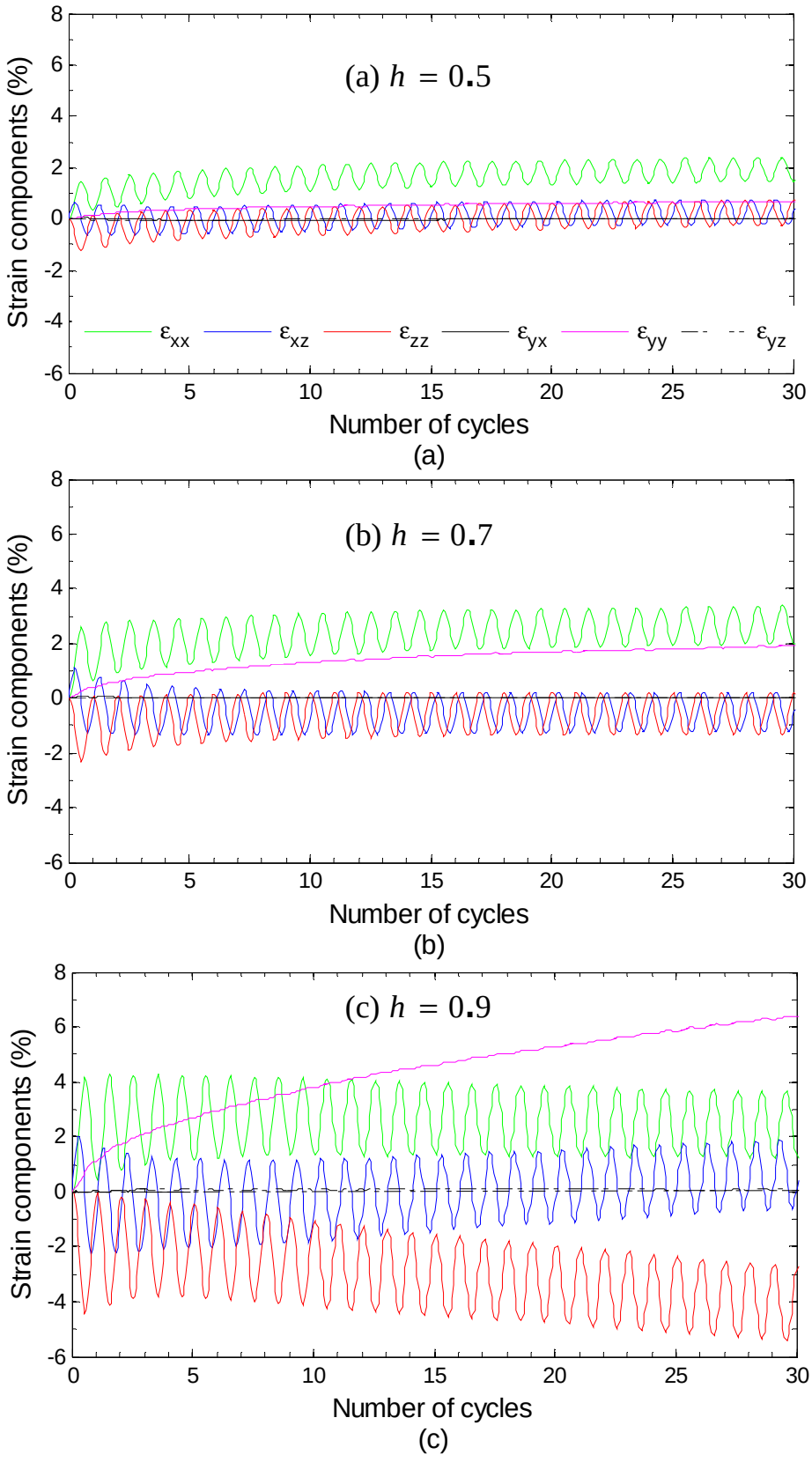

Fig. 8.2 Variation of strain components (a) $h = 0.5$ **(b)** $h = 0.7$ **(c)** $h = 0.9$

The strain trajectory for rotational shear under different stress ratios is plotted in the deviatoric plane, as shown in Fig. 8.3. To have a better view on the strain trajectory, the strain trajectories are also plotted in Fig. 8.4 at different cycles. Among the rotational shear simulations with various stress ratios, it is observed that the strain trajectories in the deviatoric strain space are open in the first cycle, indicating non-recoverable plastic strain generated. With increasing number of cycles, however, the strain trajectories, unlike the circle of stress trajectory, are spiral. The size of the strain trajectory becomes smaller with increasing number of cycles. After a large number of cycles, the strain trajectories appear to be circles, which is consistent to the observation of 2D DEM simulation (Li and Yu, 2010). Comparing the strain trajectories at different stress ratios in Fig. 8.4, the size of the strain path is larger at a greater stress ratio. Similar strain responses to different stress ratios are also observed in laboratory drained rotation shear (Yang, 2013). The critical strain trajectory in the 45^{th} cycle appears to be circles, which is different to the experimental observation of elliptical shape of strain trajectory in the 50^{th} cycle (Yang, 2013).

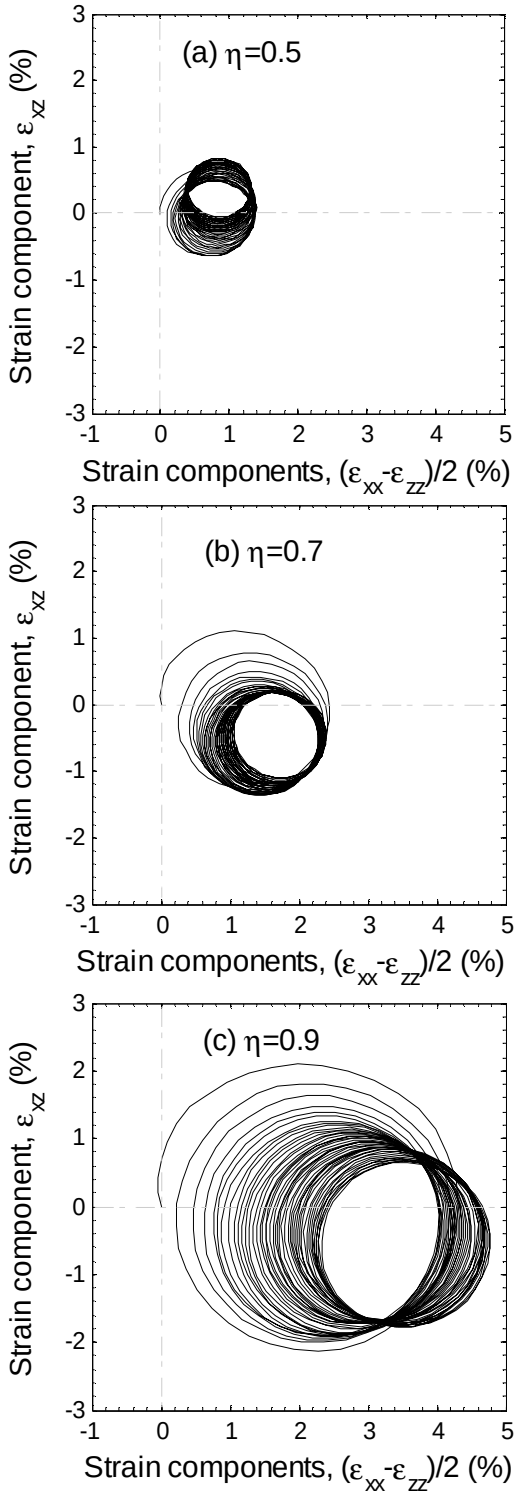

Fig. 8.3 Effect of stress ratio on strain trajectory in the deviatoric plane

(a) $h = 0.5$ **(b)** $h = 0.7$ **(c)** $h = 0.9$

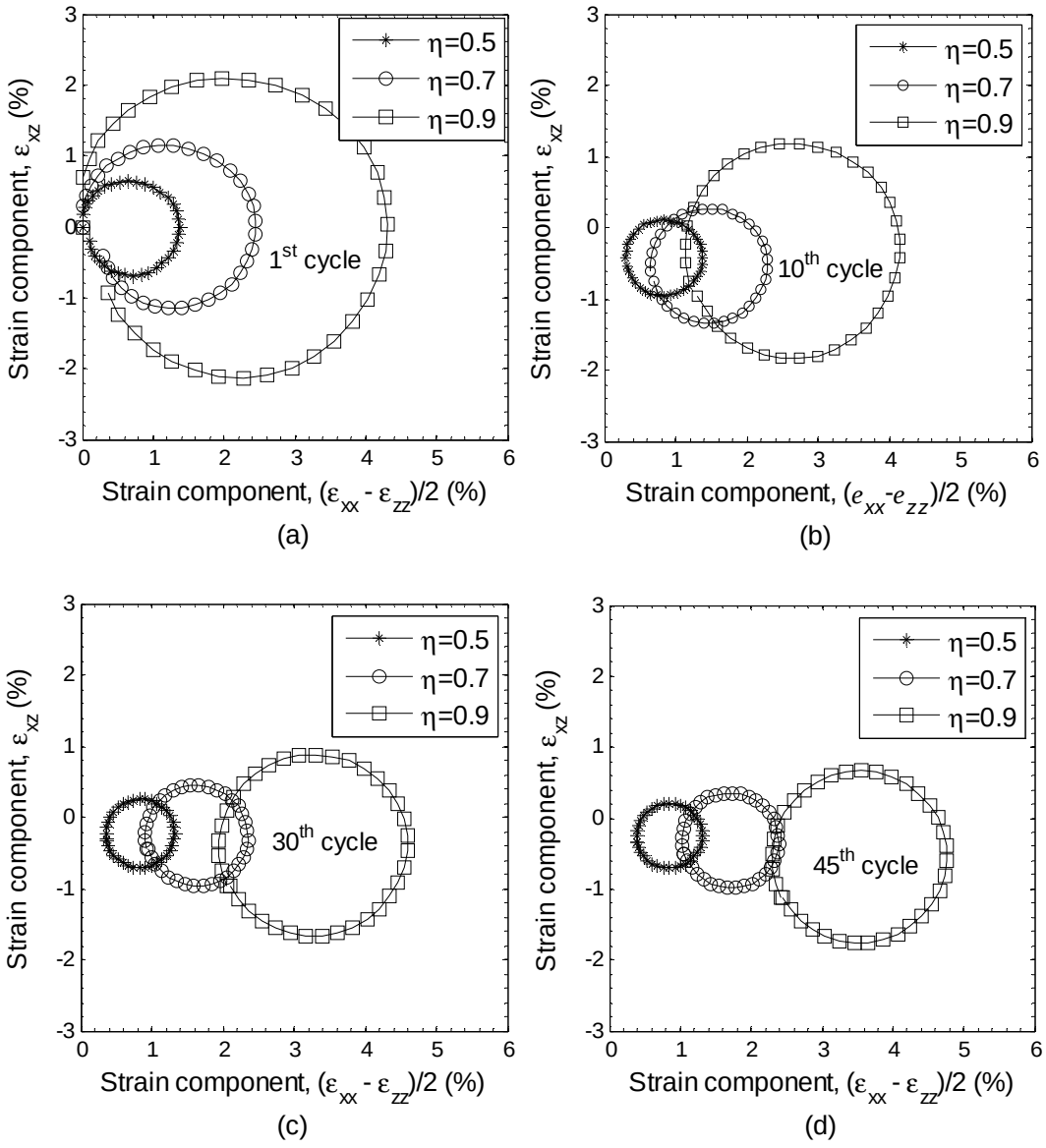

Fig. 8.4 Strain trajectory at different cycles for rotational shear at different stress ratios

The volumetric strain e_v during stress rotation is plotted in Fig. 8.5(a). It can be seen that significant volumetric contraction accumulates even when the sample is classified as a dense sample, where excess volume dilation occurs in monotonic shearing as shown in Fig. 7.7. Most of the volumetric strain accumulation occurs in the first a few cycles and the increment rate of volumetric contraction decreases for increasing number of cycles. The larger the stress ratio, the severer volume

contraction is observed. This indicates that the material ultimate void ratio (e.g., after 45 cycles) is stress ratio dependent during rotational shear shown in Fig. 8.5(b), despite similar initial void ratios before rotational shear (e.g., Table 8.1). It is interesting to see that the ultimate void ratio, which is the void ratio in the 45^{th} cycle considered as ultimate void ratio since the volumetric strain accumulation does not change much after 45 cycles, linear correlation between the ultimate void ratio and the stress ratio. It is worth to pointing out that only data three stress ratios has been reported and a wider range of data would be more convincing. The volumetric contraction has also been reported on the drained response of sand under rotational shear (Tong et al., 2010); it is also observed as larger pore pressure build-up at higher stress ratio in undrained rotational shear (Nakata et al., 1998, Yang and Li, 2007).

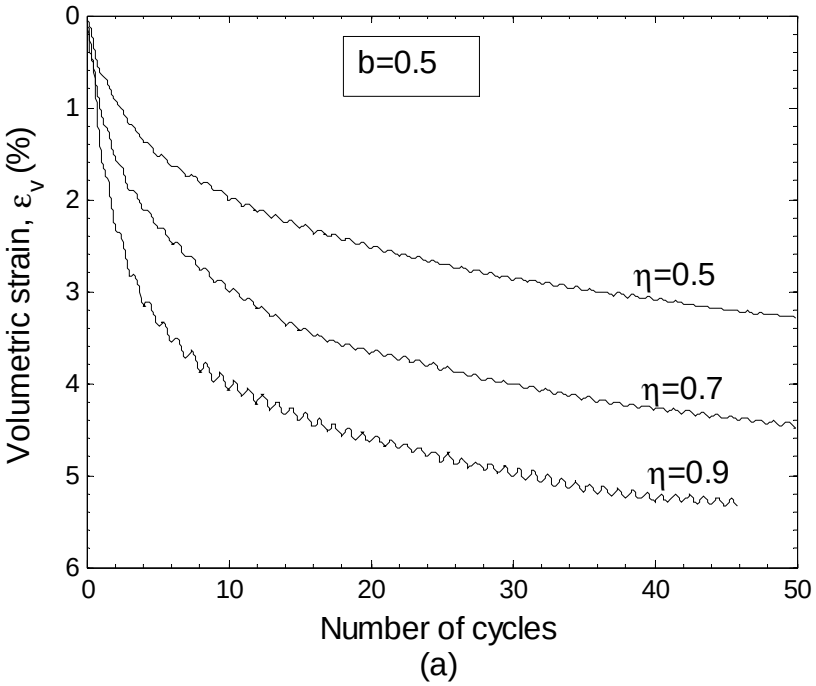

(a)

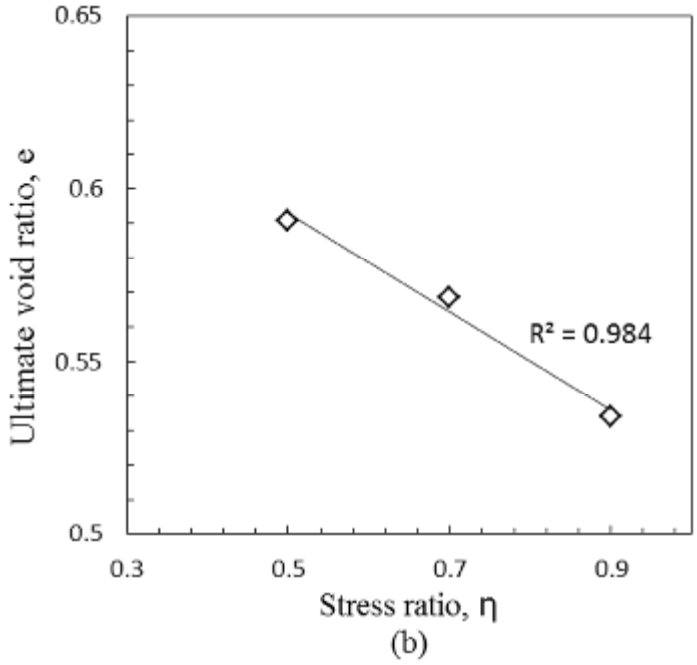

Fig. 8.5 Effect of stress ratio on volumetric strain during rotational shear

One may also see that the volumetric strain curves are jagged with both contraction and dilation in one cycle. Fig. 8.6 gives the better view of the volumetric strain evolution in the 1th and 20th cycle for rotational shear at $h = 0.7$. In the first cycle, the volumetric strain shows continuous increase with increasing a. In the 20th cycle, the volumetric strain decreases due to dilation in the first half cycle ($0^o \le a \le 90^o$) and the minimum value of e_v is achieved at $a \approx 80^o$. In the second half cycle ($90^o \le a \le 180^o$), the volumetric strain increases significantly to reach the maximum e_v at the end of the cycle. The volumetric strain at the end of the cycle is larger than that in the beginning of the cycle, resulting in total volumetric contraction in one cycle. Similar experimental results have been also produced (Miura et al., 1986, Yang, 2013).

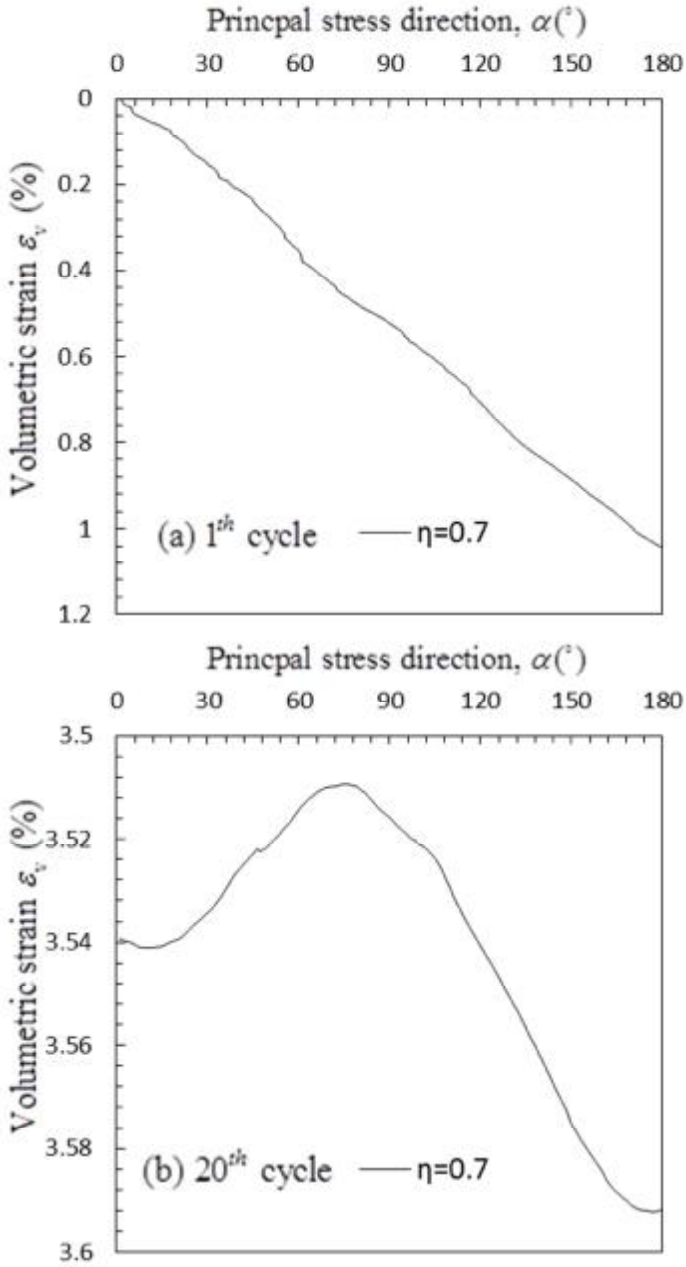

Fig. 8.6 Evolution of volumetric strain within one cycle for rotational shear at $b = 0.5, h = 0.7$

8.3.3 Deformation non-coaxiality

As it is difficult to distinguish the elastic strain increment and the plastic strain increment, the total strain increment vector is used for the following analysis

instead of the plastic strain increment due to small contribution of the elastic strain increment to the total strain increment as suggested by Gutierrez et al. (1991). The strain increment vector is obtained within a small stress increment of principal direction $\Delta a \approx 3^{o}$.

The degree of non-coaxiality, difference between the major principal strain increment direction $g_{\Delta e}$ and the major principal stress direction a, is plotted in Fig. 8.7 for rotational shear under various stress ratios. The two small figures are superimposed for better view of non-coaxiality in the 1th cycle and the 10th cycle. The angle $g_{\Delta e}$ represents the direction of total strain increment vector relative to the vertical direction and determined using Eq. (4.4). It is clear from the figure that significant degree of non-coaxiality is observed, generally lying between 30^{o} and 40^{o}. At constant stress ratio e.g., $h = 0.5$, the degree of non-coaxiality does not keep steady along stress rotation but varies with fluctuation. However, the average degree of non-coaxiality remains steady as $g_{\Delta e} - a \approx 38^{o}$ at $h = 0.5$ during continuous cyclic rotation. With increasing stress ratio, the average degree of non-coaxiality becomes smaller. This is consistent to the 2D DEM observations on non-coaxial behaviour during rotational shear under various stress ratios (Li and Yu, 2010); and similar experimental observations have also been reported on sand response to stress rotation (Gutierrez et al., 1991, Yang, 2013). A slight difference is that the non-coaxiality degree increases from $10^{o} \sim 20^{o}$ in the first a few cycles to $30^{o} \sim 40^{o}$ after 20 cycles of stress rotation (Yang, 2013).

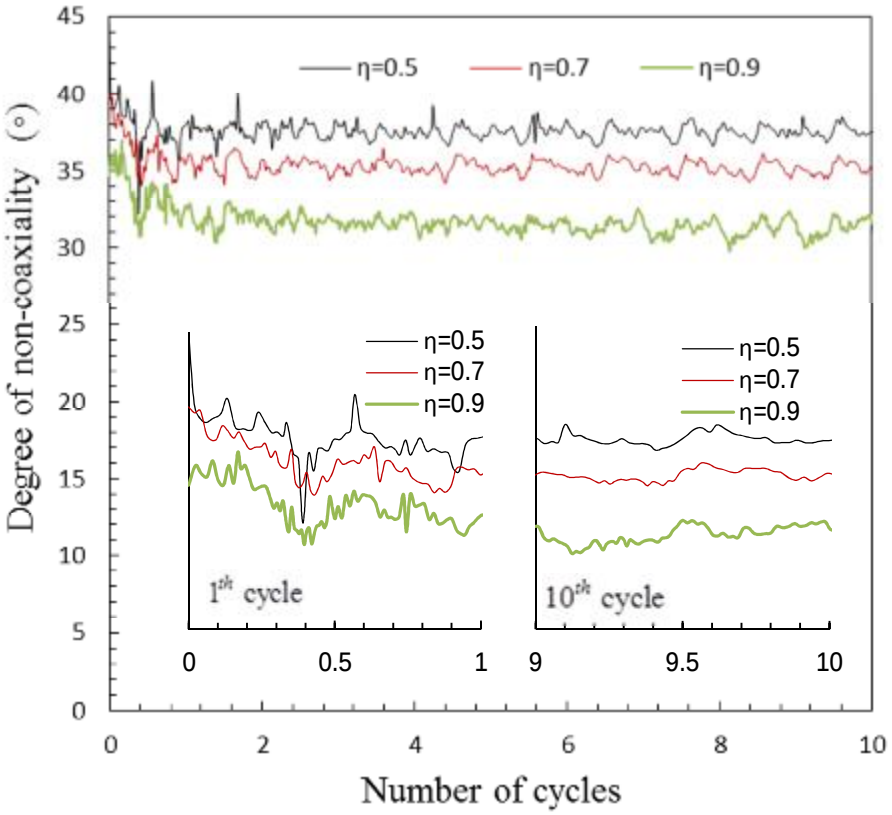

Fig. 8.7 Effects of stress ratio on degree of non-coaxiality in rotational shear

8.4 Influence of *b* value on material behaviour

The effects of the b value on the material response undergoing rotational shear at constant mean normal pressure $p = 500kPa$ and fixed stress ratio $h = 0.9$ have been investigated on samples CDED_B00Y09_RS, CDED_B05Y09_RS and CDED_B10Y09_RS, respectively. In each simulation, the intermediate principal stress was fixed in both magnitude and direction (y-axis). The major and minor principal stress directions rotated continuously in the x-z plane. The implementation details can be found in Section 4.4.3.

8.4.1 Stress path

The variation of stress components at various b values can be seen from Fig. 8.8. It shows that the stress components along the *y*-axis direction keep constant with $s_{yx} = 0, s_{yz} = 0$ and different s_{yy} values at various b values, corresponding to the target boundary conditions with fixed magnitude of intermediate principal stress and principal direction along the *y*-axis. The stress components s_{xx}, s_{zz}, s_{xz} vary periodically every one cycle, corresponding to 180º variation of major principal stress direction a . The stress trajectory in the deviatoric plane is a circle, as shown in Fig. 8.9, irrespective of various b values due to the same stress ratio $h = 0.9$. It clearly indicates that the target stress paths have been well maintained in numerical rotational shear simulations.

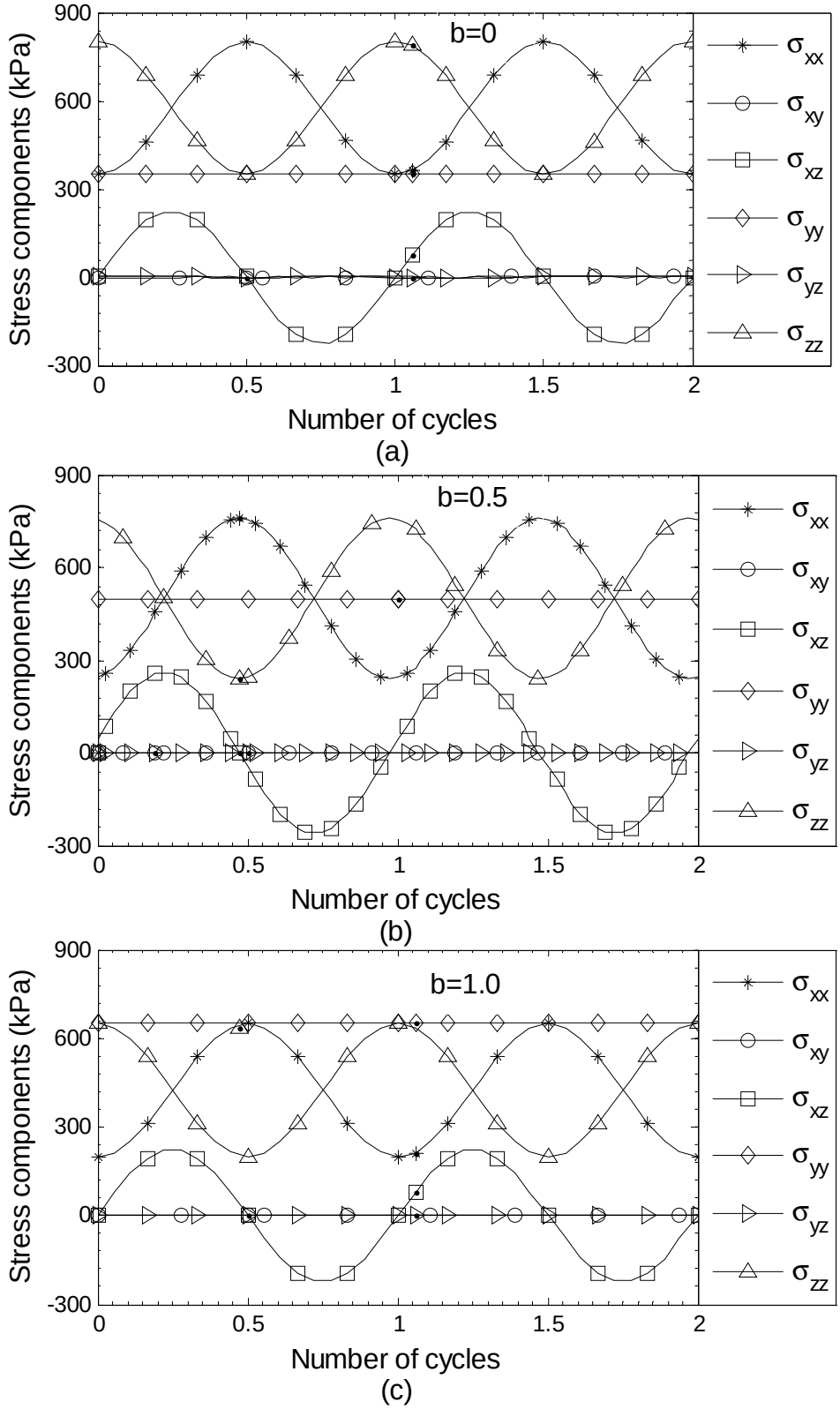

Fig. 8.8 Variation of stress components in rotational shear with various *b* values

(a) *b*=0 (b) *b*=0.5 (c) *b*=1

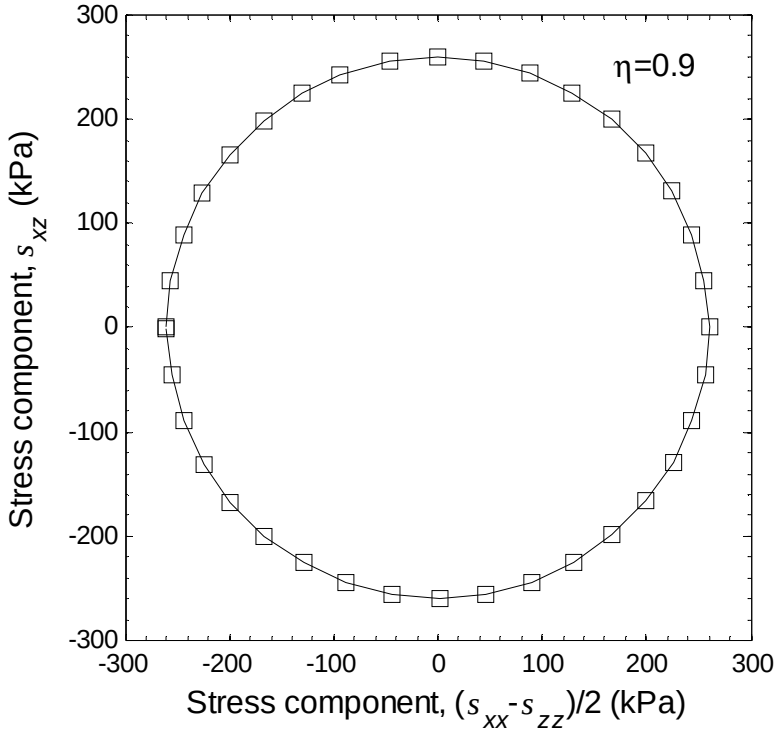

Fig. 8.9 The same stress trajectory for rotational shear at constant $h = 0.9$ with different *b* values

8.4.2 Strain response to various *b* values

The strain trajectories of rotational shear under various b values are illustrated in Fig. 8.10 in the deviatoric strain space. One may notice the size of strain trajectory becomes larger for continuous stress rotation at $b = 1$, indicating significant deviatoric strain e_q accumulated. This is due to the selected stress ratio $h = 0.9$ at $b = 1$ being higher than the critical stress ratio $h_c = 0.82$ as obtained in monotonic shearing (e.g., Fig. 7.13). The constant stress ratio $h = 0.9$ can hardly be maintained at such a high stress ratio in the numerical simulation. The sample would experience deformation failure after a few cycles as reported in the laboratory test when the stress ratio for rotational shear is greater than the critical stress ratio

obtained in monotonic shearing (Yang, 2013). This indicates that the failure of granular material subjected to rotational shear has a clear connection to the selected stress ratio relative to the critical stress ratio obtained in monotonic loading. Thus, in the following, the rotational shear results at $b = 0$ and $b = 0.5$ are mainly discussed to demonstrate the effects of b value on material rotational shear behaviour.

For the samples CDED_B00Y09_RS and CDED_B05Y09_RS, it is observed that, unlike the same circular stress trajectory in the deviatoric stress space in Fig. 8.9, the strain trajectories are spiral with continuous rotation of stress direction. The size of the strain trajectories becomes smaller with the increasing number of cycles and it stabilises to be a circle after a large number of cycles. It can be seen that the strain trajectories are quite similar during rotational shear at $b = 0$ and $b = 0.5$. The difference is that the size of strain trajectory is generally larger at $b = 0.5$ than that at $b = 0$, indicating a larger strain increment rate at a greater b value at the same rotation of principal stress axes.

The intermediate strain e_{yy} evolution is plotted in Fig. 8.11. Significant intermediate strain e_{yy} has been generated, although the intermediate stress is constant in both its magnitude and principal direction during rotational shear. For simulations with $b = 0$ and $b = 0.5$, the intermediate strain increases continuously with decreasing rate. With increasing b value, the intermediate strain e_{yy} changes from negative value (extension) at $b = 0$ to positive value (contraction) at $b = 1$. This agrees well with the experimental observations on b value effect on sand specimens to rotational shear responses (Tong et al., 2010, Yang, 2013). It shows

that the b value has a significant effect on the intermediate strain during rotational shear, which is missing in 2D DEM simulation. At $b = 1$, the contractive strain e_{yy} increases dramatically in the first four cycles, leading to deformation 'failure'.

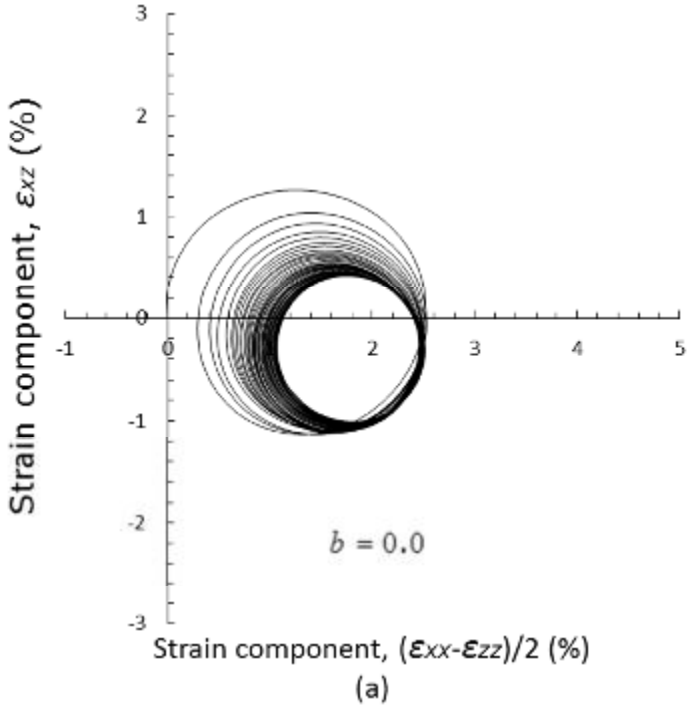

(a)

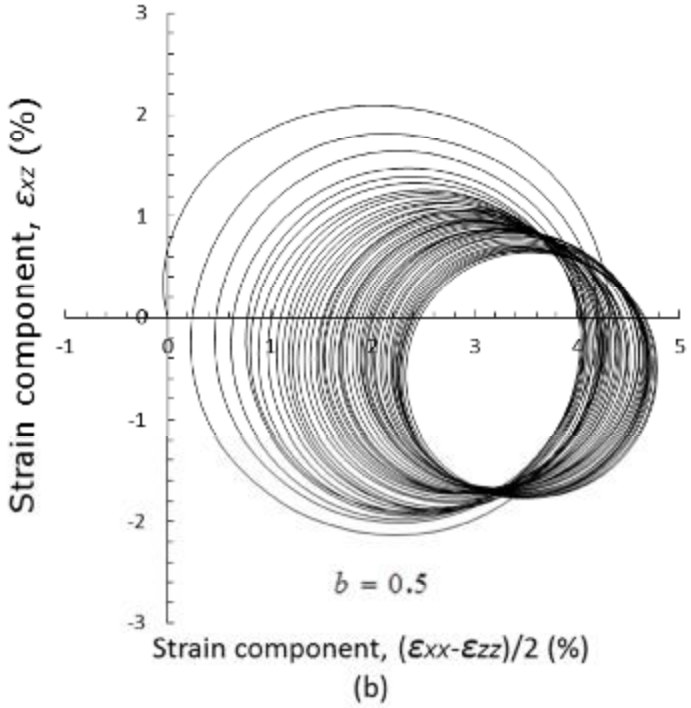

(b)

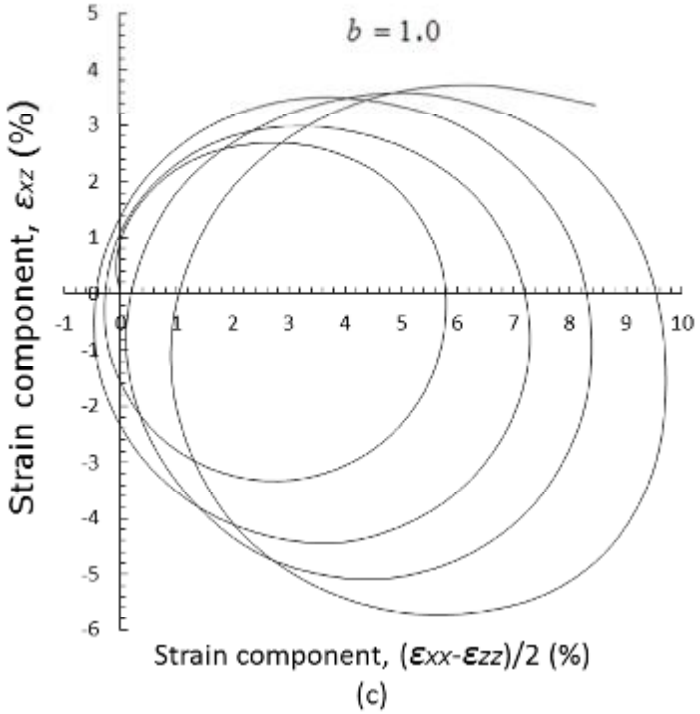

Fig. 8.10 Strain paths in rotational shear (a) *b*=0 (b) *b*=0.5 (c) *b*=1

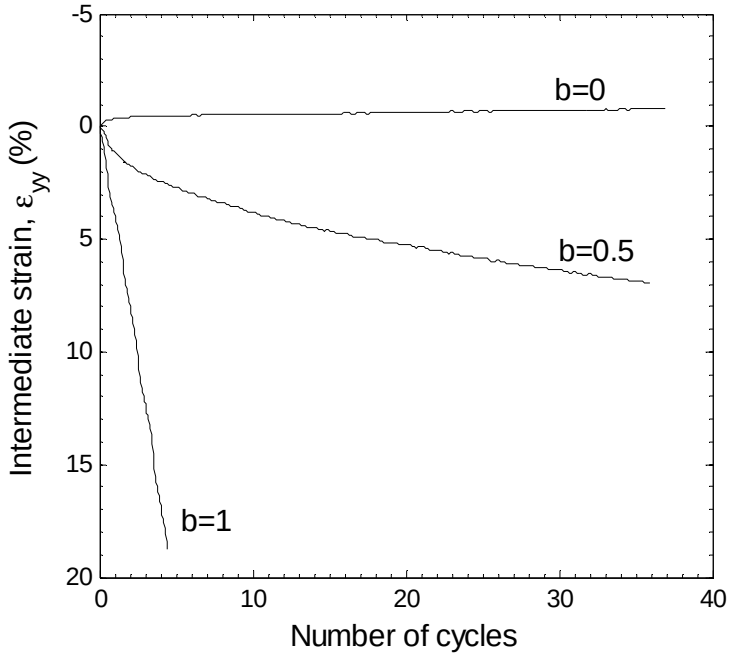

Fig. 8.11 Intermediate strain during rotational shear at different *b* values

The effects of b values on the volumetric strain and deviatoric strain during rotational shear are shown in Fig. 8.12. The three samples have similar initial void ratios and stress ratios and sheared at different b values (e.g., Table 8.1). At $b = 0$ and $b = 0.5$, it can be seen that the volumetric strain and deviatoric strain vary with oscillation. However, with the continuous rotation of principal stress direction, significant volumetric contraction and deviatoric strain accumulate in the first few cycles and slow down with decreasing increment rate. The magnitudes of the accumulated volumetric strain and deviatoric strain are larger at $b = 0.5$ than at $b = 0$, indicating significant impact of b value on deformation characteristics during shear under otherwise similar conditions. As for the rotational shear at $b = 1$, dilative volumetric strain accumulated in the first a few cycles while significant deviatoric strain is generated. This may clearly indicate the sample 'fails' due to large flow deformation even when the stress ratio $h = 0.9$ is lower than the peak stress ratio $h_p = 1.08$ obtained from monotonic loading (e.g., Fig. 7.7).

Fig. 8.13 presents the volumetric strain evolution against deviatoric strain for rotational shear at b=1.0,$h = 0.9$. It can be seen that if rotational shear continues, the dilative volumetric strain seems to increase further with increasing deviatoric strain. The ultimate dilative volumetric strain may have a connection to the critical volumetric strain in monotonic shearing as shown in Fig. 7.7. In addition, this shows that the DEM simulation for the rotational shear can continue when the sample 'fails' in advantage of a laboratory hollow cylinder rotational shear, where the sample fails with large deformation non-uniformity in the first few cycles and the test can not continue (Yang, 2013).

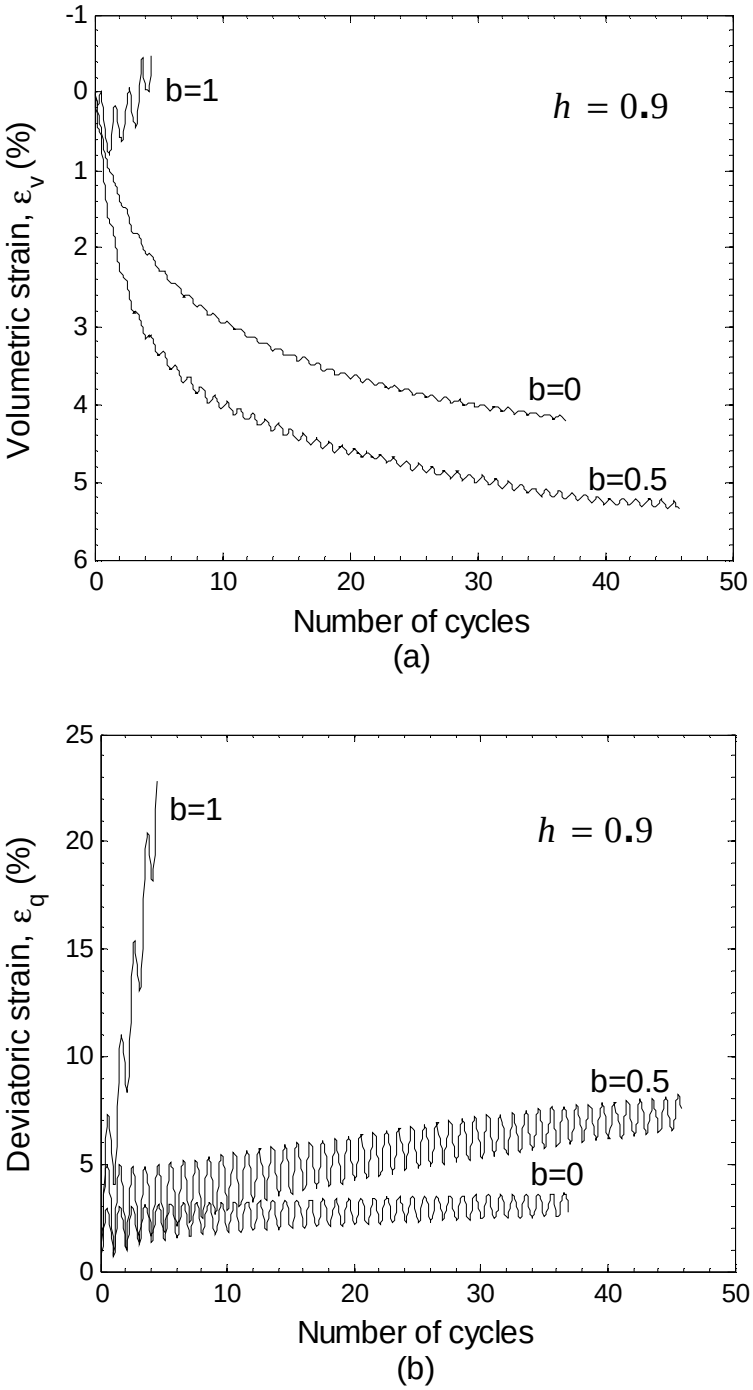

Fig. 8.12 Effects of *b* value on deformation behaviour (a) volumetric strain (b) deviatoric strain

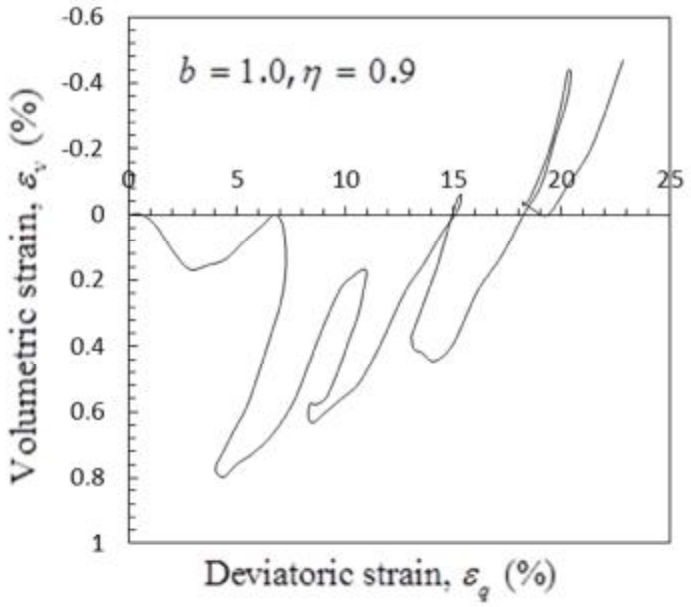

Fig. 8.13 Flow deformation for rotational shear at b=1.0,h = 0.9

8.4.3 Non-coaxiality

The degree of non-coaxiality is described as the difference of the principal plastic strain increment direction and principal stress direction. The total strain increment is used instead of the plastic strain increment. The strain increment is obtained within a small stress direction increment, i.e., $\Delta a \approx 1.5^{o}$. One cycle corresponds to 180º change of a. Fig. 8.14 shows the degree of non-coaxiality $g_{\Delta e} - a$ during rotational shear with three different b values. Significant degree of non-coaxiality is observed. Up to the same number of cycles, the degree of non-coaxiality is larger at a smaller b value. Consistent observations on the effect of b value on non-coaxiality have been reported in experimental study (Tong et al., 2010, Yang, 2013).

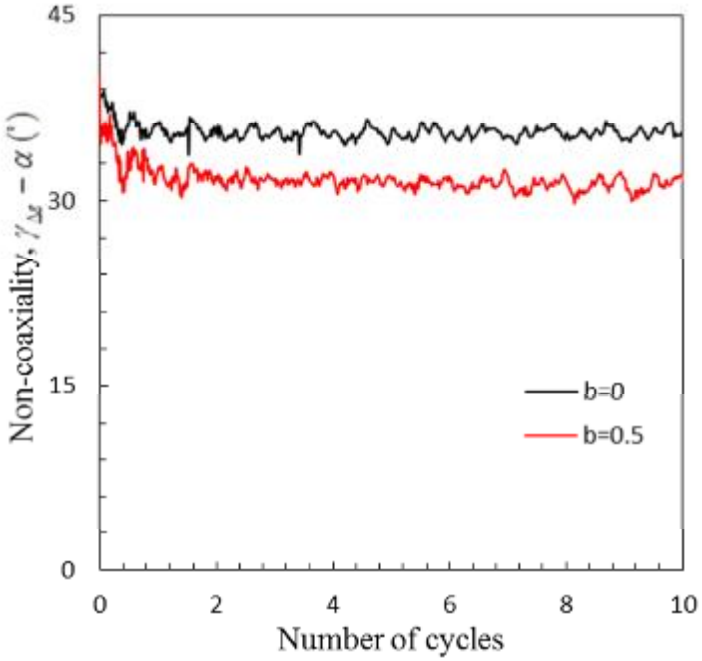

Fig. 8.14 Effects of *b* value on non-coaxiality in rotational shear

8.5 Internal structure evolution

The granular material internal structure includes the particles interactions and associated void distributions, known as the particle cell system and the void cell system (Li and Li, 2009). The internal structure evolution presented in the 2D DEM rotational shear (Li and Yu, 2010) was related to the void cell structure. In this research, the internal structure is described by the fabric tensor D_{ij} , which characterises the distribution of contact normal vectors between interacting particles.

8.5.1 Fabric response under various stress ratios

8.5.1.1 Fabric components evolution

The variation of fabric tensor components for rotational shear under various stress ratios is plotted in Fig. 8.15. The three figures share the same legend in Fig. 8.15(a). It can be seen that the fabric components D_{xy}, D_{yz} are close to zero during rotational shear, irrespective of the various stress ratios. The intermediate fabric component D_{yy} shows a tiny increase from its original value $D_{yy} = -0.13$ before rotational shear to a steady value $D_{yy} = -0.12$ at $h = 0.5$. It increases slightly in simulation with $h = 0.7$, from $D_{yy} = -0.12$ to $D_{yy} = -0.03$. Significant change of D_{yy} is observed at $h = 0.9$ with an increment up to 0.2 from its original value $D_{yy} = -0.08$. The increase of fabric component D_{yy} indicates more contacts formed along the *y*-direction, corresponding to sample contraction with positive strain component e_{yy}. Hence, the contractive strain e_{yy} is observed as shown in Fig. 8.2. And the magnitude of the strain e_{yy} is related to the increment magnitude of D_{yy}. The larger the increment of D_{yy}, the greater the strain e_{yy} generated.

Meanwhile, the fabric components D_{xx}, D_{xz}, D_{zz} vary periodically, showing a close relation to the periodical variation of stress components in Fig. 8.1. This clearly indicates that the material internal structure follows the rotation of major principal stress direction in *x*-*z* plane. The change of the internal fabric is related to the particles rearrangement. Hence, deformation is generated during stress rotation, shown as strain variations in Fig. 8.2. The oscillation amplitude of fabric components D_{xx}, D_{xz}, D_{zz} is larger at higher stress ratio. This demonstrates a greater

fabric increment rate at higher stress ratio, corresponding to the bigger strain increment rate at higher stress ratio (e.g., Fig. 8.2).

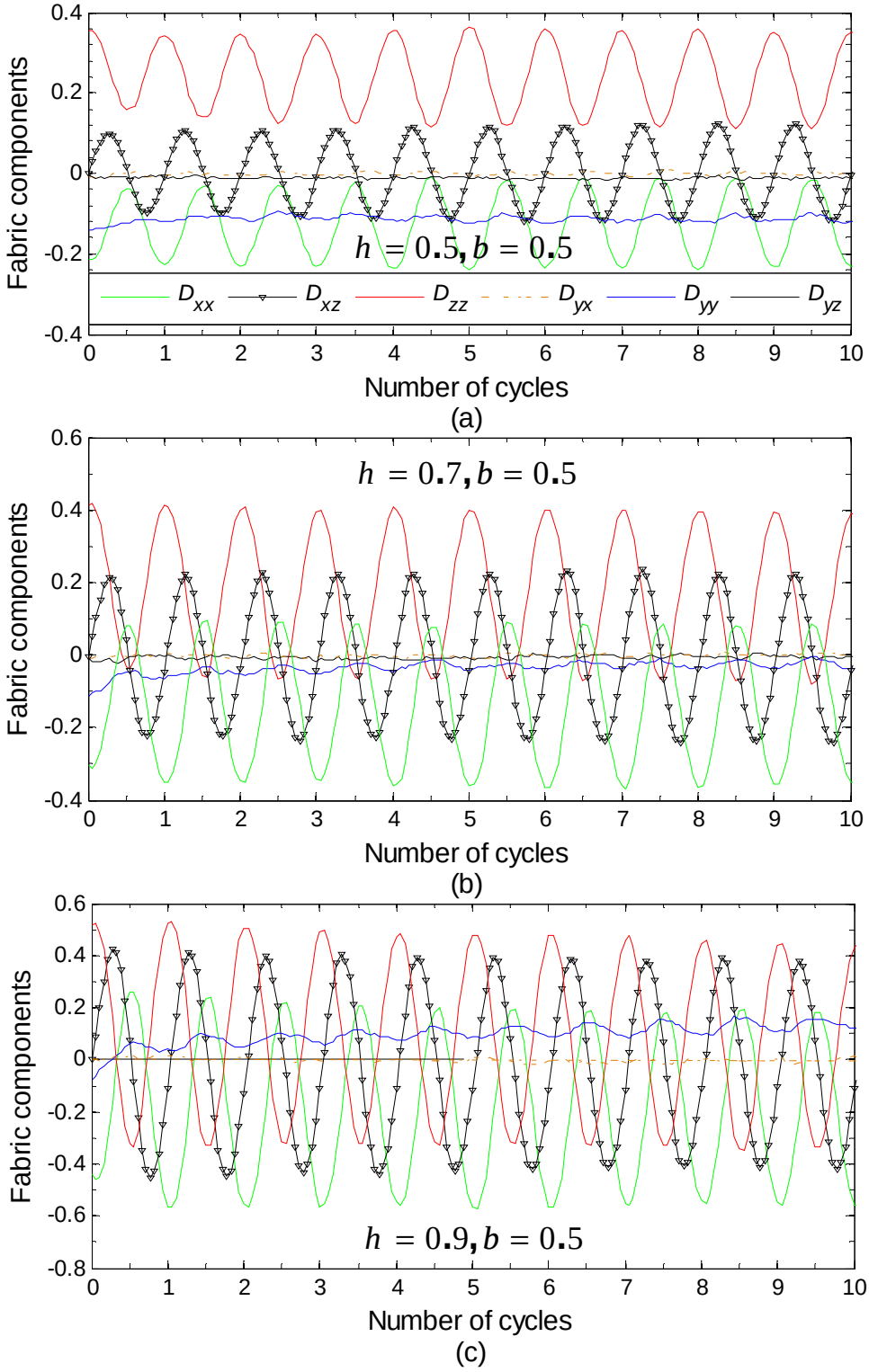

Fig. 8.15 Variations of fabric in rotational shear at various stress ratios

To have a better view of the fabric evolution, the fabric components D_{xx}, D_{xz}, D_{zz} are plotted in the deviatoric plane in terms of D_{xz} against $\left(D_{xx} - D_{zz}\right)/2$, as shown in Fig. 8.16. It shows that fabric trajectory is almost a circle, similar to the circle of the stress trajectory, with a fixed centre in the horizontal axis $\left(D_{xx} - D_{zz}\right)/2$ under continuous stress rotation. It indicates the material internal fabric anisotropy D_F remains nearly constant while the principal fabric direction rotates continuously along the stress rotation. In addition, it can be found that the centres of the fabric trajectory locate in the negative side of horizontal axis under various stress ratios due to effects of material initial anisotropy. Comparing the fabric trajectories under different stress ratios (e.g., Fig. 8.17), however, the size of the fabric trajectory is greater at larger stress ratio. This indicates that the material ultimate internal structure anisotropy is stress-ratio dependent, the larger the fabric anisotropy at bigger stress ratio. The larger internal structure anisotropy leads to larger size of strain trajectory as observed in Fig. 8.3. The reason is a larger deformation is required to achieve higher fabric anisotropy, which is confirmed in monotonic shear with tilting principal stress directions in Fig. A8. The centres of circular fabric trajectories are almost the same at $\left(D_{xx} - D_{zz}\right)/2 \approx -0.15$ at during the rotational shear regardless of various stress ratios.

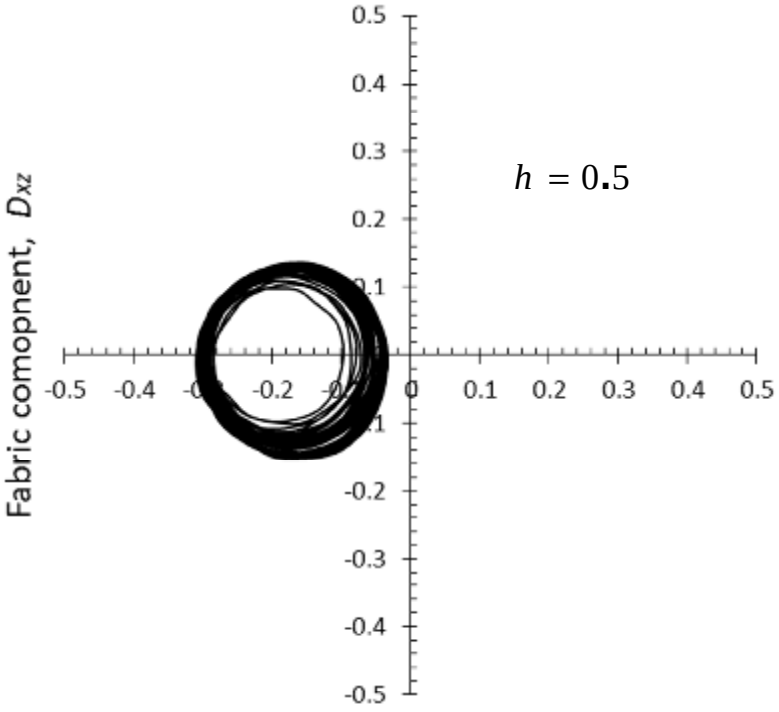
$h = 0.5$
Fabric comopnent, D_{xz}
Fabric comopnent, $(D_{xx}-D_{zz})/2$

(a)

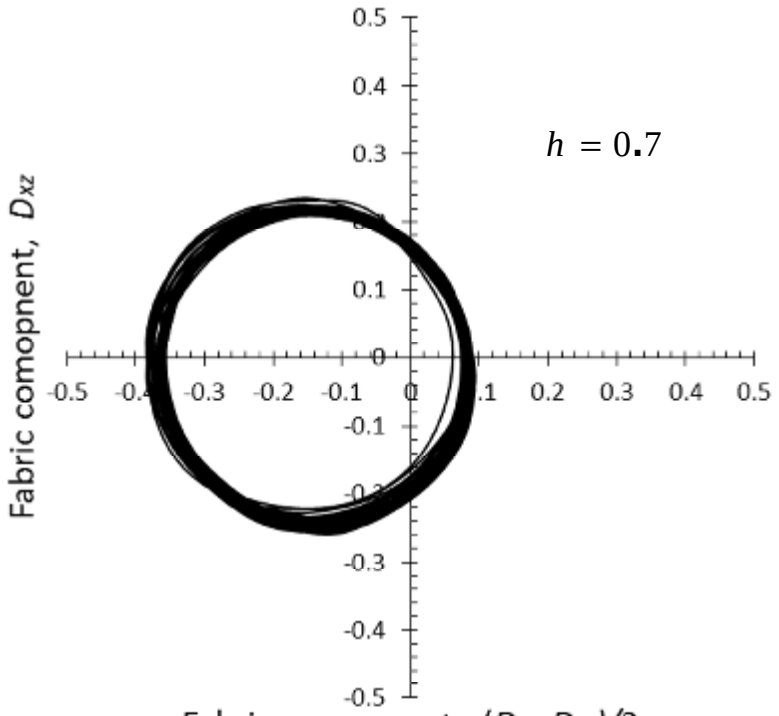
$h = 0.7$
Fabric comopnent, D_{xz}
Fabric comopnent, $(D_{xx}-D_{zz})/2$

(b)

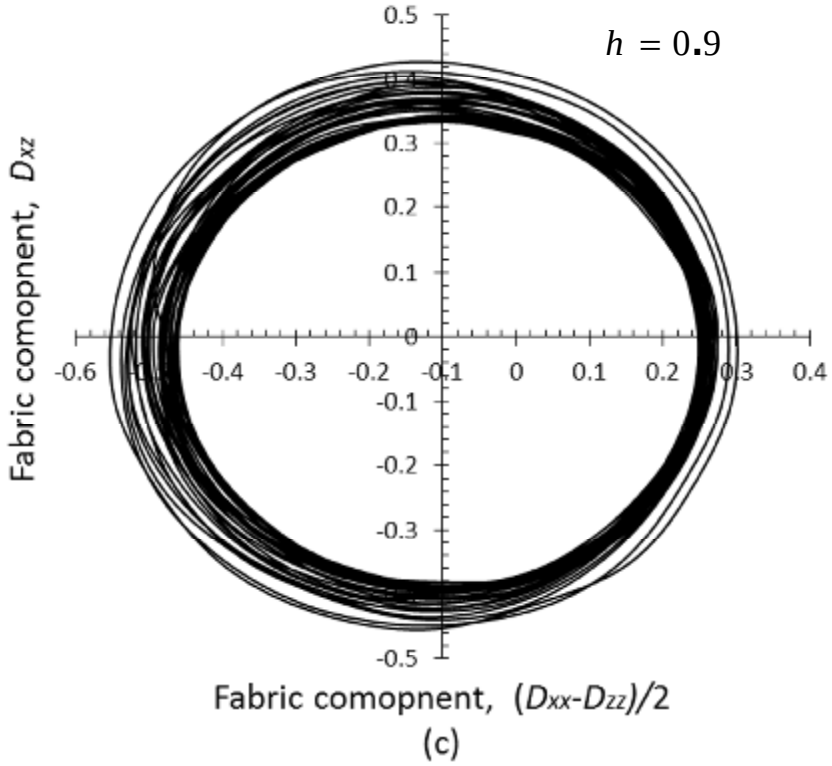

Fig. 8.16 Fabric trajectory in rotational shear at various stress ratios

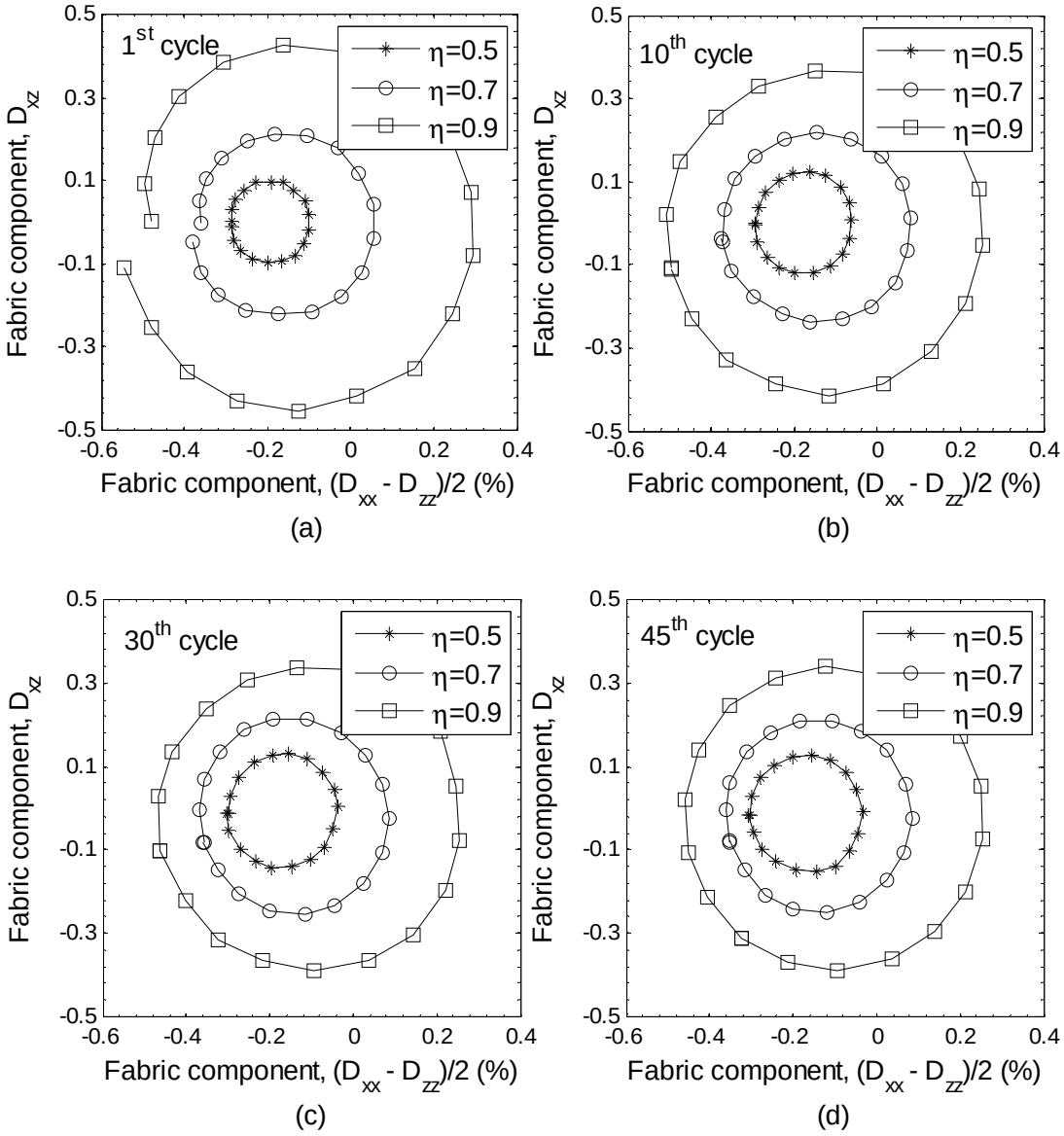

Fig. 8.17 Effect of stress ratios on fabric trajectory at different cycles

The ultimate deviatoric strain e_q^R, which is the radius of the ultimate circular strain trajectory, is plotted against the ultimate fabric anisotropy D_F^R, which is the radius of the ultimate circular fabric trajectory, as shown in Fig. 8.18. It is clear that e_q^R is linearly determined by D_F^R, although limited data obtained at three stress

ratios is presented. This is consistent to the 2D DEM observation of the linear correlation between e_q^R and D_F^R (Li et al., 2010).

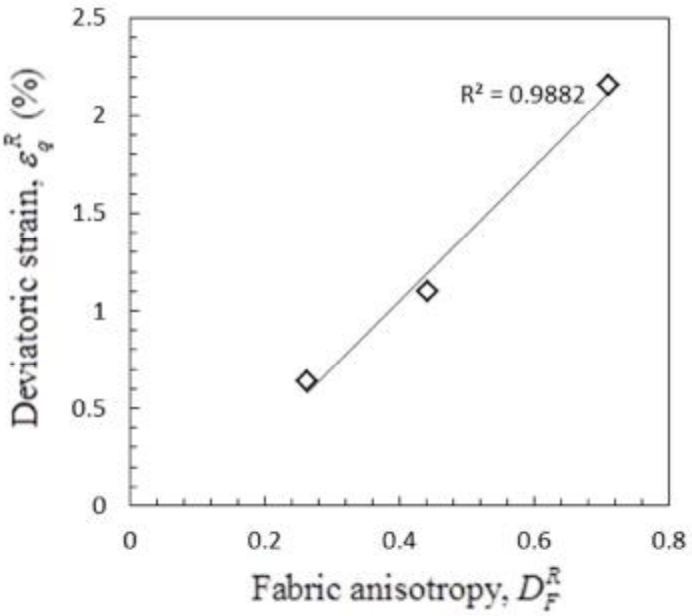

Fig. 8.18 Relation between the ultimate size of strain trajectory and the ultimate size of fabric trajectory

8.5.1.2 Principal fabric direction

Although the internal structure rotates along the major principal stress rotation, the major principal fabric direction may not exactly follow the direction of major principal stress direction. The principal fabric direction is determined by the angle g_F, which is the angle between the projection of the principal fabric vector on the *x*-*z* plane and the vertical axis. The difference of the major principal stress direction and major principal fabric direction, $a - g_F$, is plotted in Fig. 8.19. A positive value of $a - g_F$ indicates that material internal structure rotates along the major principal stress rotation with a few degrees behind the principal stress direction and the negative value, on the contrary, refers to the principal fabric

direction be ahead of the principal stress direction. It can be seen that the value of $a - g_F$ is not held constant to be zero but varies with oscillation, which demonstrates that the principal fabric direction is generally not coaxial with the principal stress direction. To have a better view of $a - g_F$ in one cycle, the evolution of $a - g_F$ is also plotted in Fig. 8.20 in the first cycle and the 45th cycle. Within the first cycle of a from 0^o to 180^o, the principal fabric direction is behind the rotation of the principal stress direction with increasing positive value $a - g_F$ as a varies from 0^o to 90^o while it becomes to be ahead of the principal stress direction with negative value $a - g_F$ for further increase of a to 180^o. This leads to the observed non-coaxial behaviour as shown in Fig. 8.7. The variation amplitude of $a - g_F$ is larger at a smaller stress ratio h, corresponding to the larger degree of non-coaxiality observed at a smaller stress ratio.

One may notice that the $a - g_F$ value can be as large as 90^o or -90^o at $h = 0.5$. This is because the principal fabric direction is always close to the vertical direction during rotational shear. In the deviatoric plane, this is shown as the fabric path being always in the negative side of the horizontal axis (e.g., Fig. 8.16(a)). Accordingly, the $a - g_F$ value can be as large as 90^o when the principal stress direction rotates to be in the horizontal direction, where the principal fabric direction is still close to the vertical direction. This may indicate that the low stress ratio, i.e., $h = 0.5$, would not be sufficient to disturb the material initial anisotropy, with preferred contact orientation in the vertical direction.

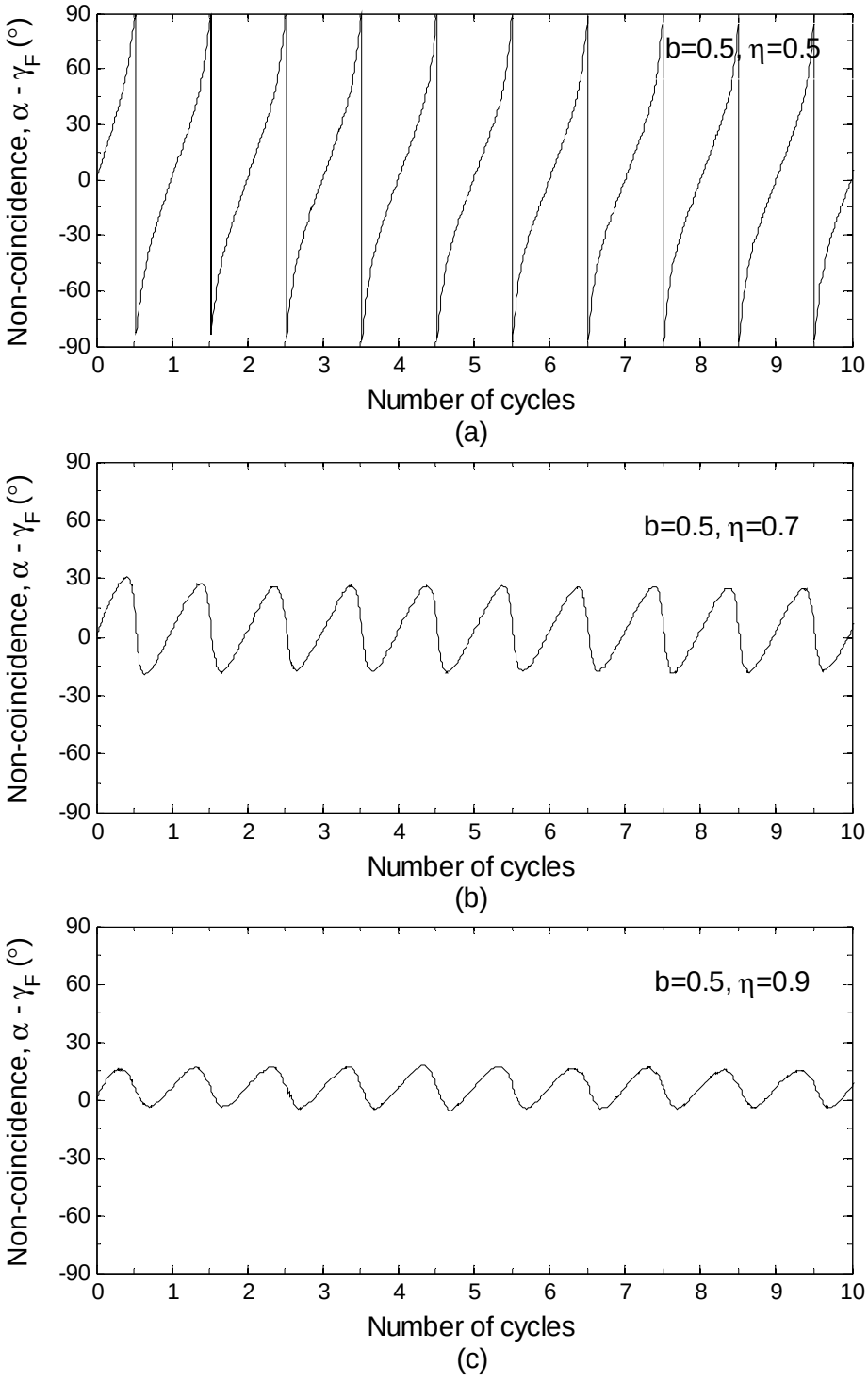

Fig. 8.19 Non-coincidence of principal stress direction and fabric direction

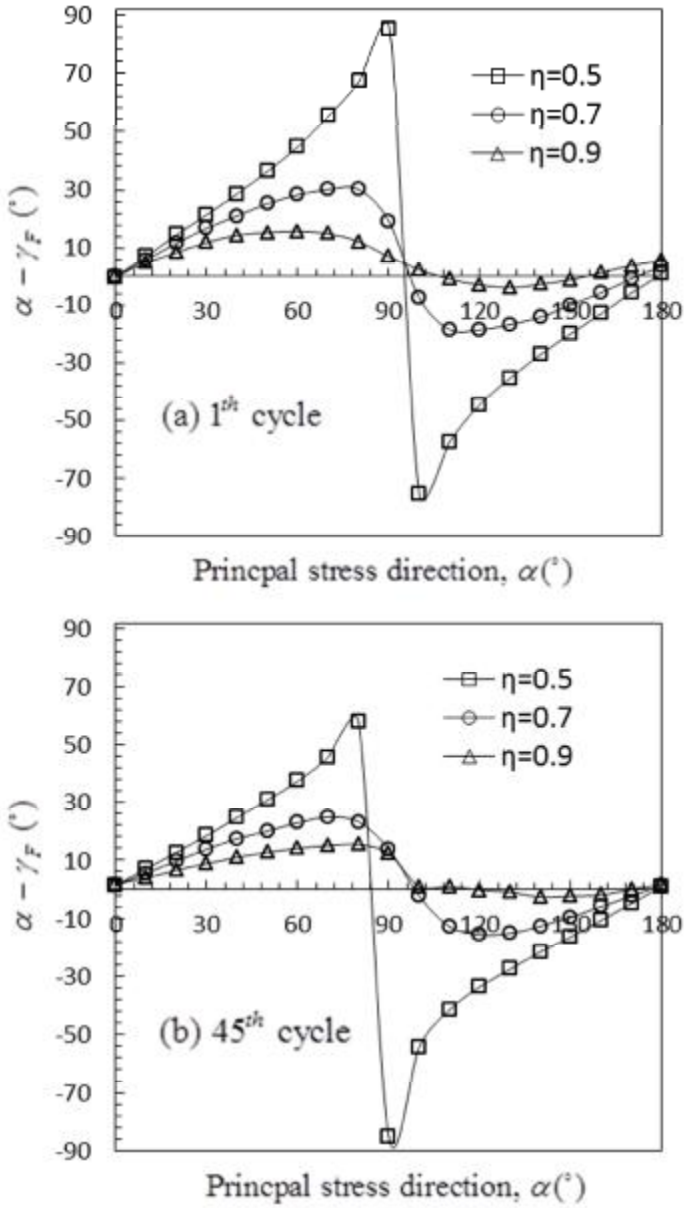

Fig. 8.20 Non-coincidence between principal stress direction and principal fabric direction at the 1th cycle and the 45th cycle

To have a better view of the fabric evolution within one cycle, the fabric paths in the deviatoric plane at $h = 0.7$ are plotted in Fig. 8.21 after the rotation of principal stress direction to $a = 45^{o}$ and $a = 135^{o}$ during the first cycle, respectively. The angle of the fabric vector, point from the origin to the end of the fabric path, relative to the horizontal axis is two times of the principal fabric

direction g_F . It is clear from the figure that the angle $2g_F$ is less than 90^o at $a = 45^o$ and greater than 270^o at $a = 135^o$, corresponding to the principal fabric direction behind the rotation of the principal stress direction and ahead of the principal stress direction, respectively. This clearly indicates that principal fabric direction does not follow the principal stress direction, or shown as the fabric vector being not parallel to the stress vector in the deviatoric plane due to the non-coincidence between the centre of fabric path circle (Fig. 8.16(b)) and the centre of stress path circle (Fig. 8.1(b)).

In addition, the dashed arrows in the figures refer to the fabric increment direction, which is tangential to the fabric path. It is interesting to see that the fabric increment direction is generally parallel to the horizontal axis at either $a = 45^o$ or $a = 135^o$, where the principal stress increment direction is also parallel to the horizontal axis. This indicates that the principal fabric increment direction is generally coaxial with the principal stress increment direction in the deviatoric plane. This observation would be useful for formulating a stress rate dependent fabric evolution law during rotational shear.

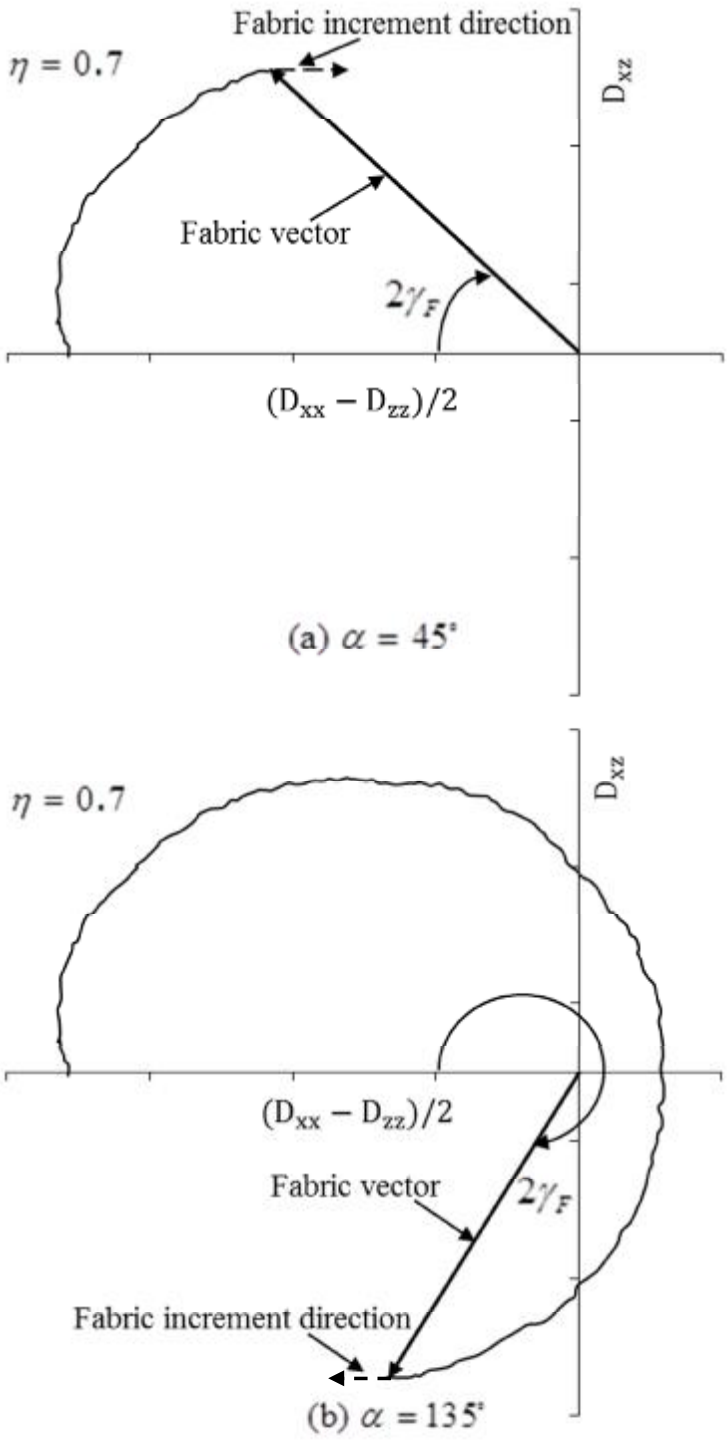

Fig. 8.21 Fabric evolution path up to particular rotation of principal stress direction for rotational shear at constant $h = 0.7, b = 0.5$

8.5.2 Fabric response under various *b* values

8.5.2.1 Fabric components evolution

The variation of fabric tensor components is plotted in Fig. 8.22. It shows that the fabric components D_{xy}, D_{yz} are close to zero during rotational shear. The intermediate fabric component D_{yy} shows a small decrease from its original value $D_{yy} = -0.24$ before rotational shear to a steady value $D_{yy} = -0.3$ at $b = 0$. It increases in simulation at $b = 0.5$, from $D_{yy} = -0.08$ to $D_{yy} = 0.22$. Significant change of D_{yy} is observed at $b = 1$ with an increment up to 0.43 from its original value of 0.07. The increase of fabric component D_{yy} indicates more contacts created in the *y*-direction, corresponding to contraction with the positive strain component e_{yy} developed. And the decrease of fabric component D_{yy} refers to contact disruption in the *y*-direction, corresponding to extension with negative strain component e_{yy}. Hence, the negative strain e_{yy} is generated at $b = 0$ and the positive strain e_{yy} is observed at other *b* values, as shown in Fig. 8.11. And the magnitude of the strain e_{yy} is related to the increment magnitude of D_{yy}. The larger the increment of D_{yy}, the greater the strain e_{yy} generated.

Meanwhile, the fabric components D_{xx}, D_{xz}, D_{zz} vary periodically. This clearly indicates that the material internal structure follows the rotation of major principal stress direction in *x*-*z* plane. The variation of the internal fabric is related to the particles rearrangement. Hence, plastic deformation is observed during stress

rotation. The variation amplitude of D_{xx}, D_{xz}, D_{zz} is larger at a greater b value, indicating larger fabric increment rate at bigger b value.

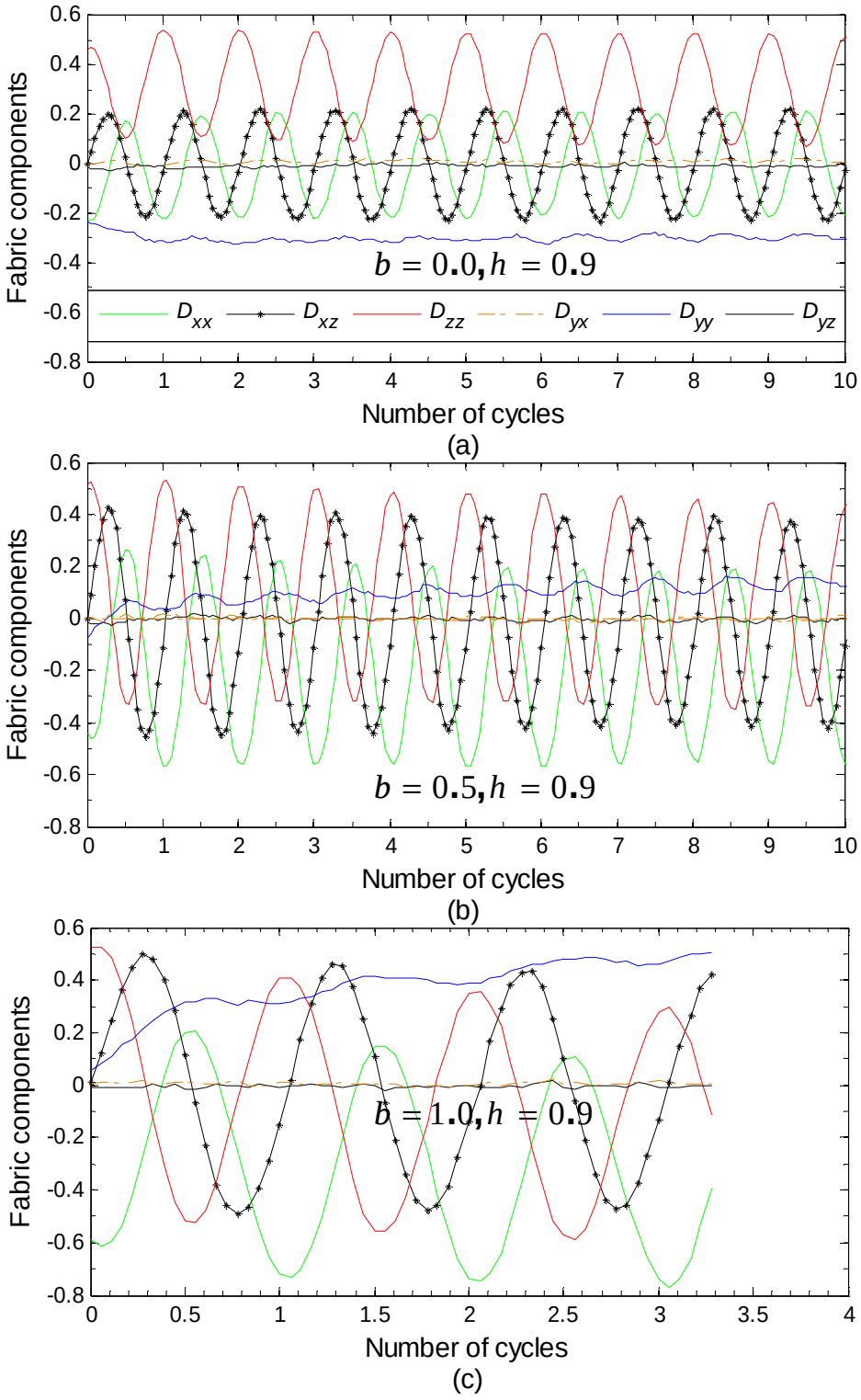

Fig. 8.22 Variation of fabric components (a) *b*=0 (b) *b*=0.5 (c) *b*=1

To have a better view of the fabric path evolution, the fabric components D_{xx}, D_{xz}, D_{zz} are plotted in the deviatoric space, as shown in Fig. 8.23. It can be found that the fabric trajectory is almost a circle with a fixed centre during rotational shear. It indicates the material internal fabric structure rotates along the stress rotation, which inevitably relates to the fabric reorganisation, accompanied by deformation behaviour. A more clear view of the fabric trajectory at different cycles is shown in Fig. 8.24. It clear shows that the fabric path has a complete circle during one cycle rotation of principal stress direction, except for the open trajectory in the first cycle. The size of the fabric trajectory circle is greater with increasing b value, indicating the internal structure anisotropy is larger at bigger b value. Hence, a larger size of strain trajectory is observed with increasing b value in Fig. 8.10.

The centres of the fabric trajectory locate in the negative side of the horizontal axis under various b values due to effects of material initial anisotropy, with preferred particle orientation in the horizontal bedding plane and contacts being more likely formed in the vertical direction. However, the centre position is around -0.1 in spite of various b values, where the stress ratio is the same as $h = 0.9$. This may indicate that the b value has negligible effect on the centre of fabric trajectory.

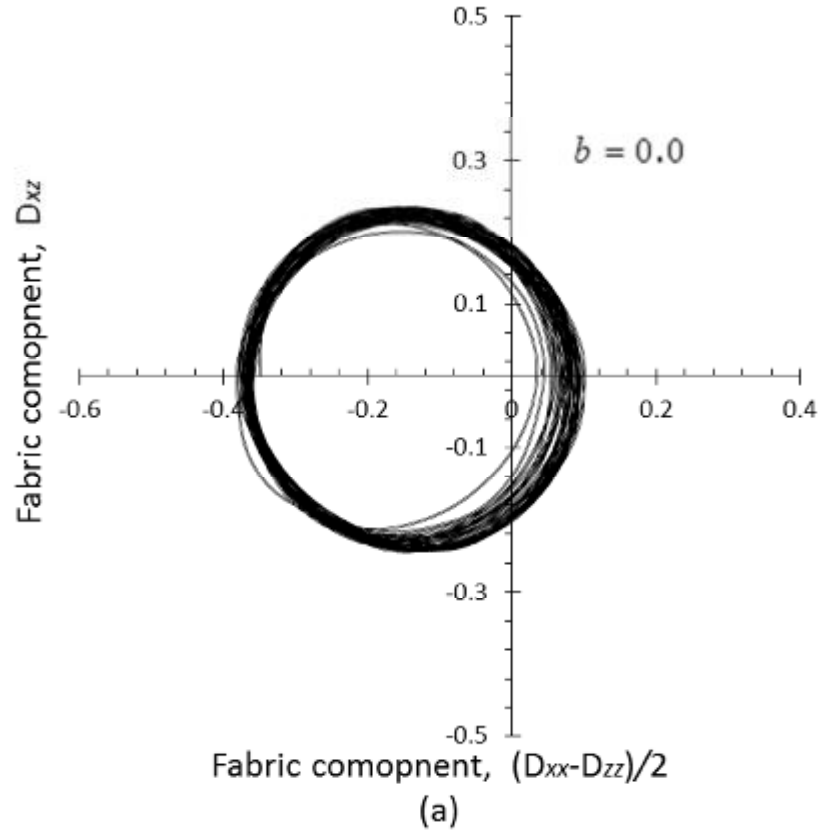
b = 0.0
Fabric comopnent, Dxz
Fabric comopnent, (Dxx-Dzz)/2
0.5
0.3
0.1
-0.1
-0.3
-0.5
-0.6
-0.4
-0.2
0
0.2
0.4

(a)

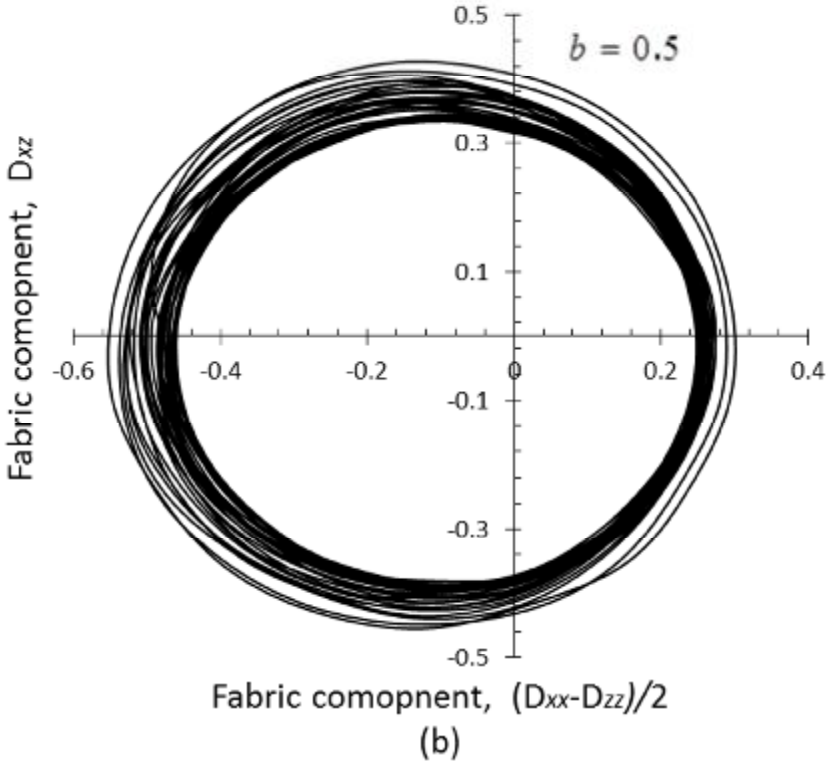
b = 0.5
Fabric comopnent, Dxz
Fabric comopnent, (Dxx-Dzz)/2
0.5
0.3
0.1
-0.1
-0.3
-0.5
-0.6
-0.4
-0.2
0
0.2
0.4

(b)

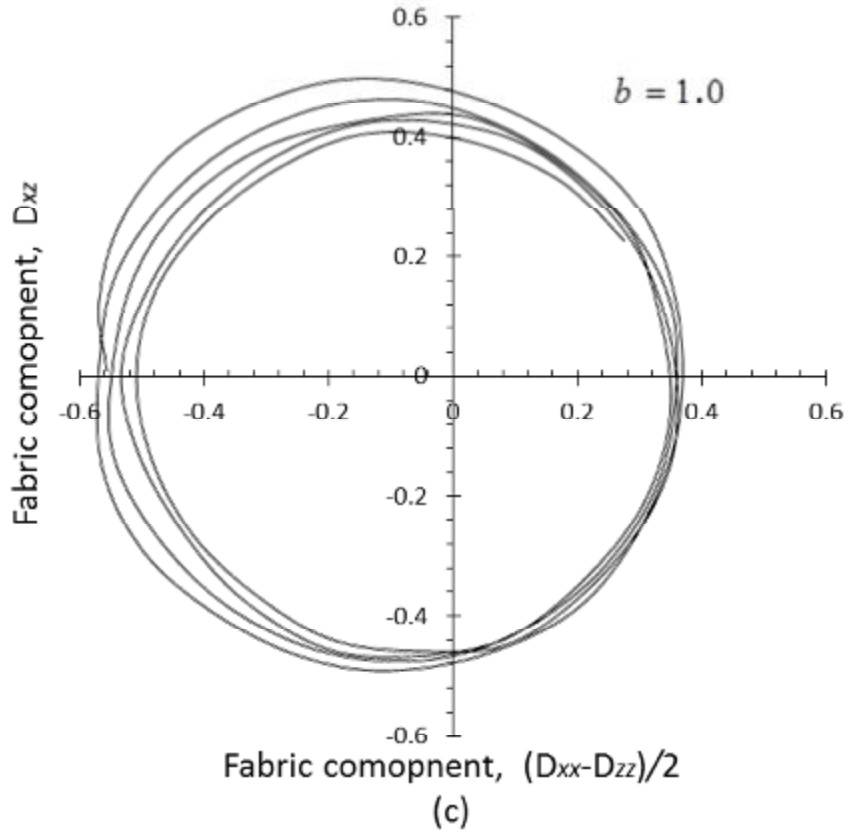

Fig. 8.23 Effects of *b* value on fabric trajectory (a) *b*=0 (b) *b*=0.5 (c) *b*=1

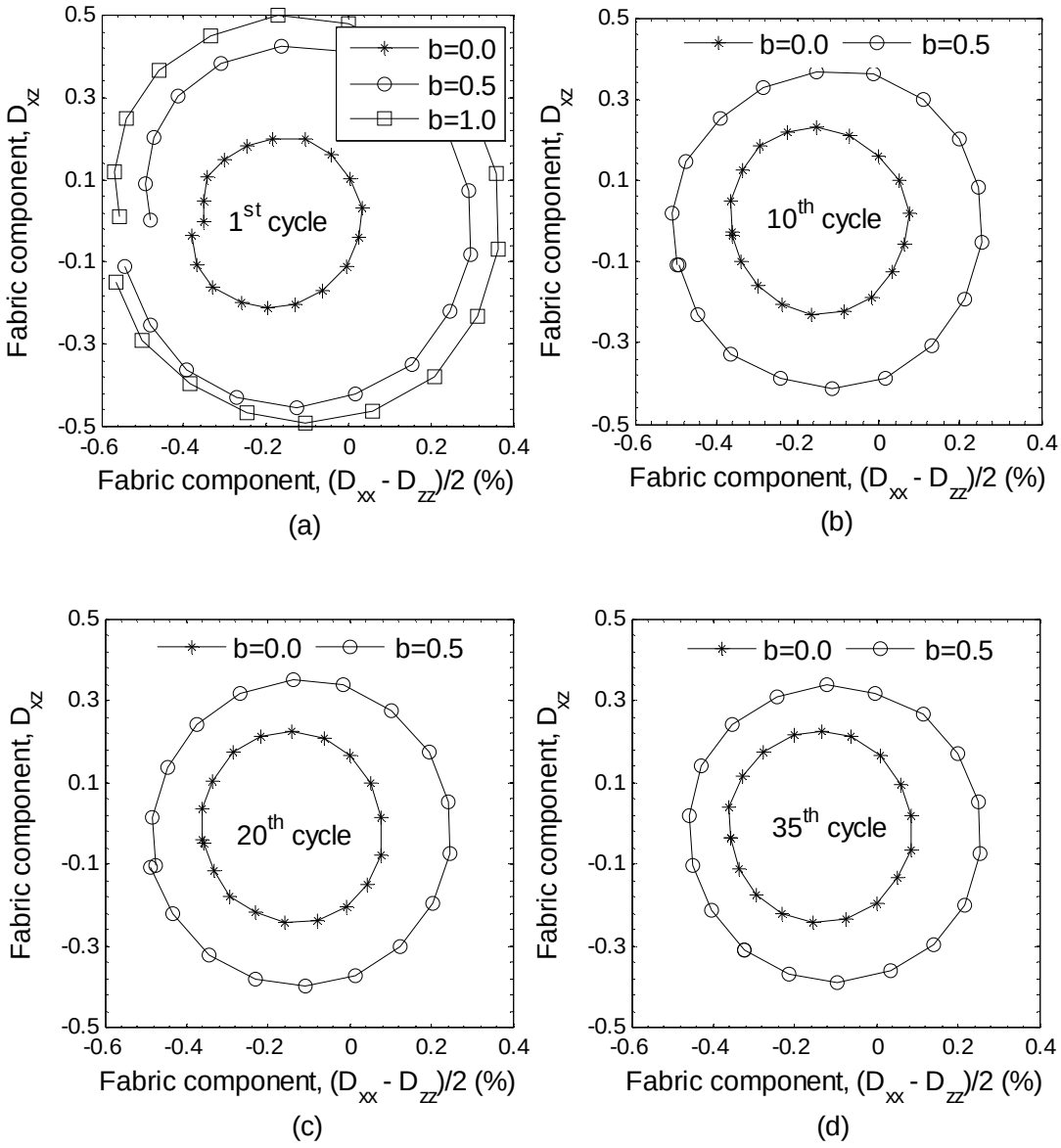

Fig. 8.24 Effect of *b* value on fabric trajectory at different cycles

8.5.2.2 Principal fabric direction

The non-coincidence of principal stress direction and principal fabric direction is illustrated in Fig. 8.25 for rotational shear at different *b* values. The principal fabric direction at $b = 1.0$ is not included as the sample is referred to 'failure'. It can be seen that the value of $\alpha - g_F$ is not held constant but varies with oscillation, which demonstrates that the principal fabric direction is generally not

coaxial with the principal stress direction. To have a better view in one cycle, the difference between principal stress direction and principal fabric direction is also shown Fig. 8.26. Within one cycle of a from 0^{o} to 180^{o}, the principal fabric direction is behind the rotation of the principal stress direction with increasing positive value $a - g_F$ as a varies from 0^{o} to 90^{o} while it becomes to be ahead of the principal stress direction with negative value $a - g_F$ with further increase of a to 180^{o}. This leads to the observed non-coaxial behaviour as shown in Fig. 8.14. The variation amplitude of $a - g_F$ is larger in simulation at $b = 0$ than at $b = 0.5$, corresponding to the slightly larger degree of non-coaxiality observed at a smaller b value in Fig. 8.14.

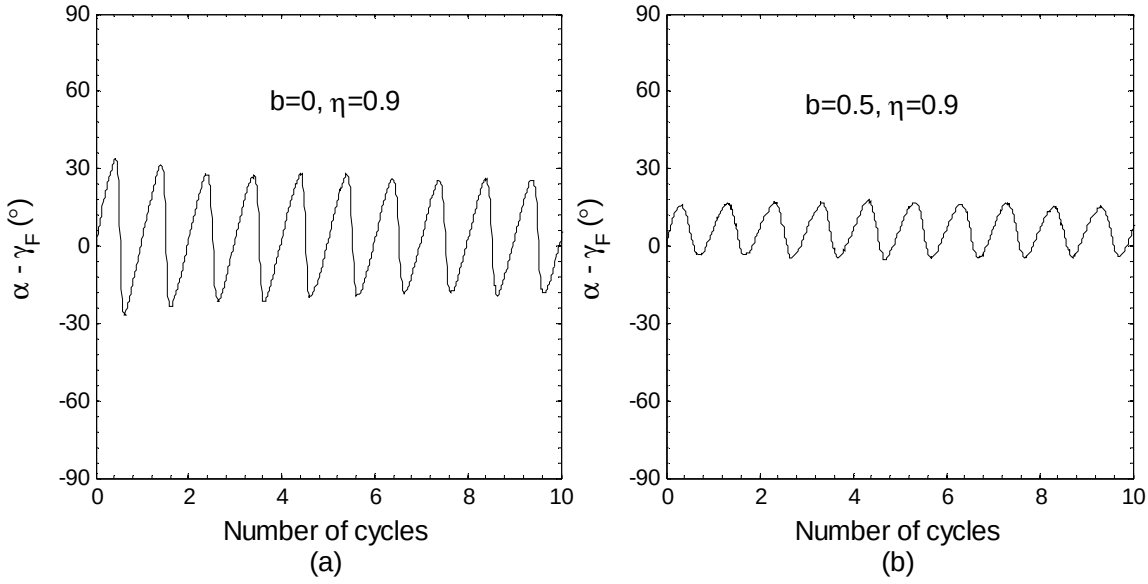

Fig. 8.25 Non-coincidence between principal stress direction and principal fabric direction at different *b* values

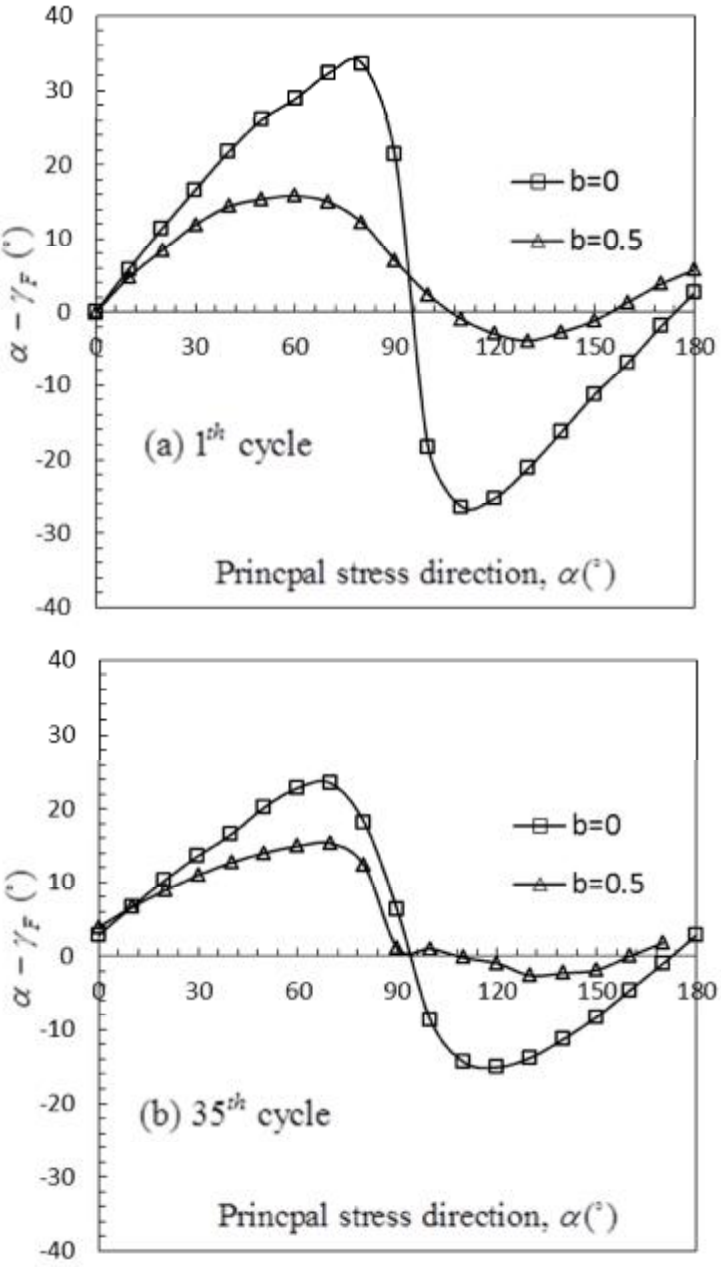

Fig. 8.26 Non-coincidence between principal stress direction and principal fabric direction in the 1th and 35th cycles

8.6 Internal structure evolution on initially isotropic samples

8.6.1 Fabric response on samples of spherical particles

For samples with spherical particles (e.g., Table 4.4) subjected to rotational shear, the internal structure response to rotational shear is described by the evolution of fabric tensor D_{ij} , which characterises the contact normal orientation density distribution in three-dimensional spaces. The fabric trajectory in the deviatoric plane is plotted in Fig. 8.27. To have a better view of the fabric trajectory, the fabric trajectories in the 1^{th} cycle and the 48^{th} cycle are plotted in Fig. 8.28. In the 1^{th} cycle, the fabric trajectory shows to be open, corresponding to the open strain trajectory. With increasing number of cycles, the fabric trajectory of the dense sample SRED_B05Y05_RS shows to be a circle with fixed centre and the size of fabric trajectory remains constant. The fabric trajectory of the loose sample SREL_B05Y05_RS is spiral with centre unchanged and the size of fabric trajectory becomes smaller to be steady after a large number of cycles, indicating an ultimate internal structure achieved. The circular variation of fabric trajectory indicates the internal structure rotates continuously along stress rotation, accompanied by deformation. Hence, the larger size of strain trajectory in the loose sample (Fig. 4.19) is due to the greater internal fabric anisotropy. The strain trajectory becomes smaller in the loose sample with increasing number of cycles, corresponding to decreasing size of fabric trajectory. After larger number of cycles, the sizes of fabric trajectory become similar for both samples (e.g., Fig. 8.28(b)), indicating the material

possessing similar internal structure regardless of initial void ratio. Hence, the samples approach the same ultimate state with similar void ratios achieved as shown in Fig. 4.21.

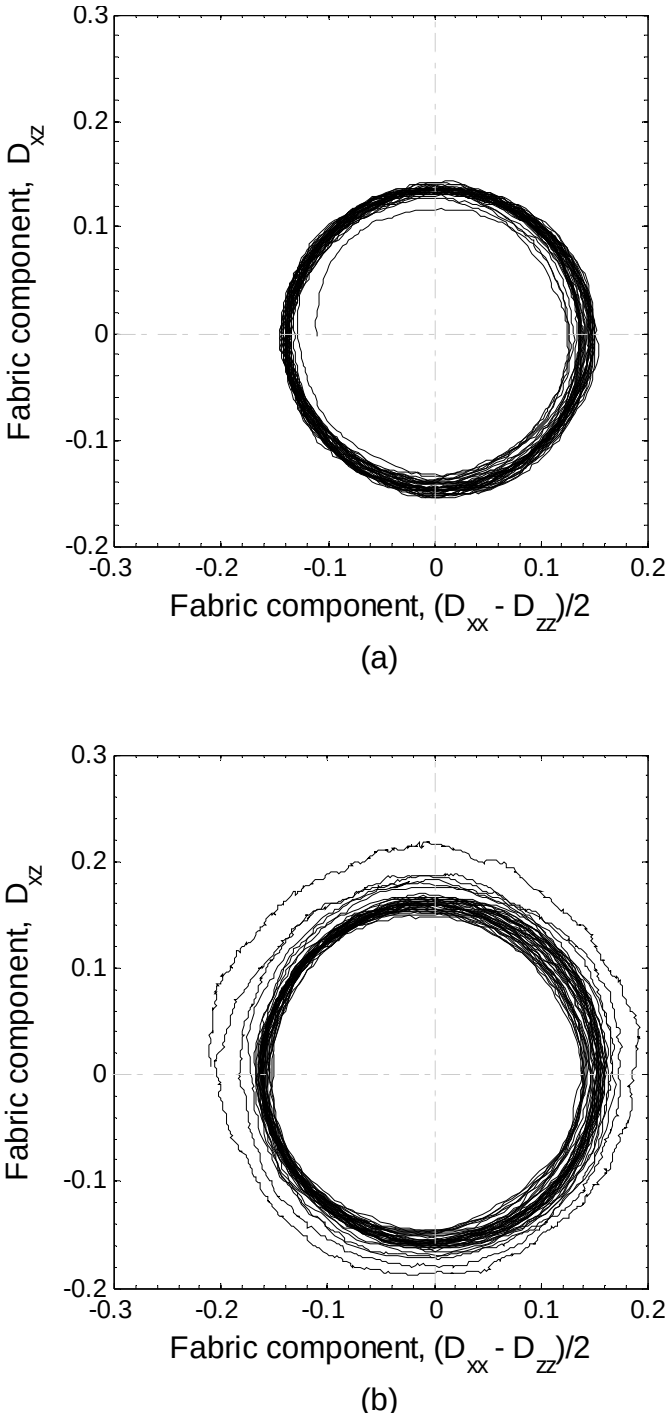

Fig. 8.27 Fabric trajectory on samples of spherical particles (a) dense sample SRED_B05Y05 (b) loose sample SREL_B05Y05

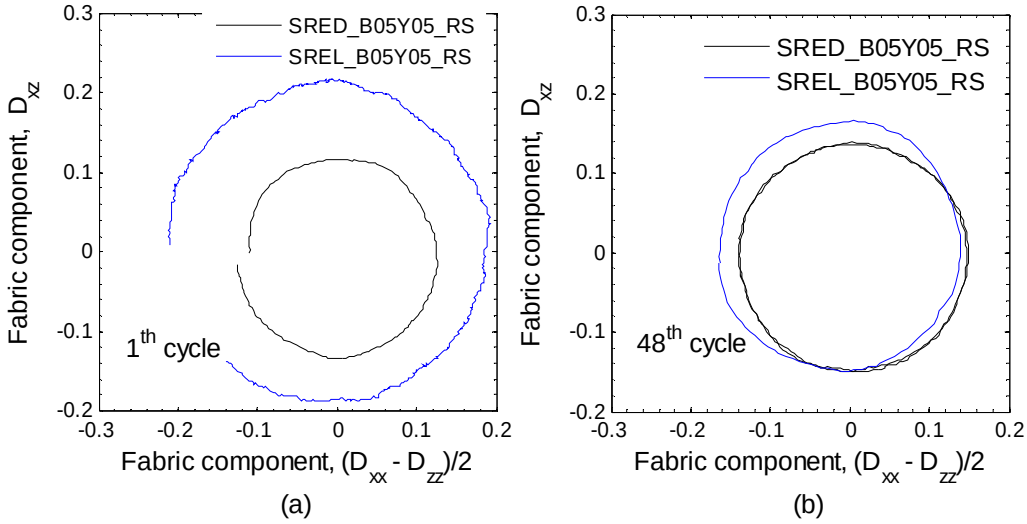

Fig. 8.28 Fabric trajectory in the 1th cycle and 48th cycle in samples of spheres

The intermediate fabric evolution is shown in Fig. 8.29. The fabric D_{yy} generally increases with increasing number of cycles for both samples, regardless of fluctuations within one cycle. The increase of fabric component D_{yy} indicates an increasing contact orientation density along the *y*-direction, corresponding to contraction with positive strain component e_{yy} in both samples. The increment of D_{yy} is larger in the loose sample than that in the dense sample, leading to a larger intermediate strain e_{yy} in the loose sample (e.g., Fig. 4.20).

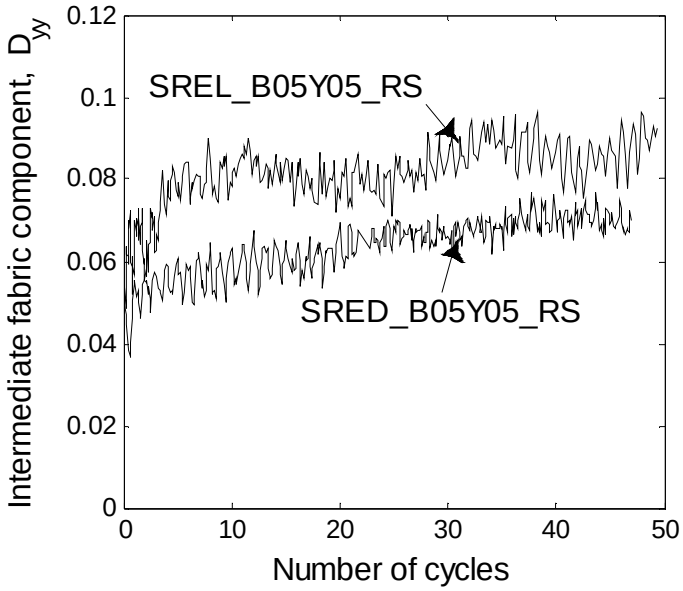

Fig. 8.29 Evolution of intermediate fabric during rotational shear

Although the internal structure rotates along stress rotation shown as circular fabric trajectory in Fig. 8.27, the principal fabric direction is not necessarily coaxial with the principal stress direction. The principal fabric direction is described by the angle g_F, which is the angle between the projection of principal fabric vector on the *x*-*z* plane and the vertical *z*-axis. The difference of the major principal stress direction and the major principal fabric direction, $a - g_F$, is plotted in Fig. 8.30. And the non-coincidence of $a - g_F$ within two cycles is superimposed for more clear view. It can be seen that the major principal fabric direction is not coaxial with major principal stress direction due to non-zero value of $a - g_F$. The variation of $a - g_F$ show periodicity. The positive value of $a - g_F$ indicates the principal fabric direction is always behind the rotation of the principal stress direction, resulting in non-coaxial behaviour. The average value of $a - g_F$ is observed to be slightly smaller in the dense sample SRED_B05Y05_RS and the loose sample

SREL_B05Y05_RS, resulting in similar degrees of non-coaxiality shown in Fig. 4.22.

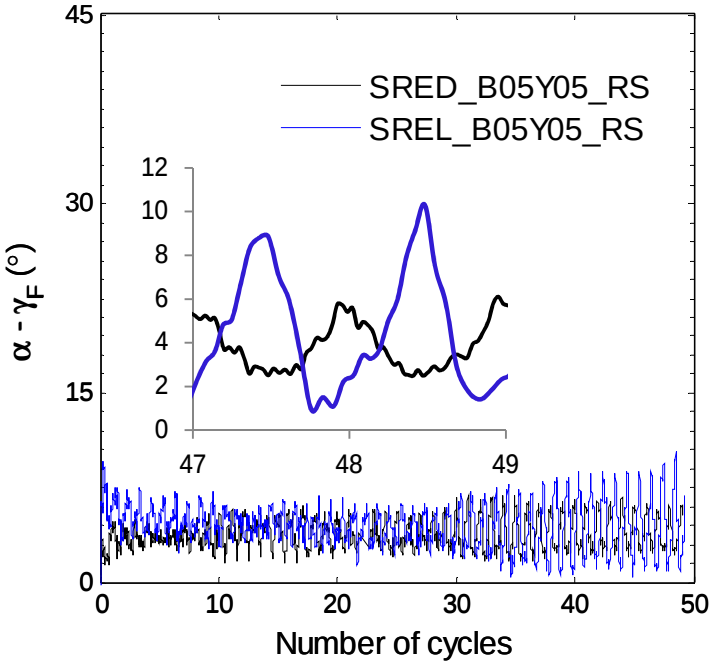

Fig. 8.30 Non-coincidence between principal stress direction and principal fabric direction

8.6.2 Fabric response on samples of non-spherical particles

The initially isotropic sample of non-spherical particles CRED_TT has been prepared by radius expansion method as shown in Table 7.1. The sample was pre-sheared at constant $p = 500kPa, b = 0.5$ to the stress ratio $h = 0.5$ for rotational shear, labelled as CRED_B05Y05_RS in Table 8.1. The micro-scale internal structure evolution is presented in this section and compared to that of the sample CDED_B05Y05_RS.

The fabric trajectory of sample CRED_B05Y05_RS is shown in Fig. 8.31(b) and is compared to that of sample CDED_B05Y05_RS. It shows that the fabric

trajectory for sample CRED_B05Y05_RS is a circle with its centre nearly coincident to the axis origin. However, the centre of fabric trajectory for the sample CDED_B05Y05_RS locates in the negative side of the axis $\left(D_{xx} - D_{zz}\right)/2$. This clearly indicates of the material initial anisotropy effect on the internal structure evolution.

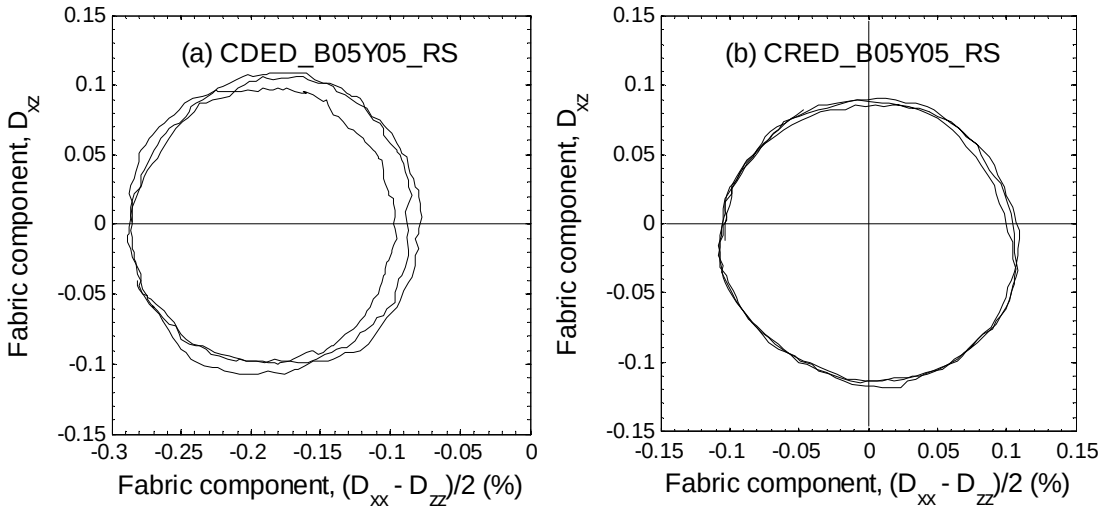

Fig. 8.31 Comparison of fabric trajectory on samples CRED_B05Y05_RS and CDED_B05Y05_RS

8.6.3 Discussion

The drained rotational shear responses of granular material under the same constant stress invariants $p = 500kPa, b = 0.5, h = 0.5$ have been reported on samples of spherical particles in Section 4.4.3 and on samples of non-spherical particles in Section 8.3. The common observations, e.g., plastic deformation and deformation non-coaxiality, have been observed, irrespective of particle shape. The strain trajectory is found to be stabilised as a circle after large number of cycles. The internal fabric trajectories are circular with its centres close the origin of axes for

initially isotropic samples of both spherical and non-spherical particles, i.e., SRED_B05Y05_RS and CRED_B05Y05_RS. It indicates the particle shape has negligible effect on the common phenonmenal observations during rotational shear.

In micro-scale observations, one may notice that the fabric trajectory path shows to be different due to different sample preparation procedures (i.e., Fig. 8.31). The centre of the circular fabric trajectory locates in the negative side of the horizontal axis $\left(D_{xx} - D_{zz}\right)/2$ for the sample CDED_B05Y05_RS, which was initially prepared by deposition method. However, the fabric trajectory seems to be symmetric about vertical axis for the sample CRED_B05Y05_RS, which was initially isotropic prepared by the radius expansion method. This may be explained as the effect of initial anisotropy. The sample CDED_B05Y05_RS had preferred distribution of particle orientations in the horizontal bedding plane during gravitational deposition. However, the sample CRED_B05Y05_RS prepared by radius expansion method had isotropic particle orientation distribution. The preferred particles orientations in the horizontal direction leads to preferred contact normal oriented in or close to the vertical direction, indicating more contact density in the vertical direction than that in the horizontal direction. Hence, Fig. 8.31(a) presents a circular fabric path with its centre deviated from the axis origin. The value of $\left(D_{xx} - D_{zz}\right)/2$ is always negative at whatever principal stress direction. As for the sample CRED_B05Y05_RS, the isotropic particle orientation distribution indicates the equal opportunity of fabric anisotropy at different principal stress direction. Fig. 8.31(b) shows a circular fabric path symmetric abouth vertical axis, with the centre generally being coincident with the axes origin.

8.7 Discussion

The conventional plasticity theory faces a challenge in modelling soil behaviour, e.g., material response under rotational shear and non-coaxial behaviour. As it has been investigated by DEM study in this research, the observations of macroscopic granular material behaviour show close connection to the material internal structure. One attempt is to formulate a micromechanical fabric-based constitutive model, where the fabric tensor bridges the gap between micromechanics and continuum theory (Yu, 2008). For example, the constitutive models incorporate the initial fabric anisotropy (Dafalias et al., 2004, Lashkari and Latifi, 2008). However, in their models, the fabric tensor parameter only describes the initial cross-anisotropic microstructure and it does not evolve under loading. This would be problematic, as it is clear from DEM results that the fabric anisotropy is not constant but varies against loading, i.e., the centre position of fabric trajectory significantly affected by the stress ratio during rotational shear, different size of fabric trajectory under various stress ratios or even under the same stress ratio while various b values. Therefore, to incorporate the fabric tensor into a constitutive model, it is necessary to define a fabric evolution law, which describes how the fabric changes upon loading.

Yu (2008) presented an implicit expression of the fabric evolution law, which describes that the fabric tensor increment is dependent on the current deviatoric stress tensor and increment of deviatoric stress. This fabric evolution law may not work quite well in some cases. For example, during rotation shear at $b = 0.5$ with various stress ratios, the intermediate principal stress is constant with direction fixed

along the *y*-axis, but we do see the intermediate fabric component D_{yy} changes, as shown in Fig. 8.15, which should be constant according to the fabric evolution law. In addition, it cannot distinguish the fabric evolution path in the hardening regime or the softening regime. Fig. 8.32 shows the relationship of fabric anisotropy against the stress ratio during true triaxial simulations of the initially isotropic dense sample SRED_TT as presented in Section 5.4. It can be seen that the fabric anisotropy increases to its maximum value during the strain hardening regime. However, during strain softening, the fabric anisotropy would decrease along the same fabric evolution path in hardening regime according to the fabric evolution law while the DEM results clearly show post-peak fabric anisotropy decreases slightly to its critical value during strain softening.

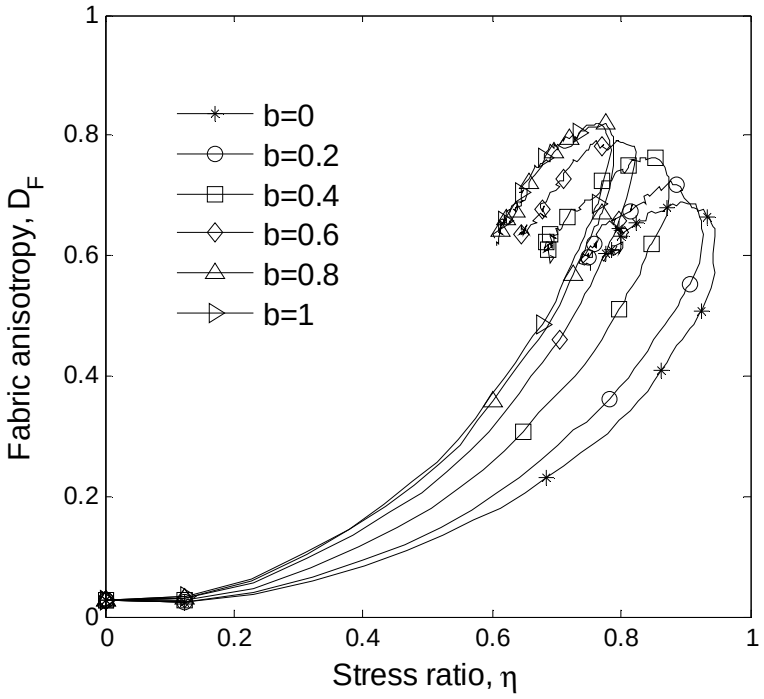

Fig. 8.32 Stress-fabric evolution for initial isotropic dense sample SRED_TT

8.8 Summary

The drained rotational shear has been carried out on a dense sample of non-spherical particles under various stress ratios and various b values. Two remarkable material responses are observed. One is that significant deformation occurred in spite of constant magnitude of stress invariants. The other one is that the flow deformation is generally non-coaxial. Microscopically, the material internal structure rotates along the rotation of major principal stress direction. The principal fabric direction does not follow the rotation of principal stress direction, resulting in non-coaxial behaviour. The fabric reorganisation mechanism accompanies plastic deformation. It is interestingly to observe that the fabric increment direction is generally the same as the stress increment direction in the deviatoric plane.

Under otherwise similar conditions, the size of fabric trajectory is larger at a greater stress ratio and larger b value. The larger size of fabric trajectory results in a greater strain trajectory in the deviatoric plane. In addition, the centre position of fabric trajectory is closer to the origin at a higher stress ratio while the b value has a negligible effect on centre position of fabric trajectory. The difference between the principal stress direction and the principal fabric direction is larger at a smaller stress ratio and at a smaller b value. Hence, lower degrees of non-coaxiality are observed with increasing stress ratio and b value.

Significant volumetric contraction is observed in rotational shear. Up to the same number of cycles, the volumetric strain is larger during rotational shear under a higher stress ratio and greater b value, leading to smaller ultimate void ratio. The

ultimate void ratio is determined by the ultimate internal structure anisotropy, the larger the stress ratio and b value, the greater the ultimate fabric anisotropy.

It was interesting to note that the sample could fail during rotational shear, resulting in significant deviatoric strain developed in the first few cycles. The sample failed at a stress ratio $h = 0.9$, which was lower than the peak stress ratio $h_p = 1.08$ obtained in monotonic loading but higher than the critical stress ratio $h_c = 0.82$. This indicated importance of considering stress rotation in geotechnical design and the material strength should be chosen based on the critical stress ratio rather than the peak value.

Significant intermediate principal strain e_{yy} has been generated during rotational shear in spite of constant intermediate principal stress. The contractive intermediate strain e_{yy} is larger at a higher stress ratio during rotation shear under constant $b = 0.5$, corresponding to the larger increment of D_{yy} at greater stress ratio. During rotational shear under various b values, the intermediate strain e_{yy} changes from extension at $b = 0.0$ to contraction at $b = 1.0$. The reason is that the intermediate fabric decreases slightly in simulation at $b = 0$ while it increases at other b values. And the larger strain e_{yy} at greater b value corresponds to bigger increment of D_{yy}.

The material initial particle orientation anisotropy has a great effect on the fabric evolution during rotational shear. The centre of the fabric trajectory coincides with the axis origin in the sample of isotropic particle orientation distribution

prepared by the radius expansion method. However, it locates in the negative side of the horizontal axis in the deviatoric plane for the sample prepared by the gravitational deposition method, with preperred particle orientations in the horizontal direction.

Chapter 9 Conclusions and future work

This work investigates the quasi-static behaviour of granular material under general three-dimensional stress paths using DEM. Comprehensive numerical simulations have been conducted with independent control of the three principal stresses in terms of both their magnitudes and principal directions. The material responses and micro-scale observations are summarised in the following.

9.1 Three-dimensional virtual experiment method

A virtual experiment model has been successfully implemented into the commercial software PFC3D for studying granular material behaviour under general stress states. The numerical technique applies loading to a granular assembly through boundary consisting of rigid mass-less walls. It is suggested that the boundary walls form a polyhedral shape with the angle between two neighbouring walls being obtuse to enhance sample uniformity. Strain-controlled boundary is achieved by directly specifying the translation and rotational velocities of the walls. A servo-control mechanism of stress boundary conditions is developed and can be combined with strain boundary conditions to achieve mixed loading conditions. The developed numerical technique is advantageous in applying general loading paths and various

loading conditions, including fully strain controlled, fully stress controlled and partially strain controlled and partially stress controlled.

The realisations of three particular loading paths are described in detail in Section 4.4. It represents the fully strain-controlled, fully stress-controlled and mixed-controlled loading conditions. The typical simulation results of undrained simple shear, drained true triaxial test and drained rotational shear, the three typical loading paths in laboratory tests, have been presented. The observation on principal stress rotation in simple shear and the significant volume contraction and deformation non-coaxiality during rotational shear are in qualitative accordance with the laboratory findings over various sand. The non-coaxial behaviour is mainly due to the non-coincidence of the principal direction of internal structure and loading direction. This supports the application of the discrete element method (DEM) and confirms the capability of the developed numerical technique as a useful tool to facilitate multi-scale investigations on the constitutive theories of granular materials.

9.2 Stress-force-fabric relations

The stress-force-fabric (SFF) relationship in Eq. (2.18) links the macroscopic stress tensor to the micro-scale coordination number, contact forces tensors, fabric tensor and branch vector tensor. The deviator stress ratio is dependent on the degrees of contact force anisotropy and fabric anisotropy while the anisotropy of branch vector is small and the contribution to stress ratio is negligible. The stress-force-fabric predicts the stress ratio with good accuracy to that calculated from the forces acting on boundary walls (e.g., Fig. 5.26). Hence, it is applicable to apply the SFF

relationship to explain the global strength-deformation characteristics in terms of coordination number, contact forces anisotropy and fabric anisotropy.

9.3 Effect of *b* value

The true triaxial simulations have been conducted on the initially isotropic sample of spherical particles as presented in Chapter 5, in order to investigate the magnitude of intermediate principal stress on granular material behaviour. The major conclusions are summarised as follows:

(1) The triaxial compression simulation results on samples with three different initial void ratios shows that the material performs stiffer and more dilative for sample of a smaller initial void ratio. Microscopically, this is due to greater anisotropy degrees of contact force tensors and fabric tensor developed in denser sample. The strain hardening and strain soften behaviour are dominated by the increase and decrease of contact force anisotropy, respectively. At large deformation, the same critical stress ratios and void ratios are achieved, irrespective of initial void ratios, due to the same internal structural anisotropy reached.

(2) A lower stress ratio and slightly more dilative behaviour are observed with increasing b value in true triaxial test on both dense and loose samples. The stress-force-fabric predicts the stress-strain behaviour quite well. Accordingly, with the stress-force-fabric relations, the effect of b value on strength characteristics can be explained. At failure, as b value rises from 0 to 1, the contact forces anisotropy decreases while the fabric anisotropy

increases. At the same b value, the normal contact force anisotropy is much higher than the fabric anisotropy; with the tangential force anisotropy smallest. Hence, the normal contact force anisotropy takes dominant contribution to the achieved stress ratio.

(3) The intermediate strain increment ratio $b_{\Delta e}$ is found to be larger than the intermediate stress ratio b except for the asymmetric stress conditions ($b = 0$ and $b = 1$). In the octahedral plane, this is shown as the non-coincidence of stress increment direction and strain increment direction. This is believed to be due to the larger intermediate fabric ratio b_F than b value.

In laboratory true triaxial test on sand, there are three different loading paths combinations of three principal stresses in considering the material initial anisotropy. The true triaxial simulation results on initially anisotropic samples with non-spherical particles have been presented in Section 7.4. It concludes as:

(1) The samples with cross-anisotropy perform softer and more contractive with increasing stress lode angle during true triaxial simulations. The failure surface in the octahedral plane shows to be cross-anisotropic. In simulations with the same b value, the friction angle obtained in Sector I is highest while the lowest value is achieved in Sector III. This is related to a lower degree of fabric anisotropy developed in Sector III than that in Sector I, with Sector II in between. However, the variation of critical fabric anisotropy in three Sectors is small. Hence, the similar critical stress ratios are generally achieved in three Sectors at constant b value.

(2) The different strength-deformation characteristics between Sector II and Sector III, where the major principal stress direction is within the bedding plane while the intermediate principal stress direction is either perpendicular to the bedding plane in Sector II or within the bedding plane in Sector III, shows clear evidence of the combined effect of b value and material anisotropy on granular material behaviour.

9.4 Effect of anisotropy

The true triaxial simulation results of initially anisotropic sample clearly shows the loading direction dependent granular material, where the principal stress direction is either in the vertical direction or in the horizontal direction. The influence of tilting principal stress direction on anisotropic granular material response has been reported in Chapter 6 on samples with spherical particles and Chapter 7 on samples with non-spherical clump particles. The findings are listed as follows:

(1) Both the initially anisotropic samples and pre-loaded samples perform softer and more contractively during the pre-failure stage in monotonic shearing with increasing tilting angle a . The anisotropic stress-strain behaviour is severer in the pre-loaded sample. Microscopic investigation on the pre-loaded sample shows that, upon the same deviatoric strain before failure, the fabric anisotropy and contact force anisotropy is much smaller at greater tilting angle a . During the post-peak shearing, the contact force anisotropy reaches similar values; the difference of fabric anisotropy becomes small at different loading directions; and their principal directions are generally coaxial with

the loading direction. Accordingly, the post-peak stress-strain behaviours are similar with the same critical stress ratios achieved, irrespective of loading direction a .

(2) The strength of anisotropic samples with non-spherical particles is loading direction dependent. In constant b simulation, with increasing angle a from 0^{o} to 90^{o} , the peak stress ratio decreases continuously with minimum strength obtained at $a = 90^{o}$. This micro-scale observations show that, at peak failure stress ratio, the principal directions of contact force and fabric become close to loading direction; and the normal and tangential contact forces anisotropy reach similar values at different loading directions while the contact normal fabric anisotropy are larger at smaller a value, leading to a lower strength obtained at greater a value.

(3) The non-coaxiality is negligible for the initial anisotropic sample while significant non-coaxial behaviour is observed on the pre-loaded sample. The non-coaxial behaviour is due to the initially non-coincidence of material microstructure direction, e.g., principal fabric direction, relative to the loading direction. And the degree of non-coaxiality is dependent on the relative directions and relative magnitudes of fabric anisotropy and contact force anisotropy. For the initially anisotropic sample, the fabric anisotropy is small and the principal fabric direction evolves rapidly to the loading direction, although the initial fabric direction is not coaxial with the loading direction. Accordingly, the general coaxial behaviour is observed. For the pre-loaded sample, the fabric anisotropy is larger and the fabric direction

rotates gradually to the loading direction. Hence, significant non-coaxial is observed. At large deformation, the principal fabric direction becomes coaxial with loading direction, leading to coaxial behaviour.

9.5 Rotational shear

The granular material response to cyclic rotation of major principal stress direction has been investigated in Section 4.4.3 on samples of spherical particles with different initial void ratios and in Chapter 8 on samples of non-spherical particles under various stress ratios and b values. The conclusions are given as:

(1) Significant volumetric contraction is induced due to continuous rotation of principal stress direction. This is explained as that the material internal structure rotates continuously along the stress rotation in order to maintain stability. The internal fabric reorganisation mechanism accompanies material irrecoverable deformation. The initial void ratio, stress ratio and b value have significant effect on the accumulated volumetric strain. The larger the influential factor, the severer the volume contraction. The ultimate void ratio is dependent on the stress ratio and b value, independent of initial void ratio. This is explained as the ultimate internal structure anisotropy is larger at a higher stress ratio and at a greater b value, leading to smaller ultimate void ratio. However, the ultimate internal structure anisotropy becomes similar, irrespective of initial void ratio. Hence, the dense and loose samples approach to the same ultimate void ratio.

(2) The non-coaxial behaviour between the principal stress direction and the principal strain increment direction is observed during rotational shear. This is due to the principal fabric direction being not coaxial with the principal stress direction. Within one cycle of a from 0^{o} to 180^{o} on samples with non-spherical particles, the principal fabric direction is behind the rotation of the principal stress direction as a varies from 0^{o} to 90^{o} while it becomes to be ahead of the principal stress direction with further increase of a to 180^{o}. The smaller the stress ratio and the b value, the higher the degree of non-coaxiality due to the larger deviation between the principal fabric direction and the principal stress direction. In addition, it is interesting to observe that the principal fabric increment direction is generally coaxial with the principal stress increment direction in the deviatoric plane.

(3) The material would experience deformation failure during rotational shear at $h = 0.9, b = 1$ even when the stress ratio is lower than the peak stress ratio $h_p = 1.08$ but larger than the critical stress ratio $h_c = 0.82$ obtained in monotonic loading, where significant deviatoric strain developed in the first few cycles. This is explained as the material internal structure can not sustain such a high stress ratio and the material deforms continuously in order to maintain the boundary stress conditions. This clearly indicates that ignorance of principal stress rotation would lead to an unsafe geotechnical design and the material strength for rotational shear should be chosen as the critical stress ratio rather than the peak stress ratio obtained from monotonic shearing.

(4) During rotational shear, the strain trajectory in the deviatoric plane is spiral with decreasing size since the material is hardened to be stronger with decreasing void ratio. After large number of cycles, the strain path becomes steady to be a circle as the ultimate anisotropic structure developed. At ultimate state, the deformation is mainly due to the rotation of the anisotropic structure. Under otherwise identical condition, the size of strain trajectory is significantly influenced by initial void ratio, stress ratio and b value. The greater the influential factor, the larger the size of strain trajectory. Microscopically, the fabric trajectory size is greater at a higher stress ratio, at larger initial void ratio and at greater b value, resulting in a greater strain trajectory in the deviatoric plane.

(5) Significant intermediate principal strain e_{yy} has been generated during rotational shear in spite of constant intermediate principal stress. The contractive intermediate strain e_{yy} is larger at a higher stress ratio during rotation shear under constant $b = 0.5$, corresponding to the larger increment of D_{yy} at greater stress ratio. During rotational shear under various b values, the intermediate strain e_{yy} changes from extension at $b = 0.0$ to contraction at $b = 1.0$. The reason is that the intermediate fabric decreases slightly in simulation at $b = 0$ while it increases at other b values. And the larger strain e_{yy} at greater b value corresponds to bigger increment of D_{yy}.

(6) The fabric trajectory is generally circular during rotational shear, irrespective of material initial anisotropy. The material initial particle orientation anisotropy, however, has significant effect on the centre of fabric trajectory.

9.6 Particle shape effect

The common observations on the anisotropic stress-strain behaviour and deformation non-coaxiality can be observed on samples with spherical or non-spherical particles under various three-dimensional stress paths. The different observations due to particle shape effect are summarised as:

(1) The sample with non-spherical particles performs much higher strength and more dilative behaviour than the sample with spherical particles during triaxial compression since the average contact friction coefficient is much higher in non-spherical particles assembly; and fabric anisotropy and contact force anisotropy degrees are considerably larger in sample with non-spherical particles.

(2) In simulations at various loading directions, similar anisotropic stress-strain behaviour and deformation non-coaxiality are observed in anisotropic samples, irrespective of particle shape. The critical fabric anisotropy reaches the same value and the principal fabric direction becomes coaxial with loading direction in spherical particles assembly. In non-spherical particles assembly, however, the value of critical fabric anisotropy differs slightly at different loading directions and the principal fabric direction approaches the loading direction but still a gap, owing to the contact normal vector being not parallel to the branch vector.

9.7 Recommendations for future work

The proposed virtual experiment technique has been shown in advantage of applying various loading paths to study granular material behaviour. As the flat rigid walls are used to form the polyhedral boundary shape, this may induce no sufficiently frictional resistance between particle-wall contacts, compared to particle-particle contacts. Accordingly, the sample uniformity may not be well maintained, with a greater stress distributed within the centre area than that near boundary. And the difference can be as large as 20%. In order to maintain sample uniformity, it is necessary to enhance the particle-wall contacts frictional resistance. For example, increase the frictional coefficient for only particle-wall contacts. However, this can not be directly realised within PFC3D. Thus, it is recommended for future DEM study to overcome the limitation.

To formulate a constitutive model incorporating the fabric tensor, one essential task is to define the fabric evolution law. In this study, the fabric evolution has been comprehensively investigated under various loading paths and it shows a strong correlation between the fabric tensor and stress tensor. The fabric evolution law should be able to predict the fabric evolution against stress for both dense and loose materials, initially isotropic or anisotropic samples, under proportional or non-proportional loading paths.

The conventional plasticity theory has been formulated based on phenomenal laboratory observations on soil behaviour. It faces challenges in constitutive modeling of anisotropic soil behaviour, e.g., non-coaxial behaviour,

rotational shear response. As it has been studied by DEM simulations in this research, the effects of material anisotropy on granular material response is strongly dependent on the microstructure evolution. Hence, the fabric tensor based constitutive model would be advantageous in modelling granular material and the fabric tensor has clear physical meaning in describing the spatial arrangement of material internal structure.

APPENDIX A: Results of anisotropic samples with non-spherical particles under various loading directions

The appendix contains the simulation results of sample with non-spherical particles under various loading directions. It is linked to the main body presentation in Section 7.5. The macro-scale stress-strain behaviours are presented for both initially anisotropic samples and pre-loaded sample. The evolution of micro-scale contact forces tensors and fabric tensors are illustrated in terms of anisotropy degrees and principal directions.

A.1 Results on initially anisotropic sample

A.1.1 Stress-strain behaviour

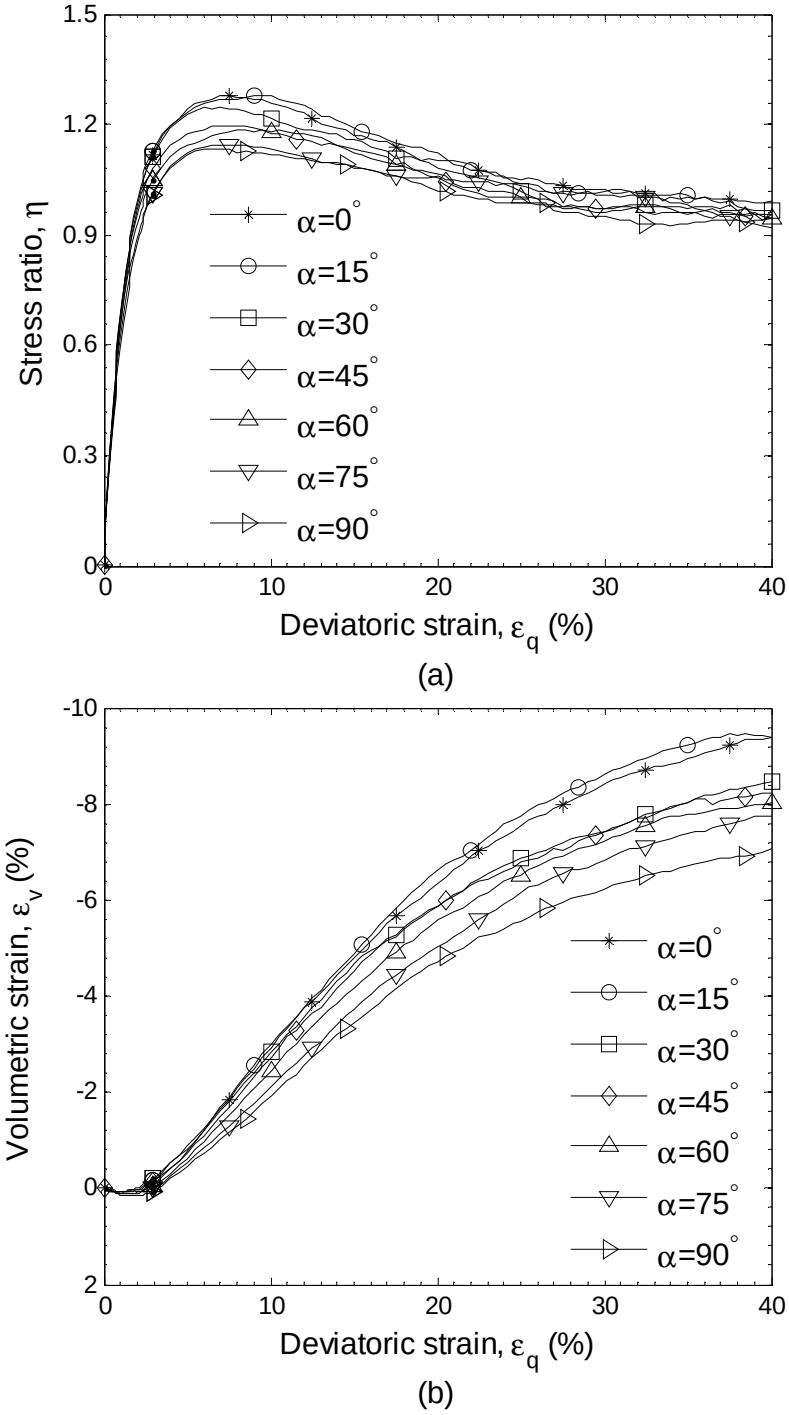

Fig. A1 Effect of loading direction on sample CDED_TT response at *b*=0.4

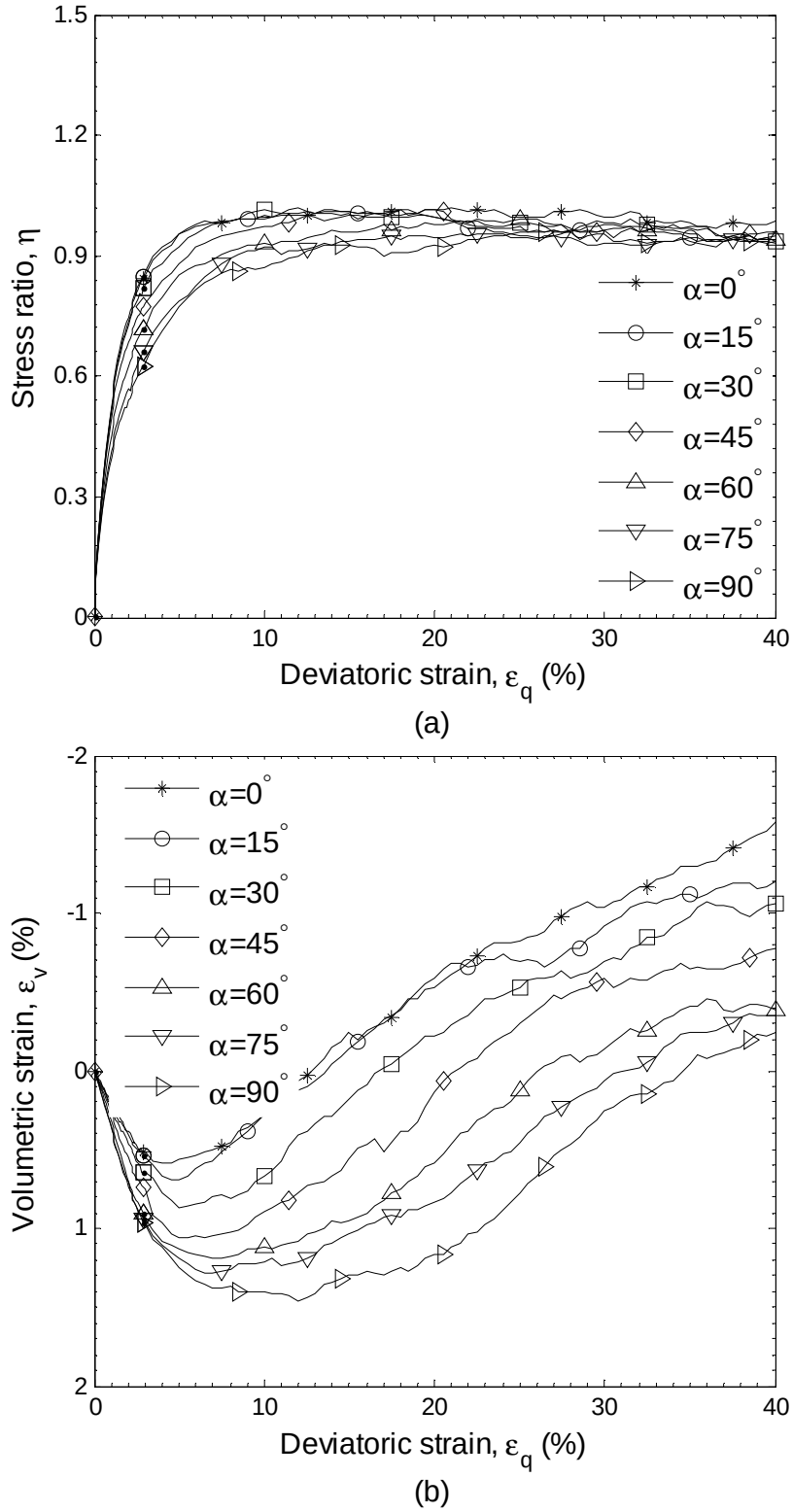

Fig. A2 Influence of loading direction on the loose sample CDEL_TT behaviour at *b*=0.4 (a) stress-strain (b) volumetric strain

A.1.2 Non-coaxiality

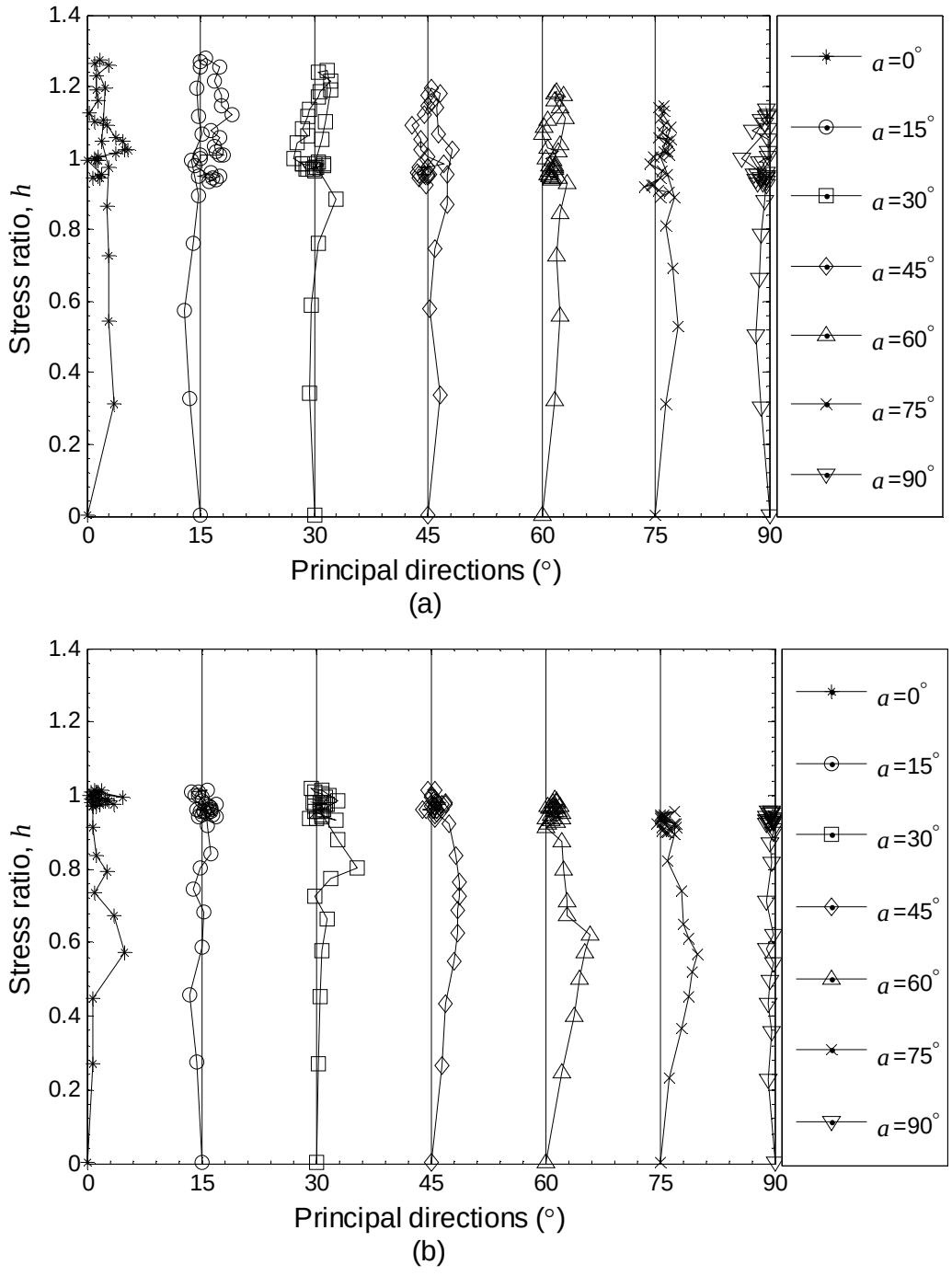

Fig. A3 Principal stress and strain increment directions at *b*=0.4 dense sample CDED_TT (b) loose sample CDEL_TT

A.1.3 Fabric evolution

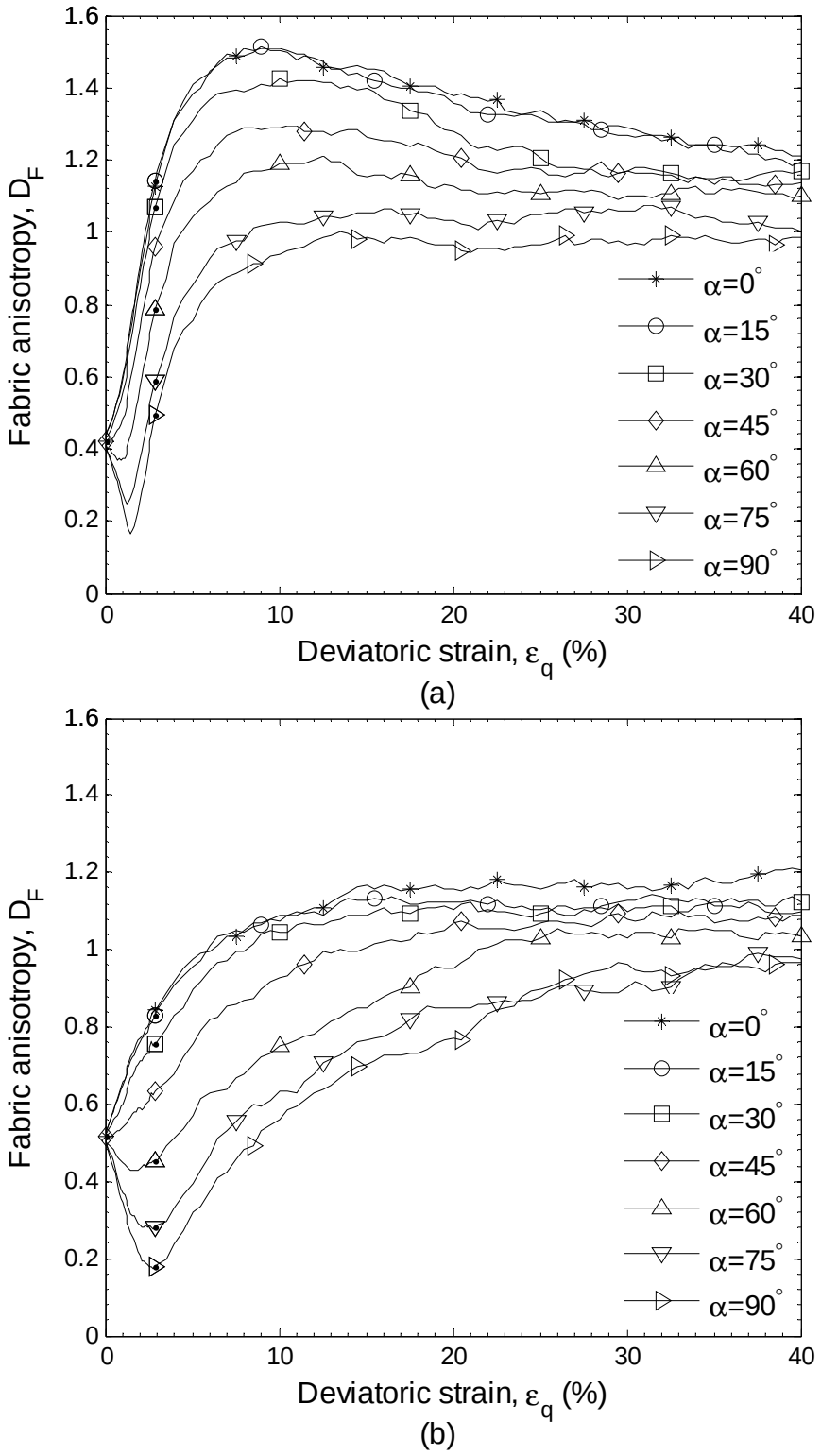

Fig. A4 Evolution of deviator fabric anisotropy at *b*=0.4 (a) dense sample CDED_TT (b) loose sample CDEL_TT

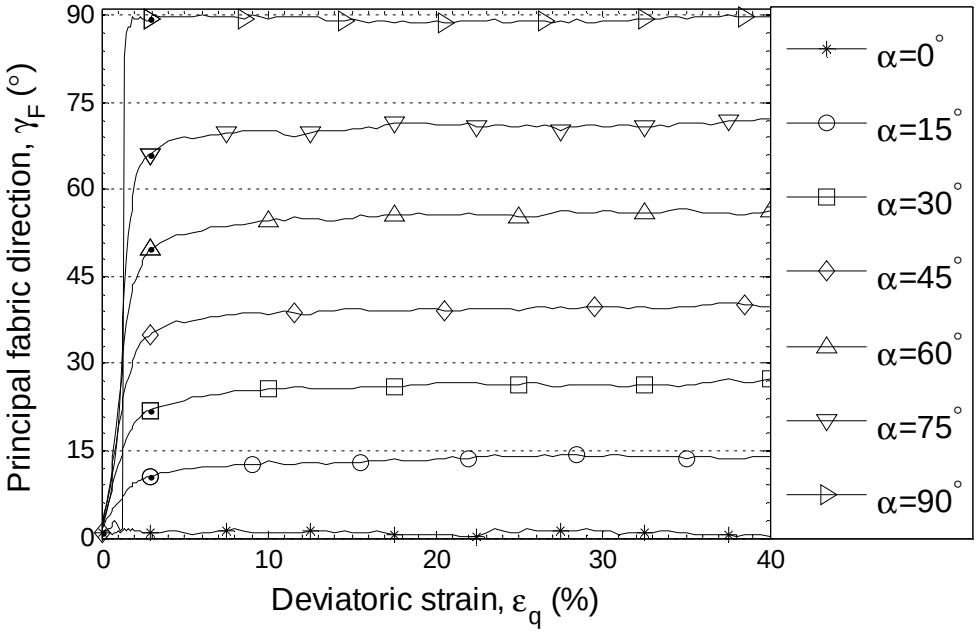

(a)

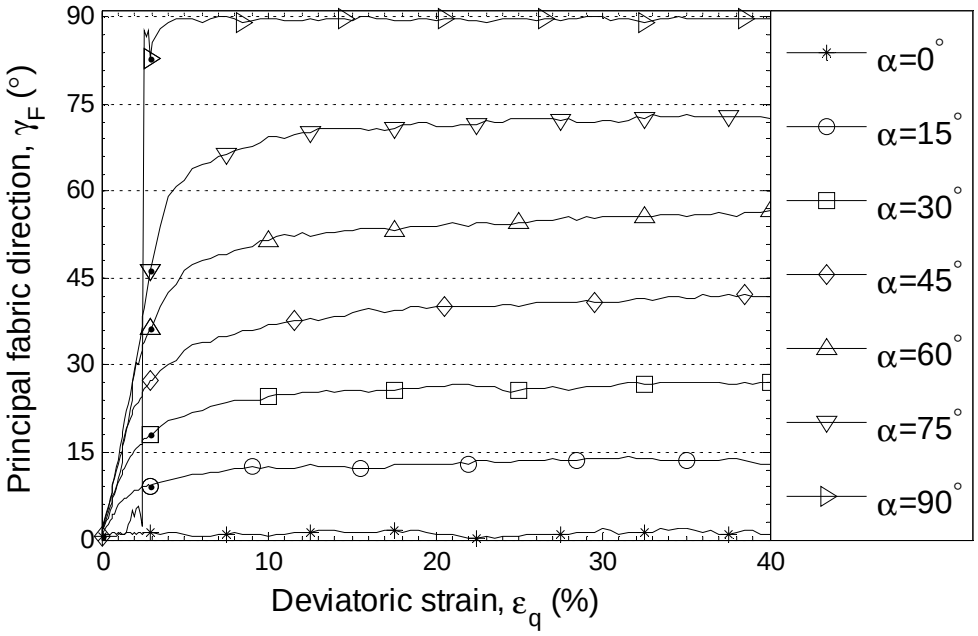

(b)

Fig. A5 Evolution of principal fabric direction at *b*=0.4 dense sample CDED_TT (b) loose sample CDEL_TT

A.1.4 Contact force evolution

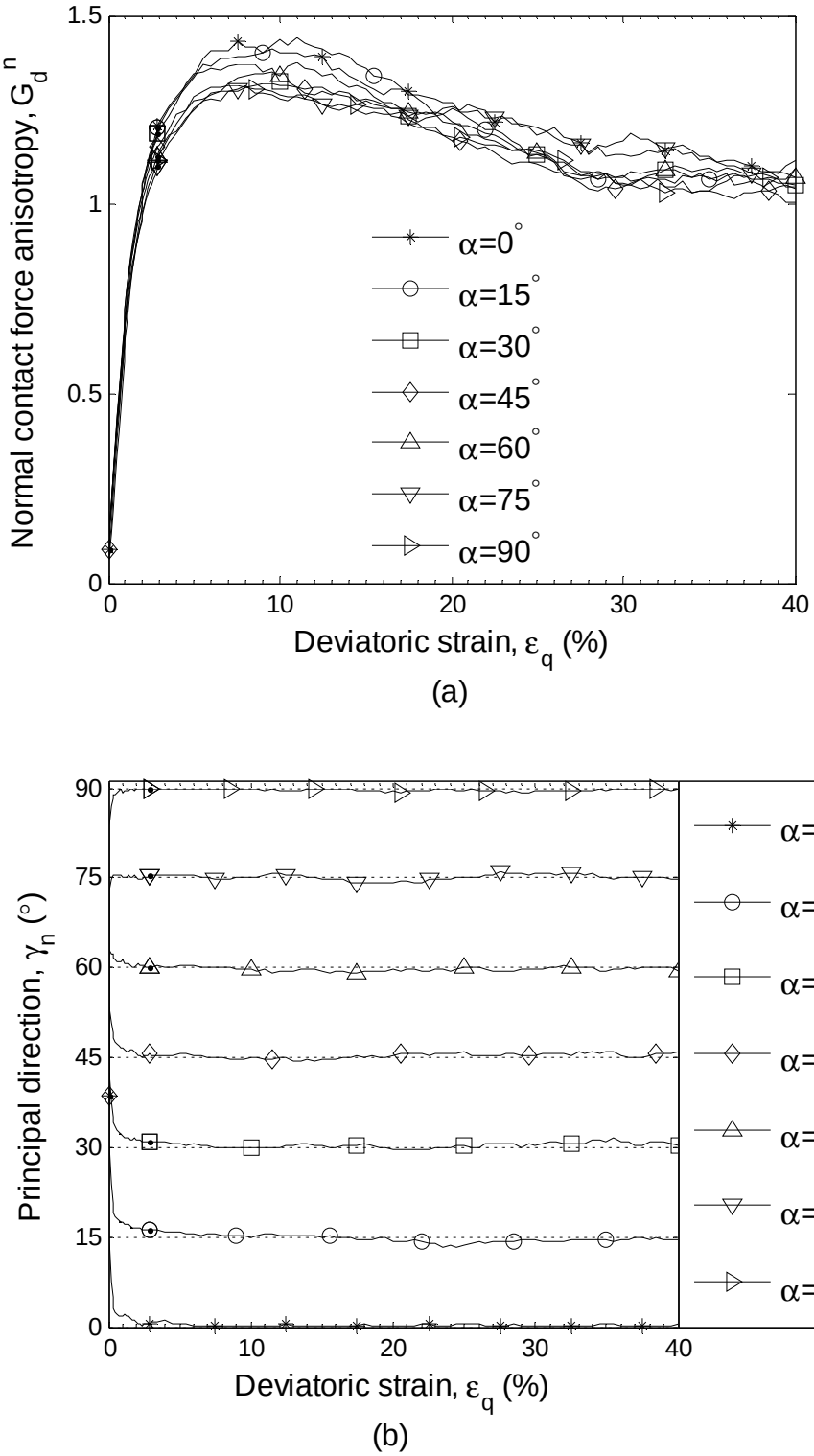

Fig. A6 Normal force anisotropy in sample CDED_TT (a) anisotropy degree (b) principal direction

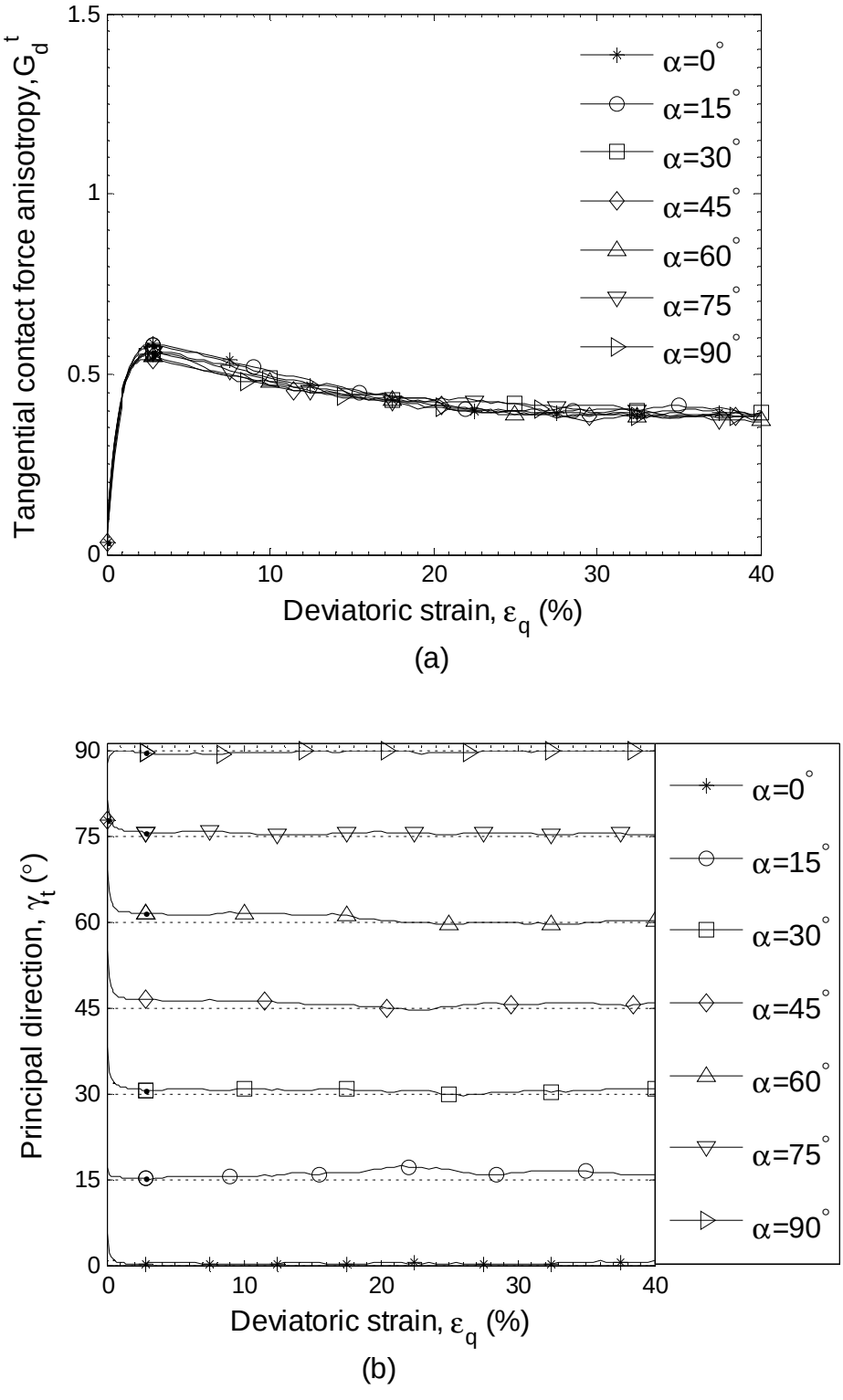

Fig. A7 Tangential contact force anisotropy in dense sample CDED_TT (a) anisotropy degree (b) principal direction

A.2 Results on pre-loaded sample

A.2.1 Stress-strain behaviour

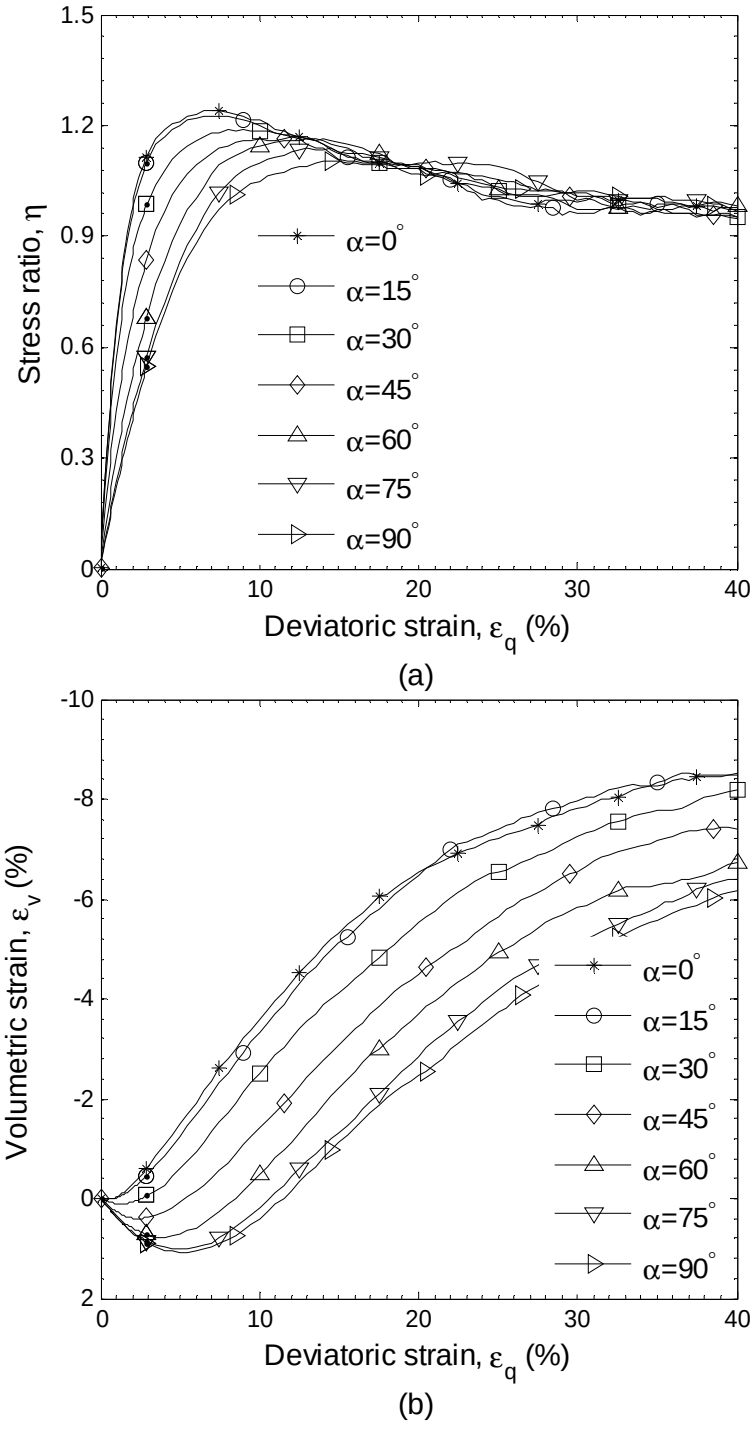

Fig. A8 Anisotropic behaviour of sample CDED_TC_TT at *b*=0.4 (a) stress-strain (b) volumetric strain

A.2.2 Non-coaxiality

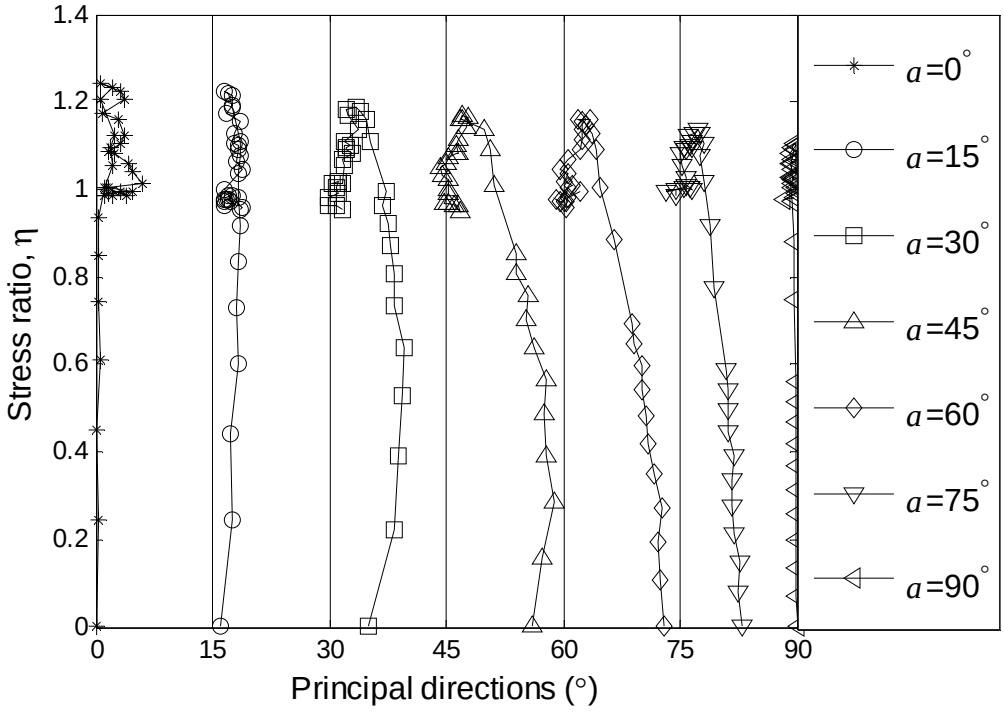

Fig. A9 Non-coaxial behaviour of sample CDED_TC_TT at *b*=0.4

A.2.3 Fabric evolution

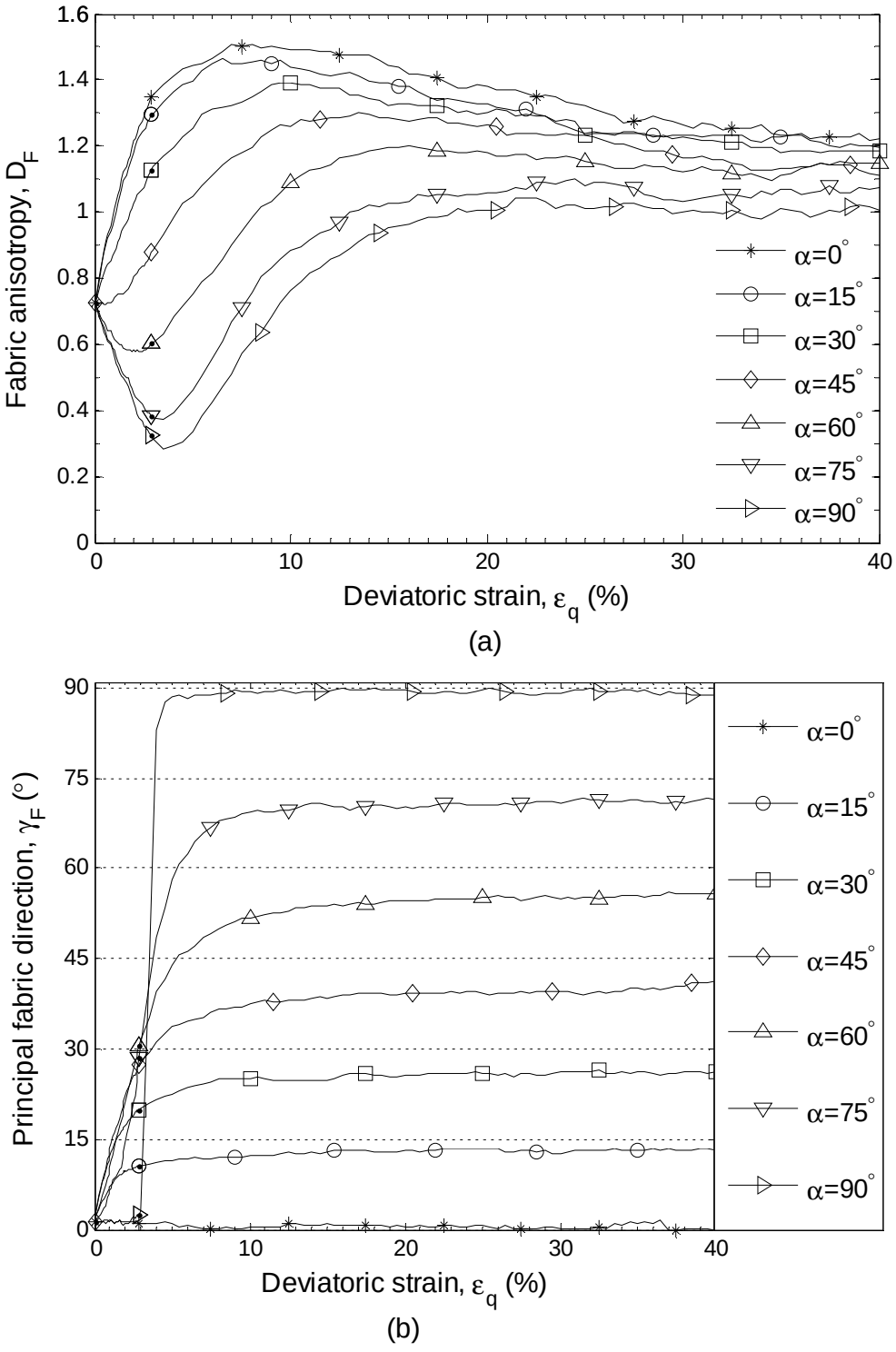

Fig. A10 Fabric evolution in sample CDED_TC_TT at *b*=0.4 (a) deviator fabric anisotropy (b) principal fabric direction

A.2.4 Contact force evolution

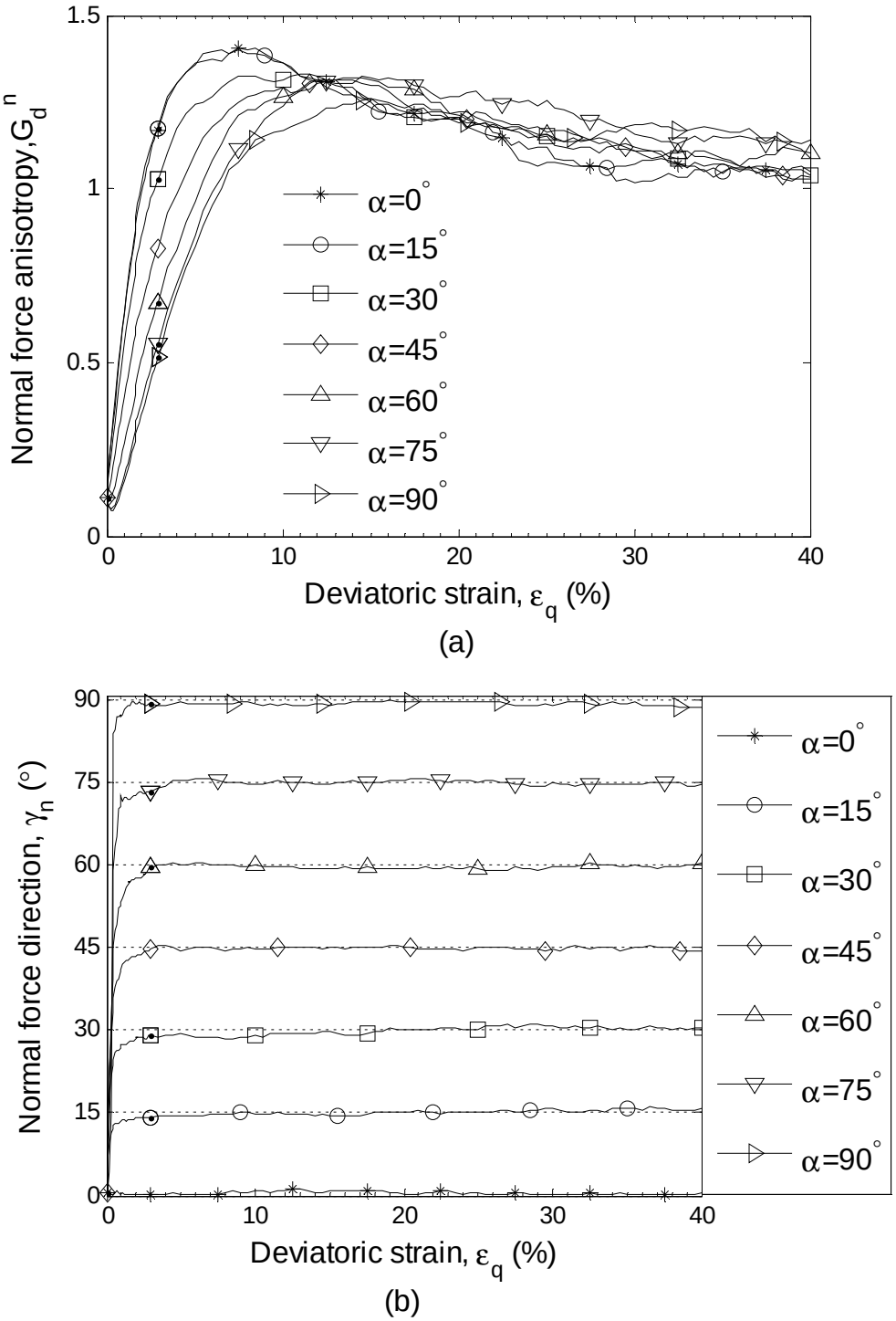

Fig. A11 Normal contact force evolution in sample CDED_TC_TT (a) normal force anisotropy (b) principal normal force direction

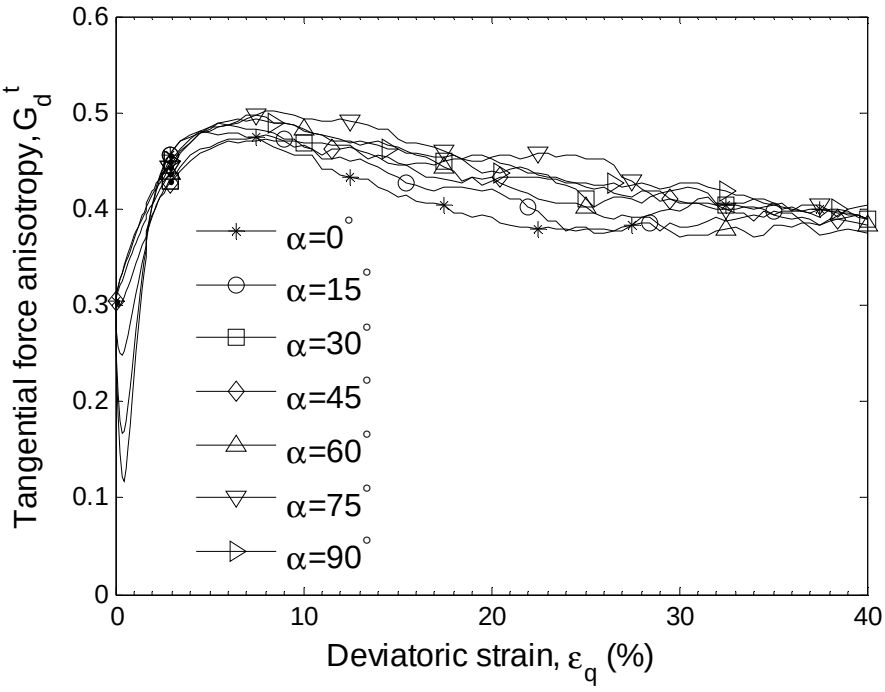

(a)

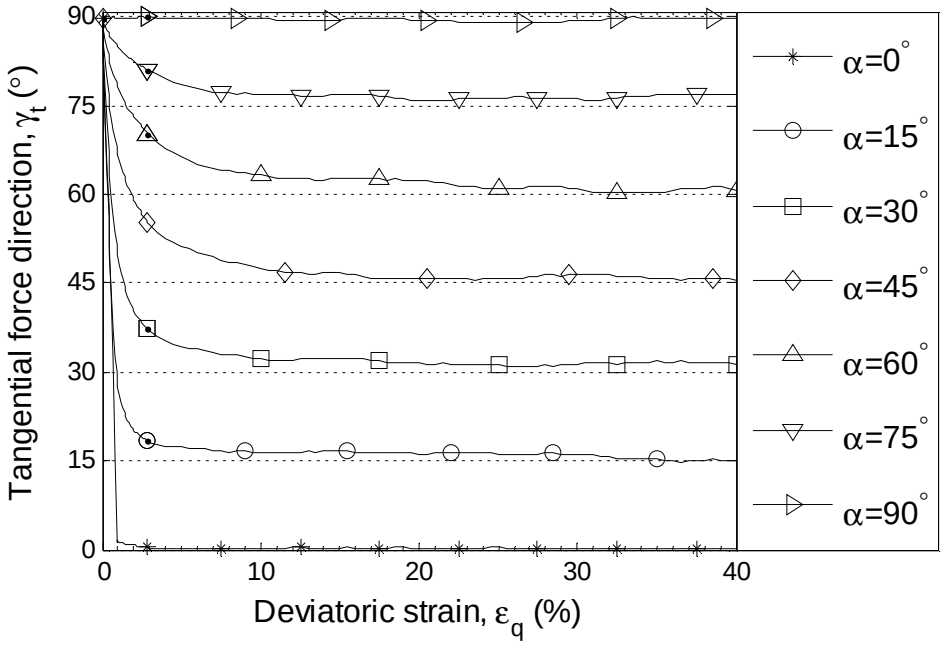

(b)

Fig. A12 Tangential contact force evolution in sample CDED_TC_TT (a) tangential force anisotropy (b) principal tangential force direction

APPENDIX B: Numerical experiment set-up

B.1 Polyhedral boundary shape

There are two common ways to form boundaries in DEM for applying external loading, particle boundaries and rigid wall boundaries. The particle boundaries can be frequently updated. Loading is applied by controlling the positions of boundary particles or forces acting on boundary particles (Thornton, 2000; Cui et al., 2007; Wang & Tonon, 2009; Fu & Dafalias 2011) . The advantage is that the boundary can deform flexibly while the disadvantage is the requirement of updating boundary particles positions continuously. This potentially affects contact force transmission when the network of boundary particles is being updated. More importantly, it is difficult to realise complex loading path, e.g., non-proportional loading.

The alternative way is to use massless rigid walls to form the boundary of a granular assembly. The Newton's second law is not applicable to those massless walls. Hence, the external loading increment is applied using servo-control mechanism. The positions of rigid wall elements are imposed, changing interacting between particles and rigid walls. The disturbances will then propagate throughout the whole specimen. The boundary control is inherently strain-controlled by directly specifying velocities of the rigid walls in each loading cycle to achieve a strain increment and the stress-controlled boundary conditions is realised through servo-control mechanism by adjusting strain increment tensor.

Most DEM simulations using rigid walls boundary form a shape of rectangular shape in 2D and cubic box in 3D similar to laboratory specimen setup (Thornton, 2000, Ng, 2005, Yimsiri and Soga, 2010, Mahmood and Iwashita, 2010). However, sample uniformity is usually not maintained with the presence of boundary friction due to arching effect (Li et al., 2011). With presence of boundary friction, arching may be developed depending on the properties of boundaries. This is believed due to the boundary geometry shape effect and the hexagonal boundary or polyhedral boundary shape is recommended in 2D or 3D, respectively (Li et al., 2013).

B.2 Polyhedral boundary generation

There are many ways to form a closed polyhedron. Here we propose a protocol to define the initial set of boundary walls forming a polyhedral volume, which has an inscribed sphere with radius R:

1. The polyhedron has two parallel surfaces, perpendicular to z coordinate axis. Both are regular n-sided polygons. The distance between the two surfaces is $2R$. The vertices of the two polygons have their z coordinate being -R and R, respectively.
2. All planes perpendicular to the polygons and passing the symmetrical axes, defined by a line passing the mid-point of one edge and centre of the polygon, of the two parallel polygons are symmetrical planes of the polyhedrons. And the intersection planes formed by the symmetrical planes and the polyhedron are also regular polygons.

The geometric characteristics of the polyhedron are summarised as follows:

- Both the transverse section and longitudinal section of polyhedron are regular n-sided polygon ($n \geq 4$, only even number used for symmetry).
- The angle between every two neighbouring walls is obtuse when $n \geq 6$.
- The top and bottom boundary walls are regular hexagons in the initial undeformed configuration. The other walls are quadrangles.
- The vector, pointing from the point of tangency between each boundary wall and the inscribed sphere to the centre of sphere, is perpendicular to the boundary wall. The coordinate of the tangent point is the average of all vertices coordinates of the individual boundary wall.
- Initially, all vertices lie in $n / 2$ horizontal planes. Each plane contains n vertices to form a regular polygon. The total number of vertex is $n^2 / 2$.
- Between every two neighbouring horizontal planes, it has n boundary walls. Together with the top and bottom walls, the total number of boundary walls equal to $(n / 2 - 1)n + 2$.

The polyhedral boundary can then be defined by only two parameters n and R, where n defines the shape of polyhedron and R controls the size of polyhedron. An example of such polyhedron with $n = 8$ is shown in Fig. B.0.1. There are totally 26 boundary walls and 32 vertices.

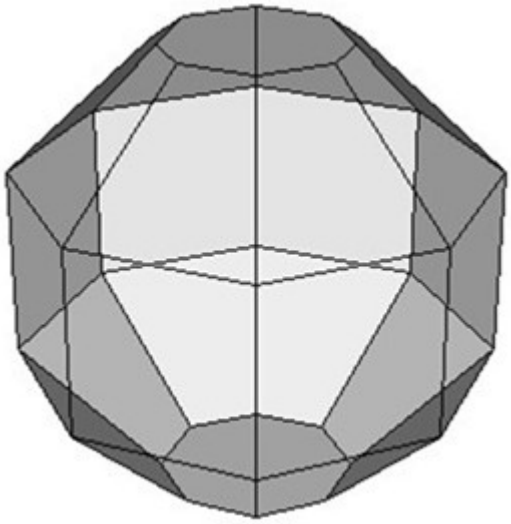

Fig. B.0.1 Example of polyhedron, *n*=8

B.2.1 Generation of boundary walls

To generate such a kind of polyhedron volume in PFC3D, a set of intersecting infinite planes of walls are generated to form the closed polyhedron. The individual wall unit normal vector **n** and a point **x** on the wall are to be specified. The Cartesian coordinate system is defined with origin being the centre of the polyhedron as shown in Fig. B.0.2. The plane function of each boundary wall is expressed as:

$$n_x x + n_y y + n_z z + d_i = 0 \tag{1}$$

$\left(n_x, n_y, n_z\right)$ is the components of the plane unit normal **n**. d_i is the constant of the plane function. It is determined by substituting the point coordinate $\left(x_i, y_i, z_i\right)$ into Eq. (1) as:

$$d_i = -\left(n_x x_i + n_y y_i + n_z z_i\right) \tag{2}$$

In the coordinate system as shown in Fig. B.0.2(a), the vector **V** of magnitude *R*, pointing from the centre of the inscribed sphere to the tangent point **x** on the boundary wall, is perpendicular to the boundary wall w. Hence, the unit vector of **V** is the unit normal vector of the boundary wall w. The orientation of the vector **V** can be described by two angles g, b, where g is the angle between the vector and the positive direction of *z*-axis, $0 \le g \le 180^{\circ}$ and b is the angle between the projection of the vector **V** on the *x*-*y* plane and the positive direction of the *x* -axis, $0 \le g \le 360^{\circ}$.

To determine the value of g, b for individual wall, each boundary wall is assigned with an id number. The top wall with the regular polygon shape is always assigned with the id number $(n / 2-1)n+1$ and the bottom wall with the regular polygon shape is always assigned with the id number $(n / 2-1)n+2$. For the rest walls, each one is labelled as w_{ij}, where the subscripts i, j are used to identify different walls ($1 \le i \le (n/2-1), (1 \le j \le n)$). The subscripts are labelled in the sequence of : 1) the walls of which vector **V** have the same angle g will be assigned with the same i; i increases from 1 to $(n/2-1)$ with increasing g ; 2) for those n walls of which the vectors **V** have the same angle g, the second subscript j is labelled from 1 to n one by one. According to these two rules, each boundary wall can be identified by subscripts i, j, e.g., plan view of the polyhedron in Fig. B.0.2(b). the walls labelled as w_{ij} and w_{ij+1} denoting two neighbouring walls of which unit normal vectors have the same angle g while different angle b,

$b_{j+1} - b_j = \left(360^o / n\right)$. The walls labelled as w_{ij} and w_{i+1j} denote two neighbouring walls of which unit normal vectors have the same angle b while different angle g, $g_{j+1} - g_j = \left(360^o / n\right)$.

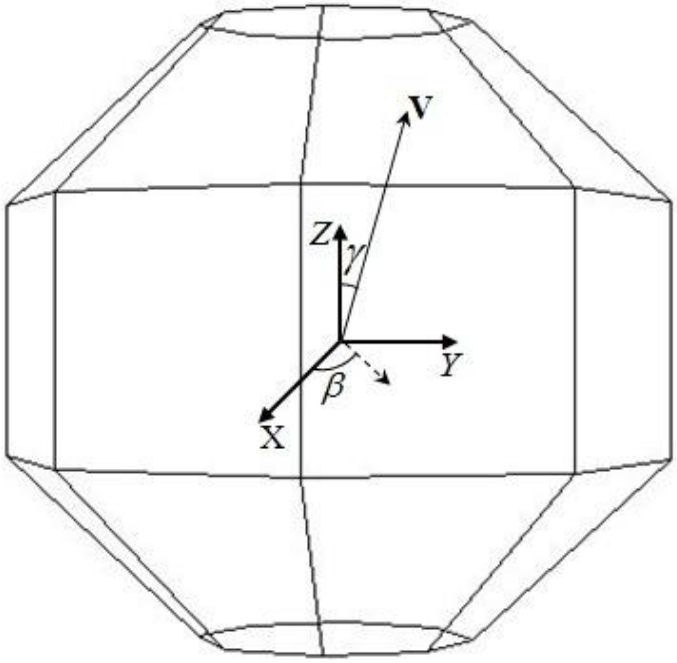

(a) front view

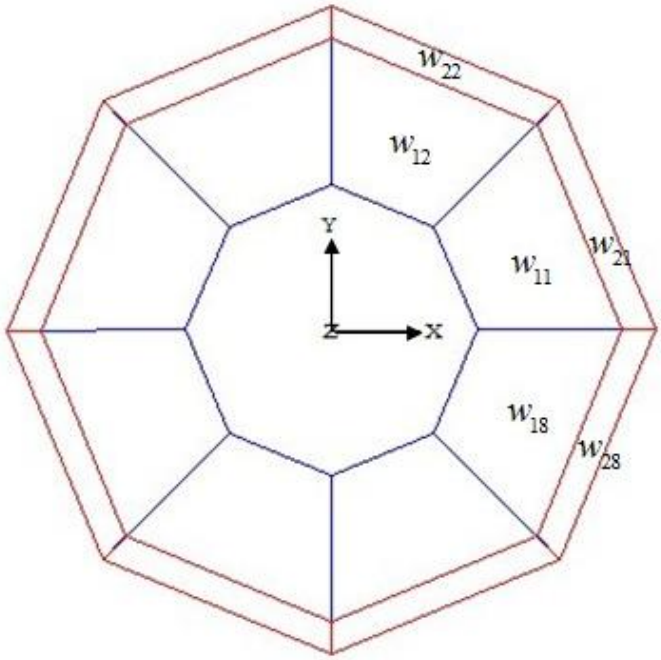

(b) vertical view

Fig. B.0.2 Labelling of polyhedron wall id

For the boundary wall w_{ij}, g, b is determined to be

$$\begin{cases} g = \dfrac{360^{\circ}}{n} i \\ b = \dfrac{360^{\circ}}{n}(j-1) \end{cases} \tag{3}$$

For top wall with id$\left(n \,/\!/\, 2-1\right)n+1$, $g = 0, b = 0$, for bottom wall with id $i = \left(n \,/\!/\, 2-1\right)n+2$, $g = 180^{\circ}$, $b = 0$.

The centre of the inscribed sphere is defined to coincide with the origin O of the defined coordinate system, the components of the vector $\mathbf{V}_{ij}$ or the tangent point vector $\mathbf{x}_{ij}$ of individual wall w_{ij} can be calculated as $\left(R\cos b \sin g, R\sin b \sin g, R\cos g\right)$. The unit normal direction $\mathbf{n}_{ij}$ of the boundary wall w_{ij}, with the active side pointing inward to the polyhedron, is the unit normal of vector $\mathbf{V}_{ij}$ with opposite direction

$$\mathbf{n}_{ij} = -\frac{\mathbf{V}_{ij}}{\left|\mathbf{V}_{ij}\right|} = \left(-\cos b \sin g, -\sin b \sin g, -\cos g\right) \tag{4}$$

Therefore, each infinite boundary wall can be generated by specifying unit normal vector $\mathbf{n}_{ij}$ and a point $\mathbf{x}_{ij}$ on the plane. Initially, the constant d_{ij} of the plane function for each boundary wall can be determined by Eq. (2) as:

$$d_{ij} = R \tag{5}$$

At this stage, all the boundary walls have been generated. Fig. B. 0.3 shows the examples of polyhedron boundary shape when n equals to 6 and 8 respectively. If n is sufficiently large, the shape of polyhedron boundary approaches to be a sphere.

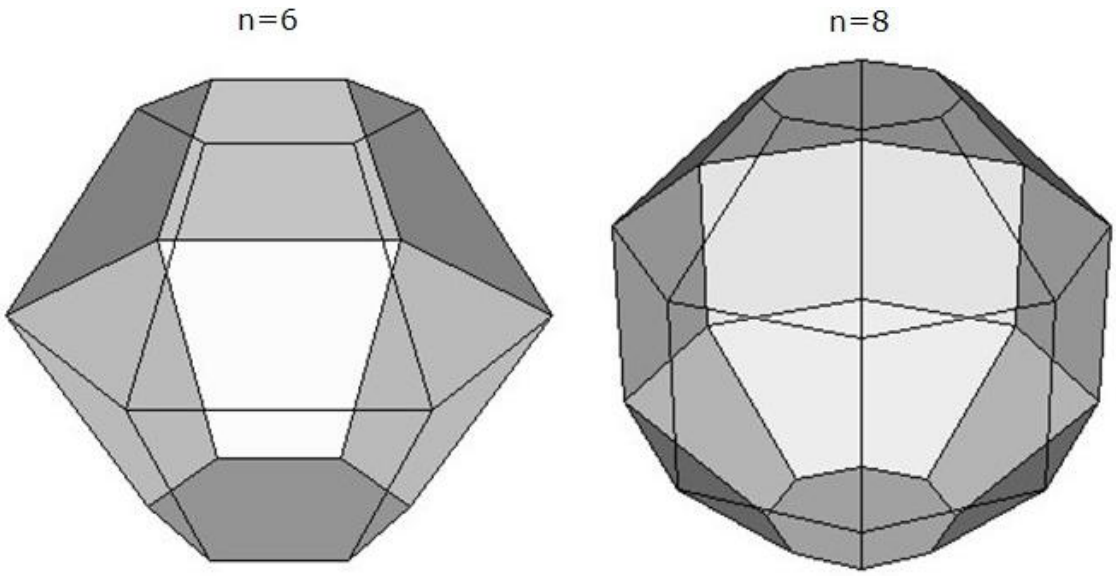

Fig. B. 0.3 Examples of polyhedron boundary

In this research, all the numerical samples with a polyhedron boundary shape are generated by setting $n = 8$ unless otherwise stated, as shown in Fig. B. 0.3.

During preparation of a numerical sample, it may be interested in the initial void ratio of the sample. The total volume of particles can be calculated according to the particle size and target number of particles. Then, it requires determining the volume of the polyhedron. Therefore, the coordinates of the vertices contained by each boundary wall need to determined.

B.2.2 Determination of vertex coordinate

In three-dimensional spaces, a point is uniquely determined by the intersection of at least three unparalleled planes with plane functions expressed in the form of Eq. (1). Consider $\mathbf{n}_1,\mathbf{n}_2,\mathbf{n}_3$ are the unit normals of the three planes and d_1,d_2,d_3 are the plane functions constants, respectively. Then, the point vector $\mathbf{X}$ of the intersection point can be calculated as:

$$\mathbf{X} = \frac{-d_1 \times (\mathbf{n}_2 \times \mathbf{n}_3) - d_2 \times (\mathbf{n}_3 \times \mathbf{n}_1) - d_3 \times (\mathbf{n}_1 \times \mathbf{n}_2)}{\mathbf{n}_1 \cdot (\mathbf{n}_2 \times \mathbf{n}_3)} \tag{6}$$

In the polyhedron as shown in Fig. B.0.2, each vertex is the intersection point of either three unparalleled plane walls or four unparalleled plane walls. Therefore, the coordinate of individual vertex can be calculated by Eq. (6) by knowing the plane functions of the walls sharing the vertex. The boundary walls plane functions can be updated at any stage of deformation by updating the wall unit normal and wall centre using intrinsic functions in PFC3D. In numerical implementation, it is necessary to identify the walls id sharing the vertex.

Vector $\mathbf{p}$ points from the origin to one vertex of the polyhedron (e.g., Fig. B.0.4). Its orientation is described by angle g and b . g is the angle between the vector and the positive direction of *z*-axis, $0 \le g \le 180^\circ$, where b is the angle between the projection of the vector on the *x-y* plane and the positive direction of the *x*-axis, $0 \le g \le 360^\circ$. Each vertex is labelled as v_{ij} , where the subscripts i, j are used to identify different vertices ($1 \le i \le n/2, 1 \le j \le n$). The subscripts are

labelled in the sequence of : 1) the vertices of which vector **p** have the same angle g will be assigned with the same i; i increases from 1 to $n/2$ with increasing g ; 2) for those n vertices of which vectors **p** have the same angle g , the second subscript j is labelled from 1 to n one by one, and the vertex of which vector **p** has a smaller angle b will be labelled in priority. According to those two rules, each vertex can be identified with i, j. The vertices labelled as v_{ij} and v_{ij+1} (e.g., Fig. B.0.4) denote two vertices of which vectors **p** have the same angle g while different angle b , $b_{j+1} - b_j = \left(360^o/n\right)$. The vertices labelled as v_{ij} and v_{i+1j} denote two vertices of which vectors **p** have the same angle b while different angle g , $g_{j+1} - g_j = \left(360^o/n\right)$.

The top and bottom boundary walls contains vertices labelled as v_{1j} and $v_{(n/2)j}$, respectively. For a wall labelled w_{ij} , it contains four vertices of which labelled as v_{ij}, v_{ij+1}, v_{i+1j}, v_{i+1j+1} ($1 \le i \le \left(n/2-1\right)$), where the second subscript $j+1$ of v_{i+1j+1} and v_{ij+1} is changed to 1 if $\left(j+1\right) = \left(n+1\right)$.

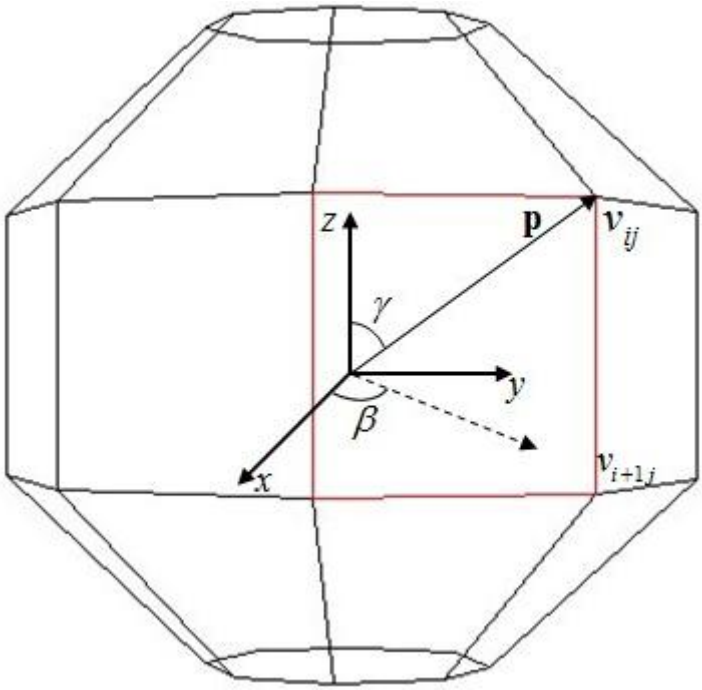

Fig. B.0.4 Assignment of id to vertices

Accordingly, each vertex can be identified by its two subscripts. For the vertex v_{ij}, it is shared by at least three boundary walls with id number detected as:

$$\begin{cases} w^1 = w_{(i-1)j} \\ w^2 = w_{i(l-1)} \\ w^3 = w_{ij} \end{cases} \tag{7}$$

And w^1, w^2, w^3 are the wall ids of the three intersecting plane walls. If the vertex is shared by the top boundary wall and two side walls, the identification of w^1 is always expressed as $w_{(nl2-1)n+1}$. If the vertex is shared by the bottom regular polygon wall and two side walls, the identification of w^1 is always expressed as $w_{(nl2-1)n+2}$. Otherwise, the vertex v_{ij} is shared by selecting three side walls identified as $w_{i-1j}, w_{ij-1}, w_{ij}$ by Eq. (7) .

For each vertex, the plane walls sharing it can be identified by the id number of three walls as shown in Eq. (7). Then, by substituting the unit vectors of the three plane walls and corresponding plane function constant d into Eq. (6), the coordinate of each vertex can be determined. In the initial configuration, the unit normal vector $\mathbf{n}_{ij}$ and constant d_i for each specific boundary wall w_{ij} plane function has been determined as Eqs. (4) and (5), respectively. Eq. (6) can also be used to determine the vertex coordinate in the deformed configuration. In the deformed configuration, the id number for individual boundary wall and vertex would not change. It still can use Eq. (7) to identify the walls sharing the vertex. The unit normal and centre position of each boundary wall can be obtained by intrinsic functions in PFC3D. Thus, the constant d can be calculated by substituting the unit normal vector and the centre position vector into the plane function of the boundary wall as formulated in Eq. (2). Accordingly, it is straightforward to calculate the vertex coordinate in the deformed configuration by substituting the updated walls unit normal and constant d into Eq. (6).

B.2.3 Determination of polyhedron volume

It may be interested to obtain the void ratio of numerical sample in the initial undeformed configuration and deformed configuration. In the deformed configuration, the top and bottom walls are hexagons while not necessary regular. The rest boundary walls are quadrangle. Thus, it is required to calculate the sample volume for a general polyhedron. The polyhedron can be subdivided into $(n \,/\, 2-1)n+2$ polygonal pyramid by a straight line connecting each vertex with

the origin of coordinate system. Then, the volume of polyhedron is the summation of individual volume V_i of a polygonal pyramid, which is given by the pyramid volume formula:

$$V_i = \frac{1}{3} A_i h_i \tag{8}$$

where A_i is the area of the base surface and h_i is the height from the boundary wall surface (base) to the origin (apex).

For a given general plane function expressed as:

$$n_x x + n_y y + n_z z + d = 0 \tag{9}$$

The distance from a point (x_0, y_0, z_0) to the plane is

$$h = \frac{\left| n_x x_0 + n_y y_0 + n_z z_0 + d \right|}{\left| n_x{}^2 + n_y{}^2 + n_z{}^2 \right|} \tag{10}$$

As the plane function of each boundary wall is expressed as Eq. (1), where (n_x, n_y, n_z) are the components of the wall unit normal vector, the distance from the origin to the i^{th} wall surface is the absolute value of the constant d_i, hence, $h_i = |d_i|$.

To calculate the area of the i^{th} wall surface, the polygonal boundary wall surface can be subdivided into a few triangles by straight lines connecting any two neighbouring vertices with the reference point $\mathbf{x}^S$ on the surface. The coordinate of the surface reference point is the average of all nodes forming the boundary wall surface. Take boundary wall with id number 1 for example, e.g. Fig. B.0.5. It forms quadrangle pyramid by connecting its nodes with the origin O using straight lines.

The boundary wall surface formed by vertices with id 1-9-16-8 (see Fig. B.0.5) serves as the base of the quadrangle pyramid as shown in Fig. B.0.5(a). The boundary wall surface is divided into four triangles. Four vectors are illustrated, pointing from the reference point $\mathbf{x}^S$ of boundary wall to its four nodes. As the coordinates of all vertices can be obtained by Eq. (6), the area A_i of the boundary surface is calculated to be:

$$A_i = \frac{1}{2}\left(\left|\mathbf{v}_1 \times \mathbf{v}_2\right| + \left|\mathbf{v}_2 \times \mathbf{v}_3\right| + \left|\mathbf{v}_3 \times \mathbf{v}_4\right| + \left|\mathbf{v}_4 \times \mathbf{v}_1\right|\right) \tag{11}$$

Then, the volume of the illustrated quadrangle pyramid is $\frac{1}{3} A_i \left|d_i\right|$. Similarly, all the volume of polygonal pyramid can be determined. And the total volume V of the polyhedron is expressed as:

$$V = \frac{1}{3} \sum_{i=1}^{(\frac{n}{2}-1)n+2} A_i \left|d_i\right| \tag{12}$$

where A_i is the area of the i^{th} boundary wall surface and d_i is the constant of the i^{th} boundary wall plane function.

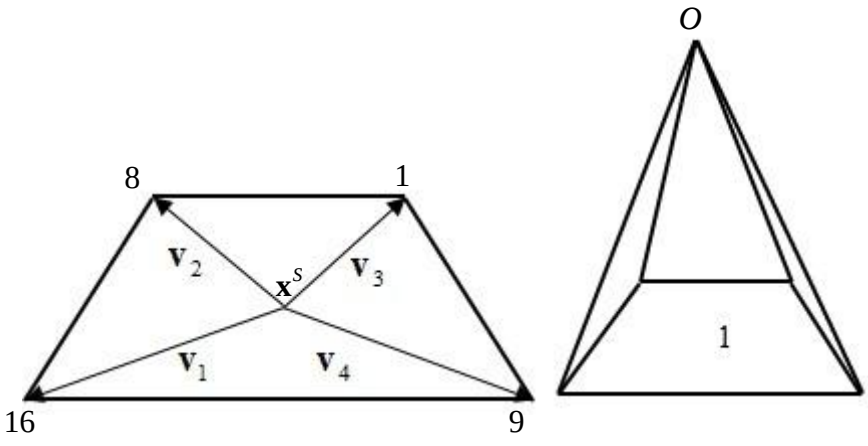

(a) Base surface (b) Quadrangle pyramid

Fig. B.0.5 Determination of quadrangle pyramid volume

Summarily, a specific polyhedron, with the entire boundary walls tangent to an inscribed sphere, can be generated by specifying infinite walls to form a closed polyhedron. A unit normal vector and a point on the wall determine the individual boundary wall. Each wall and vertex is assigned with an id number, in order to identify it for convenient programming. The void ratio of granular material is an important parameter. In order to obtain the void ratio in both initial undeformed and deformed configuration, it is necessary to calculate the volume of a general polyhedron. The polyhedral space is subdivided into polygonal pyramids, with the boundary wall surface serve as the base of the pyramid. To determine the volume of pyramid, it is required to calculate the area of individual boundary wall surface and the distance between the wall surface and the origin point. Hence, the determination of vertex position vector, intersected by at least three unparalleled planes, is introduced.

B.3 Stress and strain evaluation

The constitutive model concerns the stress-strain relationship of granular materials. Considering the heterogeneity nature of granular materials, the continuum concepts, stress/strain tensors, have been clarified and linked with the forces/displacement of the boundaries, or from local interactions/relative displacements between neighbouring particles (Li et al., 2009a, Li, 2013).

The sign convention is taken to be consistent with that defined for stress and strain in soil mechanics, as shown in Fig. B. 0.6. The positive mean normal stress and volumetric strain increment indicate compression of specimen. For the second

rank tensors, e.g., stress and strain tensor, the first subscript denotes the surface normal direction and the other subscript refers to the direction of surface traction or deformation.

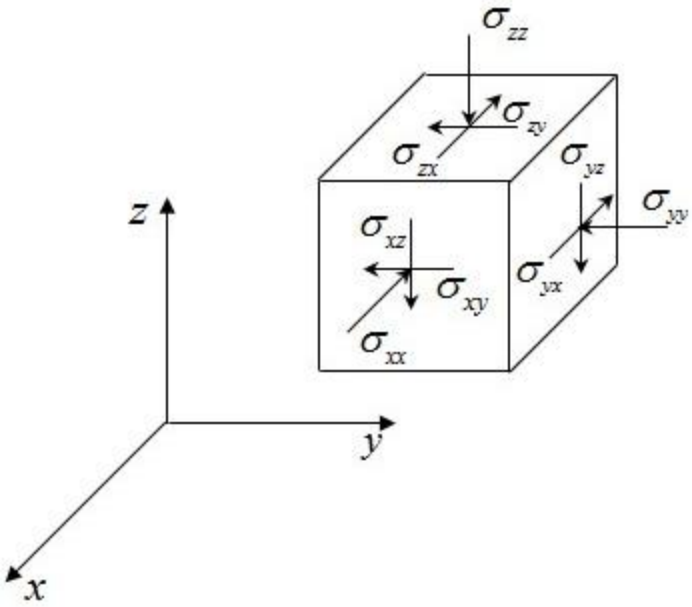

Fig. B. 0.6 Sign of convention

B.3.1 Tensor transformation

A three-dimensional symmetric second order tensor $\mathbf{A} = A_{ij}\mathbf{e}_i \otimes \mathbf{e}_j$ possesses three such invariants, $J_1(\mathbf{A}) = tr(\mathbf{A}) = A_{ii}$, $J_2(\mathbf{A}) = A_{ij}A_{ji}/2$, $J_3(\mathbf{A}) = A_{ij}A_{jk}A_{ki}/3$, and three mutually orthogonal principal directions. Tensor **A** can be written equivalently in the spectral form as $\mathbf{A} = \sum_{i=1}^{3} A_i \mathbf{n}^i \otimes \mathbf{n}^i$ with $A^i\,(i = 1,2,3)$ being the principal values and $\mathbf{n}^i\,(i = 1,2,3)$ being the corresponding principal directions. Following the convention in soil mechanics, the subscripts 1, 2 and 3 are assigned to the major, intermediate and minor principal values, respectively $(A_1 \geq A_2 \geq A_3)$. The

three invariants can be written as $J_1(\mathbf{A}) = tr(\mathbf{A}) = A_1 + A_2 + A_3$, $J_2(\mathbf{A}) = \left(A_1^2 + A_2^2 + A_3^2\right)/2$ and $J_3(\mathbf{A}) = \left(A_1^3 + A_2^3 + A_3^3\right)/3$.

A three-dimensional tensor can be decomposed as $A_{ij} = A_{kk}d_{ij}/3 + a_{ij} = md_{ij} + a_{ij}$, in which $m = A_{ii}/3 = J_1(\mathbf{A})/3$ denotes the hydrostatic mean and $a_{ij} = A_{ij} - md_{ij}$ is a deviatoric tensor. While m itself is an invariant, the deviatoric stress tensor $\mathbf{a} = a_{ij}\,\mathbf{e}_i \otimes \mathbf{e}_j$ has two non-trivial invariants $J_2(\mathbf{a}) = J_{2D}(\mathbf{A}) = J_2(\mathbf{A}) - J_1(\mathbf{A})^2/6$, $J_3(\mathbf{a}) = J_{3D}(\mathbf{A}) = J_3(\mathbf{A}) - 2J_1(\mathbf{A})J_2(\mathbf{A})/3 + 2J_1(\mathbf{A})^3/27$.

Knowing the principal values and corresponding directions, the tensor in components form can be determined from the principal tensor $\mathbf{B} = \begin{pmatrix} A^1 & 0 & 0 \\ 0 & A^2 & 0 \\ 0 & 0 & A^3 \end{pmatrix}$ and the rotation matrix $R_{ij} = \begin{pmatrix} n_1^1 & n_2^1 & n_3^1 \\ n_1^2 & n_2^2 & n_3^2 \\ n_1^3 & n_2^3 & n_3^3 \end{pmatrix}$ using the following transformation:

$$A_{ij} = R_{ik}^T B_{kl} R_{lj} \tag{13}$$

where n_j^i represents the j-th component of the principal direction $\mathbf{n}^i$.

Considering only the principal values of a three-dimensional symmetric second order tensor A_{ij}, we can define a three-dimensional principal space using the three principal values as the coordinate axes. The line passing through the origin and making equal angles with the coordinates axes is referred to as the space diagonal. The plane perpendicular to the space diagonal is called the octahedral plane, or the

deviatoric plane. The projections of the three coordinate axes on the octahedral plane are A^1', A^2' and A^3' as shown in Fig. B.0.7. The projection of the point $\left(A^1, A^2, A^3\right)$ on the octahedral plane is denoted as P. The hydrostatic part can be represented by a vector $\overrightarrow{ON}$ along the space diagonal and the deviatoric part by a vector $\overrightarrow{NP}$ on the octahedral plane. The angle between the projections of $\overrightarrow{NP}$ and the projected coordinate axes is called the Lode angle q $\left(0^o \le q \le 60^o\right)$. It can be calculated from the tensor invariants as (Khan and Huang, 1995):

$$\cos 3q = -\frac{3\sqrt{3}}{2}\frac{J_{3D}(\mathbf{A})}{J_{2D}(\mathbf{A})^{3/2}} \tag{14}$$

And the three principal values can be found as (Khan and Huang, 1995):

$$\begin{cases} A^1 = \dfrac{J_1(\mathbf{A})}{3} + \dfrac{2}{\sqrt{3}}\sqrt{J_{2D}(\mathbf{A})}\cos q \\ A^2 = \dfrac{J_1(\mathbf{A})}{3} + \dfrac{2}{\sqrt{3}}\sqrt{J_{2D}(\mathbf{A})}\cos\left(\dfrac{2p}{3} - q\right) \\ A^3 = \dfrac{J_1(\mathbf{A})}{3} + \dfrac{2}{\sqrt{3}}\sqrt{J_{2D}(\mathbf{A})}\cos\left(\dfrac{2p}{3} + q\right) \end{cases} \tag{15}$$

Denoting $b = \left(A^2 - A^3\right) / \left(A^1 - A^3\right)$, we have

$$b = \frac{A^2 - A^3}{A^1 - A^3} = \frac{\sin q}{\cos\left(\dfrac{p}{6} - q\right)} \tag{16}$$

Alternatively, the lode angle is related to *b* value as:

$$\tan q = \frac{\sqrt{3}b}{(2 - b)} \tag{17}$$

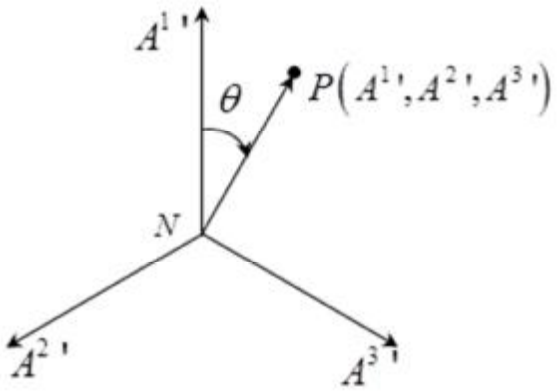

Fig. B.0.7 Illustration of Lode angle

With the three principal values determined, we will then determine the three principal directions $\mathbf{n}^i \ (i = 1, 2, 3)$, which satisfy:

$$\left(\mathbf{A} - A^i \mathbf{1}\right) \cdot \mathbf{n}^i = 0 \tag{18}$$

Or more explicitly

$$\begin{bmatrix} A_{11} - A^i & A_{12} & A_{13} \\ A_{21} & A_{22} - A^i & A_{23} \\ A_{31} & A_{32} & A_{33} - A^i \end{bmatrix} \begin{Bmatrix} n_1^{\ i} \\ n_2^{\ i} \\ n_3^{\ i} \end{Bmatrix} = 0 \tag{19}$$

When the three principal values are equal, **A** represents an isotropic tensor. The principal direction is undefined and the three vectors $\left(A_{11} - A^i, A_{12}, A_{13}\right)$, $\left(A_{21}, A_{22} - A^i, A_{23}\right)$ and $\left(A_{31}, A_{32}, A_{33} - A^i\right)$ are all zero. When two of the three principal values are equal, **A** is transversely isotropic. Only one principal direction can be determined based on the non-equal principal value. When any two of the three principal values are non-equal, there are three principal directions to determine. Note whenever there is a defined principal direction, there will be at least two of the three vectors $\left(A_{11} - A^i, A_{12}, A_{13}\right)$, $\left(A_{21}, A_{22} - A^i, A_{23}\right)$ and $\left(A_{31}, A_{32}, A_{33} - A^i\right)$ being

non-zero and the principal direction vector should be normal to non-zero vectors. This property can be used to determine the principal direction which should follow the same direction as the cross product of the two non-equal vectors and have a unit length.

B.3.2 Stress determination

In this research, the stress tensor is determined from contact forces acting on the boundary walls (Li et al., 2013):

$$s_{ij} = \frac{1}{V}\sum_{c=1}^{M} x_i^c f_j^c \tag{20}$$

where V is the volume of the polyhedron and M is the total number of contacts acting between particles and boundary walls. x_i^c is the coordinate vector of contact point c and f_j^c is the contact force vector at contact point c.

As functions of the invariants are still invariants, in the sequel, the mean normal stress $p = s_{ii}/3 = J_1(\boldsymbol{\sigma})/3$, the deviator stress ratio $h = q/p = \sqrt{3J_{2D}(\boldsymbol{\sigma})}/p$, and the intermediate principal stress ratio $b = (s_2 - s_3)/(s_1 - s_3)$ of which describes the relative magnitudes of the three principal stresses ($s_1 \geq s_2 \geq s_3$), together with the three principal directions $\mathbf{n}_s^i$ are used to describe the stress state unless otherwise specified.

For a given stress state with stress invariants p, q, b and principal direction vectors $\mathbf{n}_i^s$, the Lode angle q of the stress tensor can be determined from b

according to Eq. (17). Since $J_1(\boldsymbol{\sigma}) = 3p$ and $\sqrt{J_{2D}(\boldsymbol{\sigma})} = h\,p/\sqrt{3}$, we can calculate the three principal stresses according to Eq. (15). Together with the information on the principal directions, the stress tensor in components form can be determined from Eq. (13).

B.3.3 Strain determination

Li et al., (2009b) proposed a strain tensor for granular materials based on the void cell system, which is both valid for 2D and 3D analysis with any granular assembly tessellation subdivided into polygons in two dimensions or polyhedral elements in three dimensions. The derivation of strain expression was based on compatibility requirement along a closed boundary. This kind of strain tensor definition was evaluated to have good accuracy (Duran et al., 2010). Taking the polyhedral boundary wall as a cell system, the strain tensor is evaluated from the relative displacement of edges of the boundary wall surfaces as:

$$e_{ij} = \frac{j_{jkl}}{2V} \sum_{s} \sum_{L^{\Delta S}} h_k X_l \Delta u_i \tag{21}$$

f_{jkl} is the permutation tensor, V is volume of granular assembly. h_k is a vector from the midpoint ($X^{\Delta L}$) on line segment ($L^{\Delta S}$) to the mass centre ($X^{\Delta S}$) on boundary wall surface (ΔS), as illustrated in Fig. B.0.8. X_l is a vector pointing from midpoint ($X^{\Delta L}$) on line segment ($L^{\Delta S}$) to the origin point (O) of coordinate system. Δu_i is the relative displacement between two neighbouring nodes of the line segment.

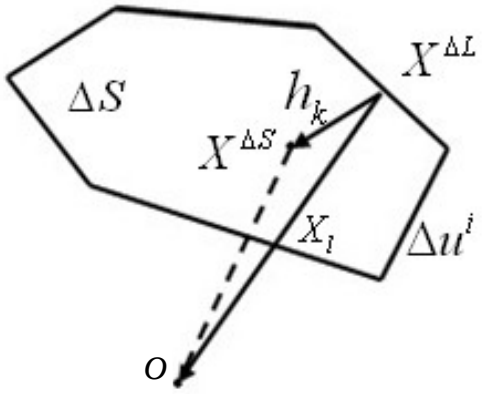

Fig. B.0.8 Diagram of vector definition

The relative displacement of the line segment can be determined by the relative change of position vectors of the nodes. The determination of the vertex position vector has been introduced in Section B.2.2. With the positions of all vertices in the deformed configuration updated, the strain tensor can be calculated from the relative displacement of line segments of each boundary wall surface using Eq. (21). To be consistent with the sign convention defined in Fig. B. 0.6, it is worth noting that the summation over individual wall surface follows the sequence of which pointing inward the sample by right hand rule.

A three-dimensional symmetric second order strain tensor, it possesses three independent invariants $J_1(\boldsymbol{\varepsilon})$, $J_2(\boldsymbol{\varepsilon})$ and $J_3(\boldsymbol{\varepsilon})$. However, it is to be emphasized that the volumetric strain definition in finite strain definition is different from $J_1(\boldsymbol{\varepsilon})$, the summation of the principal strains given in the infinitesimal deformation theory. The latter induces a significant error when the deformation is finite and large. Instead, the volumetric strain e_v should be expressed in terms of these invariants as:

$$
\begin{aligned}
e_v &= 1-\det(d_{IJ}-e_{IJ}) = e^1+e^2+e^3-e^1e^2-e^2e^3-e^1e^3+e^1e^2e^3 \\
&= J_1(\boldsymbol{\varepsilon})+J_2(\boldsymbol{\varepsilon})+J_3(\boldsymbol{\varepsilon})-\frac{1}{2}J_1(\boldsymbol{\varepsilon})^2-J_1(\boldsymbol{\varepsilon})J_2(\boldsymbol{\varepsilon})+\frac{1}{6}J_1(\boldsymbol{\varepsilon})^3
\end{aligned}
\tag{22}
$$

where $e^I\,(I=1,2,3))$ are the principal strains given in the spectral form $\boldsymbol{\varepsilon}=\sum_{I=1}^{3}e^I\mathbf{n}_e^I\otimes\mathbf{n}_e^I$, with the subscripts 1, 2 and 3 assigned to the major, intermediate and minor principal strains, respectively. The measurement and control of the specimen volume based on Eq. (22) reflects the true volume change, which is echoed by the common practice of volume measurement/control for saturated specimens in the laboratory, where the volume change is quantified by the pore fluid flowing in or out of the specimen instead of deduced from the normal strain values.

Quantifying shear deformation is not that straightforward. To assess shear deformation, we adopt two invariants: the deviatoric strain e_q and the intermediate strain ratio b_e defined as:

$$
\begin{aligned}
e_q &= 2\sqrt{J_{2D}(\boldsymbol{\varepsilon})/3} = 2\sqrt{\left[J_2(\boldsymbol{\varepsilon})-\frac{1}{6}J_1(\boldsymbol{\varepsilon})^2\right]\Big/3} \\
b_e &= \left(e^2-e^3\right)\Big/\left(e^1-e^3\right)
\end{aligned}
\tag{23}
$$

The three invariants e_v, e_q and b_e and the three principal directions $\mathbf{n}_e^1$, $\mathbf{n}_e^2$ and $\mathbf{n}_e^3$ are used to define a state of deformation.

When the invariants e_v, e_q, b_e of the strain tensor are specified, the Lode angle of the strain tensor can be determined from Eq. (16), and $J_{2D}(\boldsymbol{\varepsilon})$ can be

determined from Eq. (23) as $\sqrt{J_{2D}(\boldsymbol{\varepsilon})}=\sqrt{3}e_q/2$. Denoting

$a=\frac{2}{\sqrt{3}}\sqrt{J_{2D}(\mathbf{A})}\cos q,\ b=\frac{2}{\sqrt{3}}\sqrt{J_{2D}(\mathbf{A})}\cos\left(\frac{2p}{3}-q\right),\ c=\frac{2}{\sqrt{3}}\sqrt{J_{2D}(\mathbf{A})}\cos\left(\frac{2p}{3}+q\right)$

, we have from Eq. (15) that:

$$e_1=\frac{J_1(\boldsymbol{\varepsilon})}{3}+a,\ e_2=\frac{J_1(\boldsymbol{\varepsilon})}{3}+b,\ e_3=\frac{J_1(\boldsymbol{\varepsilon})}{3}+c \tag{24}$$

and $a+b+c=0$, $ab+bc+ca=-J_{2D}(\boldsymbol{\varepsilon})$, $abc=J_{3D}(\boldsymbol{\varepsilon})$.

When the strain is isotropic, $\sqrt{J_{2D}(\boldsymbol{\varepsilon})}=0$, and $J_1(\boldsymbol{\varepsilon})=3\left(1-\sqrt[3]{1-e_v}\right)$. Otherwise, $J_1(\boldsymbol{\varepsilon})$ can be found by solving the cubic Eq. (22). Denoting $x=1-\frac{J_1(\boldsymbol{\varepsilon})}{3}$, the cubic Eq. (22) is rewritten as:

$$\begin{aligned} y&=(1-e_1)(1-e_2)(1-e_3)\\ &=(x-a)(x-b)(x-c)=1-e_v \end{aligned} \tag{25}$$

The polynomial function $y=0$ has three real roots as $x=a,b,c$. Its derivative $y'=0$ leads to $x=\pm\sqrt{\frac{1}{3}J_{2D}}$, between which $x=-\sqrt{\frac{1}{3}J_{2D}}$ corresponds to a positive local maximal y_{high} , $y_{high}=2\left[\frac{1}{3}J_{2D}\right]^{3/2}-J_{3D}$ and $x=\sqrt{\frac{1}{3}J_{2D}}$ corresponds to a negative local minimum y_{low}, $y_{low}=-2\left[\frac{1}{3}J_{2D}\right]^{3/2}-J_{3D}$.

In numerical study of granular material elementary behaviour, the values of e_v and e_q are of limited magnitudes. In most conditions, we have $1-e_v>y_{high}$. Hence, there is only one real root to the cubic Eq. (25), which is

$$x = \sqrt[3]{-\frac{Q}{2} + \sqrt{\frac{Q^2}{4} + \frac{P^3}{27}}} + \sqrt[3]{-\frac{Q}{2} - \sqrt{\frac{Q^2}{4} + \frac{P^3}{27}}} \tag{26}$$

where $Q = \left(3m - l^2\right)/9$ and $P = \left(9lm - 27n - 2l^3\right)/54$. And l, m, n are the constants of the standard cubic equation as shown below:

$$x^3 + lx^2 + mx + n = 0 \tag{27}$$

and $l = -\left(a + b + c\right)$, $m = \left(ab + bc + ac\right)$, $n = -abc$.

Hence, the first invariant $J_1\left(\boldsymbol{\varepsilon}\right)$ can be found as:

$$J_1(\boldsymbol{\varepsilon}) = 3\left(1 - x\right) = 3\left(1 - \sqrt[3]{-\frac{Q}{2} + \sqrt{\frac{Q^2}{4} + \frac{P^3}{27}}} - \sqrt[3]{-\frac{Q}{2} - \sqrt{\frac{Q^2}{4} + \frac{P^3}{27}}}\right) \tag{28}$$

Once $J_1(\boldsymbol{\varepsilon})$ is determined, the three principal strains can be determined from Eq. (24). Together with the information on the principal directions $\mathbf{n}_e^i$, the strain tensor in components form can be determined from Eq. (13).

B.4 Implementation of general loading path

B.4.1 Strain-controlled boundary conditions

A strain controlled loading path controls the boundary deformation to a target strain state expressed in invariants form, $e_v, e_q, b_e, \mathbf{n}_i^e$. Alternatively, the target strain state can also be expressed in tensorial form e_{ij}^t by Eq. (13). The strain increment Δe_{ij} is the difference of the current strain tensor e_{ij} determined from Eq.

(21) and the target strain tensor, $\Delta e_{ij} = e_{ij}^{t} - e_{ij}$. In a strain field Δe_{jk}, fixing the position of specimen origin *O*, the position vector x_i of a material point in the deformed configuration can be determined according to the position vector X_i in the undeformed configuration as:

$$x_i = d_{ik}(d_{jk} - \Delta e_{jk})X_j \tag{29}$$

The geometry of boundary walls can be described by their centres and normal directions, which are denoted as $\mathbf{X}^w$,$\mathbf{N}^w$ in the undeformed configuration and $\mathbf{x}^w$,$\mathbf{n}^w$ in the deformed configuration. The centre $\mathbf{X}^w$ and unit normal vector $\mathbf{N}^w$ of each boundary wall can be updated by intrinsic functions within PFC3D in the undeformed configuration. Therefore, substituting the wall centre vector $\mathbf{X}^w$ into Eq. (29), the new wall centre position vector $\mathbf{x}^w$ can be determined after a strain increment Δe_{ij}. To find the boundary wall normal direction $\mathbf{n}^w$ after deformation, it is essential to use two in-plane vectors $\mathbf{t}_1^w$ and $\mathbf{t}_2^w$ to determine $\mathbf{n}^w$ in the deformed configuration as $\mathbf{n}^w = \dfrac{\mathbf{t}_1^w \times \mathbf{t}_2^w}{\left\|\mathbf{t}_1^w \times \mathbf{t}_2^w\right\|}$. $\left\|\mathbf{t}_1^w \times \mathbf{t}_2^w\right\|$ represents the Euclidean normal of vector $\mathbf{t}_1^w \times \mathbf{t}_2^w$. As the plane wall function is known by updating the $\mathbf{X}^w$,$\mathbf{N}^w$, the position vector $\mathbf{X}^v$ of the vertex forming the polyhedron can be determined using Eq. (6). Accordingly, the individual position vector $\mathbf{x}^v$ of the vertex after a strain increment Δe_{ij} can be calculated from Eq. (29). Then, it is possible to use the two in-plane vectors $\mathbf{t}_1^w$ and $\mathbf{t}_2^w$ to determine the wall unit normal vectors in the deformed configuration.

Once the boundary walls position vectors and unit normal vectors are known in both undeformed configuration and deformed configuration (after strain increment Δe_{ij}), the translational velocities v_i^w can be specified to achieve a strain increment Δe_{ij} during a timestep Δt:

$$v_i^w = \Delta x_i^w / \Delta t = -d_{iK} \Delta e_{JK} X_j^w / \Delta t \tag{30}$$

and rotational velocities w_i^w is determined as

$$w_i^w = \frac{\Delta q}{\Delta t} \frac{\left(\mathbf{N}^w \times \mathbf{n}^w\right)_i}{\left\|\mathbf{N}^w \times \mathbf{n}^w\right\|} \tag{31}$$

where Δq is the angle between the two unit vectors and $\sin \Delta q = \left\|\mathbf{N}^w \times \mathbf{n}^w\right\|$.

B.4.2 Stress-controlled boundary conditions

The stress controlled loading is described by maintaining a target stress state in terms of stress invariants $p^t, q^t, b^t, \mathbf{n}_i^t$. The expression of target stress in invariants form can be inter-transformed into stress tensor s_{ij}^t by applying Eq. (13). The stress increment tensor Δs_{ij} is calculated as the difference of the current stress tensor s_{ij} determined from Eq. (20) at any stage of loading and the target stress tensor s_{ij}^t, $\Delta s_{ij} = s_{ij}^t - s_{ij}$. The stress increment has to be applied using the following servo-control mechanism. Based on the stress increment, the corresponding strain increment is estimated by Hook's Law to be:

$$\Delta e_{ij} = \begin{cases} \dfrac{1+n}{E}\Delta s_{kk} - \dfrac{n}{E}\Delta s_{ij} & (i = j) \\ \dfrac{\Delta s_{ij} + \Delta s_{ji}}{2(1+n)E} & (i \neq j) \end{cases} \tag{32}$$

where E and n are the nominal Young's modulus and Poisson's ratio. The nominal Young's modulus E is estimated as:

$$E = \frac{\Delta s}{V \Delta e} = \frac{k_n R}{V 2\bar{r}} \tag{33}$$

k_n is the spring normal stiffness for linear contact model. R is the radius of the inscribed sphere of initial polyhedron, $\bar{r}$ is the average particle radius and V is a relaxation factor. And the bulk modulus K and shear modulus G of specimen are estimated in terms of Young's modulus and Poisson's ratio:

$$\begin{aligned} K &= \frac{E}{2(1-n)} \\ G &= \frac{E}{2(1+n)} \end{aligned} \tag{34}$$

After the estimated strain increment is determined from Eq. (32), the boundary walls velocities are specified according to Eqs. (30) and (31) to achieve the estimated strain increment accurately. As the material is not perfectly elastic, the applied strain increment estimated by Hook's Law does not necessarily result in the desired stress increment Δs_{ij}. After each calculation cycle, the stress increment $\Delta s_{ij} = s_{ij}^{t} - s_{ij}$ is updated based on the new stress state s_{ij}, and used to determine a new strain increment applied to the specimen boundaries. By repeating doing so, the specimen stress gradually approaches the target stress state. When the difference between the current stress state and the target stress state is smaller than the preset

tolerance, the boundary stress condition is considered to be satisfied. By default, $n = 0.5$ and $V = 0.8$ are used here in the following simulations.

B.4.3 Numerical test control

Monitoring boundary conditions

In numerical simulations, the boundary conditions cannot be exactly satisfied. Tolerances are set to monitor boundary conditions and the boundary conditions are considered to meet requirements if the differences between current boundary conditions and target boundary conditions are smaller than pre-set tolerance values.

For stress-controlled boundary, the boundary condition is considered to be satisfied if the stress invariants and principal directions follow Eq. (35):

$$\begin{cases} \left| p - p^t \right| < p_{tol} = h_{tol} \cdot \mathbf{max}(p, p_{lb}) \\ \left| h - h^t \right| < h_{tol} \\ \left| b_s - b_s^t \right| < b_{s\,tol}, \text{if } h > h_{tol} \\ \left| 1 - \mathbf{n}_s^i \cdot \mathbf{n}_s^{it} \right| < n_{s\,tol}, \text{if } h > h_{tol} \end{cases} \tag{35}$$

in which p^t, h^t, b^t and $\mathbf{n}_s^{it}$ represent the target mean normal stress, stress ratio, intermediate principal stress parameter and the unit direction vectors representing the i^{th} principal stress direction. $p_{tol}, h_{tol}, b_{tol}$ and $\mathbf{n}_{tol}$ are the corresponding tolerances; p_{lb} is the lower bound of the specimen mean normal stress. When the mean normal stress is lower than p_{lb}, the specimen is considered to be stress free and can flow as a liquid. Note that the repeated superscripts here do not indicate summation. $\mathbf{n}_s^i \cdot \mathbf{n}_s^{it}$ denotes the dot product of the i^{th} current and target principal

stress direction vectors. When the stress ratio h is smaller than the tolerance h_{tol}, indicating the isotropic stress state, the intermediate principal stress parameter and the principal directions are undefined. The associated boundary conditions control is released.

For strain-controlled boundary, the boundary condition is considered to be satisfied if the strain invariants and principal directions meet the following equation:

$$\begin{cases} \left| e_v - e_v^t \right| < e_{vtol} \\ \left| e_q - e_q^t \right| < e_{qtol} \\ \left| b_e - b_e^t \right| < b_{etol}, \text{if } e_q > e_{qtol} \\ \left| 1 - \mathbf{n}_e^i \cdot \mathbf{n}_e^{it} \right| < n_{etol}, \text{if } e_q > e_{qtol} \end{cases} \tag{36}$$

where e_v^t, e_q^t, b_e^t and $\mathbf{n}_e^{it}$ represent the target volumetric strain, deviatoric strain, intermediate principal strain ratio and the unit vectors representing the i^{th} principal strain directions; $e_{vtol}, e_{qtol}, b_{etol}$ and n_{etol} are the corresponding tolerances. Again, the repeated superscripts here do not indicate summation. $\mathbf{n}_e^i \cdot \mathbf{n}_e^{it}$ denotes the dot product of the i^{th} current and target principal strain direction vectors. Similarly, when the specimen strain state is isotropic, the control of the intermediate principal strain ratio and the principal directions become unnecessary.

In all numerical simulations of this research, it sets $p_{lb} = 5kPa, h_{tol} = 1\times10^{-4}$ $b_{tol} = h_{tol} / \mathbf{max}(h, h_{tol})$, $\mathbf{n}_{s\,tol} = h_{tol}$, $e_{vtol} = p_{tol}/K$, $e_{qtol} = p_{tol}/G$, $b_{etol} = e_{qtol} / \mathbf{max}(e_q, e_{qtol})$ and $\mathbf{n}_{etol} = b_{etol}$. K and G are bulk modulus and shear

modulus as determined by Eq. (34). The accuracy of the boundary conditions are hence monitored solely by the values of p_{lb} and h_{tol}.

Equilibrium monitoring

DEM simulations are inherently dynamic. However, what of interest is the quasi-static deformation behaviour and the equilibrium condition is considered to be satisfied if the ratio between the maximum unbalance force and average contact force is smaller than a pre-defined tolerance:

$$f_{unb} / f_{av} \leq f_{tol} \tag{37}$$

In all numerical simulations presented in this research, f_{tol} is set to be 0.001. Loadings are applied only if the sample equilibrium monitoring is satisfied. Otherwise, boundary walls are fixed with calculation cycles continued till force equilibrium achieved.

Choice of loading rate

To model stress-strain behaviour under quasi-static conditions, the loading increment is kept small to minimise dynamic effects. And it is associated with the tolerance of boundary conditions:

$$\begin{cases} \Delta p = \mathbf{sgn}(p^t - p)\,\mathbf{min}(\left|p^t - p\right|, l\,p_{tol}) \\ \Delta h = \mathbf{sgn}(h^t - h)\,\mathbf{min}(\left|h^t - h\right|, l\,h_{tol}) \\ \Delta b_s = \mathbf{sgn}(b_s^t - b_s)\,\mathbf{min}(\left|b_s^t - b_s\right|, l\,b_{s\,tol}) \\ \Delta \mathbf{n}_s = \mathbf{sgn}(\mathbf{n}_s^t - \mathbf{n}_s)\,\mathbf{min}(\left|\mathbf{n}_s^t - \mathbf{n}_s\right|, l\,\mathbf{n}_{s\,tol}) \end{cases}, \begin{cases} \Delta e_v = \mathbf{sgn}(e_v^t - e_v)\,\mathbf{min}(\left|e_v^t - e_v\right|, l\,e_{vtol}) \\ \Delta e_q = \mathbf{sgn}(e_q^t - e_q)\,\mathbf{min}(\left|e_q^t - e_q\right|, l\,e_{qtol}) \\ \Delta b_e = \mathbf{sgn}(b_e^t - b_e)\,\mathbf{min}(\left|b_e^t - b_e\right|, l\,b_{e\,tol}) \\ \Delta \mathbf{n}_e = \mathbf{sgn}(\mathbf{n}_e^t - \mathbf{n}_e)\,\mathbf{min}(\left|\mathbf{n}_e^t - \mathbf{n}_e\right|, l\,\mathbf{n}_{e\,tol}) \end{cases} \tag{38}$$

where l is a loading factor, which controls magnitude of loading rates by setting different values. The principal direction increment expressed in the equation is in vector form for convenience. However, in numerical implementation, principal direction increment is the angular increment $\Delta q = \mathbf{sin}^{-1}\left(\mathbf{n}_i \times \mathbf{n}_i^t\right)$.

The numerical computational time under different loading path is dominated by equilibrium control tolerance f_{tol} , boundary condition tolerance p_{lb}, h_{tol} and the loading factor l . However, a higher value of loading factor results in a greater magnitude of loading increment and possible larger unbalance force, which requires the system to run more calculation cycles to achieve equilibrium before further loading applied. Therefore, a significant high value of l would not help to improve the computation efficiency.

APPENDIX C: Table of numerical samples used for simulations

The samples used for numerical simulations in this research are summarised in the following two tables. Table C.1 includes all the numerical samples of spherical particles and Table C.2 shows all the numerical samples of non-spherical particles. The first column indicates the sample preparation method. The radius expansion method is used to prepare initially isotropic sample and the initially anisotropic sample is prepared by gravitational deposition method. Otherwise, the sample is prepared by pre-loading the initially isotropic sample or initially anisotropic sample, which results in inevitably anisotropic sample due to loading induced anisotropy. The 'PS' indicates the Plane Strain pre-shearing loading path, where more details can be found in Section 4.4.1 (Page 82). The 'TT' refers to drained True Triaxial loading at constant $p = 500kPa$. And 'TC' is the drained Triaxial Compression pre-shearing loading path with fixed $p = 500kPa$. More details about the triaxial loading path can be found in Section 4.4.2 (Page 87).

The numerical samples are labelled for easy cross-link through the thesis. The first four characters before the first underline indicate the sample preparation information. The first character 'S' refers to the particle shape as spherical and 'C' denotes to Clump, which is non-spherical particle shape of two identical overlapping balls (i.e., Fig. 3.2). The second and third characters indicate the sample preparation method. 'RE' means the Radius Expansion method for generating initially isotropic

sample and ‘DE’ refers to gravitational Deposition method for preparing initially anisotropic. The fourth character simply indicate the sample relative density, where ‘D’, ‘M’ and ‘L’ refer to the sample be ‘Dense’,’Medium’ and ‘Loose’, respectively.

The characters between two underlines, where it exists, indicate the pre-loaded history. ‘PSK05’, ‘PSK1’ and ‘PSK2’ show the radius expansion prepared dense sample of spherical particles is pre-sheared by plane strain loading to different initial K_0 conditions, $K_0 = 0.5$, $K_0 = 1$ and $K_0 = 2$, respectively. The strings ‘B05Y05’, ‘B05Y07’ and ‘B05Y09’ expresses the sample is pre-sheared by true triaxial loading at constant $b = 0.5$ to the target stress ratio $h = 0.5$, $h = 0.7$, $h = 0.9$ respectively. The strings ‘B00Y09’ and ‘B10Y09’ denote the sample is pre-sheared by true triaxial loading to the target stress ratio $h = 0.9$ at constant $b = 0.0$ and $b = 1.0$, respectively. And the string ‘TC’ indicates the sample being pre-sheared by triaxial compression to the deviatoric strain of $e_q = 10\%$ and then unloaded to the isotropic stress state. More details about the pre-shearing process have been introduced in the corresponding chapters.

The last two characters demonstrate that the prepared sample is going to be sheared at particular loading path for numerical simulation. For example, ‘TT’ shows the sample will be simulated by drained true triaxial loading path; ‘SS’ refers to undrained simple shear; ‘RS’ denotes drained rotational shear and ‘TC’ indicates drained triaxial compression. More details about loading path have been introduced in individual sections, where the results are presented.

By doing so, all the numerical samples used for numerical simulation are labelled and whenever the string of characters appears in the thesis refers to the definition in those two tables. For example, 'SRED_TT' denotes the initially isotropic dense sample of spherical particles prepared by radius expansion method, which is used for drained true triaxial simulations. And 'CDED_B05Y09_RS' is the deposited dense sample of clump particles and is followed by true triaxial pre-shearing at constant $b = 0.5$ to stress ratio $h = 0.9$. Then, it is used for rotational shear simulation.

Table C.1 Sample of spherical particles used for numerical simulations

<table>
<tr><th colspan="6">Samples of spherical particles</th></tr>
<tr><td colspan="2">Sample preparation</td><td>Sample label</td><td>Void ratio</td><td>Numerical simulations</td><td>Related results</td></tr>
<tr><td colspan="2" rowspan="3">Radius expansion</td><td>SRED_TT</td><td>$e_0 = 0.64$</td><td rowspan="3">True triaxial simulation</td><td rowspan="3">Section 4.4.2
Chapter 5</td></tr>
<tr><td>SREM_TT</td><td>$e_0 = 0.73$</td></tr>
<tr><td>SREL_TT</td><td>$e_0 = 0.78$</td></tr>
<tr><td rowspan="3">Radius expansion</td><td rowspan="3">Pre-shear (PS)</td><td>SRED_PSK05_SS</td><td>$e_0 = 0.62$</td><td rowspan="3">Undrained simple shear</td><td rowspan="3">Section 4.4.1</td></tr>
<tr><td>SRED_PSK10_SS</td><td>$e_0 = 0.64$</td></tr>
<tr><td>SRED_PSK20_SS</td><td>$e_0 = 0.65$</td></tr>
<tr><td rowspan="2">Radius expansion</td><td rowspan="2">Pre-shear (TT)</td><td>SRED_B05Y05_RS</td><td>$e_0 = 0.64$</td><td rowspan="2">Rotational shear</td><td rowspan="2">Section 4.4.3</td></tr>
<tr><td>SREL_B05Y05_RS</td><td>$e_0 = 0.75$</td></tr>
<tr><td colspan="2">Gravitational deposition</td><td>SDEM_TT</td><td>$e_0 = 0.72$</td><td rowspan="2">True triaxial, varying a</td><td>Section Chapter 6</td></tr>
<tr><td>Deposition</td><td>Pre-shear (TC)</td><td>SDEM_TC_TT</td><td>$e_0 = 0.71$</td><td>Section 6.3</td></tr>
</table>

Table C.2 Sample of non-spherical particles used for numerical simulations

<table>
<tr><th colspan="6">Samples of non-spherical particles</th></tr>
<tr><td colspan="2">Sample preparation</td><td>Sample Label</td><td>Void ratio</td><td>Numerical simulations</td><td>Related results</td></tr>
<tr><td colspan="2">Radius expansion</td><td>CRED_TC</td><td>$e_0 = 0.59$</td><td>Triaxial compression</td><td>Section 7.3</td></tr>
<tr><td colspan="2" rowspan="2">Gravitational deposition</td><td>CDED_TT</td><td>$e_0 = 0.64$</td><td rowspan="3">True triaxial
b=0.4,
$a \in [0^o, 90^o]$
15^o interval</td><td rowspan="2">Section 7.4
Section 7.5
Appendix A1</td></tr>
<tr><td>CDEL_TT</td><td>$e_0 = 0.77$</td></tr>
<tr><td>Deposition</td><td>Pre-shear (TC)</td><td>CDED_TC_TT</td><td>$e_0 = 0.65$</td><td>Section 7.5
Appendix A2</td></tr>
<tr><td rowspan="5">Deposition</td><td rowspan="3">Pre-shear (TT)
$b = 0.5$</td><td>CDED_ B05Y05_RS</td><td>$e_0 = 0.645$</td><td rowspan="5">Rotational shear</td><td rowspan="5">Chapter 8</td></tr>
<tr><td>CDED_ B05Y07_RS</td><td>$e_0 = 0.645$</td></tr>
<tr><td>CDED_ B05Y09_RS</td><td>$e_0 = 0.645$</td></tr>
<tr><td rowspan="2">Pre-shear (TT)
$h = 0.9$</td><td>CDED_ B00Y09_RS</td><td>$e_0 = 0.644$</td></tr>
<tr><td>CDED_ B10Y09_RS</td><td>$e_0 = 0.646$</td></tr>
</table>

REFERENCE

ABELEV, A. V. & LADE, P. V. 2003a. Effects of cross anisotropy on three-dimensional behaviour of sand. I: stress-strain behaviour and shear banding. *Journal of Engineering Mechanics,* 129**,** 160-166.

ANDO, E., HALL, S. A., VIGGIANI, G., DESRUES, J. & BESUELLE, P. 2012. Experimental micromechanics: grain-scale observation of sand deformation. *Géotechnique Letters,* 2**,** 107-112.

ARTHUR, J. R. F., CHUA, K. S. & DUNSTAN, T. 1977. Induced anisotropy in a sand. *Géotechnique,* 27**,** 13-30.

ARTHUR, J. R. F., DUNSTAN, T., AL-ANI, Q. A. J. & ASSADI, A. 1977a. Plastic deformation and failure in granular media. *Géotechnique,* 27**,** 53-74.

ARTHUR, J. R. F. & MENZIES, B. K. 1972. Inherent anisotropy in a sand. *Géotechnique,* 22**,** 115-128.

AZ MA, E. & RADJA , F. 2012. Force chains and contact network topology in sheared packings of elongated particles. *Phys. Rev. E,* 85.

BAGI, K. 1996. Stress and strain in granular assemblies. *Mechanics of Materials,* 22**,** 165-177.

BARDET, J. P. 1994. Observations on the effects of particle rotations on the failure of idealised granular materials. *Mechanics of Materials,* 18**,** 159-182.

BARRETO, D., O'SULLIVAN, C. & ZDRAVKOVIC, L. 2008. DEM simulations of granular materials involving principal stress rotation. *Inaugural International Conference of the Engineering Mechanics Institute - EM'08, 18-22 May 2008, Minneapolis, USA.*

BATHE, K. J. & WILSON, E. L. 1976. Numerical method in finite element analysis. *Int. J. Numer. Anal. Meth. Geomech,* 1.

BEEN, K. & JEFFERIES, M. G. 1985. A state parameter for sands. *Géotechnique,* 35**,** 99-112.

BOLTON, M. D. 1986. The strength and dilatancy of sands. *Géotechnique,* 36**,** 65-78.

BREWER, R. 1964. Fabric and mineral analysis of soils. *John Wiley and Sons, Inc,* 129-158.

BUDHU, M. & BRITTO, A. 1987. Numerical analysis of soils in simple shear devices. *Soils and Foundations,* 27**,** 31-41.

CAI, Y., YU, H. S., WANATOWSKI, D. & LI, X. 2013. Non-coaxial behaviour of sand under various stress paths. *Journal of Geotechnical and Geoenvironmental Engineering,* 139**,** 1381-1395.

CALVETTI, F., COMBE, G. & LANIER, J. 1997. Experimental micromechnical analysis of a 2D granular material: relation between structure evolution and loading path. *Mechanics of Cohesive-frictional Materials,* 2**,** 121-163.

CASAGRANDE, A. & CARRILLO, N. 1944. Shear failure of anisotropic materials. *Journal of the Boston Society of Civil Engineers,* 31**,** 122-135.

CHRISTOFFERSEN, J., MEHRABADI, M. M. & NEMAT-NASSER, S. 1981. A micromechanical description of granular material behaviour. *J. Appl. Mech,* 48**,** 339-344.

CROLL, A. B., TORDESILLAS, A., CAREY, D. & GURMESSA, B. 2013. Experimental evidence and structural mechanics analysis of force chain buckling at the microscale in a 2D polymeric granular layer. *Powders and Grains, AIP Conf. Proc,* 1542**,** 409-412.

CUI, L., O'SULLIVAN, C. & O'NEILL, S. 2007. An analysis of the triaxial apparatus using a mixed boundary three-dimensional discrete element model. *Géotechnique,* 57**,** 831-844.

CUNDALL, P. A. 1971. A computer model for simulating progressive large scale movements in blocky rock systems. *Proceedings of the Symposium of the International Society for Rock Mechanics,* 1.

CUNDALL, P. A. & STRACK, O. D. L. 1979. A discrete numerical model for granular assemblies. *Géotechnique,* 29**,** 47-65.

DAFALIAS, Y. F. & LI, X. S. 2013. Revisiting the paradigm of critical state soil mechanics: fabric effects. *Constitutive Modeling of Geomaterials, SSGG,* 13-26.

DAFALIAS, Y. F., PAPADIMITRIOU, A. G. & LI, X. S. 2004. Sand plasticity model accounting for inherent fabric anisotropy. *Journal of Engineering Mechanics,* 130**,** 1319-1333.

DRESCHER, A. & JONG, G. D. J. D. 1972. Photoelastic verification of a mechanical model for the flow of a granular material. *J. Mech. Phys. Solids,* 20**,** 337-351.

DURAN, O., KRUYT, N. P. & LUDING, S. 2010. Analysisi of three-dimensional micro-mechanical strain formulations for granular materials: Evaluation of accuracy. *International Journal of Solids and Structures,* 47**,** 251-260.

ERGUN, U. 1977. Discussion: Independent stress control and triaxial extension tests on sand. *Géotechnique,* 27.

EUGENE J. VAN DYCK, V. 2012. Effects of principal stress direction and the intermediate principal stress on the stress-strain-strength behaviour of a cross-anisotropic fine sand deposit. *PhD thesis, The Catholic University of America*.

FONSECA, J., O'SULLIVAN, C., COOP, M. R. & LEE, P. D. 2013. Quantifying the evolution of soil fabric during shearing using scalar parameters. *Géotechnique,* 63**,** 818-829.

FU, P. & DAFALIAS, Y. F. 2011. Study of anisotropic shear strength of granular materials using DEM simulation. *Int. J. Numer. Anal. Meth. Geomech,* 35**,** 1098-1126.

FU, P. & DAFALIAS;, Y. F. 2011. Study of anisotropic shear strength of granular materials using DEM simulation. *Int. J. Numer. Anal. Meth. Geomech,* 35**,** 1098-1126.

GAJO, A. & WOOD, D. M. 1999. A kinemati hardening constitutive model for sands: the multiaxial formulation. *Int. J. Numer. Anal. Meth. Geomech,* 23**,** 925-965.

GUO, N. & ZHAO, J. 2013. The signature of shear-induced anisotropy in granular media. *Computers and Geotechnics,* 47**,** 1-15.

GUO, P. J. 2008. Modified direct shear test for anisotropic strength of sand. *Journal of Geotechnical and Geoenvironmental Engineering,* 134**,** 1311-1318.

GUTIERREZ, M., ISHIHARA, K. & TOWHATA, I. 1991. Flow theory for sand during rotation of principal stress direction. *Soils and Foundations,* 31**,** 121-132.

HARUYAMA, M. 1981. Anisotropic deformation-strength characteristics of an assembly of spherical particles under three dimensional stresses. *Soils and Foundations,* 21**,** 41-55.

HOSSEININIA, E. S. 2012. Discrete element modelling of inherently anisotropic granular assemblies with polygonal particles. *Particuology,* 10**,** 542-552.

HOSSEININIA, E. S. 2013. Stress-force-fabric relationship for planar granular materials. *Géotechnique,* 63**,** 830-841.

ISHIHARA, K. 1993. Liquefaction and flow failure during earthquakes. *Géotechnique,* 43**,** 351-451.

IWASHITA, K. & ODA, M. 1998. Rolling resistance at contacts in simulation of shear band development by DEM. *Journal of Engineering Mechanics,* 124**,** 285-292.

JIANG, M. J., KONRAD, J. M. & LEROUEIL, S. 2003. An efficient technique for generating homogeneous specimens for DEM studies. *Computers and Geotechnics,* 2003**,** 579-597.

JIANG, M. J., YU, H. S. & HARRIS, D. 2005. A novel discrete model for granular material incorporating rolling resistance. *Computers and Geotechnics,* 32**,** 340-357.

JOHNSON, K. L. 1985. Contact mechanics. *the Press Syndicate of the University of Cambridge*.

JOHNSON., K. L. 1985. Contact mechanics. *the syndicate of the University of Cambrige*.

KANATANI, K.-I. 1984. Distribution of directional data and fabric tensors. *Int. J. Engng Sci.,* 22**,** 149-164.

KHAN, A. S. & HUANG, S. 1995. *Continuum theory of plasticity*, John Wiley & Sons, Inc.

KO, H.-Y. & SCOTT, R. F. 1967. A new soil testing appratus. *Géotechnique,* 17**,** 40-57.

KRUYT, N. P. 2012. Micromechanical study of fabric evolution in quasi-static deformation of granular materials. *Mechanics of Materials,* 44**,** 120-129.

KUHN, M. R. 2010. Micro-mechanics of fabric and failure in granular materials. *Mechanics of Materials,* 42**,** 827-840.

KUMRUZZAMAN, M. & YIN, J. H. 2010. Influence of principal stress direction on the stress-strain-strength behaviour of completely decomposed granite. *Architecture and Civil Engineering, Facta Universitatis.,* 8**,** 79-97.

LADE, P. V. 1977. Elasto-plastic stress-strain theory for cohesionless soil with curved yield surfaces. *International Journal of Solids and Structures,* 13**,** 1019-1035.

LADE, P. V. 2006. Assessment of test data for selection of 3-D failure criterion for sand. *Int. J. Numer. Anal. Meth. Geomech,* 30**,** 307-333.

LADE, P. V. & ABELEV, A. V. 2003b. Effects of cross anisotropy on three-dimensional behaviour of sand. II: Volume change behavior and failure. *Journal of Engineering Mechanics,* 129**,** 167-174.

LADE, P. V. & ABELEV, A. V. 2005. Characterization of cross-anisotropic soil deposits from isotropic compression tests. *Soils and Foundations,* 45**,** 89-102.

LADE, P. V. & DUNCAN, J. M. 1973. Cubical triaxial tests on cohesionless soil. *Journal of Soil Mechanics and Foundations,* 99**,** 793-812.

LAM, W.-K. & TATSUOKA, F. 1988. Effects of initial anisotropic fabric and σ_2 on strength and deformation characteristics of sand. *Soils and Foundations,* 28**,** 89-106.

LANGSTON, P., AI, J. & YU, H.-S. 2013. Simple shear in 3D DEM polyhedral particles and in a simplified 2D continuum model. *Granular Matter*.

LASHKARI, A. & LATIFI, M. 2008. A non-coaxial constitutive model for sand deformation under rotation of principal stress axes. *Int. J. Numer. Anal. Meth. Geomech,* 32**,** 1051-1086.

LI, X. 2006. Micro-scale investigation on the quasi-static behaviour of granular material. *PhD thesis, The Hong Kong University of Science and Technology*.

LI, X. & LI, X.-S. 2009. Mirco-macro quantification of the internal structure of granular materials. *Journal of Engineering Mechanics,* 135**,** 641-656.

LI, X., YU, H.-S. & LI, X.-S. 2009a. Macro-micro relations in granular mechanics. *International Journal of Solids and Structures,* 46**,** 4331-4341.

LI, X. & YU, H. S. 2009. Influence of loading direction on the behaviour of anisotropic granular materials. *International Journal of Engeering Science,* 47**,** 1284-1296.

LI, X. & YU, H. S. 2010. Numerical investigation of granular material under rotational shear. *Géotechnique,* 60**,** 381-394.

LI, X. & YU, H. S. 2011a. Applicability of stress-force-fabric relationship for non-proportional loading. *Computers and Structures,* 89**,** 1094-1102.

LI, X. & YU, H. S. 2011b. Tensorial characterisation of directional data in micromechanics. *International Journal of Solids and Structures,* 48**,** 2167-2176.

LI, X. & YU, H. S. 2013a. On the stress-force-fabric relationship for granular materials. *International Journal of Solids and Structures,* 50**,** 1285-1302.

LI, X. & YU, H. S. 2013b. Particle scale insight into deformation non-coaxiality of granular materials. *International Journal of Geomechanics,* 10.

LI, X., YU, H. S. & LI, X. S. 2009b. Macro-micro relations in granular materials. *International Journal of Solids and Structures,* 46**,** 4331-4341.

LI, X., YU, H. S. & LI, X. S. 2013. A virtual experiment technique on the elementary behaviour of granular materials with discrete element method. *Int. J. Numer. Anal. Meth. Geomech,* 37**,** 75-96.

LI, X., YU, HAI-SUI AND LI, XIANG-SONG 2013. A virtual experiment technique on the elementary behaviour of granular materials with DEM.

International Journal for Numerical and Analytical Methods in Geomechanics 37**,** 75-96.

LI, X. S. & DAFALIAS, Y. F. 2000. Dilatancy for cohesionless soils. *Géotechnique,* 50**,** 449-460.

LI, X. S. & DAFALIAS, Y. F. 2012. Anisotropic Critical State Theory: Role of Fabirc. *Journal of Engineering Mechanics,* 138**,** 263-275.

MAHMOOD, Z. & IWASHITA, K. 2010. Influence of inherent anisotropy on mechanical behaviour of granular materials based on DEM simulations. *Int. J. Numer. Anal. Meth. Geomech,* 34**,** 795-819.

MAJMUDAR, T. S. & BEHRINGER, R. P. 2005. Contact force measurements and stress-induced anisotropy in granular materials. *Nature,* 435**,** 1079-1082.

MATSUOKA, H. & NAKAI, T. 1974. Stress-deformation and strength characteristics of soil under three different principal stresses. *Proc. of JSCE.*

MIURA, K., MIURA, S. & TOKI, S. 1986. Deformation behaviour of anisotropic dense sand under principal stress axes rotation. *Soils and Foundations,* 26**,** 36-52.

NAKATA, Y., HYODO, M., MURATA, H. & YASUFUKU, N. 1998. Flow deformation of sands subjected to principal stress rotation. *Soils and Foundations,* 38**,** 115-128.

NG, T.-T. 2005. Behaviour of gravity deposited granular material under different stress paths. *Can. Geotech. J.,* 42**,** 1644-1655.

OCHIAI, H. & LADE, P. V. 1983. Three-dimensional behaviour of sand with anisotropic fabric. *Journal of Geotechnical Engineering* 109**,** 1313-1328.

ODA, M. 1972. Deformation mechanism of sand in triaxial compression tests. *Soils and Foundations,* 12**,** 45-63.

ODA, M. 1972a. Initial fabrics and their relations to mechanical properties of granular material. *Soils and Foundations,* 12**,** 17-36.

ODA, M. & IWASHITA, K. 1999. Mechanics of granular materials: An introduction. *A A Balkema Publishers.*

ODA, M., KOISHIKAWA, I. & HIGUCHI, T. 1978. Experimental study of anisotropic shear strength of sand by plane strain test. *Soils and Foundations,* 18**,** 25-38.

ODA, M. & KONISHI, J. 1974. Microscopic deformation mechanism of granular material in simple shear. *Soils and Foundations,* 14**,** 25-38.

ODA, M., NEMAT-NASSER, S. & KONISHI, J. 1985a. Stress-induced anisotropy in granular mass. *Soils and Foundations,* 25**,** 85-97.

ODA, M., NEMAT-NASSER, S. & KONISHI, J. 1985b. Stress-induced anisotropy in granular masses. *Soils and Foundations,* 25**,** 85-97.

OUADFEL, H. & ROTHENBURG, L. 2001. Stress-force-fabric relationship for assemblies of ellipsoids. *Mechanics of Materials,* 33**,** 201-221.

PRADHAN, T. B. S., TATSUOKA, F. & HORII, N. 1988. Simple shear testing on sand in a torsional shear apparatus. *Soils and Foundations,* 28**,** 95-112.

RADJAI, F., WOLF, D., ROUX, S., JEAN, M. & MOREAU, J. 1997. Force networks in dense granular media. *In Powders and Grains pp. Rotterdam: Balkema.,* 97**,** 211-214.

READES, D. W. & GREEN, G. E. 1976. Independent stress control and triaxial extension tests on sand. *Géotechnique,* 26**,** 551-576.

ROSCOE, K. H., BASSETT, R. H. & COLE, E. R. 1967. Principal axes observed during simple shear of sand. *Proc. Conference, Oslo, 1,231-237*.

ROSCOE, K. H., SCHOFIELD, A. N. & WROTH, C. P. 1958. On the yielding of soils. *Géotechnique,* 8**,** 22-53.

ROTHENBURG, L. & BATHURST, R. J. 1989. Analytical study of induced anisotropy in idealised granular material. *Géotechnique,* 39**,** 601-614.

ROTHENBURG, L. & BATHURST, R. J. 1992. Micromechanical features of granular assemblies with planar elliptical particles. *Géotechnique,* 42**,** 79-95.

ROWE, P. W. 1962. The stress-dilatancy relation for static equilibrium of an assembly of particles in contact. *Proc. R. Soc. Lond. A,* 269**,** 500-527.

SAADA, A. S. & TOWNSEND, F. C. 1981. State of the Art: Laboratory Strength Testing of Soils. *American Society for Testing and Materials***,** 7-77.

SADREKARIMI, A. & OLSON, S. M. 2011. Critical state friction angle of sands. *Géotechnique,* 61**,** 771-783.

SAYAO, A. S. F. J. 1989. Behaviour of sand under general stress paths in the hollow cylinder torsional device. *PhD thesis, The University of British Columbia*.

SCHANZ, T. & VERMEER, P. A. 1996. Angles of friction and dilatancy of sand. *Géotechnique,* 46**,** 145-151.

SITHARAM, T. G., DINESH, S. V. & SHIMIZU, N. 2002. Micromechanical modelling of monotonic drained and undrained shear behaviour of granular media using three-dimensional DEM. *Int. J. Numer. Anal. Meth. Geomech,* 26**,** 1167-1189.

SITHARAM, T. G., VINOD, J. S. & RAVISHANKAR, B. V. 2009. Post-liquefaction undrained monotonic behaviour of sands: experimentas and DEM simulations. *Géotechnique,* 59**,** 739-749.

SIVATHAYALAN, S. & VAID, Y. P. 2002. Influence of generalized initial state and principal stress rotation on the undrained response of sands. *Can. Geotech. J.,* 39**,** 63-76.

SUN, D., HUANG, W. X. & YAO, Y. P. 2008. An experimental study of failure and softening in sand under three-dimensional stress conditions. *Granular Matter,* 10**,** 187-195.

SUTHERLAND, H. B. & MESDARY, M. S. 1969. The influence of the intermediate principal stress on the strength of sand. *In Proceedings of the seventh international conference on soil mechanics and foundation engineering, Mexico city***,** 391-399.

SYMES, M. J., GENS, A. & HIGHT, D. W. 1988. Drained principal stress rotation in saturated sand. *Géotechnique,* 38**,** 59-81.

SYMES, M. J. P. R., GENS, A. & HIGHT, D. W. 1984. Undrained anisotropy and principal stress rotation in saturated sand. *Géotechnique,* 34**,** 11-27.

THORNTON, C. 2000. Numerical simulation of deviatoric shear deformation of granular media. *Géotechnique,* 50**,** 43-53.

THORNTON, C. 2011. DEM contact force models: a verificaiton exercise. *GM3 Travelling Workshop, Imperial College,* .

THORNTON, C. & ANTONY, S. J. 1998. Quasi-static deformation of particulate media. *Phil. Trans. R. Soc. Lond. A,* 356**,** 2763-2782.

THORNTON, C. & ZHANG, L. 2006. A numerical examination of shear banding and simple shear non-coaxial flow rules. *Philosophical Magazine,* 86**,** 3425-3452.

THORNTON, C. & ZHANG, L. 2010. On the evolution of stress and microstructure during general 3D deviatoric straining of granular media. *Géotechnique,* 60**,** 333-341.

TONG, Z. X., ZHANG, J. M., YU, Y. L. & ZHANG, G. 2010. Drained deformation behaviour of anisotropic sands during cyclic rotation of principal stress axes. *Journal of Geotechnical and Geoenvironmental Engineering,* 136**,** 1509-1518.

VAID, Y. P. & CHEN, J. C. 1985. Cyclic and monotonic undrained response of saturated sands. *Advances in the Art of Testing Soils Under Cyclic Conditions (ASCE),* 120-147.

VERDUGO, R. & ISHIHARA, K. 1996. The steady state of sandy soils. *Soils and Foundations,* 36**,** 81-91.

WANG, Q. & LADE, P. V. 2001. Shear banding in true triaxial tests and its effect on failure in sand. *Journal of Engineering Mechanics,* 127**,** 754-761.

WANG, Y. N. & TONON, F. 2009. Modeling triaxial test on intact rock using discrete element method with membrane boundary. *Journal of Engineering Mechanics,* 135**,** 1029-1037.

WANG, Z. L., DAFALIAS, Y. F., LI, X. S. & MAKDISI, F. I. 2002. State pressure index for modeling sand behaviour. *Journal of Geotechnical and Geoenvironmental Engineering,* 128**,** 511-519.

WOOD, D. M. 1991. Soil behaviour and critical state soil mechanics. *Cambrige University Press.*

YAMADA, Y. & ISHIHARA, K. 1979. Anisotropic deformation characteristics of sand under three dimensional stress conditions. *Soils and Foundations,* 19**,** 79-94.

YAMADA, Y. & ISHIHARA, K. 1981. Undrained deformation characteristics of loose sand under three dimensional stress conditions. *Soils and Foundations,* 21.

YANG, L. T. 2013. Experimental study of soil anisotropy using hollow cylinder testing. *PHD thesis, The University of Nottingham.*

YANG, Z. X. & LI, X. 2007. Undrained anisotropy and rotational shear in granular soil. *Géotechnique,* 57**,** 371-384.

YANG, Z. X., LI, X. S. & YANG, J. 2008. Quantifying and modelling fabric anisotropy of granular soils. *Géotechnique,* 58**,** 237-248.

YIMSIRI, S. & SOGA, K. 2010. DEM analysis of soil fabric effects on behaviour of sand. *Géotechnique,* 60**,** 483-495.

YIMSIRI, S. & SOGA, K. 2011. Effects of soil fabric on behaviours of granular soils: Microscopic modeling. *Computers and Geotechnics,* 38**,** 861-874.

YIN, Z.-Y. & CHANG, C. S. 2009. Non-uniqueness of critical state line in compression and extension conditions. *Int. J. Numer. Anal. Meth. Geomech,* 33**,** 1315-1338.

YOSHIMINE, M., ISHIHARA, K. & VARGAS, W. 1998. Effects of principal stress direction and intermediate principal stress on undrained shear behaviour of sand. *Soils and Foundations,* 38**,** 179-188.

YU, H. S. 2008. Non-coaxial theories of plasticity for granular materials. *The 12th International Conference of International Association for Computer Methods and Advances in Geomechanics, 1-6 October, Goa, India*.